Study of B0 -> K*0 gamma, Bs0 -> phi gamma and Bs0 -> K*0 gamma decays using converted photons with the LHCb detector

Léo Beaucourt

Communauté
UNIVERSITÉ Grenoble Alpes

THÈSE

Pour obtenir le grade de

DOCTEUR DE L'UNIVERSITÉ GRENOBLE ALPES

Spécialité : **Physique subatomique et astroparticules**

Arrêté ministériel : 7 août 2006

Présentée par

Léo BEAUCOURT

Thèse dirigée par **Edwige TOURNEFIER**
et co-encadrée par **Marie-Noëlle MINARD**

préparée au sein du **Laboratoire d'Annecy-le-vieux de Physique des Particules**
et de **l'École doctorale de physique de Grenoble**

Study of $B^0 \to K^{*0}\gamma$, $B_s^0 \to \phi\gamma$ and $B_s^0 \to K^{*0}\gamma$ decays using converted photons with the LHCb detector.

Étude des désintégrations $B^0 \to K^{*0}\gamma$, $B_s^0 \to \phi\gamma$ et $B_s^0 \to K^{*0}\gamma$ à l'aide de photons convertis avec le détecteur LHCb.

Thèse soutenue publiquement le **8 décembre 2016**,
devant le jury composé de :

Monsieur, Giovanni LAMANNA
Directeur de recherche, Laboratoire d'Annecy-le-Vieux de Physique des Particules, **Président**

Madame, Arantza DE OYANGUREN CAMPOS
Directeur de recherche, Instituto de Física Corpuscular, Valencia , **Rapporteur**

Madame, Isabelle RIPP-BAUDOT
Directeur de recherche, Institut pluridisciplinaire Hubert Curien, Strasbourg , **Rapporteur**

Monsieur, Diego GUADAGNOLI
Chargé de recherche, Laboratoire d'Annecy-le-Vieux de Physique Théorique, **Examinateur**

Monsieur, Olivier DESCHAMPS
Maître de Conférences, Laboratoire de Physique Corpusculaire, Clermont-Ferrand, **Examinateur**

Madame, Edwige TOURNEFIER
Directeur de recherche, Laboratoire d'Annecy-le-Vieux de Physique des Particules, **Directeur de thèse**

"*There is a theory which states that if ever anyone discovers exactly what the Universe is for and why it is here, it will instantly disappear and be replaced by something even more bizarre and inexplicable.*

There is another theory which states that this has already happened."

Douglas Adams

Résumé

Introduction théorique:

Les désintégrations radiatives des hadrons beaux, qui s'opèrent à travers le processus $b \to s(d)\gamma$, ont des rapports d'embranchement de l'ordre de $10^{-5} - 10^{-6}$ permettant à la fois une sensibilité à la Nouvelle Physique et une grande production d'événements en accélérateur. La première observation de ces désintégrations, en particulier la désintégration $B^0 \to K^{*0}\gamma$, a été faite par l'expérience CLEO en 1993. Depuis, l'observation de nombreuses autres désintégrations ainsi que des mesures de leurs rapports d'embranchement ont été faites par différentes expériences telles que Belle (II), BaBar et maintenant LHCb. L'étude de ces désintégrations permet de mesurer les coefficients de Wilson $C_{7\gamma}$ et $C'_{7\gamma}$ qui encodent les effets à courtes distances dans de cadre d'une théorie effective de l'interaction électrofaible.

Le travail présenté dans cette thèse consiste en l'analyse de trois de ces désintégrations: $B^0 \to K^{*0}\gamma$, $B^0_s \to \phi\gamma$ et $B^0_s \to K^{*0}\gamma$. Les deux premières désintégrations correspondent au processus $b \to s\gamma$ tandis que la dernière correspond au processus $b \to d\gamma$. L'analyse présentée ici consiste en la mesure du rapport de rapports d'embranchement: $r_{\mathcal{B}} = \frac{\mathcal{B}(B^0 \to K^{*0}\gamma)}{\mathcal{B}(B^0_s \to \phi\gamma)}$.

La valeur de l'asymétrie de CP directe dans le processus $B^0 \to K^{*0}\gamma$ sera également mesurée: $A_{CP}(B^0 \to K^{*0}\gamma) = \frac{\Gamma(\bar{B}^0 \to \bar{K}^{*0}\gamma) - \Gamma(B^0 \to K^{*0}\gamma)}{\Gamma(\bar{B}^0 \to \bar{K}^{*0}\gamma) + \Gamma(B^0 \to K^{*0}\gamma)}$.

La première limite supérieure sur le rapport d'embranchement du processus $B^0_s \to K^{*0}\gamma$ sera également présentée. Une estimation naïve de $\mathcal{B}(B^0_s \to K^{*0}\gamma)$ peut être réalisée: $\mathcal{B}(B^0_s \to K^{*0}\gamma)_{(th.)} \approx \mathcal{B}(B^0 \to K^{*0}\gamma) \times \left|\frac{V_{td}}{V_{ts}}\right|^2 = (2.0 \pm 0.7) \times 10^{-6}$.

Dispositif expérimental:

Pour réaliser ces mesures, les données enregistrées par le spectromètre LHCb en utilisant les protons accélérés au LHC (CERN) en 2011 et 2012 ($3\ fb^{-1}$) seront utilisées. Le détecteur LHCb[1] est constitué de différents détecteurs qui la compose:

- Le détecteur de vertex (VELO: VErtex LOcator) qui entoure le point de collisions. Il permet une mesure précise de la position des vertex ($\Delta z \sim 71\mu m$) et participe au système de trajectographie permettant une mesure de l'impulsion des traces chargées.
- Le système de trajectographie est constitué du VELO ainsi que de cinq stations. Deux sont situées avant l'aimant et trois après permettant ainsi de mesurer avec une grande précision l'impulsion des traces chargées ($\Delta p/p \approx 0.5\%$, $p \in [5, 100] GeV/c$).
- Deux détecteurs à effet Cherenkov (RICHs) placés avant et après l'aimant permettent l'identification des traces chargées.

[1]La description détaillée de l'expérience LHCb peut être trouvée dans de nombreux documents, aussi seulement une rapide présentation de ces détecteurs et de leur rôle sera faite dans ce résumé.

- Les calorimètres consistent en quatre sous-détecteurs: le SPD qui détecte le passage des traces chargées, le PreShower qui effectue une séparation des objets electromagnétiques et hadroniques et enfin les calorimètres électromagnétique et hadronique qui mesure l'énergie déposée. La résolution en énergie du calorimètre électromagnétique (utilisé pour mesurer l'énergie d'un photon) est: $\Delta E/E \approx 9\%/\sqrt{E} \oplus 0.8\%$.
- Enfin cinq détecteurs à muons: le premier est installé avant les calorimètres et les quatre autres à la fin de la chaine de détecteurs.

L'identification de la nature des particules se fait en utilisant les informations de différents détecteurs: les RICHs, les calorimètres et les stations à muons. Ces informations sont combinées pour produire des variables d'identification de particules (variables de PID). Il existe deux types de variables utilisées dans les analyses de LHCb: celles construites à partir de fonction de vraisemblance (DLL) ou celles produites par l'application d'outils d'analyses multivariables aux réponses des détecteurs (ProbNN).

Le système de déclenchement de LHCb opère en plusieurs étapes. Le niveau 0 (L0) est un système matériel qui recherche des traces de haute énergie ou impulsion transverse et les classe en fonction de leur nature (hadrons, électrons, photons, ...). Puis une deuxième étape de système, logiciel cette fois, constitué d'un mélange de lignes de sélections réalise la reconstruction des événements.

Sélection:

La particularité de cette analyse est l'utilisation de photons convertis, c'est-à-dire des photons se convertissant en une paire électron-positron par interaction avec la matière du détecteur. Les analyses précédantes utilisaient des photons direct ne se convertissant pas. L'utilisation de photons convertis entraine une perte en nombres d'événements puisque environ 20% des photons se convertissent avant l'aimant. Mais la résolution sur l'impulsion des diélectrons (donc du photon), mesurée à l'aide des trajectographes, est amélioré par rapport à résolution de l'énergie déposée dans les calorimètres par un photon direct. Ainsi la résolution sur la masse invariante reconstruite du hadron B est plus petite dans le cas des photons convertis ($\sigma_{m_{B^0}} \sim 35\ MeV/c^2$) par rapport aux analyses utilisant des photons directs ($\sigma_{m_{B^0}} \sim 90\ MeV/c^2$). Cette amélioration de la résolution rends possible une étude du canal $B_s^0 \to K^{*0}\gamma$ dont le pic de masse est caché sous le pic de $B^0 \to K^{*0}\gamma$ avec des photons directs.

La reconstruction des photons convertis commence par la recherche de deux traces de charges opposées correspondant à un électron et un positron. Avant de combiner ces traces, les photons de Bremsstrahlung sont ajoutés en tenant compte de possible double comptage. Puis une coupure sur la masse du diélectron est appliquée aux candidats photons convertis: $m_{ee} < 100 MeV/c^2$. Seules les traces ayant des impacts mesurés avant et après l'aimant sont conservées. On distingue toutefois les traces ayant des impacts dans le VELO de celles n'en ayant pas. Les candidats reconstruits avec les traces de la première catégorie seront nommés *LL* (pour *Long tracks*) et correspondent à des conversions ayant lieu dans

le VELO, donc peu de temps après l'émission du photon. Les candidats reconstruits avec les traces de la seconde catégorie seront nommés *DD* (pour *Downstream tracks*) et correspondent à des conversions plus tardives, après le VELO ou dont le passage n'a pas été mesuré par le VELO. La résolution en énergie des événements *LL* est plus élevée que celle des événements *DD* puisque les électrons (positrons) parcourent plus de matière et donc perdent plus d'énergie par diffusion multiple. L'efficacité de la reconstruction des photons convertis appliquée sur les seuls événements *LL* et *DD* est de l'ordre de 88 % [2].

Après les photons convertis, il faut reconstruire l'ensemble de la désintégration. Deux traces hadroniques de charges opposées et avec un vertex commun décalé par rapport au vertex primaire (PV: le lieu de production du hadron B) sont recherchées. Puis un candidat photon converti provenant de ce vertex est recherché. Différents critères de qualité de reconstruction des vertex et des traces ainsi que des coupures en impulsion transverse des traces et masse invariante des objets reconstruits sont appliqués. L'efficacité de cette reconstruction (incluant l'efficacité de reconstruction des photons convertis) et de l'ordre de 0.4%

Puis, les lignes du système de déclenchement correspondant aux désintégrations étudiées sont sélectionnées. Pour cette analyse on sélectionne les lignes du système de déclenchement matériel correspondant à un électron (`L0_Electron`) et à un hadron (`L0_Hadron`) ainsi qu'une ligne générale (`L0_Global`). Concernant le système de déclenchement logiciel, plusieurs lignes sont sélectionnées sur des critères topologiques (nombre et nature des traces reconstruites dans l'événement). L'efficacité de ces sélections est de l'ordre de 20% avec des différences importantes en fonction de la date d'acquisition des données (début ou fin 2011 et 2012).

Seuls les événements avec un photon d'impulsion transverse supérieure à 1.5 GeV/c^2 sont conservés. Cette coupure rejette une grande part d'événement de bruit de fond, principalement de combinatoire. Ensuite, une série de coupures est appliquée afin d'améliorer la sélection des photons convertis en rejetant du bruit de fond combinatoire et provenant de π^0. Ainsi, une coupure bi-dimensionnelle sur la masse des diélectron et la position du vertex de production du photon selon l'axe du détecteur (z) est appliquée: $m_{ee}/MeV/c^2 - 0.04 \times z_{vtx}/mm < 20$ pour les événements *DD* et $m_{ee}/MeV/c^2 - 0.083 \times z_{vtx}/mm < 17$ pour les événements *LL*. Une coupure sur la variable de PID des électrons est également appliquée: $DLL_e > -1$. Cette coupure permet de rejeter en partie le bruit de fond provenant des pions. Enfin, une coupure sur la masse des diélectrons des événements *LL* est appliquée: $m_{ee} < 60 MeV/c^2$. Pour finir, des coupures sur les masses invariantes reconstruites des mésons K^{*0} et ϕ sont appliquées afin de réduire encore le bruit de fond combinatoire et la fenêtre en masse des $B^0_{(s)}$ est également réduite.

Une sélection basée sur des variables de PID est appliquée afin de réduire le bruit de fond venant d'événements mal identifiés: $ProbNNK(K^{\pm}) > 0.2$, $ProbNNK(\pi^{\mp}) < 0.1$

[2]Les efficacités données sont toutes estimées à l'aide d'échantillons simulés (Monte Carlo) à l'exception des efficacités de PID pour lesquelles une méthode basée sur des données est utilisée.

et $ProbNNpi * (1. - ProbNNK) * (1. - ProbNNp)(\pi^{\mp}) > 0.5$, avec une efficacité de l'ordre de 79%, dans le cas d'événements $B^0 \to K^{*0}\gamma$ et $ProbNNK(K^{\pm}) > 0.1$, avec une efficacité de l'ordre de 95%, dans le cas d'événements $B^0_s \to \phi\gamma$.

Afin de réduire la contamination des événements $B^0_{(s)} \to \phi\gamma$ dans l'échantillon de $B^0 \to K^{*0}\gamma$, une coupure sur la masse invariante de la paire $(K^{\pm}\pi^{\mp})$ où l'on fait l'hypothèse que le pion est un kaon $(m_\pi \to m_K)$ est appliquée: $m_{K\pi(\to K)} > 1040\ MeV/c^2$. Cette coupure rejette la majorité des événements $\phi\gamma$ avec une efficacité sur le signal de l'ordre de 99.8%.

Pour finir, une sélection basée sur des critères cinématiques et de reconstruction de vertex a été développée afin de réduire le bruit de fond combinatoire. Tout d'abord, les candidats $B^0_{(s)}$ doivent passer la sélection suivante: $p_T(B^0_{(s)}) > 3\ GeV/c$. Ensuite, différentes variables sont utilisées en fonction de la nature des traces e^+e^-: $p_T(\gamma) > 2.1\ GeV/c$ et $|cos(\theta_H\ (V\ meson))| < 0.89$ pour les événements DD et $acos(Dira(B^0_{(s)})) < 0.008\ rad$ et $min(log(\chi^2_{IP}(e^{\pm}))) > 0.55$ pour les événements LL. Les variables ont été choisies pour leur pouvoir de discrimination signal/bruit de fond tandis que les valeurs des coupures sont celles maximisant la significance: $S = N_{signal}/\sqrt{N_{signal} + N_{bdf}}$. L'efficacité de ces sélections est de l'ordre de 94% pour les événements DD et de l'ordre de 88% pour les événements LL.

Modélisation et ajustement:

Les modèles des différentes contributions au spectre de masse invariante $m_{B^0_{(s)}}$, que ce soit signal ou bruits de fond, sont extraites d'ajustements des distributions issues d'échantillons Monte Carlo. Seul le modèle du bruit de fond combinatoire $K^{\pm}\pi^{\mp}e^+e^-$ est extrait de l'ajustement de la partie supérieure du spectre dans les données où seul ce bruit de fond contribue. Un ajustement sur les données est effectué simultanément sur six échantillons: pour chaque configuration DD et LL on distingue les événements $B^0 \to K^{*0}(K^+\pi^-)\gamma$, $\bar{B}^0 \to \bar{K}^{*0}(K^-\pi^+)\gamma$ et $B^0_s \to \phi\gamma$. De cet ajustement on extraie simultanément la valeur de l'asymétrie brute dans l'échantillon $B^0 \to K^{*0}\gamma$: $A_{RAW} = \frac{N(\bar{B}^0) - N(B^0)}{N(\bar{B}^0) + N(B^0)}$ ainsi que la valeur du rapport de nombres d'événements reconstruits: $r_y = N(B^0 \to K^{*0}\gamma)/N(B^0_s \to \phi\gamma)$.

Les paramètres libres de cet ajustement sont, en plus de A_{RAW} et r_y: le nombre total d'événements $B^0 \to K^{*0}\gamma$, le ratio d'événements DD sur le nombre total d'événement B^0 et B^0_s, la valeur centrale de la distribution en masse du B^0 dans la configuration DD, les paramètres décrivant la pente de l'exponentielle utilisée pour décrire le bruit de fond combinatoire à la désintégration $B^0_s \to \phi\gamma$ dans les configurations DD et LL et enfin douze amplitudes relatives aux bruits de fond dont la contamination n'a pas pu être estimée à l'aide d'échantillons Monte Carlo (combinatoire, $K^{*0}\pi^0 + X$). Enfin, les différences en masse entre les cas DD et LL, extraite de l'ajustement sur l'échantillon de signal Monte Carlo, et entre le B^0 et le B^0_s, mesurée expérimentalement, sont laissées libres dans l'ajustement mais une contrainte gaussienne leur est appliquée.

Le résultat de l'ajustement donne les valeurs suivantes: $A_{RAW} = (2.9 \pm 2.5)\%$ et $r_y = 7.32 \pm 0.56$. La validité de l'ajustement a été vérifié à l'aide de pseudos-données générées depuis le résultat de l'ajustement. Ces pseudos-distributions ont été ajustée à l'aide du même modèle et aucun biais n'a été observé.

Étude systématique et résultats:

Toutes les sources d'incertitudes systématiques ont été étudiées, et les valeurs d'incertitude systématique résultantes ΔA_{RAW} et $\Delta r_{\mathcal{B}}$ ont été estimée. Les sources d'incertitudes systématiques contributives sont: les différences observées entre données et simulations (distributions des variables, calculs d'efficacités et les taux d'événements dans les différentes lignes de système de déclenchement matériel), le modèle d'ajustement, l'asymétrie de CP dans la désintégration $B^0 \to K^{*0}e^+e^-$, les événements doublement mal identifiés ($K^\pm\pi^\mp \leftrightarrow \pi^\pm K^\mp$) et le changement de polarité de l'aimant de LHCb au cours des prises de données. Les incertitudes et corrections systématiques résultantes sont donc: $\Delta A_{RAW} = -0.001 \pm 0.009$ et $\Delta r_{\mathcal{B}} = +0.003 \pm 0.045$.

On peut maintenant obtenir la valeur de $r_{\mathcal{B}}$ à partir des valeurs issues de l'ajustement sur les données:

$$r_{\mathcal{B}} = \frac{\mathcal{B}(B^0 \to K^{*0}\gamma)}{\mathcal{B}(B_s^0 \to \phi\gamma)} = \frac{N_{B^0\to K^{*0}\gamma}}{N_{B_s^0\to\phi\gamma}} \times \frac{\mathcal{B}(\phi \to K^+K^-)}{\mathcal{B}(K^{*0} \to K^+\pi^-)} \times \frac{f_s}{f_d} \times \frac{\epsilon(B_s^0 \to \phi\gamma)}{\epsilon(B^0 \to K^{*0}\gamma)}$$

où: $r_y = \frac{N_{B^0\to K^{*0}\gamma}}{N_{B_s^0\to\phi\gamma}}$ est extrait de l'ajustement sur les données, $\frac{\mathcal{B}(\phi\to K^+K^-)}{\mathcal{B}(K^{*0}\to K^+\pi^-)}$ et $\frac{f_s}{f_d}$ sont estimés à partir de résultats expérimentaux et $\frac{\epsilon(B_s^0\to\phi\gamma)}{\epsilon(B^0\to K^{*0}\gamma)}$ est estimé à l'aide d'échantillons Monte-Carlo. En incluant les incertitudes systématiques, le résultat est: $r_{\mathcal{B}} = 1.63 \pm 0.13(stat) \pm 0.08(syst) \pm 0.13(f_s/f_d)$

Ce résultat est compatible avec la dernière mesure expérimentale (LHCb) à 2.3σ et avec la prédiction théorique à 1.8σ. La valeur finale de l'asymétrie de CP dans la désintégration $B^0 \to K^{*0}\gamma$ se calcule selon la formule suivante: $A_{CP}(B^0 \to K^{*0}\gamma) = A_{RAW} - A_D(K\pi) - \kappa A_P(B^0)$
où: $A_D(K\pi)$ correspond à l'asymétrie de détection qui tient compte du fait qu'un K^+ et un K^- n'interagissent pas de manière identique avec le détecteur, $A_P(B^0)$ correspond à l'asymétrie de production qui tient compte du fait que B^0 et $\bar{B}^0$ ne sont pas nécessairement produits avec des taux similaires dans les collisions proton-proton du LHC et endin κ correspond à un facteur de dilution qui tient compte des oscillations $B^0/\bar{B}^0$. Ces trois paramètres ont été estimés dans des analyses précédentes à: $+0.013 \pm 0.004$. La valeur mesurée de l'asymétrie de CP dans la désintégration $B^0 \to K^{*0}\gamma$ est: $A_{CP}(B^0 \to K^{*0}\gamma) = (4.1 \pm 2.5(stat) \pm 1.2(syst))\%$.

Ce résultat est compatible avec les mesures expérimentales à 1.4σ et avec la prédiction théorique à 1.7σ.

Comme l'ajustement sur les données ne laisse apparaître aucune contribution significative de la désintégration $B_s^0 \to K^{*0}\gamma$, une limite supérieure sur le rapport d'embranchement de cette désintégration a été estimée à l'aide d'une méthode statistique de CL_s. La limite est donnée pour les intervalles de confiance de 90% et 95%: $\mathcal{B}(B_s^0 \to K^{*0}\gamma) < 6.0(7.3) \times 10^{-6}$ *at* 90%(95%) CL.

Les principales sources d'incertitudes systématiques ont été introduites comme des contraintes gaussiennes sur certains paramètres des ajustements réalisés pour obtenir ces valeurs. C'est la première fois qu'une limite sur le rapport d'embranchement de ce processus rare est mesurée.

Conclusion :

Comme mentionné en introduction, l'étude des désintégrations radiatives (rapports d'embranchement, asymétries de CP, ...) est très intéressant dans le cadre de la recherche de Nouvelle Physique. En particulier, ces désintégrations sont sensibles aux coefficients de Wilson $C_{7\gamma}^{(\prime)}$. Les mesures effectuées dans cette analyse peuvent donc contribuer à améliorer la mesure de ces coefficients de Wilson et contraindre le champ des possibles de la Nouvelle Physique. Dans un futur proche, il sera également possible d'effectuer une mesure du rapport d'embranchement du processus rare $B_s^0 \to K^{*0}\gamma$ qui pourra également contribuer à contraindre les valeurs possibles des $C_{7\gamma}^{(\prime)}$.

Acknowledgements

I would first like to thank my supervisor Edwige Tournefier who proposed me to work on this subject and for all the valuable tips and helps she provides me during these three years (and a little bit more). Many thanks also to Marie-Noëlle Minard for all the questions she asked me which help me to go ahead in my work, and also for all the answers she provides me.

I would also thank all the members of the LHCb team at LAPP for their welcome, helps and discussions. Special thanks to Philippe Ghez with whom I shared the office all this time and for all these coffee breaks and sports discussions.

Of course, I would like to thank all the people at LAPP and in others institutes with whom I work and/or spend times.

Many thanks to all "youngs" at LAPP for all these ping-pong matches, board game sessions or (in the rare times I came) drinks after work.

A very special thanks to my family and my friends that I love so much and in particular to my wife and my son without whom I would never be able to follow through these three years.

À Camille et à Jules, les deux amours de ma vie.

Contents

Chapter 1

Introduction

The main goal of Particle Physics field is to understand the nature and the interaction between the elementary objects of the nature, the quarks and leptons, and to build a predictive theoretical model to describe it. Today, the most precise and powerful model is the Standard Model of Particles Physics. It has predicted several new particles which have been discovered in experiments and brings answers to some issues observed during the last part of the previous century, such as the masses of the fermions, which find a pleasing explanation through the introduction of the electroweak symmetry breaking into the theory. The discovery of the Higgs boson in 2012 was the latest experimental probe of the success of the Standard Model.

However, some open questions, which are discussed in this thesis, are still not resolved and point out the limits of the Standard Model. In the last decades, physicists investigated the tension points between the Standard Model and the experimental results in order to find indications of the existence and the nature of the New Physics behind the Standard Model. A way to search for New Physics is by determining with high precision physical observables related to the parameters of the Standard Model in order to constrain them. If both experimental and theoretical uncertainties on these observables are small enough, any deviation from the Standard Model predictions is a clear indication of New Physics.

This approach has been used in the B and K decays studied at BaBar, Belle and now LHCb. These experiments have measured precisely the parameters of the Cabibbo-Kobayashi-Maskawa matrix which encodes charged weak transitions in the Standard Model. Small discrepancies have been observed, but results are in a good agreement with the theory predictions. The radiative decays of B mesons (e.g. decays with a photon in the final state) are very suppressed in the Standard Moded, with branching ratios of the order of 10^{-5}, and are very good laboratories to search for New Physics. Several observables, such as their branching fraction or the CP asymmetry can be used to constrain the allowed range for New Physics.

The main difficulty to study these radiative decays is to reconstruct the energy of the

photon with a good resolution. For that, calorimeters are usualy used. The purpose of the work presented in this thesis is to study radiative decays using only events where the photon has created an electron-positron pair by interacting with the material of the detector. These photons are called *converted photons*. As the produced electron and positron are charged particles, it is possible to use the tracking system information in order to reconstruct these events. This leads to an improvement of the resolution on the reconstructed B hadron mass with respect to the non-converted photons. This thesis is focused on the $B^0 \to K^{*0}\gamma$ and $B_s^0 \to \phi\gamma$ decays and a measurement of the ratio of their branching fraction. Measuring a ratio of branching fractions cancels most of the large sources of systematic uncertainties compared to measuring branching fractions independently. These uncertainties come from the luminosity estimation, the computation of trigger and selection efficiencies which are common uncertainties for both $B^0 \to K^{*0}\gamma$ and $B_s^0 \to \phi\gamma$ decays. A measurement of the direct CP asymmetry in the $B^0 \to K^{*0}\gamma$ decay is also performed and a limit is set on the unseen $B_s^0 \to K^{*0}\gamma$ decay.

In the first chapter of this thesis, the theoretical background is presented. It begins with a brief description of the Standard Model and the CP asymmetry, then the Standard Model is reformulated into an effective theory in which it is possible to add the possible contribution from New Physics. The radiative decays and their interest for the New Physics search is presented.

The next chapter presents a description of the experimental setup: the LHC collider and the LHCb detector. The LHCb trigger as well as the reconstruction of the converted photons and the particles identification are also discussed.

The fourth and fifth chapters are dedicated to the analysis. First all the selection criteria developped to separate the signal from the different background contributions are described. All the background contributions are studied. Simulated samples are used to compute selection efficiencies.

To finish, the fifth chapter presents how the signal and background models are built from the simulation and the result of the fit of this model to the data. The results and the study of the systematic uncertainties are presented. The final results of the ratio of branching fractions of the $B^0 \to K^{*0}\gamma$ and $B_s^0 \to \phi\gamma$ decays and the direct CP asymmetry in the $B^0 \to K^{*0}\gamma$ decay are given. The method used to set a limit on the branching fraction of the $B_s^0 \to K^{*0}\gamma$ decay is presented.

Chapter 2

Theoretical framework

In this chapter, a very brief introduction to the Standard Model of the particle physics is presented. It starts with the description of the four fundamental interactions and their relative Lagrangian. Then the violation of the CP symmetry is presented in order to introduce its formalism in the Standard Model. This first part of this chapter ends with a short list of the main observed issues of the Standard Model. It allows to introduce the New Physics research. First is described how the Standard Model can be expressed as an effective theory and the way the New Physics effect can be introduced. Then, some of the main laboratories to search for New Physics in rare decays are presented and a particular attention is given to the radiative decays. Observables related to these decays, as the photon polarisation, are discussed. This chapter ends with a status on the latest constraints on some parameters of the Standard Model expressed as an effective theory for which the radiative decays are very sensitive.

2.1 Standard Model and CP violation

2.1.1 The Standard Model of particle physics

The Standard Model (SM) of Particle Physics is the theoretical framework which describes three of the four fundamental forces: the strong interaction and the electroweak interaction (the unification of the electromagnetic and weak forces into a common formalism). The SM is a gauge theory based on the symmetry group:

$$SU(3)_c \otimes SU(2)_L \otimes U(1)_Y \tag{2.1}$$

where $SU(3)_c$ is the gauge group describing the strong interaction (the c subscript corresponds to the color charge) and $SU(2)_L \otimes U(1)_Y$ is the gauge group describing the electroweak force. $SU(2)$ refers to the weak isospin (the L subscript means it involves left handed states only) and the $U(1)_Y$ refers to the weak hypercharge.

Electromagnetic interaction

The electromagnetic force is mediated by the photon and its dynamic is described by the following Lagrangian:

$$\mathcal{L} = \bar{\psi}(i\gamma^\mu \partial_\mu - m)\psi - q\bar{\psi}\gamma^\mu \psi A_\mu - \frac{1}{4}F_{\mu\nu}F^{\mu\nu} \tag{2.2}$$

where the first part is the free fermion Lagrangian and the middle term describes the interaction between the vector field and the fermion current $\bar{\psi}\gamma^\mu\psi$ with a strength measured by q, the electric charge of the fermion. A_μ is the photon field. The last term is the kinetic Lagrangian term for the vector field where $F_{\mu\nu}$ is the electromagnetic field strength tensor and is defined as:

$$F_{\mu\nu} = \partial_\mu A_\nu - \partial_\nu A_\mu \tag{2.3}$$

Strong interaction

The strong force is mediated by gluons, and is acting on quarks. This force is responsible of the quark confinement into the hadrons. The six quarks are separated into three families in which there is two flavours of quarks usually referred as *Up* and *Down* quarks with reference to the first family quarks. There is another quantum number related to the strong interaction: the color charge of the quarks, which can be red, blue or green. The Lagrangian which describes the dynamic of the strong force for a particular flavour of the quark of one family is similar to the Lagrangian of the electromagnetic force:

$$\mathcal{L} = [i\bar{\psi}\gamma^\mu \partial_\mu \psi - m\bar{\psi}\psi] - g_s(\bar{\psi}\gamma^\mu \frac{\lambda_a}{2}\psi)G^a_\mu + \frac{1}{4}g^a_{\mu\nu}g^{\mu\nu}_a \tag{2.4}$$

where, as well as for the electromagnetic Lagrangian, the first term is the free quark Lagrangian for a given flavor. The quark field ψ is made of three components, one per color charge:

$$\psi = \begin{pmatrix} \psi_r \\ \psi_b \\ \psi_g \end{pmatrix} \ , \ \bar{\psi} = (\bar{\psi_r} \ \bar{\psi_b} \ \bar{\psi_g}) \tag{2.5}$$

The second term in Eq. 2.4 describes the interaction of the quark current $j^a_\mu = \bar{\psi}\gamma^\mu\lambda_a\psi$ with the gluon field G^a_μ, where a is the color index and λ_a are the Gell-Mann matrices. There are 8 Gell-Mann matrices, corresponding to the 8 gluons (a=1,...,8). g_s is the strong force coupling constant, representing the strength of the interaction. The last term represents the kinetic term of the gluon field and $g^a_{\mu\nu}$ is the strong field strength tensor:

$$g^{\mu\nu}_a = \partial^\mu G^\nu_a - \partial^\nu G^\mu_a - g_s f_{abc} G^\mu_b G^\nu_c \tag{2.6}$$

where f_{abc} is the structure constant of the $SU(3)_c$ group and is defined as:

$$\left[\frac{\lambda_a}{2}, \frac{\lambda_b}{2}\right] = i f_{abc} \frac{\lambda_c}{2} \tag{2.7}$$

Since the $SU(3)_c$ group is non abelian, this last term introduces couplings between three or four gluons.

Electroweak interaction

With the electroweak force, fermions can interact throughout the charged currents $j^\pm_\mu$, mediated by $W^\pm$ gauge bosons or neutral currents j^Y_μ, mediated by Z and γ gauge bosons. The charged currents of the ν_e interaction with a e^- can be written as:

$$j^-_\mu = \bar{\nu_L}\gamma_\mu e_L \tag{2.8}$$

$$j^+_\mu = \bar{e_L}\gamma_\mu \nu_L \tag{2.9}$$

Only left handed fermions can interact via these charged currents. It is possible to write the quarks and leptons fields q_L and l_L as left handed doublets, the quark family structure is the same as for strong interaction with an *Up* and a *Down* quark type per doublet:

$$q_L = \begin{pmatrix} u_L \\ d_L \end{pmatrix} \ ; \ l_L = \begin{pmatrix} \nu_e \\ \bar{e_L} \end{pmatrix} \tag{2.10}$$

Fermions can also interact through neutral currents which, in the case of left handed leptons, can be written as:

$$j_\mu^3 = \frac{1}{2}\bar{\nu_{lL}}\gamma_\mu\nu_{lL} - \frac{1}{2}\bar{l_L}\gamma_\mu l_L \tag{2.11}$$

Whereas, only left handed fermions interact through charged current, right handed fermions also interact through neutral current. Only massive quarks and leptons have right handed component. Therefore, in addition to the two left handed fermions doublets q_L and l_L, three singlets are added: u_R, d_R and e_R, corresponding to right handed up, right handed down and right handed electron singlets, respectively. It is necessary to introduce the weak *hypercharge* Y defined via the Gell-Mann–Nishijima formula which links the electric charge Q of a particle to its weak isospin I_3 and Y [1] [2]:

$$Q = I_3 + \frac{Y}{2} \tag{2.12}$$

Therefore, the *weak hypercharge* j_μ^Y is written as:

$$j_\mu^Y = 2j_\mu^{EM} - 2j_\mu^3, \tag{2.13}$$

where, j_μ^{EM} is the electromagnetic current which for the leptons is written as:

$$j_\mu^{EM} = -\bar{l_L}\gamma_\mu l_L - \bar{l_R}\gamma_\mu l_R, \tag{2.14}$$

where l_R is the right handed leptons field. Then, the weak hypercharge current is:

$$j_\mu^Y = -2\bar{l_R}\gamma_\mu l_R - \bar{l_L}\gamma_\mu l_L - \bar{\nu_{lL}}\gamma_\mu\nu_{lL} \tag{2.15}$$

The neutral current mediators are a mixture of the neutral W^3 field of the weak $SU(2)_L$ and the weak hypercharge field B^μ of the $U(1)_Y$. These physical bosons are:

$$\begin{aligned} Z^\mu &= W_3^\mu cos\theta_W - B^\mu sin\theta_W \\ A^\mu &= W_3^\mu sin\theta_W + B^\mu cos\theta_W \end{aligned} \tag{2.16}$$

where, θ_W is the weak mixing angle. A^μ can be identified as the photon while Z^μ is the second neutral boson often referred as the Z. The kinetic term of the Lagrangian for the electroweak field is:

$$\mathcal{L}_{kinetic} = -\frac{1}{4}W_{\mu\nu}^i W_i^{\mu\nu} - \frac{1}{4}B_{\mu\nu}B^{\mu\nu} \tag{2.17}$$

where $W_i^{\mu\nu}$ $(i = 1, 2, 3)$ and $B^{\mu\nu}$ are the field strength tensors for the weak isospin and weak hypercharge fields, defined as follow:

$$\begin{aligned} W_i^{\mu\nu} &= \partial^\mu W_i^\nu - \partial^\nu W_i^\mu - g\epsilon_{ijk}W_j^\mu W_k^\nu \\ B^{\mu\nu} &= \partial^\mu B^\nu - \partial^\nu B^\mu \end{aligned} \tag{2.18}$$

where ϵ_{ijk} are the structure constants of the $SU(2)$ group, and defined from the Pauli matrices commutation relations:

$$\left[\frac{\sigma_i}{2}, \frac{\sigma_j}{2}\right] = i\epsilon_{ijk}\frac{\sigma_k}{2} \tag{2.19}$$

Electroweak symmetry breaking

At this point, all the masses of the boson fields and fermions vanish since the corresponding Lagrangian terms are not invariant under $SU(2) \otimes U(1)$. If the photon is indeed massless, others bosons as well as fermions are massive. Therefore, the $SU(2)_L \otimes U(1)_Y$ symmetry is broken by introducing a complex scalar field with a non zero vacuum expectation ($\frac{v}{\sqrt{2}}$), referred as ϕ [3]. The relative Lagrangian is:

$$\mathcal{L} = \partial^\mu \phi^\dagger \partial_\mu \phi - V(\phi) \tag{2.20}$$

where the potential $V(\phi)$ contains either mass and interaction terms:

$$V(\phi) = \mu^2 \phi^\dagger \phi + \lambda(\phi^\dagger \phi)^2 \tag{2.21}$$

As for the left handed fermions, a scalar $SU(2)$ doublet is introduced:

$$\phi = \begin{pmatrix} \phi^{(+)} \\ \phi^{(0)} \end{pmatrix} \tag{2.22}$$

The choice of the charge is led by the fact that, to be invariant under $SU(2)_L \otimes U(1)_Y$, the hypercharge must be 1. The Lagrangian for these scalar fields is:

$$\mathcal{L}_H = (D_\mu \phi)^\dagger (D_\mu \phi) - \mu^2 \phi^\dagger \phi - \lambda(\phi^\dagger \phi)^2 \tag{2.23}$$

with $\lambda > 0$ and $\mu^2 < 0$. D^μ is the covariant derivative:

$$D^\mu \phi = [\partial^\mu + igW^\mu + ig^{'} y_\phi B^\mu]\phi \tag{2.24}$$

Where $g = \frac{e}{sin\theta_W}$ and $g^{'} = \frac{e}{cos\theta_W}$ are the coupling constants of the electroweak interaction and y_ϕ is defined as: $y_\phi = Q_\phi - T_3 = \frac{1}{2}$ where Q_ϕ is the electromagnetic charge and T_3 is the proper value of the operator $\sigma_3/2$ for the $\phi^{(0)}$. According to the choice of the unitarity gauge, the charged field $\phi^{(+)}$ can be set to 0 and $\phi^{(0)}$ is real. Therefore, the ϕ scalar field becomes:

$$\phi = \begin{pmatrix} 0 \\ \frac{v+H}{\sqrt{2}} \end{pmatrix} \tag{2.25}$$

H is a real field corresponding to the Higgs boson. Including this expression into the Lagrangian density given in Eq. 2.23, the following couplings to the gauge bosons are obtained:

$$\mathcal{L}_H = \frac{1}{2}\partial_\mu H \partial^\mu H + \frac{g^2}{4}(v+H)^2 [W_\mu^\dagger W^\mu + \frac{1}{2cos^2\theta_W} Z_\mu Z^\mu] \tag{2.26}$$

This term introduces masses for the electroweak bosons and these masses are related:

$$M_W = \frac{1}{2} vg = M_Z cos\theta_W \tag{2.27}$$

It is not allowed to introduce a fermionic mass term such as: $\mathcal{L}_m = -m\bar{\psi}\psi$ since it breaks the gauge symmetry. However, it is possible to write a lagrangian corresponding to the coupling of the fermions doublets with the scalar doublet ϕ introduced above. The associated coupling constant can be connected to the mass of the fermions. In the unitary gauge, this Yukawa lagrangian becomes:

$$\mathcal{L}_Y = -(1 + \frac{H}{v})[m_{q_d}\bar{q_d}q_d + m_{q_u}\bar{q_u}q_u + m_l\bar{l}l] \tag{2.28}$$

The fermion masses are free parameters of the theory and have to be measured experimentally.

2.1.2 The CP symmetry violation

Symmetries in physics, which could be discrete or continuous, are seen as the invariance of a system under a certain type of transformation. The invariance under a symmetry can be translated into a conservation law. For instance, invariance under time translation results in the conservation of the energy while rotational invariance results in the conservation of the angular momentum.

In the quantum field theory, three discrete symmetries are introduced, the symmetry of charges (C), of parity (P) and of time (T). The first one is the transformation which relates a particle with its anti-particle. The P symmetry transforms the quadri-momentum of a particle as follows:

$$P : (t, \overrightarrow{x}) \mapsto (t, -\overrightarrow{x}) \tag{2.29}$$

As a direct consequence of the P symmetry, the momentum vector is also changed: $P : \overrightarrow{p} \mapsto -\overrightarrow{p}$. However, the angular momentum is conserved: $P : \overrightarrow{L} \mapsto \overrightarrow{L}$. Then, the T symmetry is the transformation which reverses the time of a system:

$$T : (t, \overrightarrow{x}) \mapsto (-t, \overrightarrow{x}) \tag{2.30}$$

These symmetries are conserved by the strong and the electromagnetic interaction. Schwinger (1951) [4], Lüders (1954) [5] and Pauli (1956) [6] have shown that, on the most general assumptions (causality, locality, Lorentz invariance), any quantum field theory is invariant under the combined operations of C, P and T. This is known as the CPT theorem and, as a direct consequence, the mass and the lifetime of a particle are exactly the same as for antiparticle. The most sensitive test of the CPT theorem to date is the K^0– $\overline{K}^0$ masses difference [7]:

$$|m_{\overline{K}^0} - m_{K^0}| < 4 \times 10^{-19}. \tag{2.31}$$

The parity violation in the weak interactions has been predicted in 1956 by Lee and Yang [8] and observed experimentally by Wu *et al.* the same year [9]. The violation of the C symmetry in the weak interactions have been demonstrated by the observation of

large differences between right handed and left handed neutrinos by Goldhaber, Grodzins and Sunyar in 1958 [10]. The CP symmetry was considered to be non violated until Christenson, Cronin, Fitch and Turlay demonstrated the CP violation in the decays of neutral kaons: $K^0_{\rm L} \to \pi^+\pi^-$ [11].

Considering a generic neutral meson M^0 produced in strong interactions. Its flavor eigenstates: $|M^0\rangle$ and $|\bar{M}^0\rangle$ are not CP eigenstates:

$$\begin{array}{l} CP|M^0\rangle = |\bar{M}^0\rangle \\ CP|\bar{M}^0\rangle = |M^0\rangle \end{array} \tag{2.32}$$

The relative CP eigenstates are constructed as follows:

$$\begin{array}{l} M_+ = \frac{1}{\sqrt{2}}(|M^0\rangle + |\bar{M}^0\rangle) \\ M_- = \frac{1}{\sqrt{2}}(|M^0\rangle - |\bar{M}^0\rangle) \end{array} \tag{2.33}$$

Therefore, the flavor eigenstates can be written in terms of the CP eigenstates (the $\frac{1}{\sqrt{2}}$ is for normalisation):

$$\begin{array}{l} M^0 = \frac{1}{\sqrt{2}}(|M_+\rangle + |M_-\rangle) \\ \bar{M}^0 = \frac{1}{\sqrt{2}}(|M_+\rangle - |M_-\rangle) \end{array} \tag{2.34}$$

The time evolution of the flavor eigenstates is described by the following equation:

$$i\frac{d}{dt}\psi = \mathcal{H}\psi, \quad \psi = \begin{pmatrix} M^0 \\ \bar{M}^0 \end{pmatrix} \tag{2.35}$$

where, $\mathcal{H}$ is the Hamiltonian. It is written as the combination of two hermitian matrices $\mathcal{M}$ and Γ which represent the mass and the decay width of the neutral meson, respectively:

$$\mathcal{H} = \mathcal{M} - \frac{i}{2}\Gamma \tag{2.36}$$

As the CPT invariance requires the masses and the decay rates of the particle and the anti-particles to be equal, the diagonal elements of the $\mathcal{H}$ matrix are equal: $\mathcal{H}_{11} = \mathcal{H}_{22}$. The fact that the $\mathcal{M}$ and Γ matrices are hermitian implies that $\mathcal{H}_{21} = \mathcal{M}^*_{12} - \frac{i}{2}\Gamma^*_{12}$. The eigenstates of this Hamiltonian are the physical states: heavy one (H) and light one (L). These eigenstates can be written as:

$$\mathcal{H}|M_{H,L}\rangle = (m_{H,L} - \frac{i}{2}\Gamma_{H,L})|M_{H,L}\rangle \tag{2.37}$$

Both M_H and M_L states have distinct masses: $m_H \neq m_L$ and distinct decay widths: $\Gamma_H \neq \Gamma_L$. The mass and decay width differences as well as the average decay width $\bar{\Gamma}$ are defined as:

$$\Delta m \equiv m_H - m_L, \quad \Delta\Gamma \equiv \Gamma_L - \Gamma_H, \quad \bar{\Gamma} \equiv \frac{1}{2}(\Gamma_H + \Gamma_L) \tag{2.38}$$

It is now possible to write the physical eigenstates in terms of the flavour eigenstates as:

$$
\begin{aligned}
|M_H\rangle &= \frac{1}{\sqrt{|q|^2+[p|^2)}}(p|M^0\rangle + q|\bar{M}^0\rangle) \\
|M_L\rangle &= \frac{1}{\sqrt{|q|^2+[p|^2)}}(p|M^0\rangle - q|\bar{M}^0\rangle)
\end{aligned}
\tag{2.39}
$$

From these equations it can be deduced that if the CP symmetry is not violated ($\frac{p}{q} = 1$), the physical states coincide with the CP eigenstates.

Three types of CP violation can be observed:

- The CP violation can occur in the mixing of the neutral meson. This is due to the fact that $|q| \neq |p|$ and so physical states do not correspond to flavour eigenstates.
- The second type of CP violation occurs if the decay amplitude of a process and its CP conjugate are not equal:

$$
\Gamma(M^0 \to f) \neq \Gamma(\bar{M}^0 \to \bar{f}) \quad \Longrightarrow \quad \left|\frac{A(\bar{M}^0 \to \bar{f})}{A(M^0 \to f)}\right| \neq 1 \tag{2.40}
$$

  where Γ are the decay widths and A the related amplitudes. This is often called "direct" CP violation and is the only one available for charged particles which cannot mix. The CP violation measurement presented in this thesis is a "direct" CP violation.

- The last type of CP violation occurs in interference of mixing and decay, when the meson and its anti-meson can decay to a common final state configuration.

$$
\Gamma(M^0 \to \bar{M}^0 \to f) \neq \Gamma(\bar{M}^0 \to M^0 \to f) \tag{2.41}
$$

2.1.3 The CKM matrix

In 1964, the CP violation was observed and the known quarks were: u, d and s. The theory of Cabibbo described the interaction between the u and the d or s quarks by introducing the Cabibbo angle [12]. In 1973, Kobayashi and Maskawa introduced the Cabibbo-Kobayashi-Maskawa (CKM) matrix which describes the interaction between the *Up* quarks and the *Down* quarks [13]. Since the CPT symmetry is not violated while the CP one is, the T symmetry should be violated too. Therefore, the CKM matrix shall be complex. The CKM matrix is a unitary matrix: $V^\dagger V = 1$. Assuming N is the number of quark families, N is also the dimension of the CKM matrix. For N = 2 families, the number of parameters for a complex unitary matrix is only one: the Cabibbo angle. But, for N = 3 families, there are four parameters, correspondings to three Cabibbo angles, referred as $\theta_{12,23,13}$, and a phase δ: the CP violation is possible.

This prediction of three quarks (and leptons) families has been experimentally confirmed by the discovery of the c quark in 1974 [14], the τ in 1975 [15], the b quark in

1977 [16] and the t quark in 1995 [17] [18].

The CKM matrix can be parametrized as follows:

$$V_{CKM} = \begin{pmatrix} V_{ud} & V_{us} & V_{ub} \\ V_{cd} & V_{cs} & V_{cb} \\ V_{td} & V_{ts} & V_{tb} \end{pmatrix} = \begin{pmatrix} c_{12}c_{13} & s_{12}c_{13} & s_{13}e^{-i\delta} \\ -s_{12}c_{23} - c_{12}s_{23}s_{13}e^{i\delta} & c_{12}c_{23} - s_{12}s_{23}s_{13}e^{i\delta} & s_{23}c_{13} \\ s_{12}s_{23} - c_{12}c_{23}s_{13}e^{i\delta} & -c_{12}s_{23} - s_{12}c_{23}s_{13}e^{i\delta} & c_{23}c_{13} \end{pmatrix} \tag{2.42}$$

where, $c_{ij} = cos\ \theta_{ij}$ and $s_{ij} = sin\ \theta_{ij}$ and θ_{ij} are the the mixing angles of the three quark families: the Cabibbo angles. The elements of the CKM matrix are measured by experiments:

- $|V_{ud}|$: study of β decays ($n \to pe^-\bar{\nu}_e$, $p \to ne^+\nu_e$)
- $|V_{us}|$: semileptonic decays of kaons: $K \to (\pi)l\nu_l$ and $\tau \to K\nu_\tau$ decay. Also accessible through $|V_{us}/V_{ud}|$ measurement ($K \to \mu\nu/\pi \to \mu\nu$ and $\tau \to K\nu/\tau \to \pi\nu$)
- $|V_{ub}|$: semileptonic decays: $B \to X_u l\nu$
- $|V_{cd}|$: semileptonic decays of D mesons, c particles production by neutrino anti-neutrino interactions
- $|V_{cs}|$: semileptonic decays of D mesons, leptonic decays of D_s^+
- $|V_{cb}|$: semileptonic decays of B mesons in c particles
- $|V_{td}|$ and $|V_{ts}|$: neutral B mesons oscillations
- $|V_{tb}|$: measurement of the ratio of branching fractions: $\frac{\mathcal{B}(t \to Wb)}{\mathcal{B}(t \to Wq)}$

The values of all the V_{ij} elements of the CKM matrix are extracted using all the experimental data. The most recent results [7] are:

$$V_{CKM} = \begin{pmatrix} |V_{ud}| = 0.97427 \pm 0.00014 & |V_{us}| = 0.22536 \pm 0.00061 & |V_{ub}| = 0.00355 \pm 0.00015 \\ |V_{cd}| = 0.22522 \pm 0.00061 & |V_{cs}| = 0.97343 \pm 0.00015 & |V_{cb}| = 0.0414 \pm 0.0012 \\ |V_{td}| = 0.00886^{+0.00033}_{-0.00032} & |V_{ts}| = 0.0405^{+0.0011}_{-0.0012} & |V_{tb}| = 0.99914 \pm 0.00005 \end{pmatrix} \tag{2.43}$$

It shall be noticed that a clear hierarchy is visible between the elements of the CKM matrix. The diagonal elements are close to 1 while a symmetry is observed between the lateral elements. The elements corresponding to the transition between the first and the second quark families are bigger than those corresponding to the transition of the second and the third families which are bigger than those corresponding to the transition of the first and the third families. The hierarchy of the elements of the CKM matrix is sketched in the Fig. 2.1.

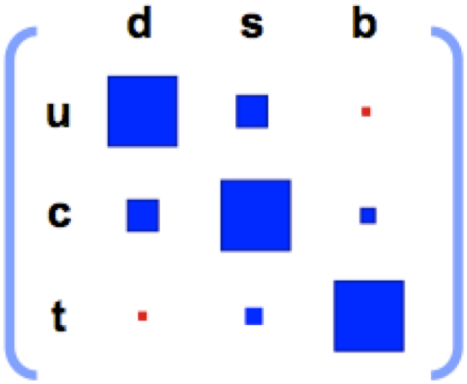

Figure 2.1: Sketch of the magnitude hierarchy between the elements of the CKM matrix.

A common parametrization of the CKM matrix is the Wolfenstein parametrization. The CKM matrix is written as a function of four parameters: λ, A, ρ and η, defined as:

$$\begin{aligned} \lambda = s_{12} = V_{us} (\approx 0.23) \\ A\lambda^2 = s_{23} = V_{cb} \\ A\lambda^3(\rho - i\eta) = s_{13} e^{-i\delta} = V_{ub} \end{aligned} \tag{2.44}$$

The CKM matrix under the Wolfenstein parametrization at the order $\mathcal{O}(\lambda^4)$ can be written as:

$$V_{CKM} = \begin{pmatrix} 1 - \frac{\lambda^2}{2} & \lambda & A\lambda^3(\rho - i\eta) \\ -\lambda & 1 - \frac{\lambda^2}{2} & A\lambda^2 \\ A\lambda^3(1 - \rho - i\eta) & -A\lambda^2 & 1 \end{pmatrix} + \mathcal{O}(\lambda^4) \tag{2.45}$$

The hierarchy structure between the elements of the CKM matrix is conserved and represented by the order in term of λ. Indeed, the transition between the first and second quark families are at the order $\mathcal{O}(\lambda)$, the transition between the second and the third are at the order $\mathcal{O}(\lambda^2)$ and the transition between the first and the third are at the order $\mathcal{O}(\lambda^3)$. η corresponds to the phase of CP violation. Since it is associated to a λ^3 in the CKM matrix, the CP violation is predicted to be small in the *SM*. Using this parametrization, there are only two complex elements: V_{ub} and V_{td}.

As the CKM matrix is a unitary matrix, it is possible to write six relations:

$$\begin{aligned} \sum_{\alpha=d,s,b} V_{i\alpha} V_{j\alpha}^* = 0 \quad (i,j) \in [(u,c),(u,t),(c,t)] \\ \sum_{i=u,c,t} V_{i\alpha} V_{i\beta}^* = 0 \quad (\alpha,\beta) \in [(d,s),(d,b),(s,b)] \end{aligned} \tag{2.46}$$

These relations can be visualised as triangles in the complex space. The triangle corresponding to the relation: $V_{ud}V_{ub}^* + V_{cd}V_{cb}^* + V_{td}V_{tb}^* = 0$ is displayed in the left part of Fig. 2.2 and is called "the" Unitary Triangle (UT) due to the fact that it can be completely

determined by performing measurements of its apex coordinate $(\bar{\rho}, \bar{\eta})$, where $\bar{\rho} \equiv \rho(1 - \frac{\lambda^2}{2})$ and $\bar{\eta} \equiv \eta(1 - \frac{\lambda^2}{2})$. The current constraints on the Unitary triangle, performed by the *CKMfitter* group are displayed in the right part of Fig. 2.2.

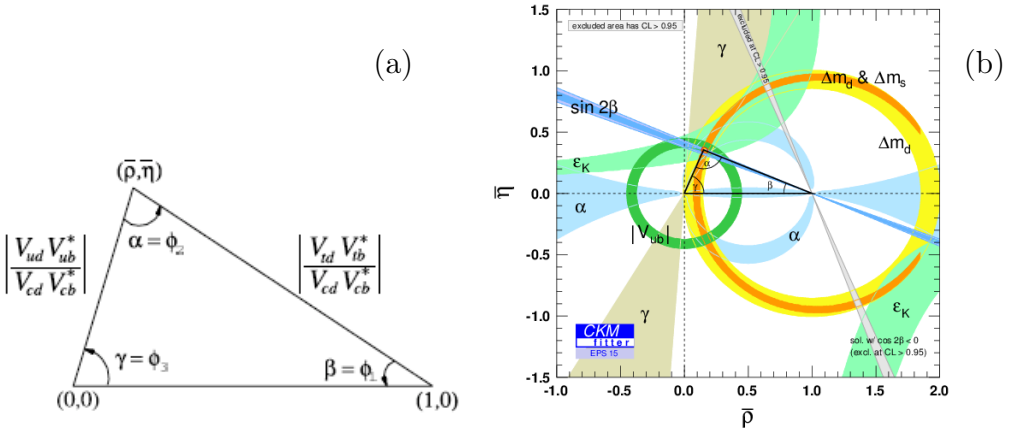

Figure 2.2: The Unitarity triangle (a). Constraints on the Unitarity triangle (b), taken from [19].

The measurement of the branching fractions of radiative decays $B \to V\gamma$ such as those of interest for the analysis presented in this thesis provides an access to $\left|\frac{V_{td}}{V_{ts}}\right|$ as well as to a cross check of the $\Delta m_{d,s}$ measurement made in ${B^0}_{d,s}$ mixing.

2.1.4 The Standard Model issues

Although the *SM* of particle physics is an extremely powerful theoretical framework whose predictions have been experimentally observed, there are a lot of open questions to which the *SM* does not provide any answer. Here comes a, non exhaustive, list of open issues of the *SM*:

- The number of free parameters in the *SM* (19), determined experimentally since the theory cannot predict their values, makes the *SM* inelegant.
- Even if the electromagnetic and the weak interaction can be described in a common Lagrangian, it is not really exact to speak about electroweak unification as there are still two independent coupling constants corresponding to $SU(2)$ and $U(1)$ symmetry groups.
- The huge range of observed masses for the fermions (from $m_e = 0.51\,\mathrm{MeV}/c^2$ to $m_t = 173\,\mathrm{GeV}/c^2$) and the number of families are not explained by the *SM*.
- The hierarchy problem: in the *SM* the gauge and the chiral symmetries avoid the gauge boson and the fermions (respectively) to have so much high masses coming

from large quantum loop corrections. But, there is no such symmetry to protect Higgs boson mass to become very large.

- As the *CP* symmetry is not a symmetry of the *SM*, there is nothing to prevent the appearance of a CP violating term in the QCD Lagrangian. But, the *CP* violation in the strong interaction sector has not been observed. This is know as the "Strong CP problem".

- The *SM* deals with the origin of the fermion masses, quark mixing angles and CP violation parameter in the flavor sector by introducing Yukawa coupling which is quite arbitrary and introduces a large number of parameters.

- The observed deficit of the electron neutrino flux from the sun and the deficit of the atmospheric muon-neutrino flux, are explained by neutrino oscillation from a flavor state to another ($\nu_e \rightarrow \nu_\mu$). The neutrino oscillation induces that the neutrinos are massive particles which is not allowed in the *SM* since only left handed neutrino and right handed anti-neutrino are considered.

- It has been observed that a large amount of the matter in the universe does not emit any radiation and its nature seems to be non-baryonic: the *dark matter*. The *SM* does not provide any non-baryonic candidate.

- Moreover, the observed energy density in the universe is largely in some unknown form. It has been suggested that this energy could be the energy of the vacuum, but in quantum field theory, the vacuum energy is divergent as the fourth power of a given energy cutoff up to which *SM* is valid: Λ. Assuming $\Lambda \sim 10^{14}\,\text{GeV}$, the vacuum energy is $\sim 10^{56}\,\text{GeV}^4$ while the measured *dark energy* density is $\sim 10^{-47}\,\text{GeV}^4$ [20].

- The observed matter anti-matter asymmetry in the universe is not explained by the *SM*. Since the predicted CP violation in the *SM* is small (at the order of $\mathcal{O}(\lambda^3)$), other CP violation sources should exist. The search of new source of CP violation is one of the topics at LHCb.

Therefore, it is admitted that the *SM* is not a complete theory and could be an effective theory, being the low energy part of a more exact theory valid at all energies. The modern particle and astro-particle physics experiments are focused on the search for the energy cutoff of the *NP*, Λ, and the search for hints of *NP* effects.

2.2 Testing the New Physics

2.2.1 An effective theory

If the *SM* can be seen as the low-energy limit of a more complete theory, the new degrees of freedom which complete the theory are expected to be at an energy scale Λ larger than the electroweak scale. Therefore, these degrees of freedom can be integrated and the

physics beyond the *SM* can be described by an effective theory. The effective Lagrangian $\mathcal{L}_{eff}$ is written as:

$$\mathcal{L}_{eff} = \mathcal{L}_{SM} + \Delta\mathcal{L}_{d>4} = \mathcal{L}_{gauge} + \mathcal{L}_{higgs} + \mathcal{L}_{yukawa} + \sum \frac{C_n}{\Lambda^{d-4}} \mathcal{Q}_n^{(d)} \tag{2.47}$$

$\mathcal{L}_{SM}$ is the renormalisable part of $\mathcal{L}_{eff}$, and $\Delta\mathcal{L}_{d>4}$ is a set of operators with a dimension $d > 4$ constructed with the *SM* field and suppressed by the inverse power of Λ.

Focussing on the weak interaction only, an effective theory of the quark interaction at low energy can be constructed using the Operator Product Expension (OPE) theoretical framework and the Renormalisation Group Equations (RGE). As the energy scale of the weak decays is low with respect to the mass of its mediator bosons W, the exchange of W in the interaction can be absorbed in a Fermi effective theory. Then, the effective Hamiltonian is written as:

$$\mathcal{H}_{eff} = \frac{-4G_F}{\sqrt{2}} \sum_i V_{CKM}^i C_i(\mu) \mathcal{Q}_i(\mu) \tag{2.48}$$

where, G_F is the Fermi constant, C_i and $\mathcal{Q}_i$ are the Wilson coefficients and the long distance operators which appear in the $\Delta\mathcal{L}_{d>4}$ part of the Lagrangian given in Eq. 2.47. μ is a renormalisation mass scale which is chosen at the order of the mass of the decaying quark (for instance: $\mu = m_b$ for B mesons decays). The amplitude of the decay $B \to f$, defined as $A(B \to f) = \langle f|\mathcal{H}|B\rangle$, shall not depend on the chosen value of μ.

The OPE framework allows to separate the Hamiltonian computation into two parts. The first part contains the short distances (high energy) parts, represented by the Wilson coefficients C_i which can be computed using perturbative methods. The second part contains the long distance (low energy) effects, represented by the operators $\mathcal{Q}_i$ and requires non perturbative methods (lattice QCD).

This effective theory will be described now using the decay $b \to cs\bar{u}$ as an exemple. As Fermi did with the β decay of the neutron, this decay can be approximated as a punctual interaction with four fermions. The Hamiltonian term describing the W boson exchange in this interaction is then modified as follows:

$$-\frac{g^2}{8} J_\mu^{(b\to c)} \left(\frac{g^{\mu\nu} - \frac{q^\mu q^\nu}{M_W^2}}{q^2 - M_W^2} \right) J_\nu^{(s\to u)} \underset{|q| \ll M_W}{\Longrightarrow} \frac{-4G_F}{\sqrt{2}} J_\mu^{(b\to c)} g^{\mu\nu} J_\nu^{(s\to u)} \tag{2.49}$$

where, $\frac{-4G_F}{\sqrt{2}} = \frac{g^2}{8M_W^2}$. Then, the local operator is expressed as the product of two left currents:

$$\begin{aligned} J_\mu^{(b\to c)} &= V_{cb} \bar{c} \gamma_\mu (1 - \gamma^5) b \\ J_\nu^{(s\to u)} &= V_{us}^* \bar{s} \gamma_\mu (1 - \gamma^5) u \end{aligned} \tag{2.50}$$

where, $\bar{q}$ represents the spinor $\bar{u}(q)$ or $\bar{v}(\bar{q})$, and q the spinor $u(q)$ or $v(\bar{q})$, V_{ij} is the element of the CKM matrix corresponding to the interaction between the quarks i and

j and $\frac{1-\gamma^5}{2}$ is the projector on the left states. Using the properties of the projector, the currents can be re-expressed in terms of left spinors only:

$$\begin{aligned} J_\mu^{(b\to c)} &= V_{cb}\bar{c_L}\gamma_\mu b_L \\ J_\nu^{(s\to u)} &= V_{us}^*\bar{s_L}\gamma_\mu u_L \end{aligned} \tag{2.51}$$

Therefore, assuming the operator $\mathcal{Q}_2$ defined as: $\mathcal{Q}_2 = (\bar{c_L^\alpha}\gamma_\mu b_L^\alpha)(\bar{s_L^\beta}\gamma_\mu u_L^\beta)$, where α and β are the color indices of the quarks, the effective Hamiltonian becomes:

$$\mathcal{H}_{eff} = \frac{-4G_F}{\sqrt{2}} V_{cb}V_{us}^*\mathcal{Q}_2 \tag{2.52}$$

The QCD corrections to this decay can be factorisable or not. The first case corresponds to the emission of a gluon between the b and the c quarks or between the s and the $\bar{u}$ quarks. Due to these corrections, the Wilson coefficient C_2 gets a dependence with μ: $C_2(\mu) \neq 1$. It shall be noticed that this exchange of gluon conserves the color of the quarks.

The non-factorisable QCD corrections correspond to diagrams with an exchange of gluon between the s and the c quark (or between the c and the $\bar{u}$ quarks, or between the b and the $\bar{u}$ quarks as well) as it is displayed in the Fig. 2.3. In this case, the c quark can have the same color (α) than the b quark, so the s quark has the same color (β) than the $\bar{u}$ quark. This QCD effect is modeled by a correction to the operator $\mathcal{Q}_2$. But, it is possible that the c quark has a different color (β) than the b quark (α) but the same as the $\bar{u}$ quark, so the s quark has the same color than the b quark (α). It is necessary to introduce a new operator: $\mathcal{Q}_1$, with the corresponding Wilson coefficients: $C_1(\mu)$. The $\mathcal{Q}_1$ is defined as: $\mathcal{Q}_1 = (\bar{c_L^\beta}\gamma_\mu b_L^\alpha)(\bar{s_L^\alpha}\gamma_\mu u_L^\beta)$, then the effective Hamiltonian is now:

$$\mathcal{H}_{eff} = \frac{-4G_F}{\sqrt{2}} V_{cb}V_{us}^*\left(C_1(\mu)\mathcal{Q}_1 + C_2(\mu)\mathcal{Q}_2\right) \tag{2.53}$$

Considering the decay $b \to sq\bar{q}$, the contributions of the penguin diagrams shall be added. Therefore, new operators $\mathcal{Q}_i$ appear. The full effective Hamiltonian for this decay is:

$$\mathcal{H}_{eff} = \frac{-4G_F}{\sqrt{2}} \left(\sum_{q=u,c} \left(\lambda_q \Big(C_1(\mu)\mathcal{Q}_1^q(\mu) + C_2(\mu)\mathcal{Q}_2^q(\mu) \Big) \right) + \lambda_t \sum_{i=3}^{10} C_i(\mu)\mathcal{Q}_i(\mu) \right) \tag{2.54}$$

where, $\lambda_q = V_{qb}V_{qs}^*$. $C_{1,2}(\mu)$ and $\mathcal{Q}_{1,2}(\mu)$ are the Wilson coefficients and operators which appears in Eq. 2.53. There are seven new Wilson coefficients and operators which appear in this equation. They correspond to the penguins loop processes contributing to this decay. Loops are made of a W boson coupling to an *Up* family quark: u, c or t. Due to the quark mass hierarchy ($m_t \gg m_c \gg m_u$), the dominant process is the loop with a t quark, the two other ones are negligible. Therefore, in the effective Hamiltonian given in Eq. 2.54, only λ_t, the elements of the CKM matrix corresponding to a t quark coupling, appears.

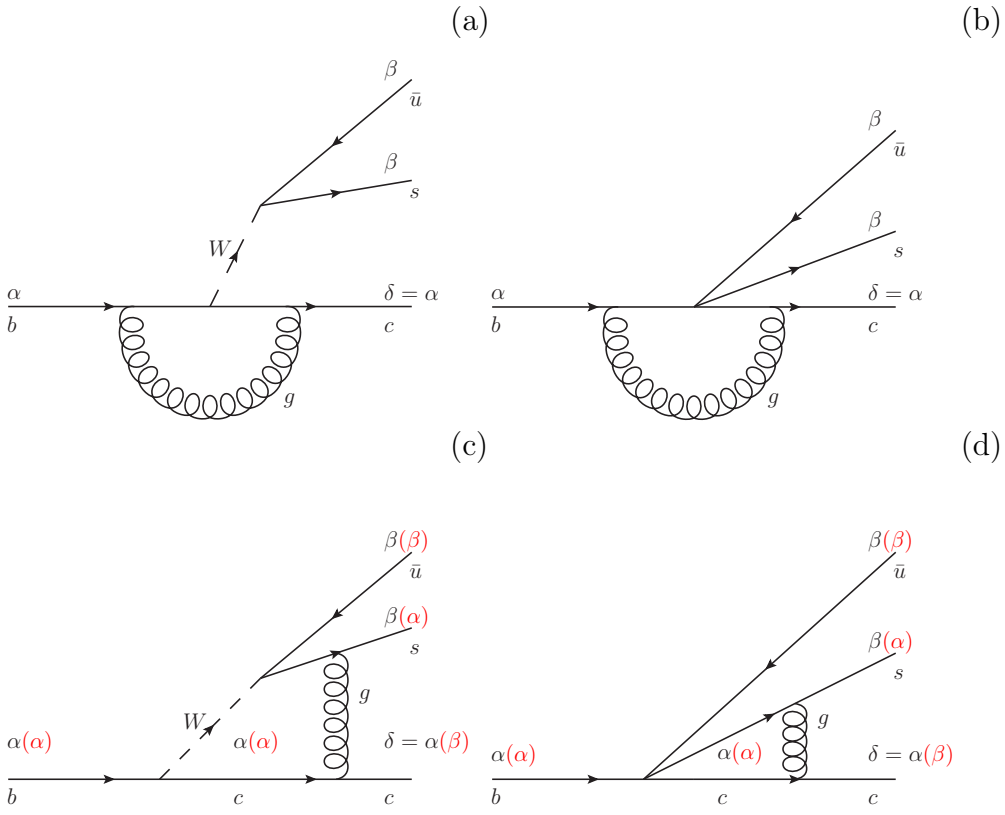

Figure 2.3: Feynman diagrams of the loop QCD corrections to $b \to cs\bar{u}$. The diagrams (a) and (c) represents the full theory whereas the diagrams (b) and (c) represent the effective theory associated to (a) and (d) respectively. In the (c) and (d) diagrams, the color index of the quarks (α, β) in black represent the case corresponding to $\mathcal{Q}_2$ operator, while the red color index represents the case corresponding to $\mathcal{Q}_1$ operator.

The penguin processes are separated into different types, corresponding to different C_i and $\mathcal{Q}_i$. The first case is the QCD penguin where the b quark decays into a s quark through a loop from which a gluon is emitted which decays into a pair of quarks: $q\bar{q}$ (here $\bar{q}$ is the antiquark of the q quark which could not be a t quark). The corresponding Feynman diagrams are shown in the part (a) of Fig. 2.4. The relative four operators corresponding to this process are:

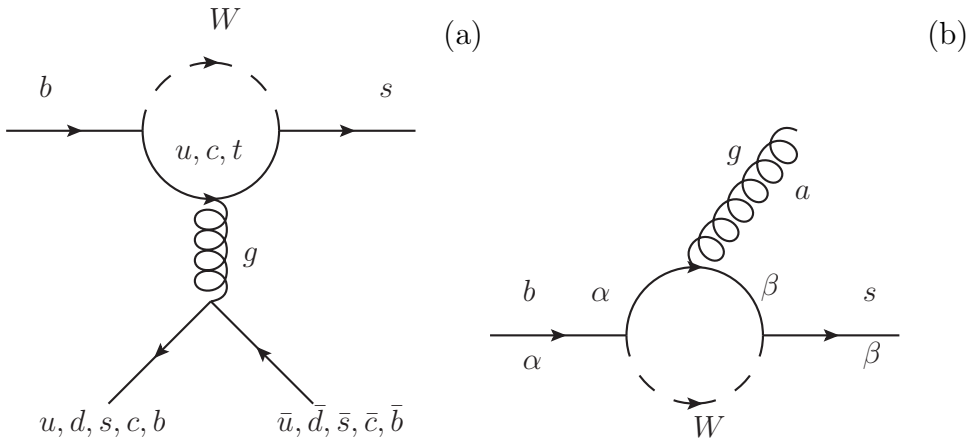

Figure 2.4: Feynman diagrams of the QCD (a) and chromomagnetic (b) penguins and contribution to $b \to sq\bar{q}$.

$$\begin{aligned}
\mathcal{Q}_3 &= [\bar{s_L^\alpha}\gamma_\mu b_L^\alpha] \sum_{q=u,d,s,c,b} \left[\bar{q_L^\beta}\gamma^\mu q_L^\beta\right] \\
\mathcal{Q}_4 &= \left[\bar{s_L^\beta}\gamma_\mu b_L^\alpha\right] \sum_{q=u,d,s,c,b} \left[\bar{q_L^\alpha}\gamma^\mu q_L^\beta\right] \\
\mathcal{Q}_5 &= [\bar{s_L^\alpha}\gamma_\mu b_L^\alpha] \sum_{q=u,d,s,c,b} \left[\bar{q_R^\beta}\gamma^\mu q_R^\beta\right] \\
\mathcal{Q}_6 &= \left[\bar{s_L^\beta}\gamma_\mu b_L^\alpha\right] \sum_{q=u,d,s,c,b} \left[\bar{q_R^\alpha}\gamma^\mu q_R^\beta\right]
\end{aligned} \tag{2.55}$$

where α and β are the color indices of the quarks. The gluon couples to left currents as well as right currents, then the produced $q\bar{q}$ pairs could be left handed ($\mathcal{Q}_{3,4}$) or right handed ($\mathcal{Q}_{5,6}$). As for $\mathcal{Q}_{1,2}$, the s quark can have the same color as the b quark ($\mathcal{Q}_{3,5}$) or a different one ($\mathcal{Q}_{4,6}$). Another operator has to be considered, corresponding to the chromomagnetic penguin case (See part (b) of the Fig. 2.4) when the gluon is an external field represented by the field strength tensor $G^a_{\mu\nu}$ given in Eq. 2.6:

$$\begin{aligned}
\mathcal{Q}_{8g} &= \tfrac{g_s}{16\pi^2} m_b \bar{s_L^\alpha} \sigma^{\mu\nu} G^a_{\mu\nu} T^a_{\alpha\beta} b_R^\beta \\
\mathcal{Q}'_{8g} &= \tfrac{g_s}{16\pi^2} m_s \bar{s_R^\alpha} \sigma^{\mu\nu} G^a_{\mu\nu} T^a_{\alpha\beta} b_L^\beta
\end{aligned} \tag{2.56}$$

with $\sigma^{\mu\nu} = \frac{i}{2}[\gamma^\mu, \gamma^\nu]$. It shall be noticed that the tensor current introduces a helicity flip in $b \to sg$ transition leading to introduce the quark mass term in the operator. As $m_s \ll m_b$, $\mathcal{Q}'_{8g}$ is negligible.

The electroweak counterpart of these QCD processes have also to be taken account. Instead of a virtual (real) gluon emitted from the loop, these electroweak penguin diagrams proceed through the emission of a virtual photon or a Z boson. The corresponding

Feynman diagrams are displayed in the part (a) and (b) of the Fig. 2.5. Whereas the coupling of a gluon with the W boson in the loop is forbidden, both photon and Z boson can couple with the W boson. The relative operators for the processes with virtual boson (γ or Z) decaying into a pair of quarks $q\bar{q}$ are:

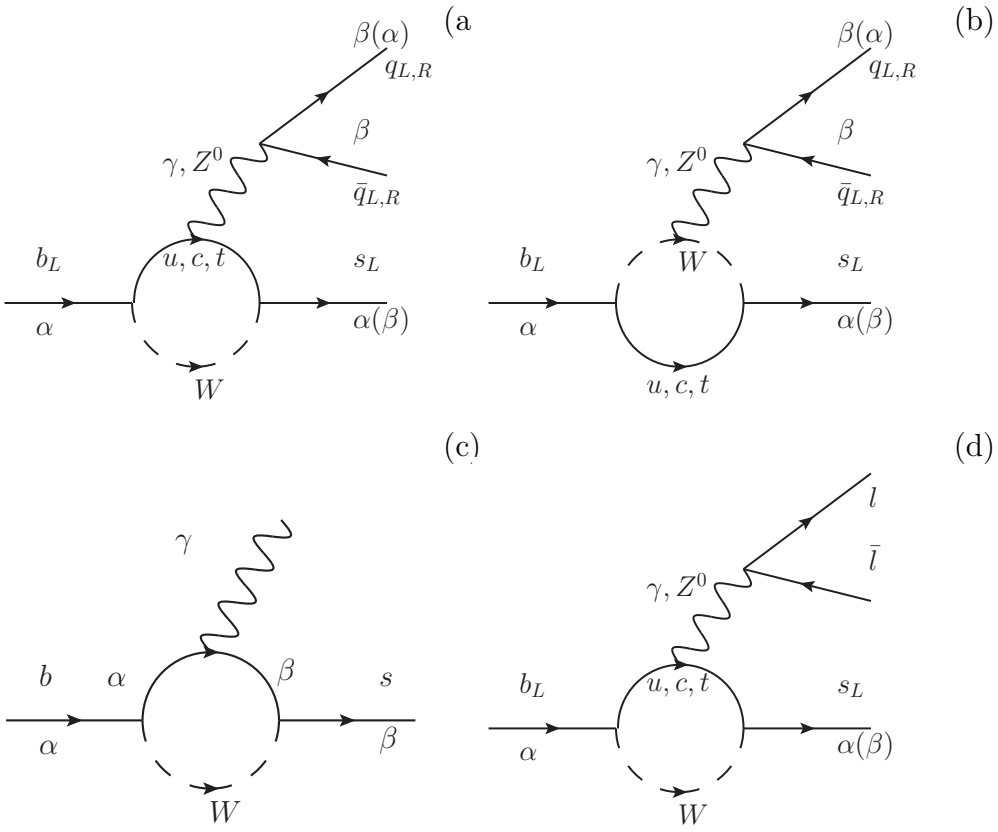

Figure 2.5: Feynman diagrams of the electroweak (a,b), electromagnetic (c) and semi-leptonic (d) penguins corrections to $b \to cs\bar{u}$.

$$
\begin{aligned}
\mathcal{Q}_7 &= \tfrac{3}{2}\bar{s_L^{\alpha}}\gamma_\mu b_L^{\alpha} \sum_{q=u,d,s,c,b} e_q(\bar{q_R^{\beta}}\gamma^\mu q_R^{\beta}) \\
\mathcal{Q}_8 &= \tfrac{3}{2}\bar{s_L^{\beta}}\gamma_\mu b_L^{\alpha} \sum_{q=u,d,s,c,b} e_q(\bar{q_R^{\alpha}}\gamma^\mu q_R^{\beta}) \\
\mathcal{Q}_9 &= \tfrac{3}{2}\bar{s_L^{\alpha}}\gamma_\mu b_L^{\alpha} \sum_{q=u,d,s,c,b} e_q(\bar{q_L^{\beta}}\gamma^\mu q_L^{\beta}) \\
\mathcal{Q}_{10} &= \tfrac{3}{2}\bar{s_L^{\beta}}\gamma_\mu b_L^{\alpha} \sum_{q=u,d,s,c,b} e_q(\bar{q_L^{\alpha}}\gamma^\mu q_L^{\beta})
\end{aligned}
\tag{2.57}
$$

The four operators $\mathcal{Q}_{7,8,9,10}$ follow the same logic as the $\mathcal{Q}_{3,4,5,6}$ where the s quark has the same color than the b quark ($\mathcal{Q}_{7,9}$) or not ($\mathcal{Q}_{8,10}$). The case where the quarks $q\bar{q}$ are left handed ($\mathcal{Q}_{9,10}$) or right handed ($\mathcal{Q}_{7,8}$) is inverted with respect to the QCD penguin

case. Similarly to the chromomagnetic penguin, the electromagnetic penguin corresponds to the decay $b \to s\gamma$ where the photon is a real one. A representation of this decay is displayed in the part (c) of the Fig. 2.5. This process corresponds to the decays of interest for the analysis presented in this thesis. Therefore, the relative operator is written as:

$$\begin{aligned} \mathcal{Q}_{7\gamma} &= \tfrac{e}{16\pi^2} m_b \bar{s_L^{\alpha}} \sigma^{\mu\nu} F_{\mu\nu} b_R^{\alpha} \\ \mathcal{Q}'_{7\gamma} &= \tfrac{e}{16\pi^2} m_s \bar{s_R^{\alpha}} \sigma^{\mu\nu} F_{\mu\nu} b_L^{\alpha} \end{aligned} \tag{2.58}$$

where $F_{\mu\nu}$ has been defined in Eq. 2.3. Like $\mathcal{Q}'_{8g}$, due to the mass hierarchy ($m_s \ll m_b$), $\mathcal{Q}'_{7\gamma}$ is negligible.

The last type of penguin processes is the semileptonic penguin which is similar to the electroweak penguin (See part (d) of the Fig. 2.5). But, instead of decaying into a pair of quarks, the virtual photon (or the Z) decay into a lepton pair $l\bar{l}$. The relative operators are:

$$\begin{aligned} \mathcal{Q}_{9V} &= \tfrac{1}{2} \bar{s_L^{\alpha}} \gamma_\mu b_l^{\alpha} \bar{l} \gamma^\mu l \\ \mathcal{Q}_{10A} &= \tfrac{1}{2} \bar{s_L^{\alpha}} \gamma_\mu b_l^{\alpha} \bar{l} \gamma^\mu \gamma^5 l \end{aligned} \tag{2.59}$$

where in $\mathcal{Q}_{9V}$, the γ^μ corresponds to the photon mediator while in $\mathcal{Q}_{10A}$, the factor $\gamma^\mu\gamma^5$ corresponds to the Z mediator.

2.2.2 New Physics laboratories

Now the Hamiltonian can be written as the sum of products of two distinct elements. The Wilson coefficients C_i describe the contributions of the *SM* particles such as t quark, W, Z and Higgs bosons as well as all the possible *NP* particles contributing to the corresponding decay and so, are sensitive to *NP* effect. The $\mathcal{Q}_i$ operators correspond to left weak currents only. In some *NP* models, right handed fermions can be introduced, then the corresponding operators $\mathcal{Q}'_i$ (which have nothing to do with the negligible operators $\mathcal{Q}'_{8g,7\gamma}$ given in Eq. 2.56 and Eq. 2.58) have to be added to the effective Hamiltonian which can be written as:

$$\mathcal{H}_{eff} = \frac{G_F}{\sqrt{2}} V_{qb} V_{qq'}^* \sum_{i=1}^{10} \Big(C_i(\mu)\mathcal{Q}_i(\mu) + C'_i(\mu)\mathcal{Q}'_i(\mu) \Big) \tag{2.60}$$

where the $C'_i(\mu)$ elements are the Wilson coefficients related to the $\mathcal{Q}'_i(\mu)$ operators of the *NP*. In addition, some *NP* models, such as the MSSM, predicts the existence of scalar and pseudo-scalar bosons which can contribute to the loop processes:

$$\begin{aligned} \mathcal{Q}_S^{(\prime)} &= \tfrac{e^2}{16\pi^2} (\bar{s_{R(L)}^{\alpha}} b_{L(R)}^{\alpha})(\bar{l}l) \\ \mathcal{Q}_P^{(\prime)} &= \tfrac{e^2}{16\pi^2} (\bar{s_{R(L)}^{\alpha}} b_{L(R)}^{\alpha})(\bar{l}\gamma^5 l) \end{aligned} \tag{2.61}$$

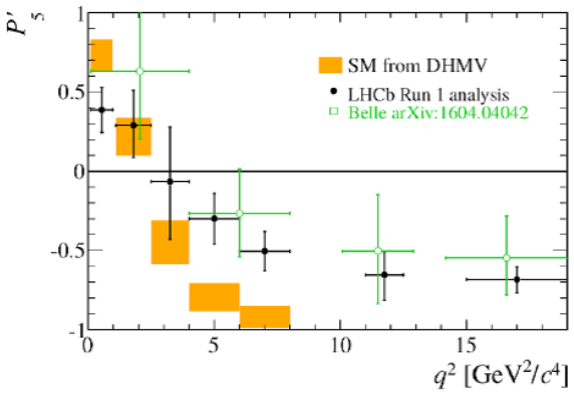

Figure 2.6: The optimised angular observables $P_5^{'}$ in bins of q^2 determined from a maximum likelihood fit to the data.

Therefore, the rare decays where the *SM* predictions of some observables, such as the branching fractions, are known with small theoretical errors are good laboratories to search for *NP* effects. Measuring with an excellent precision these quantities provides constraints on the *SM* Wilson coefficients and operators. Then, it allows to explore the possible range for the *NP*. The operators which are more sensitive to *NP* effects are: $\mathcal{Q}_{7\gamma}$, $\mathcal{Q}_{9V}$, $\mathcal{Q}_{10A}$, $\mathcal{Q}_S$, $\mathcal{Q}_P$ and the corresponding $\mathcal{Q}^{'}$ operators.

There are three types of measurements which are possible with loop decays: the decay rates, providing probe on the couplings and the masses of the *NP* particles, the *CP* violation observables give constraints on the phases of the *NP* and the angular observables, giving information on the helicity structure of the *NP* (it shall be noted that a time-dependant analysis of the decays rates gives also information on the helicity structure). The rare decays going through loop processes can be separated into three categories: semi-leptonic decays: $b \to s\bar{l}l$, leptonic decays: $b \to \bar{l}l$ and radiative decays: $b \to s\gamma$.

The semi-leptonic decays such as $B^0 \to K^{*0}\mu^+\mu^-$ or $B^0 \to K^{*0}e^+e^-$ provide constraints on the following Wilson coefficients: $C_{7\gamma}$, $C'_{7\gamma}$, C_{9V}, C'_{9V} C_{10A} and C'_{10A}. *NP* could affect the branching fractions, the differential branching fraction ($\frac{d\mathcal{B}}{dq^2}$) and the angular distributions. LHCb performed angular analyses of both decays using the full data stored between 2011 and 2012 (corresponding to integrated luminosity of 3 fb^{-1}). If the results from the $B^0 \to K^{*0}e^+e^-$ analysis are compatible with the *SM* [21], the analysis of the $B^0 \to K^{*0}\mu^+\mu^-$ decay indicates differences with the *SM* at the level of 3.4 standard deviations [22] as displayed in Fig. 2.6.

The leptonic decays $B^0_{(s)} \to l^+l^-$ are Flavor Changing Neutral Current (FCNC) transitions which are strongly suppressed in the *SM*. The branching fractions of these decays are proportional to the mass of the leptons m_l, due to the helicity constraints on this process. The simplest decay to observe is the $B^0_{(s)} \to \mu^+\mu^-$, as its branching ratio is predicted to

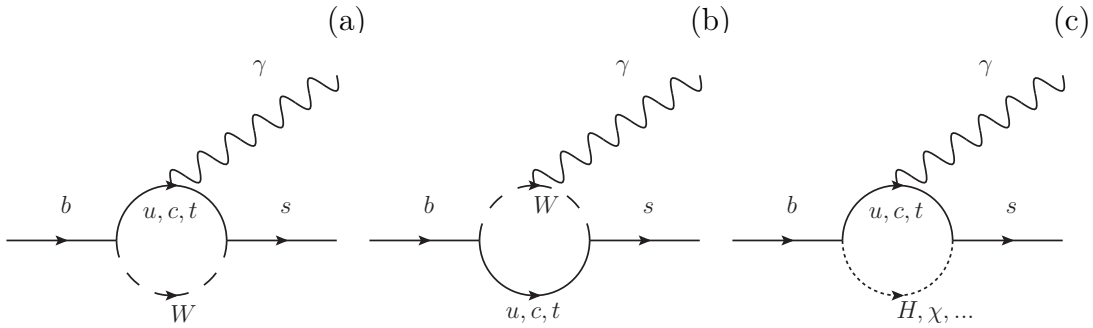

Figure 2.7: Feynman diagrams of the radiative $b \to s\gamma$ transition including the possible *NP* contributions in the loop (c).

be five orders of magnitude larger ($\sim 10^{-10}$) than the branching fraction of the decay involving electrons ($\sim 10^{-15}$). Although the branching fraction of $B^0_{(s)} \to \tau^+\tau^-$ is even larger, the muons are particles with a long flying distance compared to the τ leptons and so, it is simpler to reconstruct decays with muons than with τ particles.

The very low branching fraction of these decays maximises their potential sensitivity to *NP* effects: they are used to put constraints on the following Wilson coefficients: C_{10}, C_S, C_P, C'_{10}, C'_S and C'_P ($C_S^{(\prime)}$ and $C_P^{(\prime)}$ are the Wilson coefficients relative to the operators introduced by *NP* given in Eqs. 2.61). CMS and LHCb have provided the first observation of the $B^0_s \to \mu^+\mu^-$ decay and an evidence of the $B^0 \to \mu^+\mu^-$ using the full available data stored during 2011 and 2012 [23]. A measurement of the branching fraction of the B^0_s decay has been performed and found to be consistent with *SM* predictions [24]:

$$\begin{aligned} \mathcal{B}(B^0_s \to \mu^+\mu^-)_{(th)} &= (3.25 \pm 0.17) \ \times 10^{-9} \\ \mathcal{B}(B^0_s \to \mu^+\mu^-)_{(exp)} &= (2.7^{-1.1}_{-0.9}) \ \times 10^{-9} \end{aligned} \tag{2.62}$$

2.2.3 The radiative decays

The analysis presented in this thesis is focused on the third type of rare decays: the radiative decays of B mesons ($b \to s\gamma$). These decays are FCNC and loop processes of electromagnetic penguin types. Therefore, it is possible to set constraints in the $C_{7\gamma}$ and $C'_{7\gamma}$ Wilson coefficients through the study of these decays [25]. To illustrate the radiative decays, the relative Feynman diagrams are displayed in the Fig. 2.7. The *NP* could have an impact on the branching fractions, the *CP* violation observable or the photon polarisation.

Branching ratios of radiative decays and direct CP asymmetry in $B^0 \to K^{*0}\gamma$ decay are interesting parameters to measure since they are supposed to have a limited sensitivity to hadronic uncertainties and they are theoretically-clean observables.

Latest predictions of radiative decays branching ratios are given by NNLO calculations

Table 2.1: Current theoretical predictions of decays $B^0 \to K^{*0}\gamma$ and $B_s^0 \to \phi\gamma$ branching ratios (from [26]).

	$\mathcal{B}_{SM,NNLO}$ $(\times 10^{-5})$
$B^0 \to K^{*0}\gamma$	4.3 ± 1.4
$B_s^0 \to \phi\gamma$	4.3 ± 1.4

using Soft-Collinear Effective Theory (SCET) [26] (see Tab. 2.1). The ratio of $\mathcal{B}(B^0 \to K^{*0}\gamma)$ and $\mathcal{B}(B_s^0 \to \phi\gamma)$ is predicted to be:

$$\frac{\mathcal{B}(B^0 \to K^{*0}\gamma)}{\mathcal{B}(B_s^0 \to \phi\gamma)} = 1.0 \pm 0.2. \tag{2.63}$$

Measuring the ratio of branching fractions ensures the cancellation of most of the systematic uncertainties relative to individual branching ratio measurement, especially those coming from hadronisation factors.

The first experimental evidence for radiative decays of the B^0 meson, in particular the $B^0 \to K^{*0}\gamma$ decay, was obtained by the CLEO collaboration in 1993 [27]. Following this result, precise measurements of the branching fraction of this decay have been performed during the last decade by experiments at B factories such as BaBar and Belle as well as at LEP collider. In 2007 the Belle collaboration running at the $\Upsilon(5S)$, reported the first observation of $B_s^0 \to \phi\gamma$ decay [28].

Latest results of $\mathcal{B}(B^0 \to K^{*0}\gamma)$, $\mathcal{B}(B_s^0 \to \phi\gamma)$ and world average values are shown in Tab. 2.2 and the current experimental ratio between the two branching ratios is [29]:

$$\frac{\mathcal{B}(B^0 \to K^{*0}\gamma)}{\mathcal{B}(B_s^0 \to \phi\gamma)} = 1.23 \pm 0.06(stat) \pm 0.04(syst) \pm 0.10(f_s/f_d) \tag{2.64}$$

where f_s and f_d are the hadronisation fraction of b and $\overline{b}$ into a B_s^0 and a B^0 meson, respectively. The direct CP asymmetry is defined as a ratio of yields:

$$\mathcal{A}_{CP} = \frac{\Gamma(\overline{B} \to \overline{K}^{*0}\gamma) - \Gamma(B \to K^{*0}\gamma)}{\Gamma(\overline{B} \to \overline{K}^{*0}\gamma) + \Gamma(B \to K^{*0}\gamma)}. \tag{2.65}$$

Theoretical predictions of ratios are less dependant on hadronic parameters than those of individual branching ratios. Experimental results on this measurement are also less affected by systematic uncertainties than branching ratio measurements. For these reasons, CP violation measurement of $B^0 \to K^{*0}\gamma$ decay, and radiative decays in general, are an efficient way to search for *NP*. As radiative decays are mainly caused by the $\mathcal{Q}_7$ operator, and other contributions which interfere are small, the CP asymmetry in this decay is expected to be very small [34]:

Table 2.2: Summary of current measurements of the radiative decay branching ratios from CLEO, Belle, BaBar and LHCb collaborations. Average values from the Particle Data Group (*PDG*) [7] are also given.

	$\mathcal{B}(B^0 \to K^{*0}\gamma)$ $(\times 10^{-5})$	$\mathcal{B}(B_s^0 \to \phi\gamma)$ $(\times 10^{-5})$
CLEO	$4.55^{+0.72}_{-0.68} \pm 0.34$ [30]	
Belle	$4.01 \pm 0.21 \pm 0.17$ [31]	$3.6 \pm 0.5 \pm 0.7$ [32]
BaBar	$4.47 \pm 0.10 \pm 0.16$ [33]	
LHCb		$3.51 \pm 0.35 \pm 0.12$ [29]
PDG	4.33 ± 0.15	3.52 ± 0.34

Table 2.3: Current Measurements of the CP asymmetry in the $B^0 \to K^{*0}\gamma$ decay from BaBar and LHCb collaborations. It also include, the average value performed by the Particle Data Group (*PDG*) [7].

	$\mathcal{A}_{CP}(B^0 \to K^{*0}\gamma)$
BaBar	-0.016 $\pm$ 0.022 $\pm$ 0.007 [33]
LHCb	0.008 $\pm$ 0.017 $\pm$ 0.009 [29]
PDG	-0.002 $\pm$ 0.015

$$\mathcal{A}_{CP} = -(6.1 \pm 4.6) \times 10^{-3}. \tag{2.66}$$

The direct CP asymmetry in $b \to s\gamma$ transition was first measured by the CLEO collaboration in 1999 [30]. Latest results and world average, which are found to be compatible with no CP violation, are shown in Tab. 2.3.

In the analysis presented in this thesis, a measurement of the ratio of branching fractions $\frac{\mathcal{B}(B^0 \to K^{*0}\gamma)}{\mathcal{B}(B_s^0 \to \phi\gamma)}$ and of the *CP* asymmetry of the $B^0 \to K^{*0}\gamma$ decay are proposed. This analysis uses converted photons instead of calorimetric photons as was done by all previous analyses of radiative decays. The converted photons have first been used in LHCb with the χ_c and χ_b analysis [35] and the search for $B_s^0 \to J/\psi\,\gamma$ decay [36].

In LHCb, about 20 % of the photons convert before the magnet and are then reconstructible as a pair of electron tracks [37], the expected yields are lower than the ones of calorimetric photons, but the expected resolution on the reconstructed mass of the B mesons is improved, since the resolution of the tracking system is better than the resolution of the calorimeter (See Sec. 3.2.2 and 3.2.5). This improved resolution allows to probe the $B_s^0 \to K^{*0}\gamma$ decay which has not yet been observed. Given the previous $\mathcal{B}(B^0 \to K^{*0}\gamma)$ theoretical prediction and latest experimental results of *CKM* matrix elements $\left|\frac{V_{td}}{V_{ts}}\right| =$

$0.216 \pm 0.001 \pm 0.011$ [7], the branching ratio of the $B_s^0 \to K^{*0}\gamma$ decay is expected to be

$$\mathcal{B}_{th}(B_s^0 \to K^{*0}\gamma) \cong \mathcal{B}(B^0 \to K^{*0}\gamma) \times \left|\frac{V_{td}}{V_{ts}}\right|^2 = (2.0 \pm 0.7) \times 10^{-6}, \tag{2.67}$$

since the virtual top quark in the loop coupling with a strange quark introduces a $|V_{ts}|^2$ factor in the case of the $B^0 \to K^{*0}\gamma$ decay and its coupling to a down quark introduces a $|V_{td}|^2$ factor in the case of the $B_s^0 \to K^{*0}\gamma$ decay. This decay proceeds through the same process as the other radiative decays (e.g. a FCNC penguin) but, instead of an s quark in the final state of the b quark decay, there is a d quark. Therefore, the measurement of the branching fraction of this decay provides information on the CKM matrix elements $\frac{V_{td}}{V_{ts}}$ as well as constraints on the $C_7^{(\prime)}$ Wilson coefficients.

2.2.4 The photon polarisation

Another parameter with potential high sensitivity to *NP* effects is the photon polarisation which can be experimentally measured by studying the radiative decays. In the *SM*, the s quark coupling to the W boson in the $b \to s\gamma$ decay is mostly left handed as it can be deduced from the $\mathcal{Q}_{7\gamma}$ expression given in the first equation of Eqs. 2.58 where the s quark spinor, $\bar{s_L}$, represents a left current. The *SM* predicts also a small fraction of radiative decays with a right handed s quark, represented by the operator $\mathcal{Q}'_{7\gamma}$ given in the second equation of Eqs. 2.58. The fraction of decays with a right handed s quark is reduced with respect to the decays with a left handed s quark by a factor $\frac{m_s}{m_d} \approx 0.02$. The polarisation of the photon, i.e. if the photon is left or right handed, is constrained by the s quark one due to the conservation of the angular momentum. In the *SM*, the photon is mostly left handed in $b \to s\gamma$ decays, and mostly right handed in $\bar{b} \to \bar{s}\gamma$ decays. Therefore, a measurement of right handed (resp. left handed) photons in $b \to s\gamma$ (resp. $\bar{b} \to \bar{s}\gamma$) decays at the order of $\sim 5\%$ is considered as a clear sign of *NP*.

Several methods to measure the photon polarisation in radiative decays have been suggested. The first one has been done at LHCb by studying the $B^+ \to K^+\pi^-\pi^+\gamma$ decay [38]. The photon polarisation is proportional to the Up-Down asymmetry (A_{UD}) of this decay, which is an observable defined with the angle of the photon momentum with the normal to the plane defined by the momenta of the three charged tracks in the final state in the center of mass of the decay. From this analysis, a non zero Up-Down asymmetry (displayed in the Fig. 2.8) has been measured with a significance of about ~ 5.2 standard deviations, leading to the first observation of a polarisation of the photon in this decay. Due to the several $K\pi\pi$ resonance contributions, it is not possible to extract the photon polarisation value.

Another method used to measure the photon polarisation is an indirect measurement through a time-dependent analysis of decays such as: $B^0 \to X_s^{CP}\gamma$ where X_s^{CP} corresponds

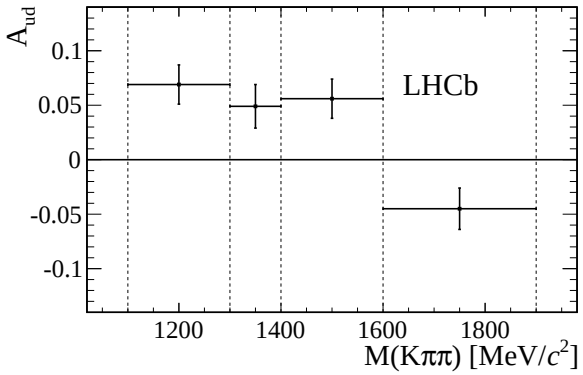

Figure 2.8: Measured up-Down asymmetry in the $B^+ \to K^+\pi^-\pi^+\gamma$ decay.

to a *CP* eigenstate. The decay rate of the B mesons is proportional to the ratio of the amplitudes between decays with a right handed and a left handed photon which is predicted by the *SM* to be: $\frac{A_R}{A_L} \sim 0.05$, where $A_{R(L)}$ is the decay amplitude with right (left) photon. This method has been used at LHCb to perform the first study of the photon polarisation in the $B_s^0 \to \phi\gamma$ decay [39]. Assuming that $tan\Psi = \left|\frac{A_R}{A_L}\right|$, the result of the measurement gives: $A^\Delta = -0.98^{+0.46+0.23}_{-0.52-0.20}$ with $A^\Delta = sin2\Psi$. This result is consistent with the *SM* prediction within two standard deviations.

Finally, it has been suggested that a direct measurement of the photon polarisation should be possible using $B^0 \to K^{*0}\gamma$ decay with converted photons [40] [41] by measuring the azimuthal angle ϕ of the plane defined by the e^+e^- pair with respect to the z axis. The distribution of this angle is depending on the interference between the right and left polarisation of the photon:

$$\frac{d\sigma}{d\phi} \propto 1 + \xi\frac{A_L A_R}{A_L^2 + A_R^2} cos(2\phi + \delta) \tag{2.68}$$

where, ξ and δ are parameters related to hadronic effects. The feasibility of this measurement for dielectron pair created early in the detector has been studied for the analysis of the $B^0 \to K^{*0}e^+e^-$ decay [42], which have also a sensibility to the photon polarisation. The resolution on ϕ is proportional to the inverse of $m^2_{e^+e^-}$. In the very low mass region covered by converted photons, the resolution on the ϕ parameter is dominated by multiple scattering and does not allow to perform a precise measurement of the photon polarisation as displayed in the Fig. 2.9.

The angular analysis of the $B^0 \to K^{*0}e^+e^-$ decay in the low m_{ee} region [21] performs with 2011 and 2012 LHCb data provides measurements of the angular observables $A_T^{(2)}$ and A_T^{Im} defined as:

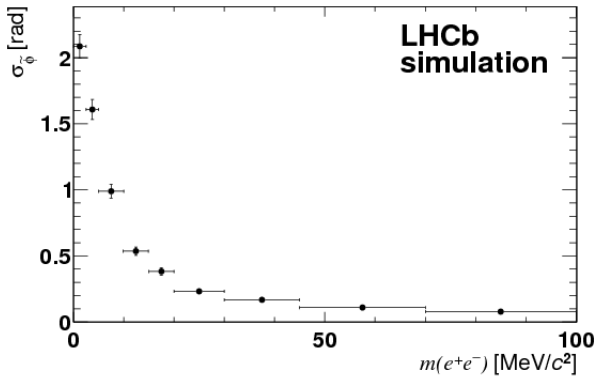

Figure 2.9: Resolution on the ϕ angle as a function of the e^+e^- invariant mass as obtained from LHCb simulated events. This figure has been taken from Ref. [21].

$$A_T^{(2)} = \frac{|A_\perp|^2 - |A_\parallel|^2}{|A_\perp|^2 + |A_\parallel|^2}$$
$$A_T^{Im} = \frac{2\ \mathcal{I}\Updownarrow(A_{\parallel L} A_{\perp L}^* + A_{\parallel R} A_{\perp R}^*)}{|A_\perp|^2 + |A_\parallel|^2} \tag{2.69}$$

where the amplitudes $A_\parallel$ and $A_\perp$ correspond to different polarisation states of the K^{*0} in the decay and the labels L and R refer to the left and right chirality of the dielectron system. The measured values are: $A_T^{(2)} = -0.23 \pm 0.23 \pm 0.05$ and $A_T^{Im} = 0.14 \pm 0.22 \pm 0.05$. These results are consistent with Standard Model predictions.

2.2.5 Constraints on the C_7 and $C_7^{'}$ Wilson coefficients

The allowed values of the Wilson coefficients are used to constrain the parameter space of *NP* models (i.e. the allowed range of the parameter values in *NP* models). In the last years, several global fits of these coefficients have been performed using the available data of $b \to s l^+ l^-$ and $b \to s\gamma$.

A recent status of the constraints on NP contributions to the Wilson coefficients C_7 and $C_7^{'}$ can be found in Ref. [43]. Constraints are computed taking into account the recent measurements of the $B^0 \to K^{*0} e^+ e^-$ angular distribution [21], untagged time-dependant $B_s^0 \to \phi\gamma$ decay rate [39], $A^\Delta = sin 2\Psi$ (see Sec.2.2.4), performed by LHCb as well as the current best measurements of the direct CP asymmetry in $B^0 \to K^{*0}\gamma$ and radiative decay branching fractions. These constraints in the $Re(C_7^{'NP})$ – $Re(C_7^{NP})$ and $Im(C_7^{'})$ – $Re(C_7^{'NP})$ planes are displayed in Fig.2.10. The $C_7^{(')NP}$ are the *NP* contributions to the relatives $C_7^{(')}$ Wilson coefficients. The best fit values for the real and imaginary part of C_7 are :

$$\begin{aligned} &Re(C_7^{NP})(m_b) \in [-0.043, 0.030] \ \ at\ 95\%\ CL \\ &Im(C_7^{NP})(m_b) \in [-0.064, 0.094] \ \ at\ 95\%\ CL \ \ \text{using } B^0 \to K^{*0}\gamma \end{aligned} \tag{2.70}$$

where, $m_b = 4.8$ GeV/c^2 is the mass of the b quark. The best fit values for the real and imaginary part of $C_7^{'}$ are:

$$\begin{pmatrix} Re(C_7^{'NP}) \\ Im(C_7^{'}) \end{pmatrix} = \begin{pmatrix} 0.052 \pm 0.039 \\ 0.006 \pm 0.042 \end{pmatrix} \tag{2.71}$$

including the measurement of A^{Δ} mentionned before.

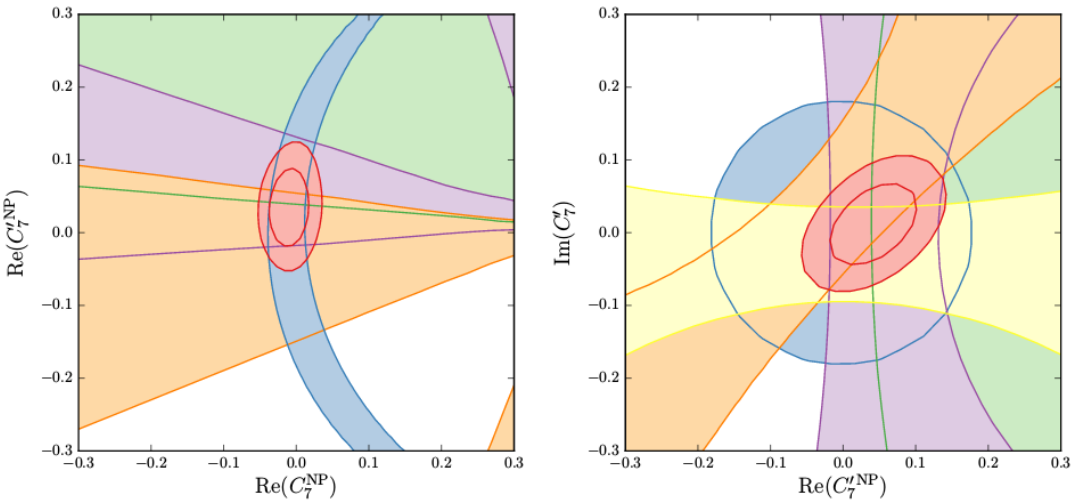

Figure 2.10: Constraints on NP contributions to the Wilson coefficients C_7 and $C_7^{'}$. For the global constraints (in red), 1 and 2 σ contours are shown, while the individual constraints are shown at the 1 σ level. Individual constraints are: radiative decays branching fractions (blue) [7], direct CP asymmetry in $B^0 \to K^{*0}\gamma$ (orange) [33] [29], A^{Δ} measurement in $B_s^0 \to \phi\gamma$ (green) [39] and angular variables in $B^0 \to K^{*0}e^+e^-$ (purple and yellow) [21]. The *SM* value is at $(0, 0)$ for both. This figure is taken from [43]

.

Chapter 3

Experimental setup

In this chapter, the experimental setup used to collect the data used in this thesis is described. First, a description of the LHC, the circular collider used to accelerate and collide the proton beams, is proposed. The four major experiments installed around the LHC are named. The physic processes in which pairs of $b\bar{b}$ are produced from a pp collision are presented and a description of the flavor physics studies in accelerators is proposed. Then, the LHCb spectrometer is fully described, including all its sub-detectors. Performances of the important detectors of LHCb for the current analysis are given. This chapter ends with a description of the LHCb trigger system, of the particle identification online algorithm and of an offline tool to compute related efficiencies, and of the reconstruction of the converted photons with LHCb.

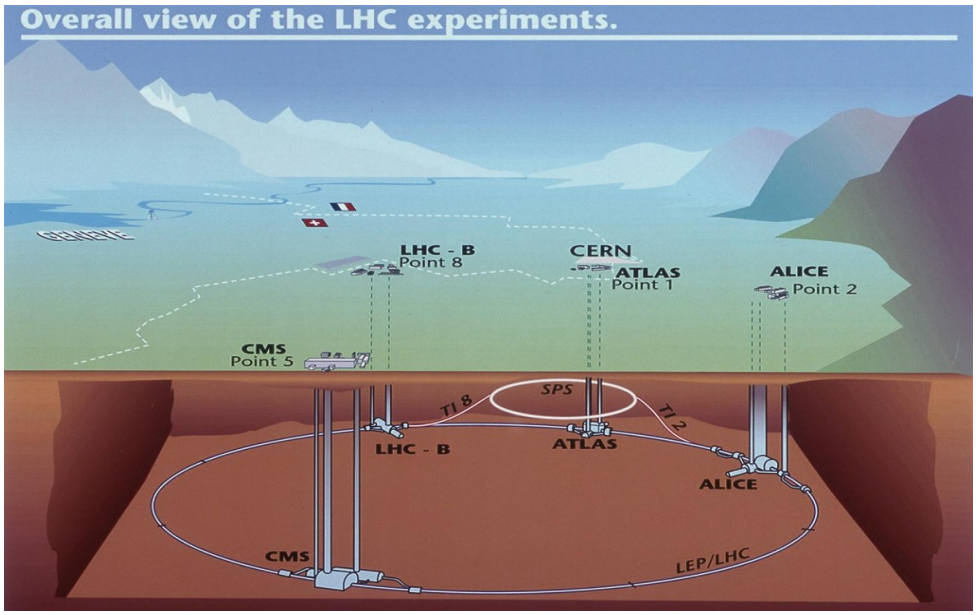

Figure 3.1: View of the LHC with the four major experiments: ATLAS, CMS, LHCb and ALICE.

3.1 The Large Hadron Collider

3.1.1 The collider, the particles and the detectors

The Large Hadron Collider (LHC) [44] is a proton-proton circular collider located at the European Organization for Nuclear Research (CERN) near Geneva and is installed in the 27 km of circumference tunnel built for its predecessor, the Large Electron-Positron Collider (LEP). The LHC is the most energetic instrument built so far to study particle physics. It was designed to accelerate and collide two beams of protons (Au and Pb ions can also be used) at the nominal energy of 7 TeV, corresponding to an energy in the center of mass of $\sqrt{s} = 14$ TeV. Both beams move in opposite direction and collide at four points. At these points are placed the four major experiments at the LHC: ATLAS (*A Toroidal LHC ApparatuS*) [45], CMS (*Compact Muon Solenoid*) [46], LHCb [47] and ALICE (*A Large Ion Collider Experiment*) [48]. The position of each detector along the LHC ring is shown in Fig. 3.1.

ATLAS and CMS are two general purpose experiments dedicated to the direct search of new particles such as the Higgs boson discovered in 2012 [49] [50] as well as unexpected particles which would prove the existence of New Physics (NP) beyond the Standard Model (SM). These two detectors are 4π detectors, which means that they cover 4π solid angle, or also commonly named as General Purpose Detectors (GPDs). Using this geometry allows to detect and reconstruct almost the full event for each collision even if up to 20 collisions are recorded in the same beam crossing. ALICE is an experiment which focus on the study of the plasma of quarks and gluons, in particular by using ion

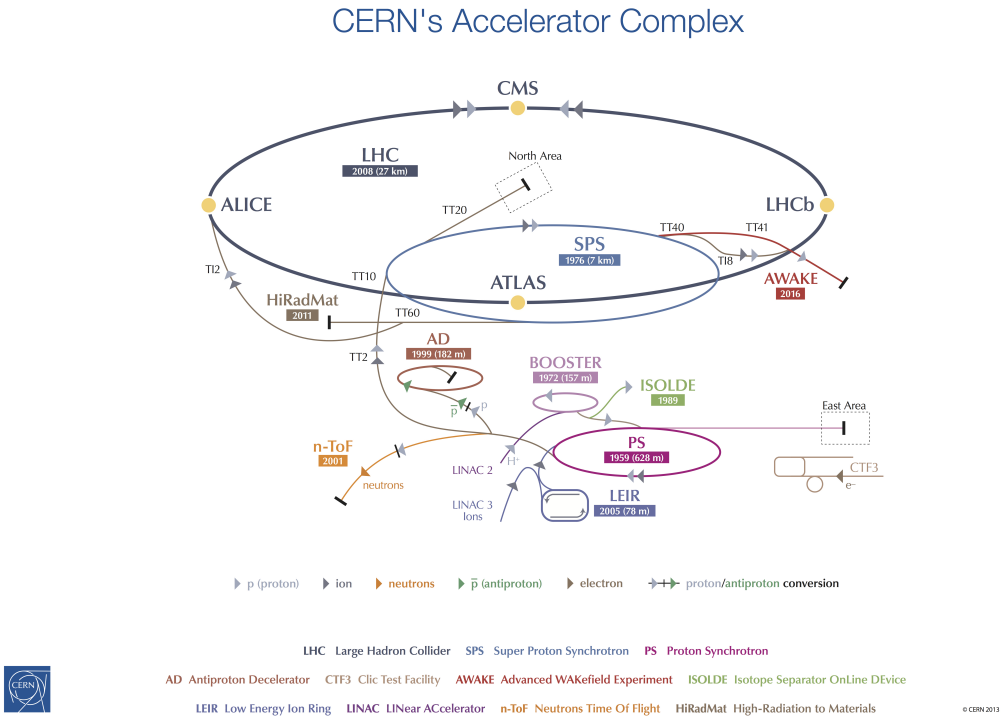

Figure 3.2: The CERN accelerator complex.

collisions provided each year in dedicated runs by the LHC. The LHCb detector has the particularity to be a single arm spectrometer (as can be seen in Sec. 3.2.1). The core of the physics subject at LHCb is the study of b and c hadrons [51]. LHCb performs precise measurements of the *CKM* matrix parameters in order to constrain the *SM* and also search for possible hint of *NP* in rare decays as described in Sec. 2.2.3.

3.1.2 Accelerating protons

The protons used in the LHC are produced by removing the electron of hydrogen atoms coming from a bottle of di-hydrogen. Then, these protons are accelerated by passing through a network of consecutive acceleration devices as displayed in Fig. 3.2. First, the LINAC increases the energy of the protons up to 50 MeV. Then, the Proton Synchrotron Booster (*PSB*, also referred as Booster) brings them to an energy of 1.4 GeV. Protons are injected in the Proton Synchrotron (*PS*) which accelerates them to an energy of 26 GeV. The last stage before the injection in the LHC is the Super Proton Synchrotron (*SPS*) which accelerates protons to an energy of 450 GeV. Once in the LHC, protons are accelerated to their nominal energy, designed to be 7 TeV, but during the first years of the LHC, the protons have been accelerated to a lower nominal energy of 3.5 TeV in 2011 and 4 TeV in 2012. Since *2015*, proton beams are accelerated up to 6.5 TeV.

The acceleration of the protons is made by a succession of radiofrequency (RF) cavities along the different accelerating devices. The oscillating frequency of the electromagnetic field inside the cavities arranges protons into discrete packets called bunches by accelerating protons arriving later and decelerating those arriving first. This way, protons are not injected into the LHC as a continuous flow but by packets. There are sixteen RF cavities inside the LHC, placed into four cylindrical refrigerators (two per beam), in order to accelerate protons to their nominal energy and to keep them inside the bunches. The time between two collision bunches has been designed to be 25 ns which corresponds to a bunch crossing frequency of 40 MHz. In 2011 and 2012, the LHC was opered with a time separation between two bunches of 50 ns. Once proton beams start to collide, the number of protons in the LHC slowly decreases. When the instantaneous luminosity, which is a function of the number of protons (See Eq. 3.1), goes below a certain value at the end of the fill, the beams are destroyed by deflecting them to a collision target. Then, new protons are accelerated and injected into the LHC and a new run begins.

The instantaneous luminosity of the LHC at an interaction point is given by:

$$\mathcal{L} = \frac{fnN_1N_2\gamma F}{4\pi\beta^*\epsilon_n}, \tag{3.1}$$

where f is the beam revolution frequency, n is the total number of bunches in each beam, N_i is the number of protons in each bunch of the beam i, $\gamma = E_p/m_p$ is the Lorentz factor and F a factor smaller than one, due to the angle between the beams at the collision point. The normalised emittance of the beam ϵ_n is a parameter which measures the smallness of the beams and the function β^* represents the capability of the magnets to concentrate the beam into a collision point. This last parameter could be seen as the size of the collision area. The LHC has been designed to run at a maximum instantaneous luminosity of 10^{34} cm^{-2} s^{-1}. LHCb has not been designed to work at this high level of luminosity which induces a high number of collision points, called primary vertices (PV), leading to a high multiplicity of tracks in the detector which is incompatible with the precise measurements foreseen at LHCb. Therefore, the instantaneous luminosity recorded at LHCb between 2011 and 2012 was 4.0×10^{32} cm^{-2} s^{-1} while the maximum at ATLAS and CMS was 7.7×10^{33} cm^{-2} s^{-1}. The way the instantaneous luminosity is reduced at LHCb is described in Sec 3.1.4.

3.1.3 b-hadron production at LHC

Main Feynman diagrams for the production of a pair of $b\bar{b}$ quarks from a proton collision are given in Fig 3.3 for the first order processes and in Fig. 3.4 for the second order processes. As these mechanisms involve vectors, and considering also the boost given to the outcoming particles, the final states of these processes are produced with an angular distribution very closed to 0 or π rad as it is shown in Fig. 3.5. In other words, the b-hadrons coming from the proton collisions have a flying direction which tends to be

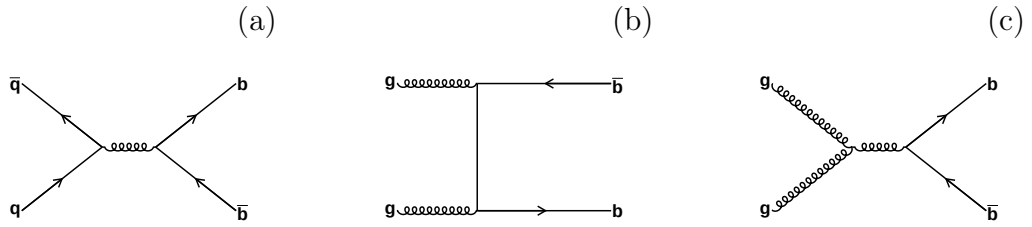

Figure 3.3: Feynmann diagrams of *QCD* processes at the first order leading to a $b\bar{b}$ production. The $q\bar{q}$ annihilation (a) and the fusion of gluons (b) processes represent 16 % of the produced $b\bar{b}$ pairs at LHC at $\sqrt{s}$ = 14 TeV while 27 % are produced through the separation of gluon process (c) [52].

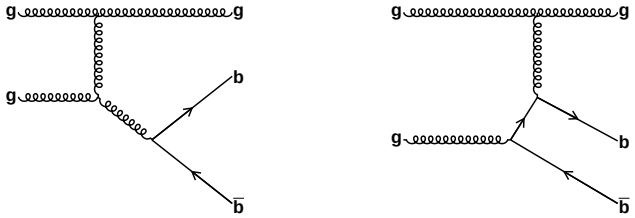

Figure 3.4: Feynmann diagrams of *QCD* processes at the second order leading to a $b\bar{b}$ production. These flavor excitations processes represent 57% of the produced $b\bar{b}$ pairs at LHC at $\sqrt{s}$ = 14 TeV [52].

collinear with the beam axis. This particularity of the b-hadron production at LHC is the reason for the original design of LHCb as a one arm spectrometer. It was chosen to instrument only one side of the collision point.

The total $b\bar{b}$ cross-section has been measured for an energy in the center of mass of $\sqrt{s}$ = 7 TeV during 2011 runs [53] and found to be:

$$\sigma(pp \to b\bar{b}X) = (284 \pm 20 \pm 49)\,\mu\text{b}. \tag{3.2}$$

Once they are produced, the b-quarks hadronise with other quarks to produce b-hadrons. In the Tab. 3.1 are listed the main b-hadrons produced with their relative hadronisation fraction, which corresponds to the fraction of b-quark which hadronise in this hadron type, and their mass and lifetime.

3.1.4 Flavor physics at LHC

LHCb is dedicated to the study of flavor physics and aims at constraining the *SM* by performing precise measurements of its parameters. Indirect search for *NP* beyond the *SM* can also be conducted. Some of the main achievements of the LHCb collaboration

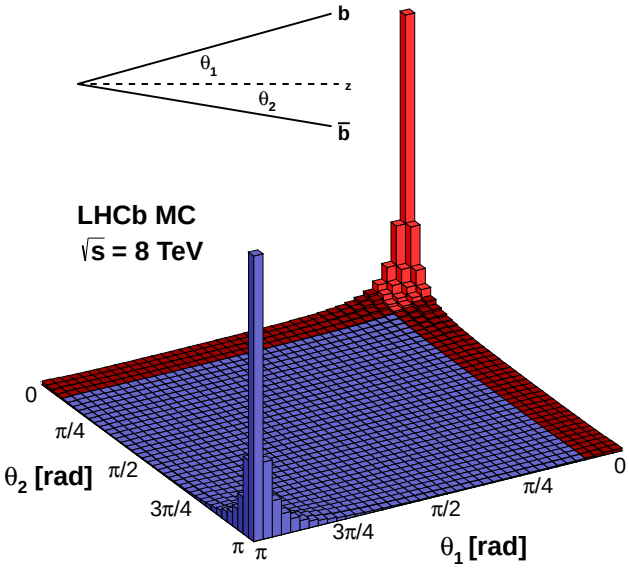

Figure 3.5: The $b\bar{b}$ production angular distribution at LHCb.

Table 3.1: Measured production fractions of the different b-hadrons in the LHCb acceptance [7]. The hadronisation fraction quoted for the Λ_b^0 stands for all the b baryons, while the Λ_b^0 is expected to be the dominant one.

b-hadrons	Hadronisation fraction (f_q)	Mass (MeV/c^2)	Lifetime ($10^{-12}s$)
B^+ (u$\bar{b}$)	0.404 ± 0.006	5279.26 ± 0.17	1.638 ± 0.004
B^0 (d$\bar{b}$)	0.404 ± 0.006	5279.58 ± 0.17	1.519 ± 0.005
B_s^0 (s$\bar{b}$)	0.103 ± 0.005	5366.77 ± 0.24	1.512 ± 0.007
Λ_b^0 (udb)	0.089 ± 0.013	5619.5 ± 0.4	1.466 ± 0.013

with the 2011 and 2012 data taking are the measurement of the *CKM* angle γ [54], the *CP*-violating phase ϕ_s [55] [56], the observation of D^0- $\overline{D}^0$ oscillations [57], the observation of the $B_s^0 \to \mu^+\mu^-$ decay [58] [59].

Previous experiments designed to study flavor physics are the b-factories BaBar and Belle, located respectively on the e^+e^- collider PEP-II (SLAC, USA) and KEKB (KEK, Japan). The e^+e^- collision environment is very clean and provides a perfect laboratory to perform precise measurements but the energy reached does not allow the B_s^0 decay analysis. The LHC *pp* collisions cannot provide such a clean environment, but

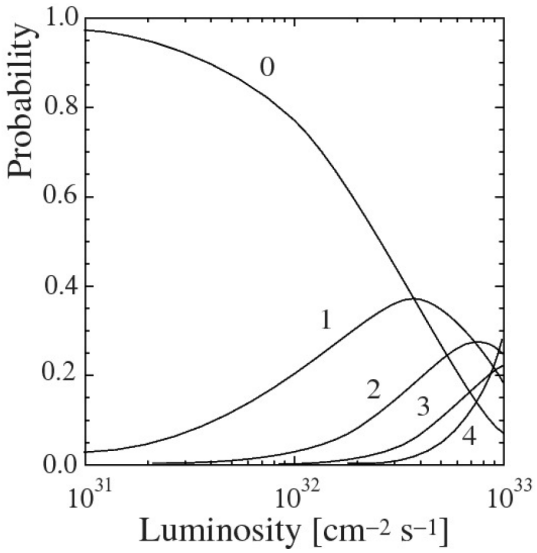

Figure 3.6: Probability to have a given number of interactions per beam crossing as a function of the instantaneous luminosity.

due to the higher reachable energy in the center of mass, they provide a number of $b\bar{b}$ pairs much larger than what was available for BaBar and Belle. The $b\bar{b}$ production cross-section is 284 μb for an energy in the center of mass of 7 TeV (See Eq. 3.2),while at the peak of the $\Upsilon(4S)$, $\sqrt{s} = 10.58$ GeV, it is: $\sigma(e^+e^- \to b\bar{b}) \approx 1.10$ nb. As a comparison, during their full running time, BaBar and Belle have collected respectively 7.7×10^8 and 4.7×10^8 $b\bar{b}$ pairs while between 2011 and 2012, LHCb has collected 2.6×10^{11} $b\bar{b}$ pairs.

A clean environment at the collision point is necessary to achieve a precise reconstruction of the primary vertex (PV) and to fully reconstruct complicated cascade and hadronic exclusive B decays. Therefore, LHCb was not designed to operate at the LHC nominal instantaneous luminosity of 10^{34} cm^{-2} s^{-1} since the number of interactions per beam crossing would be too high. The optimal instantaneous luminosity chosen by the collaboration is $\mathcal{L} = 2.10^{32}$ cm^{-2} s^{-1} which corresponds to an average number of interactions per beam crossing of $\mu = 0.55$ (see Fig. 3.6). During 2011 and 2012, LHCb ran whit an instantaneous luminosity of $\mathcal{L} = 4.10^{32}$ cm^{-2} s^{-1} ($\mu = 1.7$).

At the LHCb collision point, the beams can be adjusted with respect to each other in order to adjust the instantaneous luminosity to the desired one. This allows to reduce the delivered luminosity by two order of magnitude. Moreover, during a run the instantaneous luminosity slowly decreases but, by using the same method, it has been possible to keep it constant.

The heavy hadrons (D, B) studied by LHCb are produced with a high transverse momentum, and their lifetime is long enough to allow them to fly in the detector over a distance of the order of few cm. This long flying distance permits to precisely reconstruct

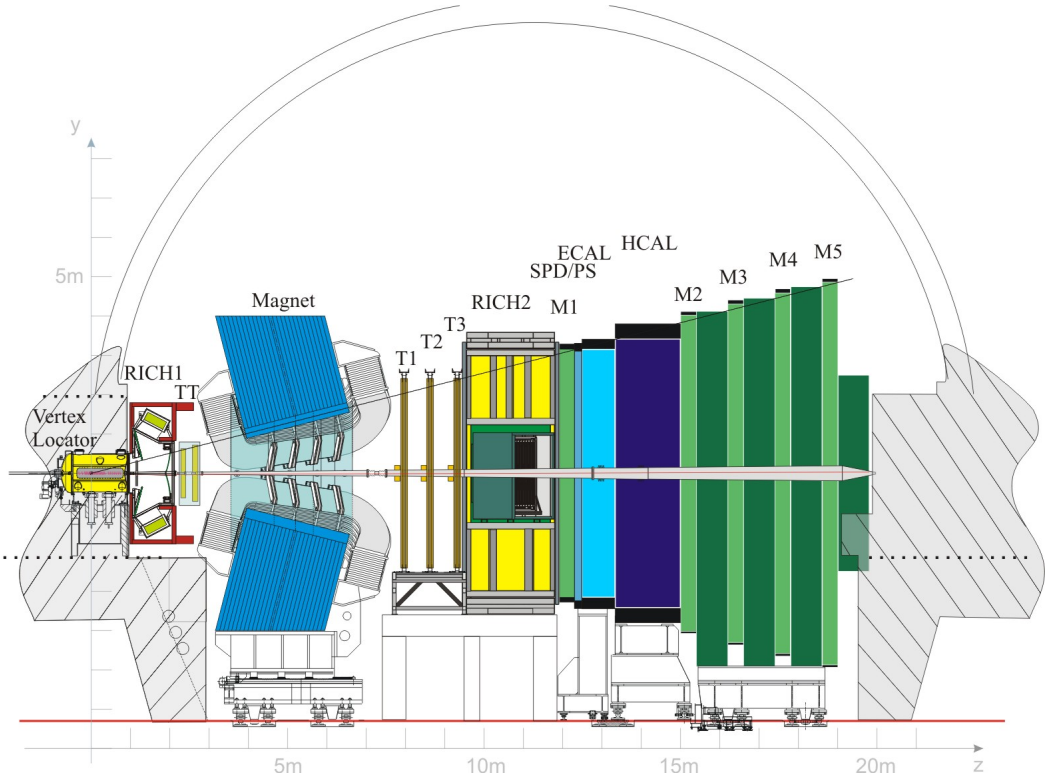

Figure 3.7: View of the LHCb detector.

the decay vertex position and the momentum of the tracks coming from these vertices. To perform these measurements, the LHCb detector has a good resolution on the vertex position, a good resolution on the track momentum, a good identification of the nature of the particles (kaons, pions, electrons, muons, ...) and an efficient trigger system in order to select the events of interest.

3.2 The LHCb spectrometer

3.2.1 Overview of the detector

The LHCb detector is a single arm spectrometer with a forward angular coverage from 10 mrad to 300 mrad in the bending plane corresponding to the pseudorapidity [1] range $2 < \eta < 5$. The layout of the detector is displayed in Fig. 3.7 where the coordinate system is a (O,x,y,z) reference frame centered at the collision point, the z axis is along the beam axis and the y axis is along the vertical.

[1] The pseudorapidity, η, is defined as: $\eta = -ln\,(tan(\theta/2))$, where θ is the angle of a particle relative to the beam axis. It can be also expressed by: $\eta = \frac{1}{2} ln\left(\frac{E+p_L}{E-p_L}\right)$, where E and p_L are the energy and the longitudinal momentum of the particle.

The LHCb detector is made of several sub-detectors, each one being dedicated to a specific task. A magnet delivers a magnetic field of 4 T.m which curves the path of the charged particles, allowing a measurement of their momentum with the tracking system. The VErtex LOcator (VELO) allows to realise a very precise measurement of the vertex position and provides information to the trigger system. The tracking system includes the VELO and a succession of tracking stations, the Trigger Tracker (TT) located before the magnet and the *T1*, *T2* and *T3* stations located after the magnet, each being made of two parts: the Inner Tracker (IT) and the Outer Tracker (OT).

The nature of the particles is determined thanks to two Cherenkov detectors, the Ring Imaging CHerenkov (RICH (1,2)). RICH1 is located before the TT station while RICH2 is located after the *T3* station.

Then, the calorimeter system measures the energy of the incoming particles and provides information on their nature. The calorimeter information is a key element in the trigger system allowing to trigger on high transverse momentum electrons, photons and hadrons. The calorimeter system is made of four detectors: the Scintillator Pad Detector (SPD) which detects charged particles, the PreShower (PS), located after a Pb radiator in which the electrons and photons start to deposit energy, the Electromagnetic CALorimeter (ECAL) which is dedicated to the electromagnetic particles (electrons, photons) and the Hadronic CALorimeter (HCAL) dedicated to the hadrons.

The last part of the LHCb detector is the muon chambers with five stations, called *M1* to *M5*, used to sign the presence of muons for the trigger system and to measure their momentum. *M1* is located between the RICH2 and the calorimeter system and *M2* to *M5* stations are located at the end of the line, after the calorimeters.

3.2.2 The vertexing and the tracking system

The VELO is made of two half detectors on either side of the (y, z) plane, each of them consists of a series of silicon modules arranged along the beam direction. Each module consists of two half-disc sensors dedicated to measure the track position in ϕ, r. The cylindrical coordinates are used, one sensor is measuring r and the other is measuring ϕ while each module has a fixed z value. The two half detectors of the VELO have a shift of 1.5 cm along the z axis in order to let the two opposite modules slightly overlap to cover the full azimuthal angle. Two opposite silicon modules are displayed in the Fig. 3.8.

The two halves of the VELO are made of 21 modules located after the collision point ($z > 0$), 5 of these modules are located before the collision point ($z < 0$) and two more modules containing r sensors only are located before all the previous modules and are used for the trigger system. The location of the modules inside the VELO is shown in the Fig. 3.9.

The VELO detector is designed to do a precise reconstruction of the vertex and measure the impact parameter (IP) of the tracks with respect to these vertices. The IP is defined as the minimal distance between the trajectory of a track and the associated Primary Vertex (PV). This variable is very useful to determine from which vertex each track is coming. The resolution on the position of a vertex is close to 13 µm in the (x,y)

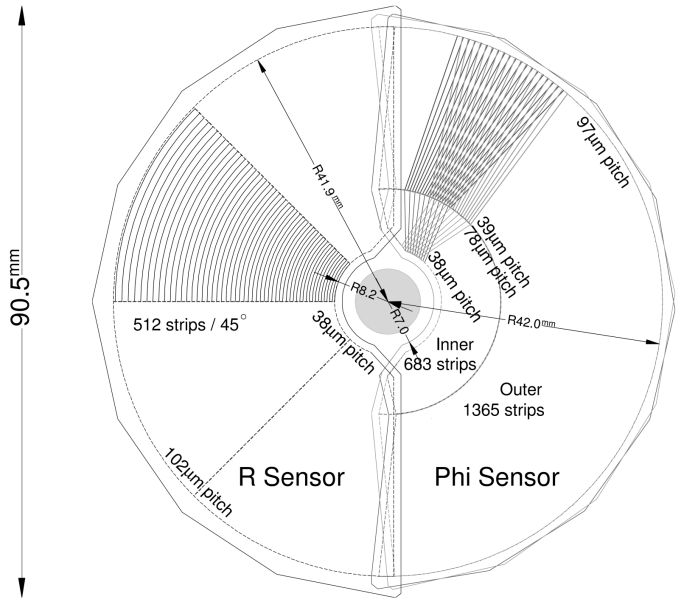

Figure 3.8: Illustration of the r ϕ geometry of the VELO sensors.

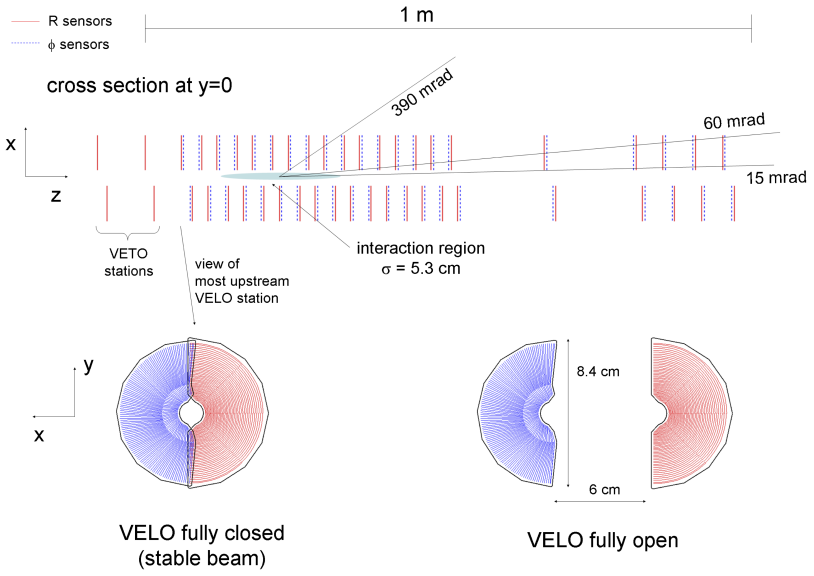

Figure 3.9: The placement of the silicon modules in the VELO.

plan and close to 71 μm along the z axis [60]. The resolution σ_{IP} on the impact parameter is a function of the transverse momentum of the track p_{T}. For example, the IP resolution for a kaon with a $p_{\mathrm{T}} = 2\,\mathrm{GeV}/c$ is: $\sigma_{IP} \approx 23\,\mu\mathrm{m}$. The performance of the VELO for the vertex and IP resolution are given in Figs. 3.10 and 3.11, respectively. More information

on the VELO detector is given in Ref. [61]. A complete report on the VELO performance is given in Ref. [60].

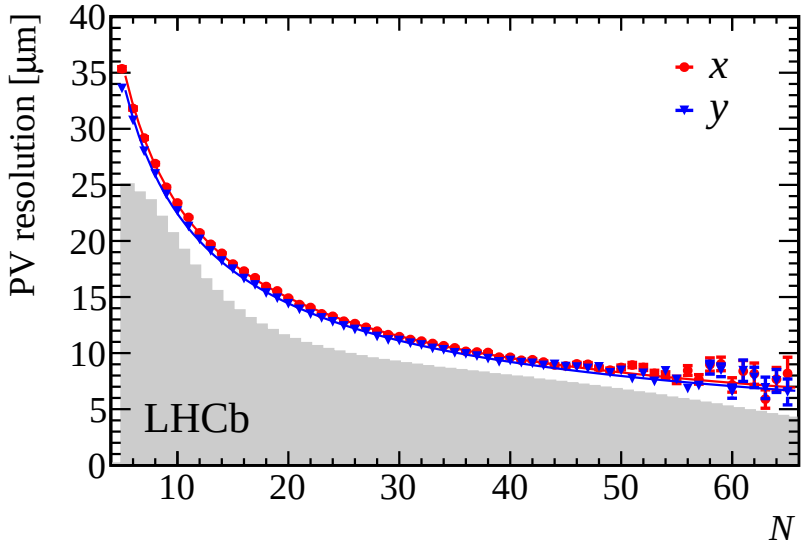

Figure 3.10: Resolution on the x (red dots) and y (blue dots) coordinates of the vertex position determined with the VELO detector as a function of the number of tracks. This plot is produced with 2012 data with only one PV.

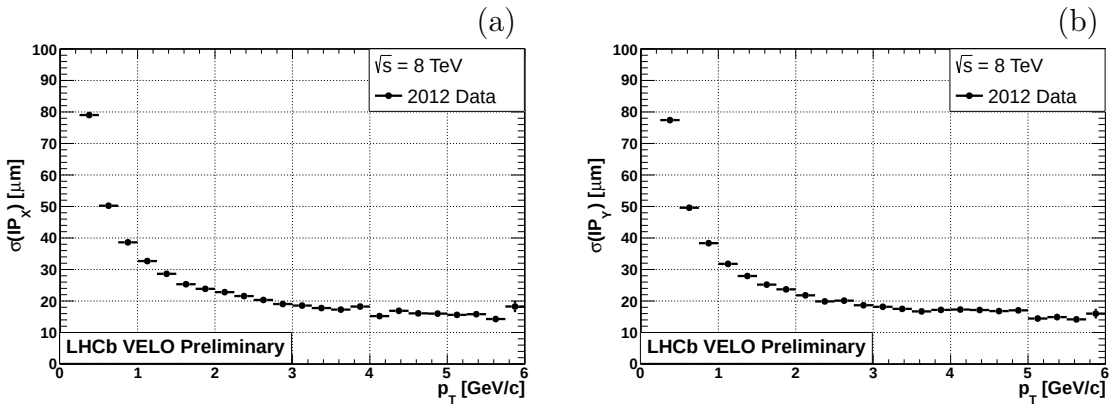

Figure 3.11: Resolution on the x (a) and y (b) coordinates of the impact parameter with the VELO detector as a function of the transverse momentum of the tracks. This plot is produced with 2012 data.

The tracking system is made of the VELO detector and several stations. The first detector is the Trigger Tracker (TT) which is located in front of the magnet. The TT covers the full detector acceptance and uses silicon microstrip sensors with a pitch of

183 µm for the two TT stations and 198 µm for the inner part of the three stations located after the magnet. This ensures a single-hit resolution of about 50 µm.

The TT is made of four detection layers organised in a (x-u-v-x) arrangement where the first and the last detection layers are vertical while the second and the third layer are rotated by a stereo angle of -5° and +5°, respectively. This arrangement is displayed in the Fig. 3.12. Since the particle occupancy quickly decrease in the outermost region of the TT, different readout strip lengths were chosen for different regions of the detector to keep strip occupancies at the level of a few percent. In the Fig. 3.12, the different readout sectors are indicated by different shadings.

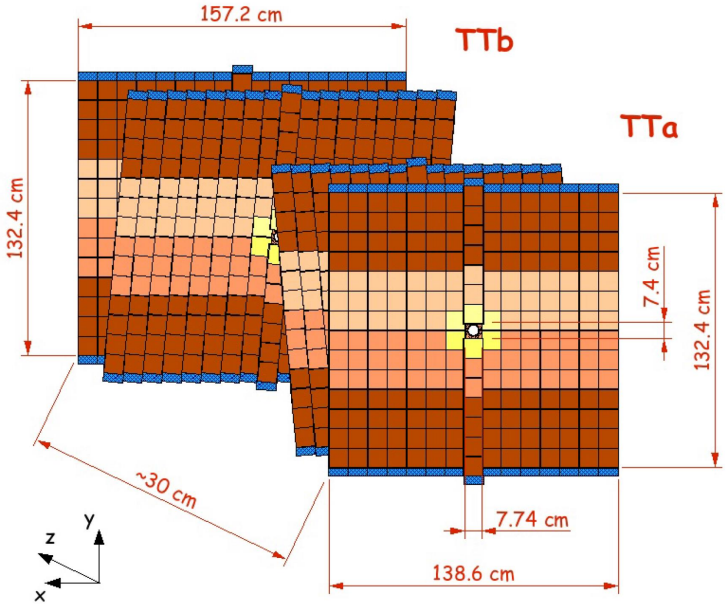

Figure 3.12: Layout of the four TT detection layers. This figure is taken from Ref. [47].

There are three tracking stations located after the magnet: *T1*, *T2* and *T3* stations. As for the TT, each station is made of four detection layers organised in the (x-u-v-x) arrangement. Each detection layer is made of two part, the Inner Tracker (IT) and the Outer Tracker (OT). The IT uses the same silicon technology than the TT as both are dedicated to the reconstruction of the tracks in the closest region to the beam pipe where the track density is the largest. The hit resolution in the IT is of the same order as for the TT. The IT stations layout is displayed in Fig. 3.13.

The OT is a drift-time detector and is designed as an array of individual straw-tube modules, each containing two staggered layers of drift tubes. The counting medium is a mixture of gases (Argon, 70 % and CO2, 30 %). This design has been chosen in order to provide a short drift-time (less than 50 ns) and a good resolution on the coordinate of the hits (lower than 200 µm).

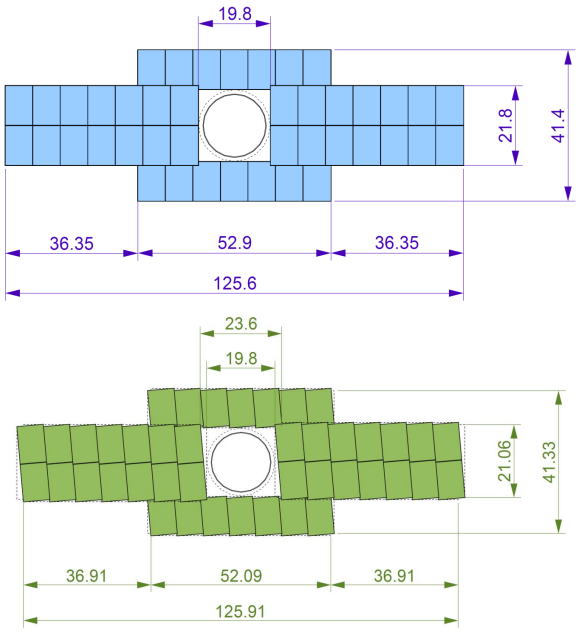

Figure 3.13: Layout of the two IT detection layers. The top one correspond to the configuration of the first and the last layers with vertical strips and the bottom one correspond to the configuration of the third layer with a stereo angle of $+5°$. The given numbers are expressed in cm. This figure is taken from Ref. [62].

With the three trackers: TT, IT, OT and the use of VELO information, a precise measurement of the momentum of the charged tracks is done. The resolution for tracks with a momentum of about 5 GeV/c is: $\Delta p/p \approx 0.4$ % while for tracks with a momentum of about 100 GeV/c, the resolution is: $\Delta p/p \approx 0.6$ %. A full description of the IT and the OT is given in Ref. [62] and Ref. [63], respectively. The TT is described in detail in Ref. [47].

A good vertex and track reconstruction, as well as a precise measurement of parameters such as the IP and the momentum of the tracks are very important requirements for all the analysis performed with LHCb. In particular for the analysis of the decays of interest in this thesis: $B^0 \to K^{*0}\gamma$ and $B_s^0 \to \phi\gamma$ decays using converted photon, i.e. photon converting into an electron-positron pair by interacting with the detector's material before the magnet. The photons which convert after the magnet or do not convert are only measured by the calorimeter and are referred to as calorimetric photons. The vertexing and the tracking system are crucial for the reconstruction of the hadrons coming from the decay of the K^{*0} and the ϕ. The tracking system measures the particle's momentum with a better resolution than the energy resolution provided by the calorimeter system (see Sec. 3.2.5). Therefore, using converted photon instead of calorimetric photon provides a better resolution on the reconstructed mass of the B mesons.

3.2.3 The magnet

The magnet is required to measure the momentum of the charged particles. Charged particles are bent by the magnetic field of 4 T.m delivered by the magnet and their tracks are reconstructed using the tracking system. LHCb uses a dipole magnet made of two coils symmetric with respect to the beam pipe. The total weight of the yoke is 1500 tons and the two coils are weighting 54 tons. The magnet is represented on Fig. 3.14.

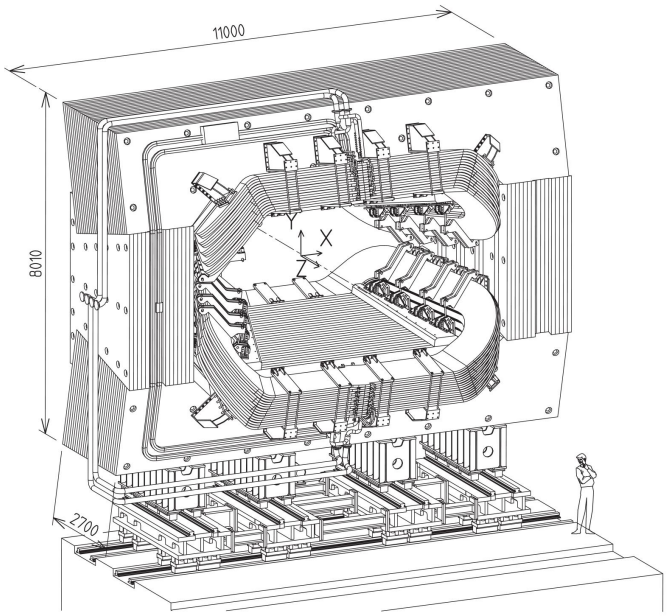

Figure 3.14: Perspective view of the LHCb dipole magnet (units in mm). This figure is taken from the Ref. [47].

The geometry of the magnet has been designed to provide a strong magnetic field between the TT and the $T1$ and a negligible field in the two RICH regions since the photodetectors used for the RICH and the calorimeters use the electron drifts and have degraded performances in the presence of a magnetic field. The intensity of the magnetic field in the full region of the detector is regularly measured [64] with a granularity of a few millimeters. The distribution of the intensity of the magnetic field along the y axis as a function of the position along the z axis is shown in Fig. 3.15. It can be seen that at the location point of the RICH1 ($\approx$ 200 cm) and of the RICH2 ($\approx$ 1000 cm), the magnetic field is negligible. There is a non negligible residual field in the TT stations which allows a measurement of the charged particle's momentum using VELO and TT information. This is used to perform the fast reconstruction made at the first stage of the software trigger HLT1 (see Sec. 3.3.3).

For CP asymmetry measurements, it is important to control the systematic effects induced by any asymmetry of the detector material which leads to a asymmetric interaction

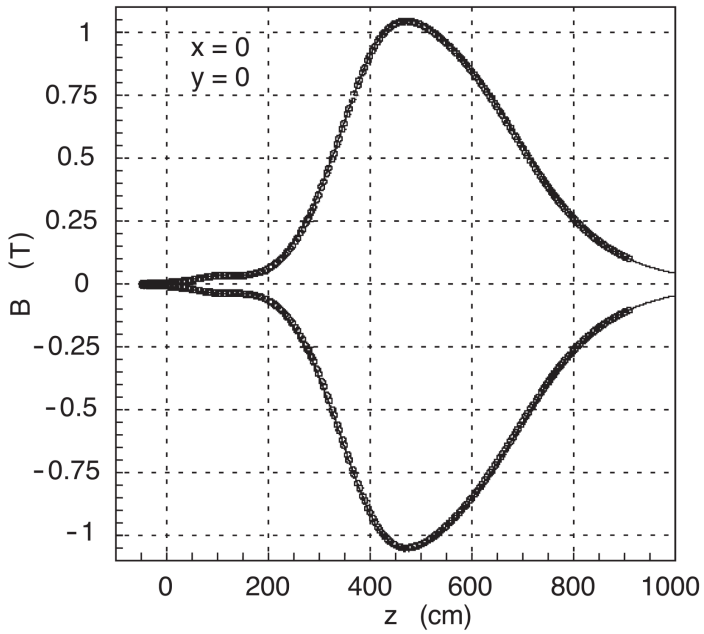

Figure 3.15: Distribution of the intensity of the magnetic field along the y axis (B_y) as a function of the position along the z axis. This figure is taken from the Ref. [47].

of the particles with the detector. Moreover, the different quark content of a particle and its antiparticle could introduce different interaction behaviours in a given region of the detector. This is performed by changing regularly the direction of the magnetic field. Therefore, about one half of the stored data has been recorded using a *Down* magnet polarity ($B_y < 0$), and the rest using an *Up* magnet polarity ($B_y > 0$).

3.2.4 The charged particle identification system

The identification of the nature of the particles is an essential requirement for most of the analysis performed with the LHCb experiment. The identification of the particles permits to distinguish between several decays with the same topology such as the two body decays $B \to h^+h^-$, where $h^\pm$ can be kaons, pions or protons. In particular for the decays of interest in this thesis, a good particle identification allows to separate the $B^0 \to K^{*0}\gamma$ from the $B_s^0 \to \phi\gamma$ events, since the difference between both decays is the nature of the final state hadrons: $(K^+\pi^-)$ and (K^+K^-), respectively. Fig. 3.16 illustrates the impact of particle identification requirements for an analysis.

The identification of the charged particles is made using information from the VELO, calorimeter system, muon chambers and two Cherenkov detectors, the RICH detectors, located between the VELO and the *TT* (RICH1) and after the *T3* station (RICH2). These detectors are based on the Cherenkov effect: when a charged particle goes through a medium with a speed higher than the speed of light in this medium,

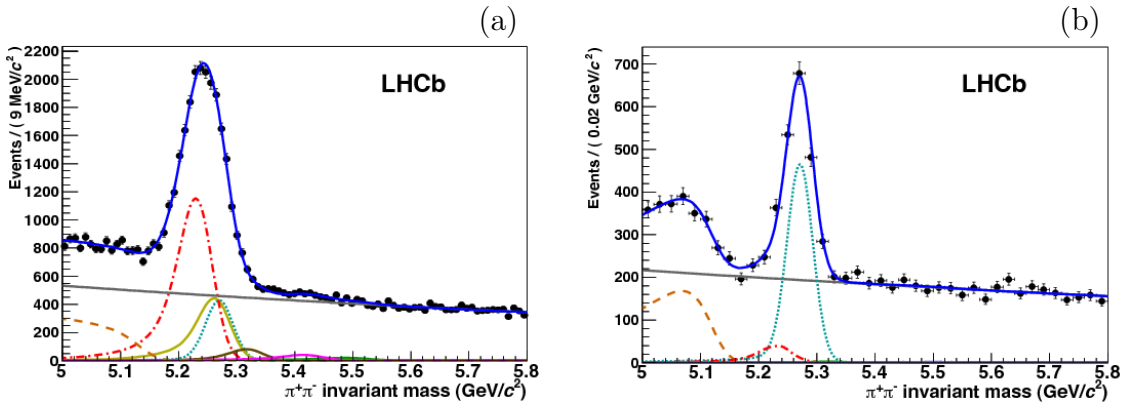

Figure 3.16: Invariant mass distribution for $B \to h^+h^-$ decays with the LHCb data before the use of the RICH information (a), and after applying RICH particle identification (b). The studied signal is the $B \to \pi^+\pi^-$ (turquoise dotted line).The different background contributions from b-hadron decay modes are strongly reduced by applying the particle identification constraints. These plots are extracted from the Ref. [65].

photons are emitted with an angle θ with respect to the direction of the particle defined as: $cos\theta = \frac{1}{n\beta}$, where n is the refractive index of the medium and β is the relativistic boost of the particle ($\beta = v/c$). Measuring the Cherenkov radiation angle θ gives a measurement of its speed. Then, using the momentum measured by the tracking system, the mass of the particle is computed and the nature of the particle is deduced. Fig. 3.17 gives the distribution of the opening angle of the Cherenkov radiation as a function of the momentum of the tracks for one of the medium used in the RICH detectors. The nature of the particle is easily determined according to its momentum range.

In order to cover the full momentum spectrum, which becomes harder when polar angles decreases, it has been chosen to build two RICH detectors using three different mediums. The RICH1, covering the low momentum range from 1 to 60 GeV/c, uses aerogel and C_4F_{10} radiators. The RICH2, covering the high momentum range from about 15 GeV/c to beyond 100 GeV/c, uses a CF_4 radiator. The Cherenkov radiation angle distributions for the different radiators are displayed in Fig. 3.18. In both RICH detectors, the emitted photons are focused using a combination of spherical and flat mirrors to reflect the image out of the spectrometer acceptance. Then, the photons are detected by Hybrid Photon Detectors (HPD). The layout of the two RICH detectors is displayed in the Fig. 3.19.

The two RICH detectors cover the full LHCb acceptance and have typically an efficiency to identify a kaon of the order of 95 %, while the efficiency to misidentify a pion as a kaon is about 10 % for momentum values bellow 100 MeV/c (See Sec. 3.3.5).

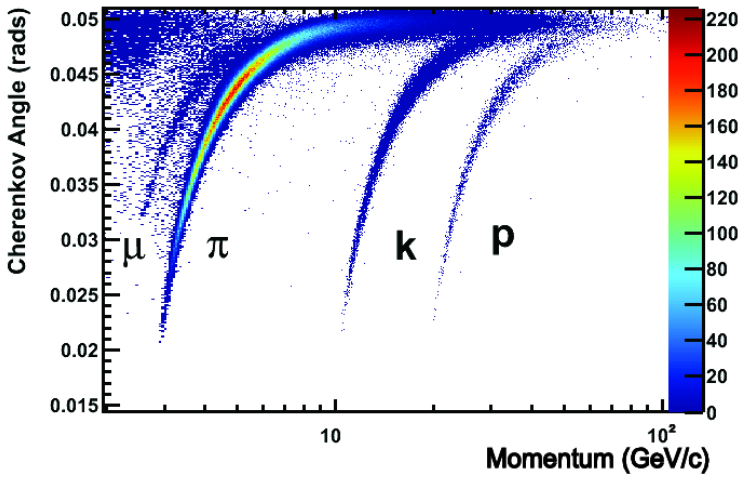

Figure 3.17: Reconstructed Cherenkov angle as a function of the track momentum in the C_4F_{10} radiator (RICH1). This figure is taken from the Ref. [65].

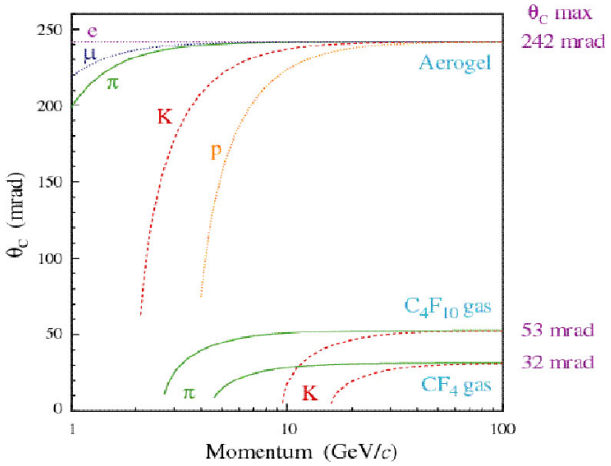

Figure 3.18: Cherenkov angle as a function of the particle momentum for the three RICH radiators.

3.2.5 The calorimeters

The calorimeter system has several functions. The first one is to select high transverse energy hadron, electron, photon and π^0 candidates for the hardware trigger (L0, see Sec. 3.3.2). It provides the identification of electrons, photons and neutral particles and the measurement of their energies and positions. A precise measurement of the energy and the position of electrons and photons is important for the analysis using radiative decays (i.e. with a photon in the final state). Even if the analysis presented in this thesis uses converted photons instead of calorimetric photons, the performance of the calorimeters on photon parameters is important since the electrons emit bremsstrahlung photons by

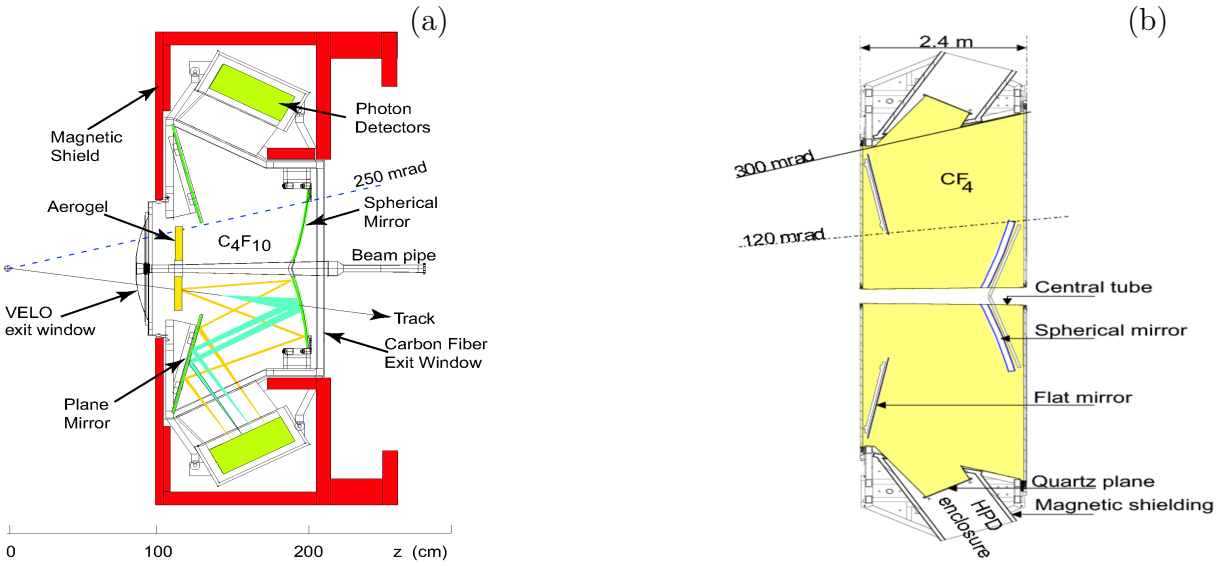

Figure 3.19: RICH1 (a) and RICH2 (b) layout.

interacting with the material of the detector. The energy of these photons should be measured with a good precision and the position of the photons is needed to identify from which track they come from. The calorimeter is also essential for the identification of electrons.

The fast identification of an electromagnetic particle (electron, photon) in a high hadronic multiplicity environment requires a longitudinal segmentation of the shower. To perform that, a dedicated detector, the PreShower (PS) is placed after a lead absorber featuring 2.5 radiation lengths X_0. The main interaction process with the material for electrons is the Bremsstrahlung effect (X_0 is the mean distance over which a high-energy electron loses $1/e$ of its energy) and for photons is the pair production (X_0 is 7/9 of the mean free path length). Electrons and photons can start to interact in the lead absorber and therefore, the PS helps to measure the shape of the resulting electromagnetic shower and allows to distinguish between hadronic and electromagnetic clusters (as displayed in Fig. 3.20) and also between electrons and photons as primary electrons deposit more energy than photons into the PS because the Bremsstrahlung's cross section is higher than the pair production one.

The full separation between neutral and charged particles is performed by a Scintillator Pad Detector (SPD) plane set in front of the PS. The Electromagnetic CALorimeter (ECAL) is installed after the PS. The last sub-detector, the Hadronic CALorimeter (HCAL) is dedicated to the hadronic objects and use information from the SPD to tag the charged or the neutral particles.

The hit density over the calorimeter surface heavily increases when moving closer to the beam pipe. Therefore, the four detectors use a variable lateral segmentation as it is

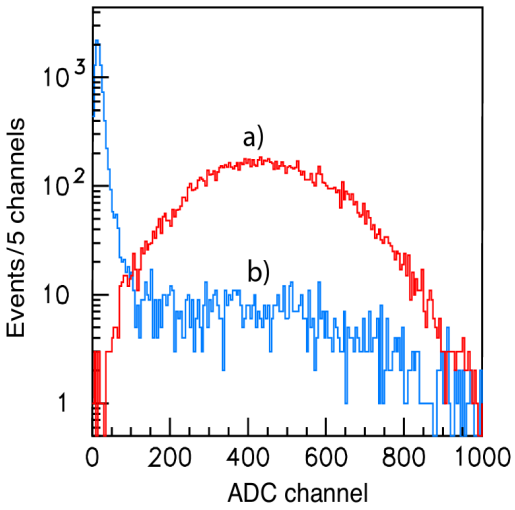

Figure 3.20: Energy deposition of 50 GeV electrons (a) and pions (b) in the *PS*. This figure has been taken from Ref. [66]

shown in the Fig. 3.21. The SPD, *PS* and ECAL have three different sections in which the size of the cells increases with the distance to the beam pipe, 1536 cells with a size of 40.4 mm in the closest region, follow a section with 1792 cells with a size of 60.6 mm and 2688 cells with a size of 121.2 mm in the third section. The pads of the SPD, *S* and ECAL detectors are in a projective geometry. Therefore, each relative pads in the three detector layers corresponds to the same solid angle.

The HCAL has only two sections with larger cell size, due to the larger dimensions of the hadronic showers with respect to the electromagnetic ones. The closest section to the beam pipe is made of 860 cubic cells with a size of 131.3 mm while the outer section is made of 608 cubic cells with a size of 262.6 mm.

The four calorimeter detectors use scintillators. The ECAL uses a Shashlik calorimeter technology, which is made of a sampling structure, alternating between scintillator and lead plates readout by plastic wavelength shifting fibres. There are 66 modules, each consists of a lead layer of 2 mm thick, then two scintillators layers of 120 µm and 4 mm thick. The total stack corresponds to a radiation length of 25 X_0 with a Moliere radius[2] of 3.5 cm. The choice to use this technology is related to the LHCb requirements: a modest energy resolution, a fast time response and a good radiation resistance. The energy resolution of the ECAL is: $\sigma_E/E \approx 9\%/\sqrt{E} \oplus 0.8\%$ [68] (E in GeV). This can be compared to the resolution of the tracking system. As an exemple, the resolution of the momentum of a charged particle with $p = 100\,\mathrm{GeV}/c$ is: $\Delta p \approx 0.6\,\mathrm{GeV}/c$ (from Sec. 3.2.2) while the resolution of the energy of a particle with $E = 100\,\mathrm{GeV}/c^2$ is: $\Delta E \approx 1.20\,\mathrm{GeV}/c^2$.

The performance of high energy photon reconstruction is illustrated by the reconstructed $B^0 \to K^{*0}\gamma$ and $B_s^0 \to \phi\gamma$ mass distribution as displayed in the Fig. 3.22.

[2]The Moliere radius is the radius of a cylinder containing 90 % of the shower's energy deposition.

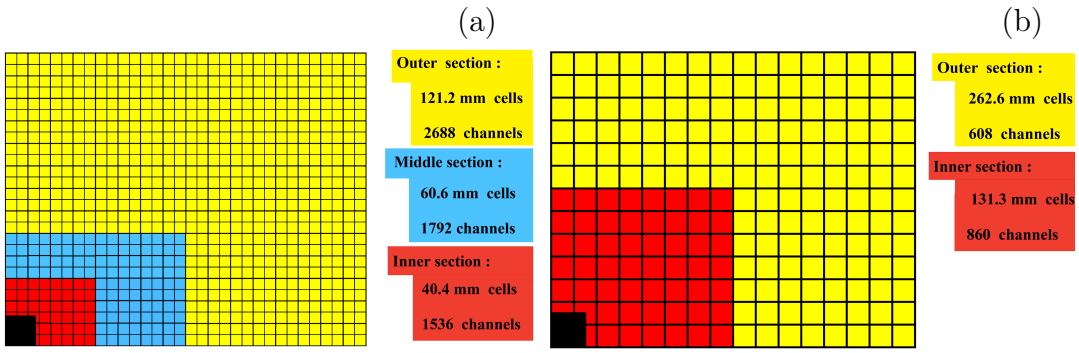

Figure 3.21: Lateral segmentation of the SPD, *PS* and ECAL (a) and the HCAL (b). Only one quarter of detector front face is represented, but the number of cells corresponds to the entire detector plane. This figure is taken from Ref. [67].

The resolution on the reconstructed mass of the B^0 (B_s^0) using calorimetric photons is $\approx 90\,\mathrm{MeV}/c^2$ and is dominated by the calorimeter system resolution. Later in this thesis, it will be shown that using converted photons improves this resolution by a factor 2 to 3.

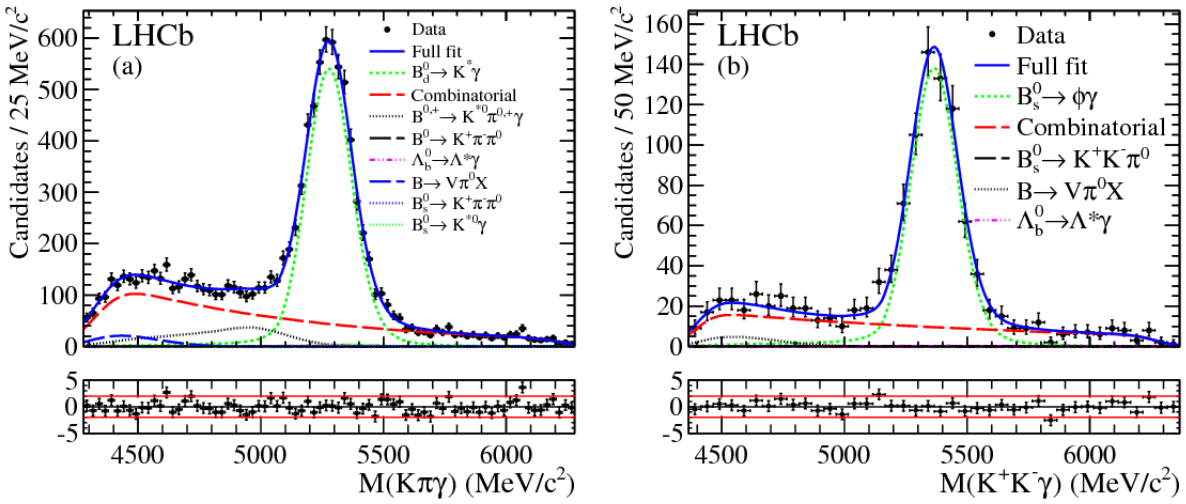

Figure 3.22: Distributions of the reconstructed mass of the $B^0 \to K^{*0}\gamma$ (a) and $B_s^0 \to \phi\gamma$ (b) decays obtained with the 1 fb^{-1} 2011 data. These plots are taken from Ref. [69].

The HCAL is also a sampling device made of iron absorber and scintillating tiles readout by plastic wavelength shifting fibres. While the tiles in the ECAL are perpendicular to the z axis, the tiles in the HCAL are parallel to the z axis. In the transverse direction, the tiles are separated by 1 cm of iron, whereas in the longitudinal direction the length of the scintillating and iron tiles is the hadron interaction length λ_I in steel. The total

length of the HCAL corresponds to 5.6 λ_I (6.8 with the ECAL). The energy resolution of the HCAL is: $\sigma_E/E = 69\%/\sqrt{E} \oplus 9\%$ [68] (E in GeV).

3.2.6 The muon chambers

A good identification of the muons is required by several main analyses at LHCb as, for example: the very rare decay $B_s^0 \to \mu^+\mu^-$ [58] [59], the measurement of the *CP*-violating phase ϕ_s in the $B_s^0 \to J/\psi\,\phi$ decay [70] where $J/\psi \to \mu^+\mu^-$ or the $B^0 \to K^{*0}\mu^+\mu^-$ [22]. The muon system of LHCb consists of five stations *M1* to *M5* installed along the beam axis and provides information for the hardware trigger and muon identification.

The five stations are made of Multi Wire Proportional Chambers (MWPC) with the exception of the inner part of the *M1*, where the particle flow is higher, which is made of triple Gas Electron Multiplier (GEM) whereas the outer part is made of MWPC. The *M1* station is set before the calorimeters in order to improve the transverse momentum measurement for the trigger. The others stations are located at the end of the line just behind the HCAL. The *M2* to *M5* stations are interleaved with 80 cm thick iron absorbers in order to stop hadrons. The total thickness of the full muon system corresponds to 20 nuclear interaction lengths which means that only muons with a minimum momentum of 6 GeV/c can cross the five stations. The Fig. 3.23 shows the organisation of the five stations. Each detector is split into rectangular logical pads whose dimension define the x and y resolution.

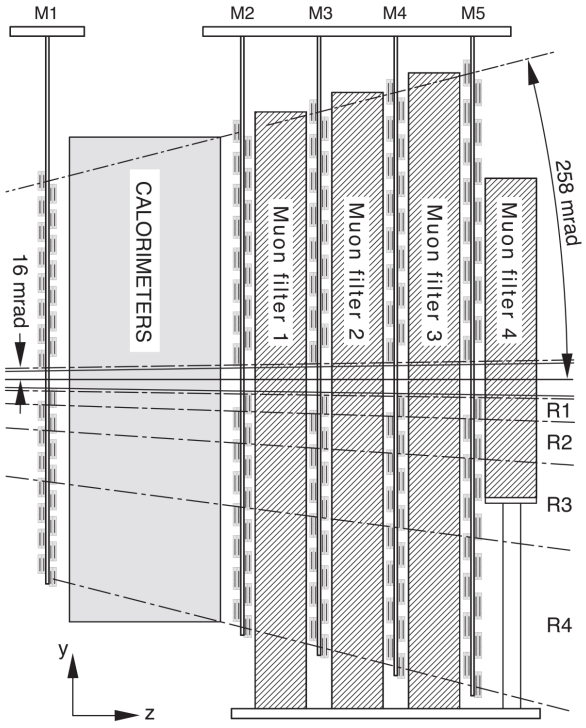

Figure 3.23: Side view of the muon system. This figure is taken from the Ref. [47].

The stations *M1* to *M3* have a better spatial resolution along the x axis than the stations *M4* and *M5*. Therefore the three first stations are used to define the track direction and compute the p_{T} of the muon candidate with a resolution of 20 %, while the two last stations provide information on the identification of the penetrating particles. The logical pad size of the first stations is: $\Delta x = 0.5\,\mathrm{cm}$, $\Delta y = 2.5\,\mathrm{cm}$, while for the *M4* and *M5* stations it is: $\Delta x = 2.0\,\mathrm{cm}$, $\Delta y = 2.5\,\mathrm{cm}$.

3.3 The LHCb trigger system and software environment

3.3.1 The trigger

LHCb was designed to run at the instantaneous luminosity of $2 \times 10^{32}\ \mathrm{cm}^{-2}s^{-1}$. The maximum reached instantaneous luminosity was $2.65 \times 10^{32}\ \mathrm{cm}^{-2}s^{-1}$ in 2011 and $3.90 \times 10^{32}\ \mathrm{cm}^{-2}s^{-1}$ in 2012, so twice the design one. The number of proton-proton interactions per beam crossing is close to one while LHCb was designed to run at ≈ 0.5 interactions per beam crossing (See Fig. 3.6). This translates into an effective crossing frequency (with visible interactions) close to 10 MHz.

The output rate is limited by the electronic to 1 MHz. Therefore, the first step of the LHCb trigger is a hardware selection of events with high transverse momentum hadrons, electrons, photons or muons. Events are then tagged as a function of which trigger has been fired. This trigger is referred to as the L0-trigger and reduces the 10 MHz interaction rate to the required 1 MHz.

It is followed by a two step software trigger. First are selected events with B mesons, then a complete reconstruction of the event is performed. These two triggers are adjustable, in particular the last stage is made of a given number of selection lines corresponding to the different physics analyses. After these three trigger levels, the event rate to storage is about a few kHz. The full trigger system is summarised in the Fig. 3.24.

3.3.2 The hardware level 0 trigger

The L0-trigger collects information from three detectors in order to make a decision per bunch crossing. The L0-trigger uses information from the RICH detectors, the muon chambers and the calorimeters. A veto is set on the events with a too high number of tracks using the *pile-up* information from the VELO.

The muon chambers perform a fast reconstruction of the muon track candidates (due to the low multiplicity of tracks after the calorimeters) with a p_{T} resolution of 20 %. The L0-muon trigger selects the two muon candidates with the highest p_{T} for each quadrant of the muon detector.

The L0-calorimeter trigger system is searching for high E_{T} particles and is split into the different particle natures (electron, photon, hadron). Hadrons are identified by their

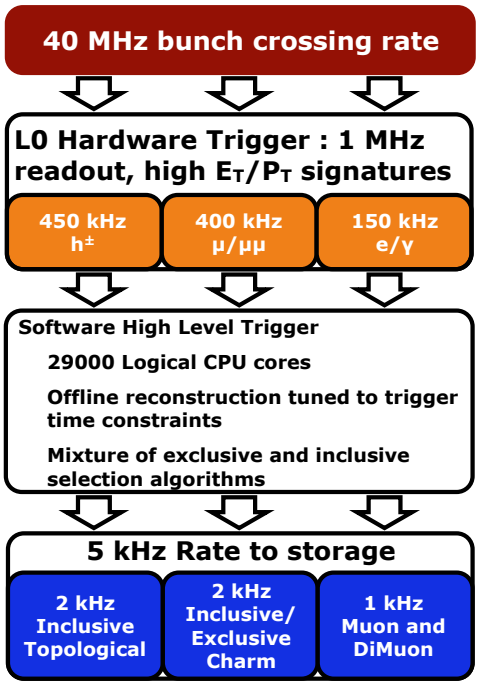

Figure 3.24: Logical sketch of the LHCb trigger.

energy deposition in the ECAL and HCAL and the absence of hits in the PS. Electrons are identified by energy deposition in the PS and the ECAL and hits in the SPD while photons have no hits in the SPD. Energy thresholds are set for each case and events with lower energy are rejected. The `L0Electron` and `L0Photon` lines require the presence of an ECAL cluster with a transverse energy larger than 2.5 GeV while the *L0Hadron* line requires the presence of an ECAL plus a HCAL cluster with a total transverse energy (ECAL + HCAL deposit energy) larger than 3.5 GeV.

Then, the information from the L0 sub-systems is sent to the L0-Decision Unit (*L0DU*) which performs a simple logic to combine the signatures into one decision per bunch crossing. Events are tagged depending on which L0-trigger they fired. The time between the collision and the L0 decision, including the time-of-flight of the particles, electronic delay and process time, is 4 μs. The L0 trigger is adjusted to a nominal rate of 1 MHz and the fraction of rate per nature (electron, hadron, photon or muon) is also adjustable. Accepted events are sent to the HLT trigger.

3.3.3 The software trigger

The software trigger of LHCb, referred to as the HLT, is made of two stages: HLT1 and HLT2. Whereas a partial reconstruction is performed at the HLT1 level using information from the vertexing and tracking system, a full reconstruction of the event is made at the HLT2 level using information from all the sub-detectors.

The HLT1 performs PV reconstruction and search for secondary vertices, the tracks are also reconstructed (with a lower precision than what is done afterwards). PV are reconstructed by searching for five tracks coming from a same point with an uncertainty of $\pm$ 300 µm along the z axis. The tracks are selected by applying a requirement on their impact parameter (IP) with respect to all the PV candidates. The vertex corresponding to the minimum IP value is set as the originating vertex of the track. Therefore, it is possible to determine if the track is originating from a primary or a secondary vertex. The quality of the vertex reconstruction is also computed from the number of hits in the VELO used to reconstruct the track, this vertex quality is expressed as a χ^2 value. High p_{T} tracks are also reconstructed at the HLT1 level. A preliminary measurement of the transverse momentum of the tracks is done using the residual magnetic field in the TT stations.

A full reconstruction of the event is done at the HLT2 level which is completely configurable. A large number of selection lines are defined by the different working groups. There are exclusive lines dedicated to a particular decay as well as inclusive lines based on topology requirements. The selections applied by these lines are either simple cuts or more complex methods using multivariate analyses such as *Boosted Decision Trees* [71].

The HLT-trigger reduces the incoming 1 MHz rate at the output of the L0-trigger to a few kHz rate which is recorded on a disc.

3.3.4 Triggered on signal, or not

Once an event has fired at least one line in each of the three trigger levels, the full event is stored. Each proton-proton collision event is the superposition of several interaction leading to possibly several high energy particles in the detector. In addition, several proton-proton collisions per beam crossing can occur. Therefore, a signal decay is generally accompanied by several unrelated energetic particles, each of them can trigger an L0 line.

If a signal decay is stored because one of its final state particle has triggered a trigger line, it is tagged as *Triggered On Signal* (TOS) with respect to this line. On the other hand, if a signal decay is stored because other particles in the event have triggered the line, it is tagged as *Triggered Independent of Signal* (TIS) with respect to this trigger line. These two labels are dependent of the choice of the signal decay.

3.3.5 The particle identification algorithm

The identification of the nature of the particles is made through an algorithm using information from the RICH, the calorimeter systems and the muon chambers. The detector responses are compared with reference distributions for each particle type (more information can be found in Ref [72]) and the logarithm of the likelihood function [3] is built in each case. Then, a combined likelihood function is built as the product of all the subdetector likelihood functions. The likelihood function is referred to as: $\mathcal{L}_K$, $\mathcal{L}_\pi$ or $\mathcal{L}_e$ for the K, π en e hypothesis respectively.

[3]The likelihood function is the probability, under the assumption of a model, to observe the data which were actually obtained.

The variable used to make a selection based on Particle IDentification (*PID*) are the difference between the logarithm of the likelihood function of two hypotheses. As an exemple, given the kaon and the pion hypotheses for a particle candidate, this variable is:

$$\Delta\ ln\ \mathcal{L}(K-\pi)\ =\ ln\ \mathcal{L}_K - ln\ \mathcal{L}_\pi, \tag{3.3}$$

The higher the variable $\Delta\ ln\ \mathcal{L}(K-\pi)$ is, the higher the probability of the particle candidate to be a kaon. This variable is also referred to $\mathrm{DLL}_{K\pi}$, and all the particle type hypotheses could be combined. To illustrate the use of these variables and the particle identification efficiency, distributions of the efficiency to identify a kaon, a pion and a proton as a function of the particle momentum are displayed in the Fig. 3.25.

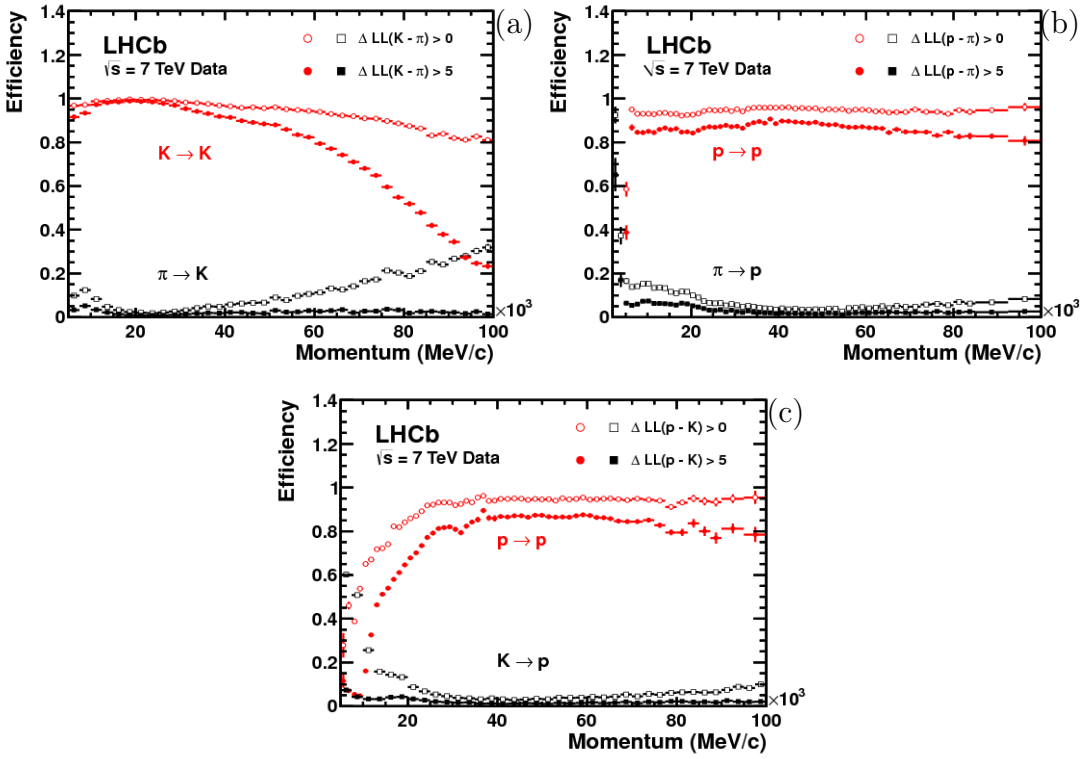

Figure 3.25: Efficiency to identify a kaon as a kaon and a pion as a kaon (a). Efficiency to identify a proton as a proton and a pion as a proton (b). Efficiency to identify a proton as a proton and a kaon as a proton (c). All efficiencies are determined as a function of the particle's momentum and the efficiency relative to two different values of the difference of the logarithm of likelihood are shown.

Analyses use also a second *PID* variable which is built by running multivariate analysis tools based on the detector *PID* information. While the likelihood functions are combined without taking into account the correlation between the information coming from the different detectors, the multivariate analyses take into account these correlations and

produce an output variable similar to a probability. These variables are referred to as: ProbNN_K, ProbNN_π or ProbNN_p according to the particle type hypothesis being tested (the NN refers to the multivariate analysis algorithm used to build these variables: a *Neural-Network*). Therefore, the variable ProbNN_K represents the probability for the particle candidate to be a kaon. These variables a more efficient to distinguish between kaon, pion and proton hypothesis and it is possible to build a linear combination of them such as: $\text{ProbNN}_K \times (1. - \text{ProbNN}_\pi) \times (1. - \text{ProbNN}_p)$ which corresponds to the probability for the particle candidate to be a kaon and not a pion nor a proton.

In the analysis presented in the next chapter of this thesis, the ProbNN variables are used to identify the nature of the hadrons (kaon, pion and proton) while the DLL (likelihood variables) are used to identify the electrons.

3.3.6 Efficiency of the particle identification requirements

The LHCb physics analyses use the event samples stored by the trigger system. But, the number of background events can be much larger than the number of signal events and they can fake the signal. A difficult task is to separate signal and background with a minimal loss of the signal yield. The *PID* variables described in Sec. 3.3.5 are very usefull to this purpose.

It is a known issue that the simulation does not well reproduce the *PID* variable behaviour, therefore it is not possible to use it to estimate the efficiencies of the *PID* selection.

A software tool (*PIDCalib*) has been developed at LHCb, using a data-driven method, in order to get the efficiencies of the *PID* selections. This tool uses a calibration decay where the type of the final state particles is known without any *PID* requirements on them. As an exemple, the sample used to get the efficiencies of *PID* selection on kaons and pions is made of $D^0 \to K^-\pi^+$ decay, where the D^0 is coming from $D^{*+} \to D^0{\pi^+}_s$. Events are selected using only kinematic and topological requirements. The π coming from the D^0 decay is defined as the track having the same electric charge than that of the soft pion ${\pi^+}_s$ (soft pion means that the pion has been produced with a low momentum). The $m_{K\pi}$ distribution is shown in Fig. 3.26.

A mass fit is performed on this calibration sample, and a pure sample is extracted using the result of the fit. Then the *PID* cuts are applied to this pure sample to extract the corresponding efficiency (the ratio between the number of events after and before applying the *PID* requirement). A full description of this tool can be found in the Ref. [73].

In the analysis described in this thesis, only *PID* selection efficiencies on kaon, pion and electron are required. Since there is no selected electron sample available for *PIDCalib* with the same kinematic behaviour than electrons coming from the converted photon, the efficiencies of the *PID* selection on DLL variables applied on electron candidate are taken from simulation. Since the cuts are very loose, the impact of the difference between the simulation and data is expected to be low and will be investigated as a systematic effect.

PIDCalib provides tables of efficiencies as a function of the momentum p and the pseudorapidity η of the track. The efficiencies are also given as a function of the occupancy

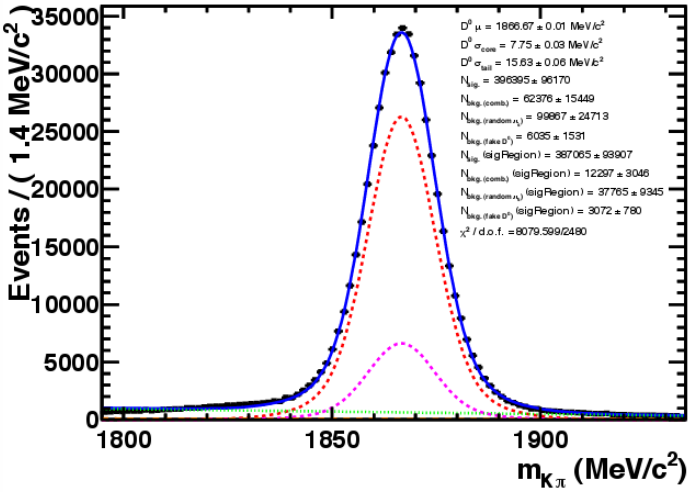

Figure 3.26: $m_{K\pi}$ distribution in 2011 data. Red dashed line correspond to $D^0 \to K^-\pi^+$ decay.

in the detector illustrated by the number of hits in the SPD. Events are also separated according to data acquisition date (2011 or 2012) and magnet polarity configuration (*MagDown* or *MagUp*). The used binning scheme is the default one dedicated to kaon and pion identification and extended to 300 GeV/c in momentum instead of the default 100 GeV/c limit. It consists of 19 bins in p between 3 and 300 GeV/c, 4 bins in η between 1.5 and 5.0 and 4 bins of track multiplicity between 0 and 500.

The generated efficiency tables are used to compute the *PID* selection efficiencies as the mean of efficiencies for each event, which are taken as the product of the efficiency of the final state tracks on which a *PID* requirement is applied. Statistical uncertainty related to a *PID* selection efficiency can be considered as the variance of the mean (the *PID* efficiency of a given sample) estimator realisation, given by [73]

$$\Delta\epsilon_{PID} = \sqrt{\frac{1}{N \times (N-1)} \times \sum_e (\epsilon_e - \epsilon_{PID})^2} \tag{3.4}$$

where N is the number of events before *PID* selection, ϵ_e is the *PID* efficiency of the event e and ϵ_{PID} is the overall *PID* efficiency of the sample. This equation is true if one considers there is no a-priori knowledge of the mean and the sigma of the random variable ϵ_e.

3.3.7 The converted photons reconstruction algorithm

Before explaining the reconstruction of the converted photons at LHCb, a brief description of the naming of the charged tracks is required. As said in Sec. 3.2.2, the charged tracks are reconstructed using information from the whole tracking system. Tracks are not required to have hits in all stations. The reconstructed tracks are named according to which stations have recorded hits along its path, as shown in Fig. 3.27.

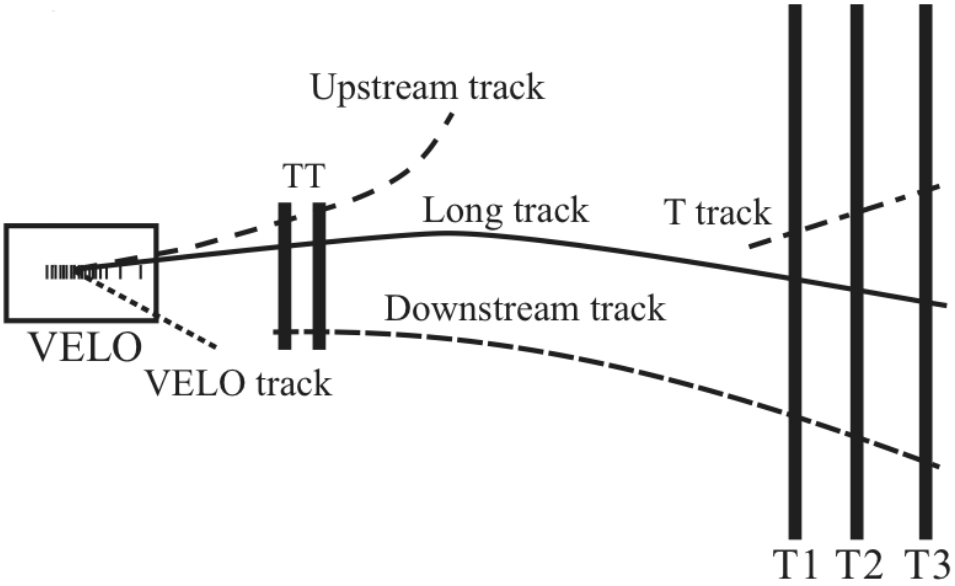

Figure 3.27: The different track types at LHCb according to which detector provided information to reconstruct it.

VELO and T tracks have hits only in the VELO and T stations, respectively. The Upstream tracks have hits in the VELO and TT stations and are deflected by the magnetic field outside of the detector acceptance before reaching the T stations. The Downstream and Long tracks have hits in both TT and T stations on either side of the magnet and the Long tracks have hits also in the VELO while the Downstream ones do not. To measure precisely the momentum of a charged track, its path shall be reconstructed before and after the magnet with hits in the VELO and (or) the TT stations and hits in the T stations which is the case of Long and Downstream tracks. The momentum of the Upstream tracks is measured, with a resolution which is much worse than for Downstream and Long tracks, as the magnetic fields is low in the VELO and TT region. Moreover, there is no calorimeter information associated to Upstream tracks. Therefore, the identification of the particle type is also not as good. So, only electron-positron corresponding to Downstream and Long track types are used to reconstruct photon conversions.

Converted photon reconstruction is fully described in [37]. Conversions are recontructed from opposite sign electron-positron tracks. Long tracks correspond to conversions occurring in the first part of the VELO and Downstream tracks correspond to later conversions, after or too late in the VELO to be reconstructed as Long tracks, but before the magnet. A bremsstrahlung correction is applied on the pair. Photons which are located between the electron track linear extrapolation from the first state and from the TT and which have passed a dedicated selection based on a photon identification with a measured transverse momentum ($p_{\mathrm{T}} > 75\,\mathrm{MeV}/c$) are added to the related electron track if not already added to the other electron of the pair. Then, converted photons candidates

are requested to pass the cut: $m_{ee} < 100\,\mathrm{MeV}/c^2$. The resolution for Long pairs is not as good as for Downstream pairs because if the photon converts early in the detector, electrons see more material and have a higher probability to interact with the detector before reaching the ECAL than for later conversions.

At LHCb, about 23 % of the photons convert before the magnet. Half of these conversions have both tracks reconstructed and only about 34 % are reconstructed in Downstream-Downstream (DD) or Long-Long (LL) configuration. The efficiency of the reconstruction algorithm on these converted photons is about 88 %, leading to a conversion reconstruction efficiency close to 30 %. As it has been shown in the Refs. [35] and [37], the efficiency of the converted photon reconstruction and selection varies almost linearly with the transverse momentum of the photon. Typical ϕ distribution of the converted photons is shown in Fig. 3.28 while Fig. 3.29 displays the position of the conversion vertex along the y axis (Up-Down of the detector) versus its position along the z axis (the beam pipe). These distributions are related to the location of detector's material.

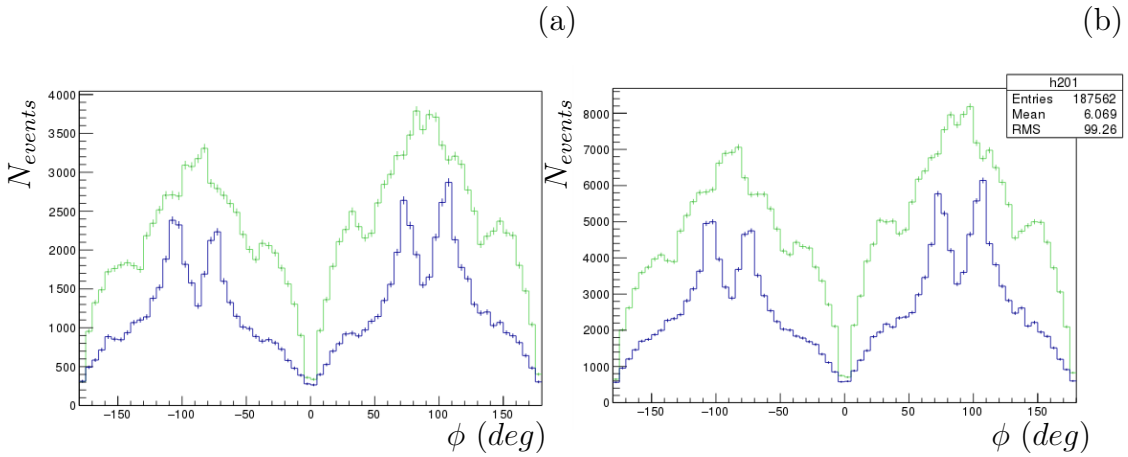

Figure 3.28: ϕ distribution of the conversions in 2011 data for *MagDown* (a) and *MagUp* (b) configuration and DD (green) or LL (blue) dielectron track types. Plots come from Ref. [37].

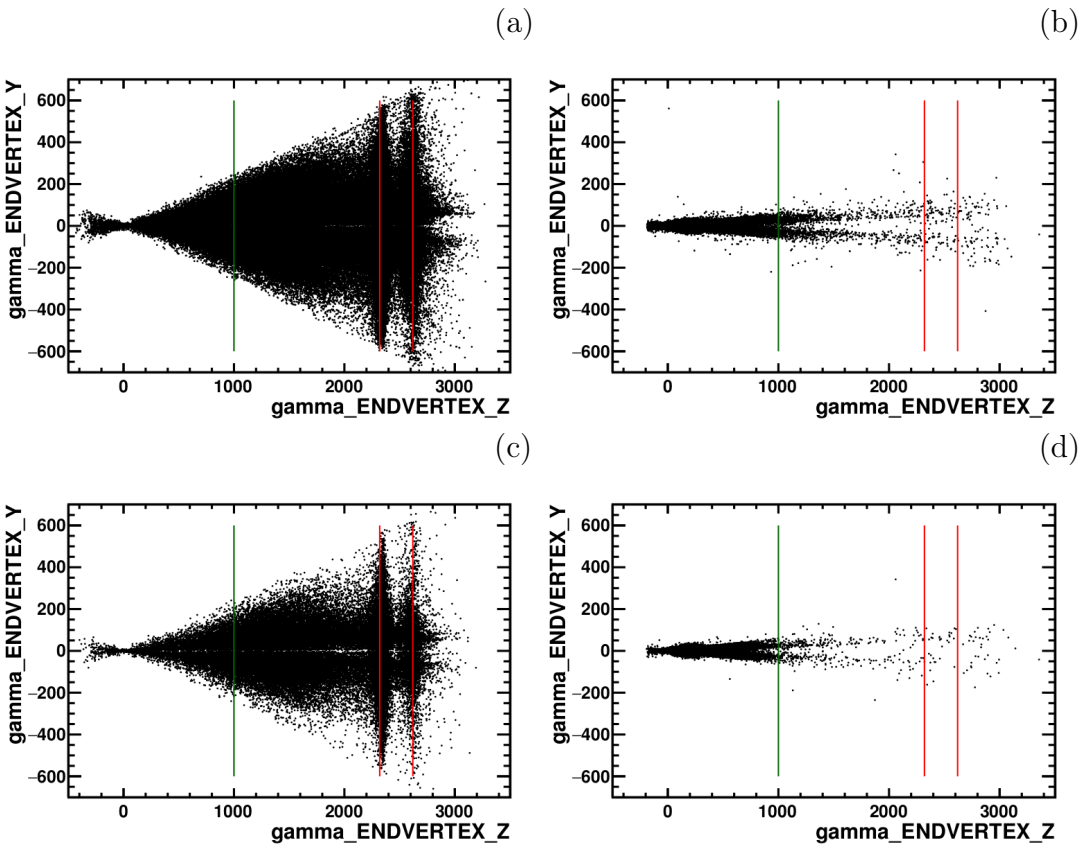

Figure 3.29: Position of the conversion vertex along the y axis versus its position along the z axis in $B^0 \to K^{*0}\gamma(e^+e^-)$ data (a,b) and $B_s^0 \to \phi\gamma(e^+e^-)$ data (c,d). Figures (a) and (c) correspond to DD dielectron track type configuration and figures (b) and (d) correspond to LL ones. The green line corresponds to the end of the VELO (i.e. the beginning of the RICH1) and red lines correspond to the two detection planes of the TT (each of them is made of two layers).

Chapter 4

Signal selection

The samples used for this analysis are described in the beginning of this chapter. It is explained how the data are separated into different samples and how the simulations of the different contributions to the data are performed. The preselections used to increase the signal purity are described. Then, the background composition for both $B^0 \to K^{*0}\gamma$ and $B_s^0 \to \phi\gamma$ signal decays is studied and dedicated vetos are developed. All preselection and selection criteria are based on kinematic, topological and particle identification variables. Efficiencies are computed with simulated samples of signal events. Finally, the total selection efficiencies are computed as well as the expected contamination from some particular backgrounds.

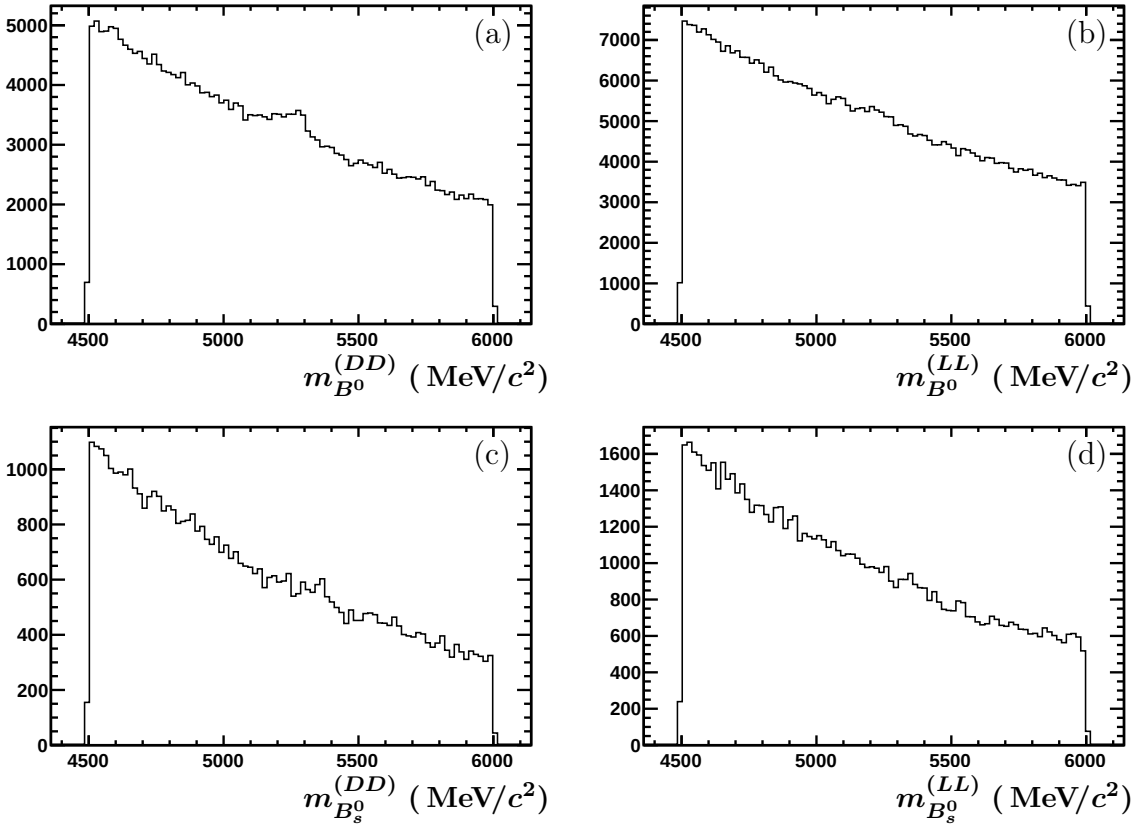

Figure 4.1: Distributions of the reconstructed B mass in data after the preselection described in Sec. 4.2.1. Distributions are from $B^0 \to K^{*0}\gamma(e^+e^-)$, DD (a) and LL (b) and $B_s^0 \to \phi\gamma(e^+e^-)$, DD (c) and LL (d) samples. In order to reduce the size of samples, a cut on the $p_T(\gamma) > 1500\,\text{MeV}/c$ is applied to the $B^0 \to K^{*0}\gamma$ samples (more details about this cut are given in Sec. 4.2.5).

4.1 Samples and simulation

4.1.1 Data samples

The analysis is performed on the full data set collected by the LHCb experiment during the first run of the LHC during years 2011 and 2012. This corresponds to an integrated luminosity of 1 fb^{-1} of pp collisions at $\sqrt{s} = 7$ TeV in 2011 and 2 fb^{-1} at $\sqrt{s} = 8$ TeV in 2012. In 2012, half of the data was taken with the magnet polarity Up and the other half with the magnet polarity Down (as explained in Sec. 3.2.3). In 2011 about 55 % of the data were collected with magnet polarity Down. For illustration, the distribution of the reconstructed B mass after the preselection described in Sec. 4.2.1 in the data for $B^0 \to K^{*0}\gamma$ and $B_s^0 \to \phi\gamma$ decay in both dielectron track type DD and LL (see Sec. 3.3.7) configuration is displayed in Fig. 4.1.

Available HLT2 trigger lines were different in 2011 and 2012. Therefore, samples are splitted by year and different HLT2 trigger line selections are performed (see

Table 4.1: Absolute and relative value of the integrated luminosity for the three sub-samples.

	2011low	*2011high*	*2012*	*all*
$\mathcal{L}$ (fb^{-1})	0.389	0.719	2.082	3.191
$f_{\mathcal{L}}$	0.122	0.225	0.653	1.000

Table 4.2: Estimated number of signal events in the detector acceptance for the full data set : $\mathcal{L}$ = 3 fb^{-1}.

decay channel	$N_{expected}$
$B^0 \to K^{*0}\gamma$	$\mathcal{O}$ (700 k)
$B_s^0 \to \phi\gamma$	$\mathcal{O}$ (150 k)
$B_s^0 \to K^{*0}\gamma$	$\mathcal{O}$ (8 k)

Sec 4.2.4). Furthermore, new HLT2 lines, `Hlt2RadiativeTopoTrackTOS_TOS` and `Hlt2RadiativeTopoPhotonL0_TOS`, have been added in July 2011. Hence, the sub-sample called *2011low* corresponds to the first 0.389 fb^{-1} of 2011 and the sub-sample called *2011high* correspond to the rest of 2011. Relative proportions of integrated luminosity for each of the three sub-samples are given in Tab. 4.1.

Using the integrated luminosity $\mathcal{L}$, the measured branching fractions $\mathcal{B}(B_q \to V_s\gamma)$, b quark fragmentation fraction theoretical values [74] f_q, the $b\bar{b}$ production cross-section at LHC [53] $\sigma(pp \to b\bar{b}X)_{(acc)}$ [1] and the fraction of photons which convert before the magnet in LHCb $f_{(\gamma \to e^+e^-)} \cong 20$ % [37], the estimated number of signal events in the detector acceptance can be computed using Eq. 4.1, numbers are given in Tab. 4.2.

$$N_{expected} = \mathcal{L} \times \sigma(pp \to b\bar{b}X)_{(acc)} \times f_q \times \mathcal{B}(B_q \to V_s\gamma) \times f_{(\gamma \to e^+e^-)} \tag{4.1}$$

4.1.2 Simulation

Simulated samples

To study signal and background, simulated samples have been generated using the physics generator Pythia 8 (Sim08) [75]. These samples are called Monte Carlo (MC) samples as a reference to the Monte-Carlo method used to product them. Moreover, signal MC sample productions using former Pythia 6 (Sim06) have been used to study the impact

[1] $b\bar{b}$ cross-section measurement was done using 1 fb^{-1} events at $\sqrt{s}$ = 7 TeV, it is assumed that the value is the same for 2012 events at $\sqrt{s}$ = 8 TeV.

Table 4.3: *MC* signal (upper section) and background (lower section) samples used for this analysis.

Decay channel	PYTHIA	$p_{\mathrm{T}\gamma}$ cut
$B^0 \to K^{*0}\gamma$	Sim08	yes
	Sim06	no
$B_s^0 \to \phi\gamma$	Sim08	yes
	Sim06	no
$B^0 \to \rho^0\gamma$	Sim08	yes
$\Lambda_b^0 \to \Lambda^*\gamma$	Sim08	yes
$B^0 \to K^{*0}e^+e^-$	Sim08	no
$B_s^0 \to \phi e^+e^-$	Sim08	no
$B^0 \to K_1(1270)\gamma$	Sim08	yes
$B^+ \to K^{*+}\gamma$	Sim08	yes
$B^+ \to K_1(1270)^+\gamma$	Sim08	yes
$B^+ \to K_1(1400)^+\gamma$	Sim08	yes
$B^+ \to K_2(1430)^+\gamma$	Sim08	yes
$B^0 \to K^{*0}\eta$	Sim08	no
$B^+ \to \phi K^+\gamma$	Sim08	yes
$B^0 \to K^+\pi^-\pi^0$	Sim08	no
$B^0 \to K^+\pi^-\pi^0$ (Dalitz)	Sim08	no

of the cut on the transverse momentum of the photon applied to some Sim08 productions. Tab. 4.3 summarises the different *MC* samples used in the analysis.

The latest Sim08 *MC* production of $B^0 \to K^{*0}\gamma$ and $B_s^0 \to \phi\gamma$ decays for 2011 has been generated including `Hlt2RadiativeTopoTrackTOS_TOS` and `Hlt2RadiativeTopoPhotonL0_TOS` lines. Hence, this sample is used to study both *2011low* and *2011high* sub-samples. In order to get efficiencies for the whole 2011 dataset, *MC* events are splitted in two independent samples and the different trigger selections are applied to them, then the two datasets are merged with a weight corresponding to their expected fraction.

Efficiencies of simulated events generation

All *MC* samples have been produced requiring the daughter tracks (e.g. the two final charged hadrons and the dielectron pairs) to be in the acceptance of the detector. Furthermore, some Sim08 productions also required the photon to have a transverse momentum larger than 1.5 GeV (see Tab. 4.3) in order to minimise the size of generated samples since events with low photon's transverse momentum are mostly background events.

Table 4.4: *MC* number of generated events which have passed the acceptance and photon's transverse momentum selection and corresponding efficiencies for signal Sim08 samples for each year and magnet configuration. Note that the efficiencies are estimated using only a fraction of the full generated events.

Decay channel	year	magnet	N_{evt} ($\times 10^6$)	ϵ_{gen} (%)
$B^0 \to K^{*0}\gamma$	2011	MagUp	2.34	21.247 ± 0.039
		MagDown	2.31	21.277 ± 0.039
	2012	MagUp	4.53	21.523 ± 0.054
		MagDown	4.52	21.434 ± 0.055
$B_s^0 \to \phi\gamma$	2011	MagUp	2.25	23.145 ± 0.043
		MagDown	2.29	23.153 ± 0.042
	2012	MagUp	4.54	23.485 ± 0.058
		MagDown	4.52	23.553 ± 0.059

Efficiencies, including both acceptance and photon's transverse momentum cut efficiencies (which is ≈ 88 % for all categories), for signal Sim08 samples are shown in the Tab. 4.4.

4.2 Signal preselection

In order to minimise the size of samples to perform background and signal studies, a set of preselections is applied to real and simulation data. First, a loose preselection, called *stripping*, is applied on events. Then, specific trigger lines are selected. *MC* samples have been generated with a cut on the transverse momentum of the photon and this cut is applied on data samples too. Finally, B and vector mesons are requested to have a reconstructed mass matching the reference values given by the Particle Data Group [7] within a given mass value window.

4.2.1 Stripping

After being triggered and stored, events are reconstructed and a loose preselection is applied in order to minimise the computing time and the storage capacity. This preselection step is called the *stripping* at LHCb and is made of a combination of different lines, corresponding to the different physics analyses requirements, which performs inclusive or exclusive selections of events. Therefore, several different sub-samples of incoming data are stored instead of a single large set of data, making the data handling easier for the analysists.

Two specific exclusive stripping lines have been developed at LHCb to select $B^0 \to K^{*0}\gamma(e^+e^-)$ and $B_s^0 \to \phi\gamma(e^+e^-)$ events: `StrippingB2KstGammaConv_Line` and

`StrippingB2PhiGammaConv_Line`, respectively. These lines search for two opposite charge hadrons without any PID requirement but, with a common vertex and two opposite charge electron-positron compatible with a photon conversion (it is the converted photon reconstruction process described in Sec. 3.3.7). Then, a common vertex, shifted from the PV, is searched for the two reconstructed mothers (e.g. the photon and the two hadron mother). Cuts are applied at each step of this process, based on kinematic, topological and PID (for the electron and the positron only) variables.

The mass of the $B^0_{(s)}$ shall be included in the range [4000,7000] MeV/c^2. The χ^2 per degree of freedom of the vertex of a track corresponds to the quality of the candidate vertex fit. The χ^2_{vtx}/ndf is requested to be lower than 9 for the B and the vector meson and the photon. The *DIRA* of a particle is the cosine of the angle between the reconstructed momentum of the particle and the direction vector from a given vertex (PV, ...) to the end vertex of the particle. The *DIRA* of the $B^0_{(s)}$ is requested to be greater than 0.9998 which corresponds to a very low angle. The χ^2 of the impact parameter of a track is related to a given vertex and corresponds to the impact of the addition of this track to the vertex reconstruction. Therefore, a high χ^2_{IP} means that the track seems incompatible with coming from the relative vertex. The χ^2_{IP} of the B candidate is requested to be lower than 9.

Then, the K^{*0} and ϕ candidate are requested to have a transverse momentum greater than 1500 MeV/c and a maximum (absolute) difference from the mass given in Ref. [7] and the reconstructed mass below 150 MeV/c^2 for the K^{*0} and 15 MeV/c^2 for the ϕ. The χ^2 significance of the determination of the flying distance of the K^{*0} and the ϕ candidate shall be greater than 81. The photon candidate is requested to have a transverse momentum greater than 200 MeV/c and the dielectron mass shall be below 100 MeV/c^2.

Finally, the final state hadrons (kaon or pion) are requested to have a transverse momentum greater than 500 MeV/c and a momentum greater than 3000 MeV/c. The minimum of the χ^2_{IP} with any PV shall be greater than 16 and the χ^2 significance of the fit of the track per degree of freedom shall be below 3. Electrons and positrons are requested to be well identified and have a DLL_e greater than -2 (see Sec. 3.3.5).

The list of all cuts applied by each of these lines is given in Tab. 4.5 and the distribution of the reconstructed B mass are shown in Fig. 4.1.

MC samples are used to compute stripping efficiencies. However, cuts listed in Tab. 4.5 are applied again on data and *MC* since events which shall be removed by the cuts are still present in the samples. This is due to differences in the reconstruction of some variables before and after the stripping. This has been corrected in the latter stripping version. Stripping efficiencies, included the re-stripping are given in Tab. 4.6.

4.2.2 True signal sample definition

Applying reconstruction and stripping to a simulated signal sample generates also some background events. These events are artefacts of the reconstruction and stripping processes: two charged hadron tracks are gathered to come from the same particle decay vertex

Table 4.5: Stripping cuts from `StrippingB2Kst(Phi)GammaConv_Line` used to select $B^0 \to K^{*0}\gamma(e^+e^-)$ ($B_s^0 \to \phi\gamma(e^+e^-)$) events.

Particle	Stripping Cut
$B^0_{(s)}$	$m_{B^0_{(s)}} \in [4000, 7000]\,\mathrm{MeV}/c^2$
	$\chi^2_{\mathrm{vtx}}/\mathrm{ndf} < 9$
	$DIRA > 0.9998$
	$\chi^2_{\mathrm{IP}} < 9$
K^{*0} (ϕ)	$p_{\mathrm{T}} > 1500\,\mathrm{MeV}/c$
	$\Delta m_{K^{*0}(\phi)} < 150(15)\,\mathrm{MeV}/c^2$
	$\chi^2_{\mathrm{vtx}}/\mathrm{ndf} < 9$
	$\chi^2_{FD} > 81$
$\gamma \to e^+e^-$	$p_{\mathrm{T}} > 200\,\mathrm{MeV}/c$
	$\chi^2_{\mathrm{vtx}}/\mathrm{ndf} < 9$
	$m_{e^+e^-} < 100\,\mathrm{MeV}/c^2$
K / π (K)	$p_{\mathrm{T}} > 500\,\mathrm{MeV}/c$
	$p > 3000\,\mathrm{MeV}/c$
	$min(\chi^2_{\mathrm{IP}}) > 16$
	$\chi^2_{track}/ndf < 3$
	$P_{ghost-track} < 0.4$
e	$combDLL_e > -2.0$

Table 4.6: Stripping efficiencies estimated in *MC* including re-stripping ones, before trigger lines selection is applied.

Decay channel	year	$\epsilon_{stripping}$ ($\times 10^{-2}$)
$B^0 \to K^{*0}\gamma$	2011	0.430 ± 0.003
	2012	0.388 ± 0.002
$B^0_s \to \phi\gamma$	2011	0.391 ± 0.003
	2012	0.356 ± 0.002

without PID requirement. In the case of the $B^0 \to K^{*0}\gamma$ decay, two particle hypotheses are generated ($K\pi$ or πK), and in some cases the algorithm cannot decide which one is the correct hypothesis and both are kept, generating two candidates for the same event.

Therefore, a method to choose true and well reconstructed signal events is mandatory. The `BKGCAT` variable [76] is a helpful tool to perform it. Each candidate is tagged as *signal* (`BKGCAT` = 0), *reflection* (`BKGCAT` = 30), *ghost* (`BKGCAT` = 60), and several other categories according to a succession of tests on the reconstructed event in order to check if it corresponds to the related true simulated event (using *MC* truth information, i.e. the

true value of all decay's observables at the generation level, as well).

A simple way to select true signal events and reject mis-identified ones is to get only *signal* (`BKGCAT` = 0) tagged candidates. Unfortunately, this method removes $\approx 20\%$ of *ghost* events, which are events where one or more reconstructed track is not matched with an *MC* truth information but part of these events are in fact signal ones.

An alternative way is proposed here, based on the `BKGCAT` variable and *MC* truth information as the true nature (kaon, pion, ...) of the generated particle and its true origin vertex. First events are selected according to the background category as defined by the `BKGCAT` variable :

1. Signal event: `BKGCAT` = 0, the reconstructed decay matches perfectly with one generated true decay.

2. Low mass background event: `BKGCAT` = 50, all reconstructed tracks are matched with true particles which have the same corresponding true mothers. But all true particles originating from the true vertices of the mothers are not matched to final state daughters of the candidate. However, all candidate's final state daughters are well identified and the difference between the common true mother and candidate mother masses is bellow 100 MeV. This can correspond to events where a Bremsstrahlung photon is emitted and not reconstructed. This category contains events which populate the low part of the B meson reconstructed mass spectra as shown in Fig. 4.2.

3. Ghost background event: `BKGCAT` = 60, one or more of the final state daughters does not match with any true generated particle.

Additional requirements, based on *MC* truth information (the true ID), are applied on these events. For the first two categories, true daughter particles are requested to have the expected particle type, the two reconstructed hadrons in the final state should correspond to the generated kaon and pion in the case of the $B^0 \to K^{*0}\gamma$ decay and the two kaons in the case of the $B_s^0 \to \phi\gamma$ decay, similarly the reconstructed dielectron should correspond to the generated electrons. For the third category (`BKGCAT` = 60), events where more than one particle of the final state is not matched with the *MC* truth information are rejected and additional requirements are applied on remaining events:

- For events where one of the final state hadrons is not matched to a true *MC* particle, other final state tracks are required to have the correct *MC* true nature. In addition, since both electron and positron are matched and are compatible with a photon conversion vertex, the matched hadron and the photon are required to have a common true origin vertex.

- For events where the final electron or positron are not matched, other final state tracks are required to have a correct *MC* true nature and final state hadrons should have a common true origin vertex.

Table 4.7: Fractions of true signal event for both $B^0 \to K^{*0}\gamma$ and $B_s^0 \to \phi\gamma$ decay using `BKGCAT` variable and *MC* truth information based alternative method. Fractions for the simple method using only `BKGCAT` = 0 events are also given.

decay channel	year sample	alternative method	simple method
$B^0 \to K^{*0}\gamma$	2011	60.3 %	49.9 %
	2012	59.8 %	47.1 %
$B_s^0 \to \phi\gamma$	2011	94.3 %	76.7 %
	2012	94.0 %	76.0 %

Using the alternative method removes a large part of events with multiple candidates, in particular in the case of the $B^0 \to K^{*0}\gamma$ decay where ≈ 30 % of the events have double misidentified hadrons, i.e. the true kaon is reconstructed as a pion and the true pion is reconstructed as a kaon.

According to `BKGCAT` variable, the correct candidate is tagged as a *signal* event and the other as a *reflection* event and is removed by the previous true event selection. However, some multiple candidates remain and are removed according to the following algorithm: if there are *signal* (or *low mass background*) candidates with other candidates, then only *signal* (*low mass background*) candidates are kept. Then, for the remaining multiple candidate events, the one with the reconstructed B mass closest to the expected value given by PDG [7] is kept. This last case represents less than 0.2% of the events and so the bias introduced is considered as negligible.

Pure signal samples without any multiple candidates for both $B^0 \to K^{*0}\gamma$ and $B_s^0 \to \phi\gamma$ decays have been selected with this method, corresponding to the fractions shown in Tab. 4.7. From now on, and if it is not mentioned, all Sim08 *MC* signal samples are defined this way.

4.2.3 Dielectron track type samples

The mass resolution for Long pairs is not as good as for Downstream pairs (as defined in Sec. 3.3.7) by a factor close to 1.2 (from *MC*, see Sec. 5.1.1). Because for early conversion in the detector, electrons see more material and interact more before reaching the ECAL than for later conversions, they radiate more photons. Therefore, data and *MC* are splitted according to the dielectron track type: events with Downstream-Downstream (*DD*) and Long-Long (*LL*) pair. Different selections have been developed for both track type category's sub-samples. Fractions of *DD* and *LL* events in the true signal event selected *MC* samples are shown in Tab. 4.8.

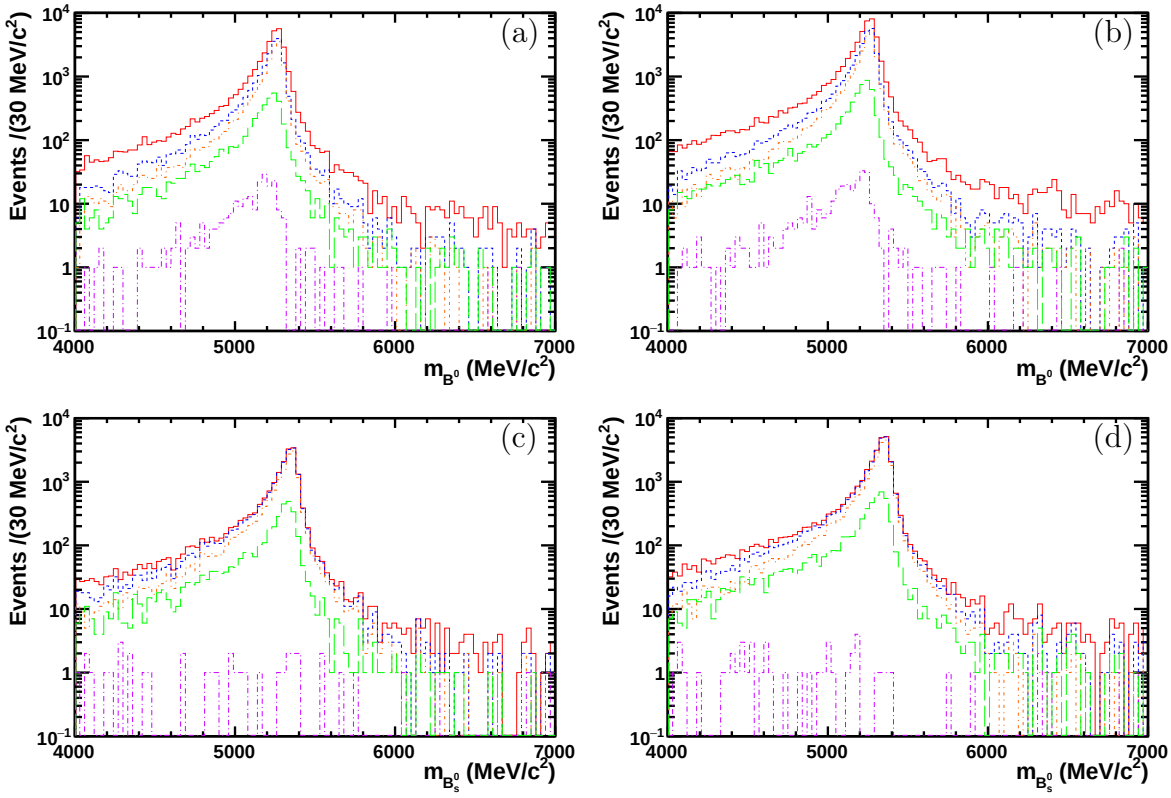

Figure 4.2: Distribution of the reconstructed B mass for Sim08 *MC* events, for $B^0 \to K^{*0}\gamma$ decay, 2011 (a) and 2012 (b) samples and $B_s^0 \to \phi\gamma$ decay, 2011 (c) and 2012 (d) samples. The impact of true signal event selection is shown, the full red line represents the distribution before `BKGCAT` selection and the dashed blue line, the distribution once the `BKGCAT` selection is applied, the short-dashed doted orange line represents events with `BKGCAT` = 0, the long-dashed doted violet line events with `BKGCAT` = 50 and the long-dashed green line events with `BKGCAT` = 60.

Table 4.8: Fractions of *DD* and *LL* events in signal *MC* samples.

Decay channel	year	f_{DD}	f_{LL}
$B^0 \to K^{*0}\gamma$	2011	60.2 %	39.8 %
	2012	60.4 %	39.6 %
$B_s^0 \to \phi\gamma$	2011	55.4 %	44.6 %
	2012	56.3 %	43.7 %

Table 4.9: Selected L0 trigger line efficiencies after stripping, computed using *MC* (Sim08) samples. ϵ_{L0} is the efficiency of the full L0 trigger selection while the $\epsilon_{\texttt{L0Something}}$ are the efficiencies when only the L0 line `L0Something` is selected.

Decay chan.	year	$tt_{(e^+e^-)}$	ϵ_{L0}	$\epsilon_{\texttt{L0ElectronTOS}}$	$\epsilon_{\texttt{L0HadronTOS}}$	$\epsilon_{\texttt{L0GlobalTIS}}$
$B^0 \to K^{*0}\gamma$	2011	DD	0.636 ± 0.004	0.410 ± 0.004	0.204 ± 0.004	0.315 ± 0.004
		LL	0.573 ± 0.006	0.267 ± 0.005	0.184 ± 0.004	0.338 ± 0.005
	2012	DD	0.577 ± 0.004	0.321 ± 0.004	0.197 ± 0.003	0.300 ± 0.003
		LL	0.524 ± 0.005	0.195 ± 0.004	0.180 ± 0.004	0.329 ± 0.004
$B_s^0 \to \phi\gamma$	2011	DD	0.632 ± 0.005	0.416 ± 0.005	0.169 ± 0.004	0.310 ± 0.005
		LL	0.550 ± 0.006	0.261 ± 0.005	0.141 ± 0.004	0.331 ± 0.005
	2012	DD	0.567 ± 0.004	0.343 ± 0.004	0.158 ± 0.003	0.289 ± 0.004
		LL	0.489 ± 0.005	0.203 ± 0.004	0.127 ± 0.003	0.307 ± 0.004

4.2.4 Trigger selection

Hardware trigger

The LHCb trigger system has been described in the Sec. 3.3. Events must trigger at least one trigger line at each level (L0, HLT1 and HLT2) to be stored. A dedicated selection of trigger lines is performed to increase the purity of the sample. *MC* samples are used to get the efficiency of trigger line selection.

Events are requested to fire at least one of the following L0 trigger lines: `L0Electron_TOS`, `L0Hadron_TOS` (See Sec. 3.3.2) or `L0Global_TIS` which corresponds to the global response of the L0-trigger including all lines. The line dedicated to photons, `L0Photon_TOS` (See Sec. 3.3.2), has not been taken since less than 3 % of events fire this line. In the first two cases L0 trigger is required to be *Trigger On Signal* (*TOS*) while the third case is *Trigger Independant of Signal* (*TIS*). The difference between *TOS* and *TIS* has been explained in Sec. 3.3.1. As the efficiency of `L0Electron_TOS` and `L0Hadron_TOS` triggers is quite low, `L0GlobalTIS` line has been added. In this case any particle could have triggered this line.

Efficiencies of selected L0 trigger lines are computed independently using *MC* samples and given in the Tab. 4.9 with the global L0 selection efficiency. The observed differences between *2011* and *2012* way be due to the different energy thresholds used. These thresholds have been changed several times during *2011* and *2012*. The sum of each line's efficiency is not equal to the one of the total L0 since one event may have triggered several lines.

Table 4.10: Selected HLT1 trigger line efficiencies after stripping and L0 trigger selection, computed using *MC* (Sim08) samples.

Decay channel	year	$tt_{(e^+e^-)}$	ϵ_{HLT1}	$\epsilon_{\texttt{Hlt1TrackAllL0\_TOS}}$	$\epsilon_{\texttt{Hlt1TrackPhoton\_TOS}}$
$B^0 \to K^{*0}\gamma$	2011	DD	0.657 ± 0.005	0.606 ± 0.006	0.238 ± 0.005
		LL	0.717 ± 0.007	0.691 ± 0.007	0.182 ± 0.006
	2012	DD	0.680 ± 0.005	0.639 ± 0.005	0.263 ± 0.004
		LL	0.748 ± 0.006	0.724 ± 0.006	0.206 ± 0.005
$B_s^0 \to \phi\gamma$	2011	DD	0.614 ± 0.006	0.548 ± 0.006	0.249 ± 0.005
		LL	0.661 ± 0.007	0.619 ± 0.007	0.181 ± 0.006
	2012	DD	0.661 ± 0.005	0.603 ± 0.005	0.281 ± 0.005
		LL	0.708 ± 0.006	0.668 ± 0.006	0.215 ± 0.005

Software trigger

After the L0 trigger selection, events are requested to have triggered `Hlt1TrackAllL0_TOS` or `Hlt1TrackPhoton_TOS`. HLT1 decision requires the event to have triggered any L0 line for `Hlt1TrackAllL0_TOS` while `Hlt1TrackPhoton_TOS` requires the event to have triggered `L0Electron_TOS` or `L0Photon_TOS`. In addition, a track in the event should have a transverse momentum greater than 1800 MeV/c for `Hlt1TrackAllL0_TOS` and greater than 1200 MeV/c for `Hlt1TrackPhoton_TOS`, a momentum greater than 10000 MeV/c, an impact parameter χ^2 greater than 16 and a track χ^2 lower than 3 for both lines. Efficiencies for HLT1 selected lines are given in Tab. 4.10.

The HLT2 selection has been limited to the inclusive topological [77] and radiative lines. In the first case, a given number of charged tracks coming from a vertex which is not the PV are searched while, in the second case, a photon is combined with additional charged track(s). The topological lines proceed as follows: tracks with $p_{\mathrm{T}} > 500$ MeV/c and $p > 5000$ MeV are reconstructed, their impact parameter χ^2 (χ^2_{IP}) is requested to be greater than 16 and their track χ^2 (χ^2_{track}) to be lower than 5. Only tracks passing this selection are kept. Particles are combined to form a 2-body object, then another particle is combined with the 2-object to form a 3-object, the action is repeated to form a 4-object depending on the line. A cut on the distance of closest approach is applied for each combination step. Then a Boosted Decision Tree is trained with different kinematic and topological variables and a cut on the output variable is applied on the remaining events. For the `Hlt2TopoEnBodyBBDT` (n = 2,3,4) tracks are requested to have a PIDe greater than -2.0.

The two radiative lines used in addition to the topological lines are: `Hlt2RadiativeTopoTrack(TOS)_TOS` and `Hlt2RadiativePhoton(L0)_TOS` [78]. They are based on the same strategy, but without the use of a Boosted Decision Tree and with few differences in cut values. In these cases, tracks should have a $p_{\mathrm{T}} > 700$ MeV/c and an

impact parameter χ^2 greater than 10 and are combined to form a 2-object which is combined with a photon candidate of $E_{\mathrm{T}} > 2500$ MeV/c. The `Hlt2RadiativePhotonL0_TOS` line runs on events that have passed either the `L0Electron_TOS` or the `L0Photon_TOS`.

Lines are chosen according to their efficiency, taking the most efficient then removing events which have triggered it and taking the next most efficient line and so on, while the cumulative efficiencies increase by more than about 1 %. This selection has been applied independently on decay sub-samples according to the data acquisition time and dielectron track type but, in order to minimise systematic uncertainties in the ratio of branching fractions, the same lines are chosen for both $B^0 \to K^{*0}\gamma$ and $B^0_s \to \phi\gamma$ in each sub-sample.

Selected HLT2 lines and respective efficiencies for all sub-samples are summarised in the Tab. 4.11. The order of the HLT2 lines is presented for each sub-sample is the order following which the lines have been chosen, the first one being the most efficient. Therefore, cumulated efficiencies are presented for each step of the selection.

As said in the Sect. 4.1.1, available HLT2 lines are different for the three *2011low*, *2011high* and *2012* sub-samples. The main topological lines `Hlt2Topo(E)XBodyBBDT` are available for the full dataset, but `Hlt2RadiativeTopoTrackTOS_TOS` and `Hlt2RadiativeTopoPhotonL0_TOS` are only available for the *2011high* and the *2012* sub-samples. The addition of `Hlt2RadiativeTopoTrackTOS_TOS` (DD) and `Hlt2RadiativeTopoPhotonL0_TOS` (LL) increase the efficiency in *2011high* samples with respect to *2011low* samples.

Due to CPU constraints, HLT2 searches only for long tracks based on VELO hits. Therefore, DD events are recovered mainly using 2 body lines which have been triggered by hadrons in the final state. This explains the lower efficiencies for DD samples observed in Tab. 4.11. Full HLT2 trigger selection corresponds to efficiencies written in bold. The full trigger efficiency for each sub-sample is given in Tab. 4.12.

4.2.5 High γ p_{T} generation cut

As it was said in Sec. 4.1.2, some Sim08 *MC* samples have been produced requiring that at least one photon in the event has a transverse momentum higher than 1500 MeV/c. The event selection therefore starts with a cut on the reconstructed photon p_{T} at 1500 MeV/c. The efficiency of this cut, which is generally around 90 %, is included in the generation efficiency. The photon with high transverse momentum was not required to originate from the B decay, but could come from another part of the event. Hence some $B^0_{(s)} \to K^{*0}(\phi)\gamma$ events with a photon with a true transverse momentum (from the truth information in *MC*) lower than 1.5 GeV/c can pass the cut (around 2 % of events after stripping and trigger selection).

Sim06 *MC* samples which have been generated without any requirement except the cut on the acceptance of the detector are used to search for a bias introduced

Table 4.11: Selected HLT2 trigger lines and cumulative efficiencies after stripping, L0 and HLT1 selection, computed using *MC* (Sim08) samples. Bold written efficiencies correspond to the full HLT2 trigger selection efficiency.

year	$tt_{(e^+e^-)}$	HLT2 line	$\epsilon_{B^0\to K^{*0}\gamma}$	$\epsilon_{B^0_s\to\phi\gamma}$
2011low	DD	`Hlt2Topo2BodyBBDT_TOS`	0.305 ± 0.006	0.373 ± 0.008
		`Hlt2TopoE2BodyBBDT_TOS`	**0.327 ± 0.007**	**0.393 ± 0.008**
2011low	LL	`Hlt2Topo3BodyBBDT_TOS`	0.610 ± 0.009	0.637 ± 0.009
		`Hlt2Topo2BodyBBDT_TOS`	0.706 ± 0.008	0.712 ± 0.008
		`Hlt2TopoE3BodyBBDT_TOS`	0.733 ± 0.008	0.745 ± 0.008
		`Hlt2TopoE2BodyBBDT_TOS`	**0.745 ± 0.008**	**0.755 ± 0.008**
2011high	DD	`Hlt2RadiativeTopoTrackTOS_TOS`	0.466 ± 0.007	0.466 ± 0.008
		`Hlt2Topo2BodyBBDT_TOS`	0.581 ± 0.007	0.621 ± 0.008
		`Hlt2TopoE2BodyBBDT_TOS`	**0.587 ± 0.007**	**0.626 ± 0.008**
2011high	LL	`Hlt2Topo3BodyBBDT_TOS`	0.610 ± 0.009	0.637 ± 0.009
		`Hlt2Topo2BodyBBDT_TOS`	0.706 ± 0.008	0.712 ± 0.008
		`Hlt2RadiativeTopoPhotonL0_TOS`	0.752 ± 0.008	0.749 ± 0.008
		`Hlt2TopoE3BodyBBDT_TOS`	0.768 ± 0.007	0.777 ± 0.008
		`Hlt2TopoE2BodyBBDT_TOS`	**0.776 ± 0.007**	**0.784 ± 0.008**
2012	DD	`Hlt2RadiativeTopoPhoton_TOS`	0.431 ± 0.006	0.438 ± 0.007
		`Hlt2Topo2BodyBBDT_TOS`	0.596 ± 0.006	0.614 ± 0.006
		`Hlt2Topo3BodyBBDT_TOS`	0.632 ± 0.006	0.661 ± 0.006
		`Hlt2TopoE2BodyBBDT_TOS`	0.636 ± 0.006	0.664 ± 0.006
		`Hlt2RadiativeTopoTrack_TOS`	**0.643 ± 0.006**	**0.666 ± 0.006**
2012	LL	`Hlt2Topo3BodyBBDT_TOS`	0.687 ± 0.007	0.703 ± 0.007
		`Hlt2Topo2BodyBBDT_TOS`	0.753 ± 0.006	0.762 ± 0.007
		`Hlt2Topo4BodyBBDT_TOS`	0.762 ± 0.006	0.776 ± 0.007
		`Hlt2TopoE3BodyBBDT_TOS`	0.772 ± 0.006	0.788 ± 0.006
		`Hlt2RadiativeTopoPhoton_TOS`	**0.783 ± 0.006**	**0.797 ± 0.006**

by this cut. All samples are considered after being stripped and triggered. For the $B^0 \to K^{*0}\gamma$ sample (values are similar in $B^0_s \to \phi\gamma$ samples), the fraction of events in Sim06 *MC* samples with a true transverse momentum lower than 1.5 GeV/c is around 4.5 %. When keeping only events if the photon reconstructed transverse momentum is: ${p_{\rm T}}^{(rec)} > 1.5\,\text{GeV}/c$, the fraction of remaining events with the photon true transverse momentum ${p_{\rm T}}^{(true)} \leq 1.5\,\text{GeV}/c$ (from the simulation truth information) is around 0.14 % for *Sim06* samples (≈ 0.02 % for *Sim08*). Therefore the efficiency computed with *Sim08* samples is underestimated by about 0.1 % which is considered negligible.

It was concluded that a cut on the reconstructed transverse momentum at 1.5 GeV/c

Table 4.12: Efficiencies of the full trigger selection including L0, HLT1 and HLT2 after stripping.

Decay channel	year	$tt_{(e^+e^-)}$	$\epsilon_{trigger}$
$B^0 \to K^{*0}\gamma$	2011low	DD	0.137 ± 0.003
		LL	0.306 ± 0.005
	2011high	DD	0.246 ± 0.004
		LL	0.319 ± 0.005
	2012	DD	0.253 ± 0.003
		LL	0.307 ± 0.004
$B_s^0 \to \phi\gamma$	2011low	DD	0.152 ± 0.004
		LL	0.275 ± 0.005
	2011high	DD	0.243 ± 0.004
		LL	0.285 ± 0.005
	2012	DD	0.250 ± 0.004
		LL	0.275 ± 0.004

Table 4.13: $p_{\mathrm{T}}(\gamma) > 1500\,\mathrm{MeV}/c$ cut efficiencies, computed using Sim08 *MC* events after stripping and trigger selection.

Decay channel	year	$tt_{(e^+e^-)}$	$\epsilon_{highpTCut}$
$B^0 \to K^{*0}\gamma$	2011low	DD	0.970 ± 0.004
		LL	0.957 ± 0.004
	2011high	DD	0.983 ± 0.002
		LL	0.959 ± 0.004
	2012	DD	0.978 ± 0.002
		LL	0.968 ± 0.003
$B_s^0 \to \phi\gamma$	2011low	DD	0.961 ± 0.005
		LL	0.966 ± 0.004
	2011high	DD	0.975 ± 0.003
		LL	0.967 ± 0.004
	2012	DD	0.980 ± 0.002
		LL	0.968 ± 0.003

removes most of the events with a true transverse momentum lower than $1.5\,\mathrm{GeV}/c$. The efficiency of the generation cut is already included in the generation efficiencies given in Sec. 4.1.2. Efficiencies of the cut on reconstructed transverse momentum are given in Tab. 4.13.

4.2.6 Converted photon selection

A dedicated selection has been developed in [37] in order to select converted photons. Since LL events have a track segment in the VELO, the dielectron mass is more precisely measured than for DD events as it can be seen in Fig. 4.3. Hence LL events are required to have a reconstructed dielectron mass $m_{(e^+e^-)}$ lower than 60 MeV/c^2 while DD events are kept up to 100 MeV/c^2.

Fig. 4.4 shows the reconstructed dielectron mass versus the z coordinate of the photon vertex in data for DD and LL samples in $B^0 \to K^{*0}\gamma$ decay (distribution is expected to be the same for $B_s^0 \to \phi\gamma$) in MC samples for pure signal, and in data. Events with high mass and low z are clearly background in both DD and LL samples. In the LL case, this region is also contaminated by π^0 dalitz decays if the e^+e^- pair originates from the primary vertex and has an invariant mass between 0 and the π^0 mass. A 2D cut based on these two variables is applied to remove these background events, $m_{ee}/\,\mathrm{MeV}/c^2 - 0.04 \times z_{vtx}/mm < 20$ in DD case and $m_{ee}/\,\mathrm{MeV}/c^2 - 0.083 \times z_{vtx}/mm < 17$ in LL case. The impact of this cut is also shown in Fig. 4.4.

In addition to these cuts, electrons are required to have a $CombDLL_e$ (see Sec. 3.3.5) greater than -1 in order to remove pions contamination. The distribution of this variable for both electron and positron in data and MC samples are shown in Fig. 4.5. Efficiencies related to this selection, including the cut on the reconstructed dielectron mass in LL events and 2D cut, are given in Tab. 4.14.

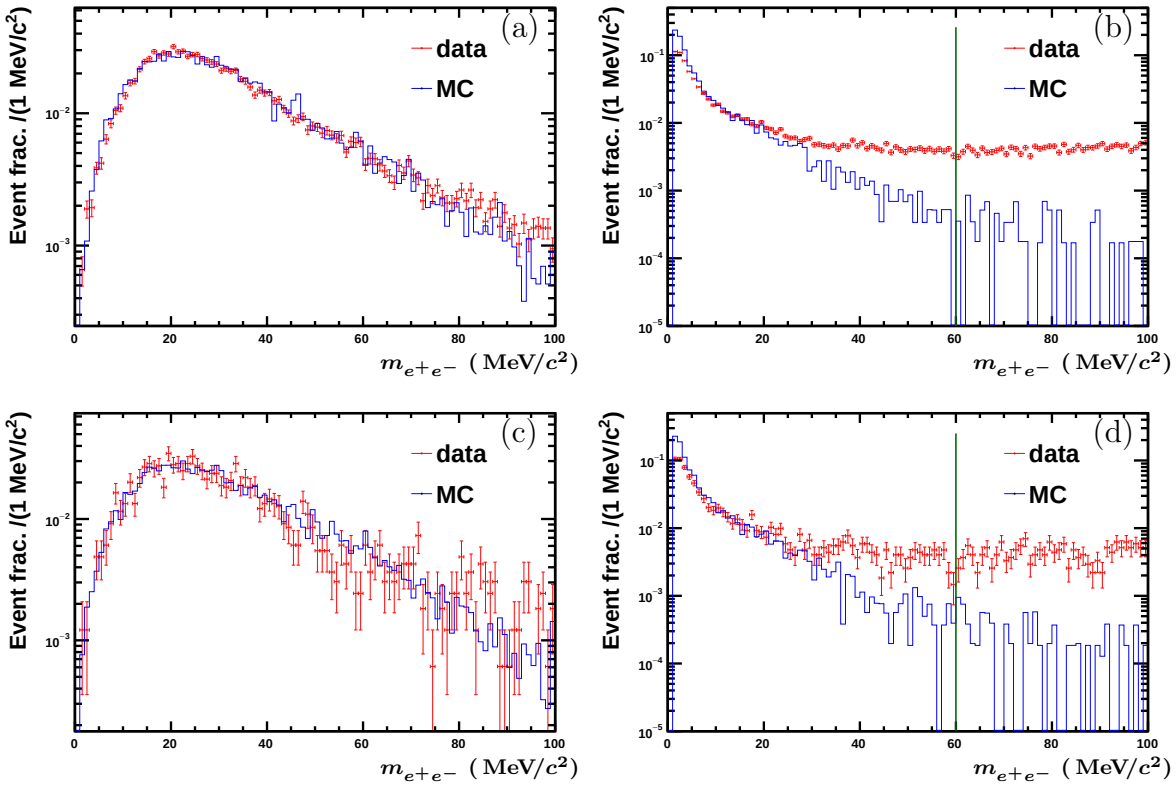

Figure 4.3: Reconstructed dielectron mass in the full $B^0 \to K^{*0}\gamma$ decay dataset for DD (a) and LL (b) configuration and $B_s^0 \to \phi\gamma$ decay for DD (c) and LL (d) configuration. All data samples are merged. The cut value is shown with the green line.

Table 4.14: Converted photon selection efficiencies, computed using Sim08 MC events.

Decay channel	year	$tt_{(e^+e^-)}$	$\epsilon_{convPhoton}$
$B^0 \to K^{*0}\gamma$	2011low	DD	0.955 ± 0.005
		LL	0.941 ± 0.005
	2011high	DD	0.957 ± 0.004
		LL	0.941 ± 0.005
	2012	DD	0.957 ± 0.003
		LL	0.948 ± 0.004
$B_s^0 \to \phi\gamma$	2011low	DD	0.958 ± 0.005
		LL	0.950 ± 0.005
	2011high	DD	0.959 ± 0.004
		LL	0.949 ± 0.005
	2012	DD	0.958 ± 0.003
		LL	0.950 ± 0.004

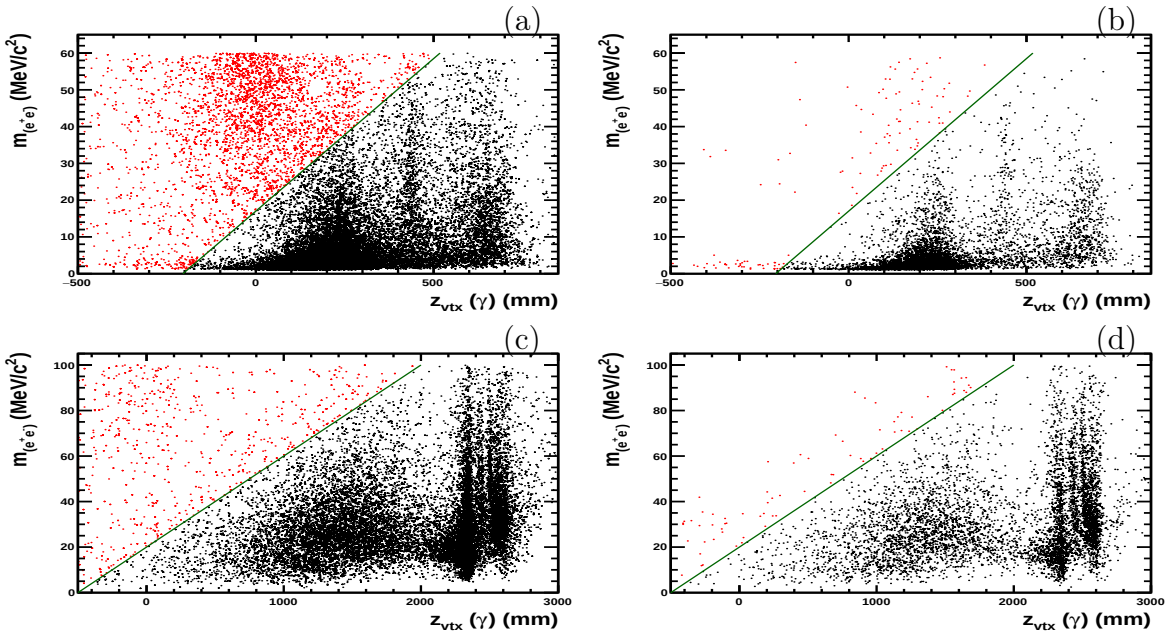

Figure 4.4: Reconstructed dielectron mass versus the z coordinate of the reconstructed vertex for $B^0 \to K^{*0}\gamma$ decay for LL events in data (a) and MC (b) and for DD events in data (c) and MC (d). Red dots correspond to events which have been removed by the 2D-cut. All data acquisition time samples are merged. The cut value is shown with the green line.

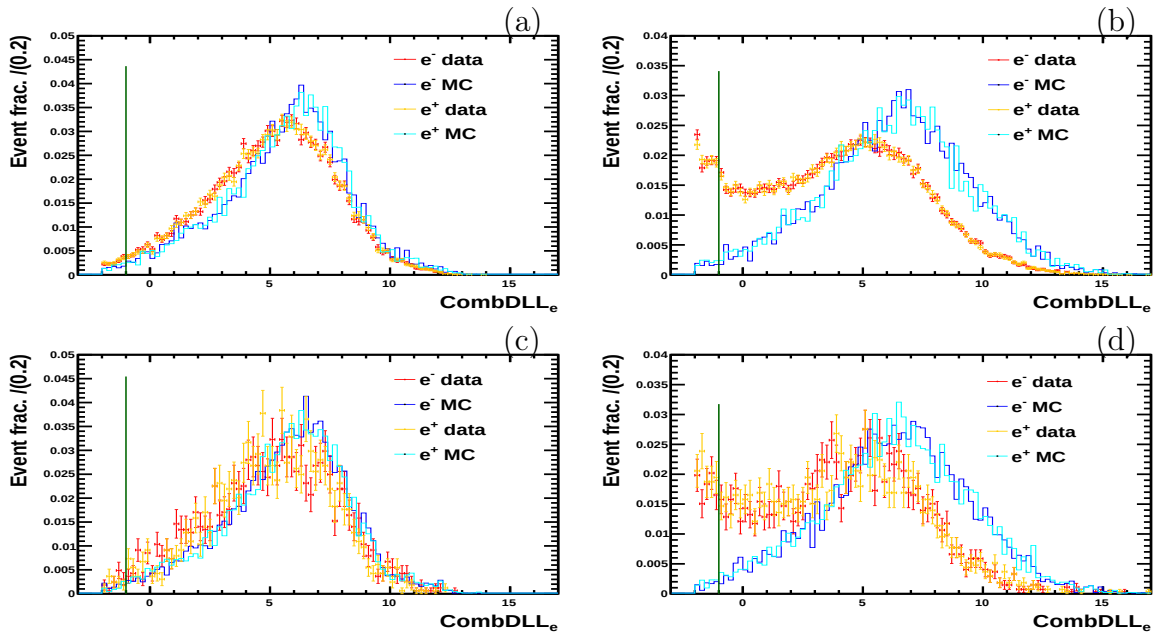

Figure 4.5: $CombDLL_e$ variable for $B^0 \to K^{*0}\gamma$ decay for DD (a) and LL (b) configurations and $B_s^0 \to \phi\gamma$ decay for DD (c) and LL (d) configurations. All data acquisition time samples are merged. The cut value is shown with the green line.

Table 4.15: Mass windows efficiencies, computed using Sim08 *MC* events.

Decay channel	year	$tt_{(e^+e^-)}$	$\epsilon_{VmesonCut}$	ϵ_{Bcut}	ϵ_{allCut}
$B^0 \to K^{*0}\gamma$	2011low	DD	0.944 ± 0.006	0.988 ± 0.003	0.931 ± 0.006
		LL	0.946 ± 0.005	0.985 ± 0.003	0.933 ± 0.005
	2011high	DD	0.946 ± 0.004	0.987 ± 0.002	0.934 ± 0.005
		LL	0.946 ± 0.005	0.984 ± 0.003	0.932 ± 0.005
	2012	DD	0.950 ± 0.003	0.986 ± 0.002	0.936 ± 0.004
		LL	0.946 ± 0.004	0.974 ± 0.003	0.920 ± 0.005
$B_s^0 \to \phi\gamma$	2011low	DD	0.943 ± 0.006	0.985 ± 0.003	0.929 ± 0.007
		LL	0.944 ± 0.005	0.987 ± 0.003	0.931 ± 0.006
	2011high	DD	0.939 ± 0.005	0.985 ± 0.003	0.925 ± 0.006
		LL	0.944 ± 0.005	0.987 ± 0.002	0.932 ± 0.006
	2012	DD	0.943 ± 0.004	0.984 ± 0.002	0.926 ± 0.004
		LL	0.951 ± 0.004	0.987 ± 0.002	0.938 ± 0.004

4.2.7 Mass windows

In addition to these selections, a cut is applied on the reconstructed Vector meson mass (K^{*0} or ϕ). The absolute difference between the reconstructed mass and the nominative mass (taken from [7]) should be less than 100 MeV/c for K^{*0} and less than 10 MeV/c for ϕ. This cut removes a large part of background in data ($\sim$ 25 %) with a good efficiency (around 95 % in all samples). The background is mainly composed of combinatorial background made of false vector meson or false γ due to random hadrons and electrons combination or false B due to random combination of real vector meson and γ.

The reconstructed B mass region is also reduced to be between 4500 MeV/c^2 and 6000 MeV/c^2 for both decays. This mass region is centered on the signal peak and gives enough events in both high and low regions to estimate and model the background. Combining this cut with the cut on the Vector meson mass reject around 65 % of events in data with an efficiency about 98 % on signal. Efficiencies of this mass selection for each sub-samples are given in Tab. 4.15, while distributions of vector and B meson mass are shown in Fig. 4.6.

4.2.8 Events with multiple candidates

As described in Sec. 4.2.2, multiple candidates are generated in $B^0 \to K^{*0}\gamma$ samples by the reconstruction software. They mostly originate from the fact that both particle nature hypothesis are given to the two hadrons from K^{*0}. In simulation, one of these is tagged as *reflection* event according to `BKGCAT` variable while the other is tagged as *signal*. A negligible fraction of events with multiple candidates is also found in $B_s^0 \to \phi\gamma$. The rate

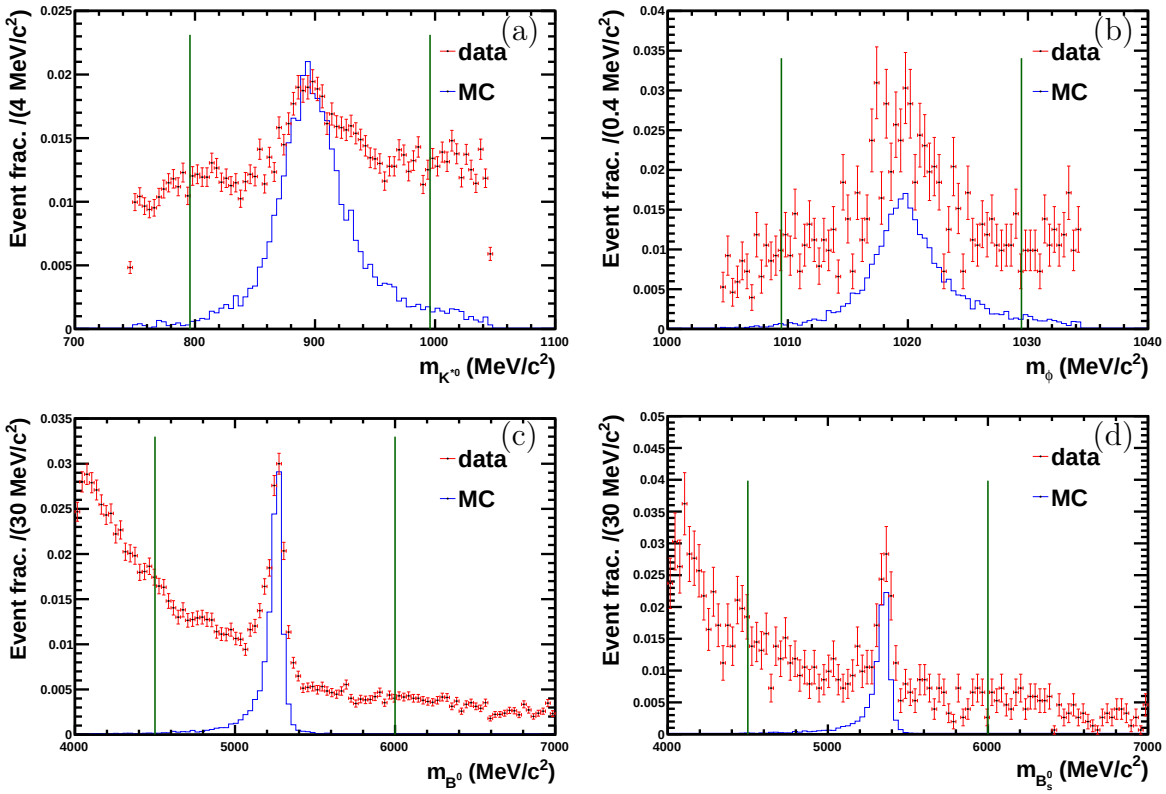

Figure 4.6: Reconstructed Vector (a,b) and B (c,d) mass in full dataset for $B^0 \to K^{*0}\gamma$ decay for DD (a,c) configuration and $B_s^0 \to \phi\gamma$ decay for DD (b,d) configuration. All data acquisition time samples are merged. The cut value is shown with the green line.

of events with multiple candidates is at the same order of magnitude in data and *MC*. This fraction is shown in Tab. 4.16 for each sample of $B^0 \to K^{*0}\gamma$ and $B_s^0 \to \phi\gamma$ in data and *MC*.

To remove these events, an orthogonal cut on a specific *PID* variable is applied: using the Neural-Network based *PID* variable, `ProbNNK`, kaons are required to have `ProbNNK` > 0.2 and pions are required to have `ProbNNK` < 0.2. Applying this cut on data reduces the fraction of events with multiple candidates to a negligible level, less than 1 %, as shown in Tab. 4.17. No event with more than two candidates is found.

The *PIDCalib* tool, described in Sec. 3.3.6, is used to compute the efficiencies of this orthogonal *PID* selection on signal. The efficiencies of the *PIDCalib* binning in p, η and *nTrack* is computed using *MC* samples, the obtained efficiencies for both $B^0 \to K^{*0}\gamma$ and $B_s^0 \to \phi\gamma$ decays are given in Tab. 4.18. Then, the orthogonal *PID* selection efficiencies on $B^0 \to K^{*0}\gamma$, computed using *PIDCalib* are given in Tab. 4.19.

Table 4.16: Fraction of events (in %) with multiple candidates in data (*MC* without true signal selection).

Decay channel	year	$tt_{(e^+e^-)}$	Number of candidate per event		
			1	2	>2
$B^0 \to K^{*0}\gamma$	2011low	DD	61.14 (*55.24*)	38.86 (*44.76*)	0.00 (*0.00*)
		LL	77.05 (*63.54*)	22.43 (*36.32*)	0.52 (*0.14*)
	2011high	DD	71.47 (*59.01*)	28.37 (*40.99*)	0.16 (*0.00*)
		LL	75.93 (*64.02*)	23.81 (*35.85*)	0.26 (*0.13*)
	2012	DD	74.69 (*63.52*)	25.13 (*36.46*)	0.18 (*0.02*)
		LL	75.53 (*65.00*)	23.90 (*34.74*)	0.57 (*0.26*)
$B_s^0 \to \phi\gamma$	2011low	DD	100.0 (*99.85*)	0.00 (*0.15*)	0.00 (*0.00*)
		LL	98.51 (*99.52*)	1.49 (*0.48*)	0.00 (*0.00*)
	2011high	DD	98.97 (*99.81*)	1.03 (*0.19*)	0.00 (*0.00*)
		LL	99.37 (*99.54*)	0.63 (*0.46*)	0.00 (*0.00*)
	2012	DD	100.0 (*99.78*)	0.00 (*0.22*)	0.00 (*0.00*)
		LL	99.47 (*99.18*)	0.53 (*0.78*)	0.00 (*0.04*)

Table 4.17: Fraction of event with multiple candidates in data, after orthogonal *PID* cut. Statistical uncertainties are also given.

Decay channel	year	$tt_{(e^+e^-)}$	Number of candidate per event (%)	
			1	2
$B^0 \to K^{*0}\gamma$	2011low	DD	100.0 ± 0.0	0.00 ± 0.0
		LL	99.31 ± 0.49	0.69 ± 0.49
	2011high	DD	99.82 ± 0.18	0.18 ± 0.18
		LL	98.87 ± 0.42	1.13 ± 0.42
	2012	DD	99.71 ± 0.12	0.29 ± 0.12
		LL	99.30 ± 0.21	0.70 ± 0.21

4.3 Background rejection

The first source of background comes from misidentified events, where one (or more) particle in the final state is misidentified, for example a proton which is identified as a kaon. These events correspond to a decay similar to the signal one with the same topology. The misidentification of the nature of a particle in the final state introduces a small shift in the reconstructed mass of the B meson candidate. This shift can lead to these backgrounds contaminating the signal region.

Table 4.18: PIDCalib binning cuts efficiencies. Computed using *MC* samples.

Decay channel	year	$tt_{(e^+e^-)}$	$\epsilon_{PIDCalibbinning}$
$B^0 \to K^{*0}\gamma$	2011low	DD	0.9986 ± 0.0010
		LL	0.9990 ± 0.0007
	2011high	DD	0.9988 ± 0.0007
		LL	0.9991 ± 0.0007
	2012	DD	0.9992 ± 0.0004
		LL	0.9960 ± 0.0012
$B_s^0 \to \phi\gamma$	2011low	DD	1.0000 ± 0.0000
		LL	1.0000 ± 0.0000
	2011high	DD	0.9995 ± 0.0005
		LL	1.0000 ± 0.0000
	2012	DD	0.9991 ± 0.0005
		LL	0.9986 ± 0.0007

Table 4.19: Orthogonal PID cut (*ProbNNK(K) > 0.2 & ProbNNK(π) < 0.2*) efficiencies for $B^0 \to K^{*0}\gamma$.

Decay channel	year	$tt_{(e^+e^-)}$	ϵ_{PID}
$B^0 \to K^{*0}\gamma$	2011low	DD	0.849 ± 0.004
		LL	0.840 ± 0.003
	2011high	DD	0.876 ± 0.003
		LL	0.842 ± 0.003
	2012	DD	0.867 ± 0.002
		LL	0.843 ± 0.003

Another source of peaking background which is located in the signal region is the decays with a prompt e^+e^- pair such as $B^0 \to K^{*0}e^+e^-$. This background is very difficult to treat since the final state is exactly the same as for signal decays and they are peaking underneath the signal peak. *MC* samples of these decays are used to get the relative contamination and the shape of the reconstructed mass of the B candidate (see Sec. 4.3.2).

Partially reconstructed decays where one (or more) of the final state's particle is missed in the reconstruction may also lead to events being reconstructed as signal events. This background populates the low B mass distribution, but with large tails which overflow underneath the signal region. As for backgrounds with prompt e^+e^-, *MC* samples of these decays are used to get the relative contamination and the shape of the reconstructed mass of the B candidate (see Sec. 4.3.3).

Finally, the combinatorial background corresponds to events where the final state particles have the requested particle type, but they not originating from a signal decay. A dedicated selection using topological and kinematic variables is developed to reject these events (see Sec. 4.3.4).

4.3.1 Contamination from misidentified events

Several decays which can lead to misidentified backgrounds are considered: $B^0 \to \rho^0\gamma$, $\Lambda_b^0 \to \Lambda^*\gamma$, crossfeed contamination of $B^0 \to K^{*0}\gamma$ and $B_s^0 \to \phi\gamma$ and the double misidentification of $B^0 \to K^{*0}\gamma$ events (where the $(K\pi)$ pair is reconstructed as (πK)). A PID selection is developed to reduce the contamination from these decays. A veto on the ϕ contamination in the $B^0 \to K^{*0}\gamma$ is also used.

Relevant background decays

$B^0 \to \rho^0\gamma$ decay (with $\rho^0 \to \pi^+\pi^-$) is investigated and found to be negligible due to its low branching fraction which is two orders of magnitude below the branching ratio of the $B^0 \to K^{*0}\gamma$ ($(8.6 \pm 1.5) \times 10^{-7}$ [7]).

A dedicated selection to remove the signal crossfeed contamination of $B_s^0 \to \phi\gamma$ to $B^0 \to K^{*0}\gamma$, where one of the kaons coming from the decay of the ϕ is identidied as a pion, is developed while the counterpart contamination of $B^0 \to K^{*0}\gamma$ to $B_s^0 \to \phi\gamma$ (the pion is identified as a kaon) is found to be negligible, due to the tight mass window of the ϕ.

A misidentified decay which contributes as a background for both $B^0 \to K^{*0}\gamma$ and $B_s^0 \to \phi\gamma$ is the $\Lambda_b^0 \to \Lambda^*\gamma$ decay. Since the Λ^* mass is above the strong interaction threshold, it decays into a proton and a kaon through the strong interaction with a topology similar to the signal decays. If the proton in the final state is misidentified as a pion or a kaon, the event is reconstructed as a $B^0 \to K^{*0}\gamma$ or a $B_s^0 \to \phi\gamma$ decay. The mass difference between a proton and a pion or a kaon introduces an important mass shift leading to a contribution which is peaking underneath the signal region even if the mass of the Λ_b^0 is higher than the mass of the $B_{(s)}^0$. Fig 4.7 shows the reconstructed B mass from $B^0 \to K^{*0}\gamma$ and misidentified $\Lambda_b^0 \to \Lambda^*\gamma$ decays using *MC* 2012 samples for *DD* and *LL* configurations.

A specific contamination to $B^0 \to K^{*0}\gamma$ is due to doubly misidentified events where the $K\pi$ pair in the final state is reconstructed as a πK pair and not removed by the orthogonal PID selection (see Sec. 4.2.8). This background has no impact on the measurement of the ratio of branching fractions but has a large impact on the measurement of the CP asymmetry in the $B^0 \to K^{*0}\gamma$ decay since the charge of the kaon is used to tag the event as a B^0 or a $\overline{B}^0$ decay, as a B^0 decays into a K^{*0} which decays into a $(K^+\pi^-)$ pair while a $\overline{B}^0$ decays into a $\overline{K}^{*0}$ which decays into a $(K^-\pi^+)$ pair. This contamination can introduce a large systematic uncertainty.

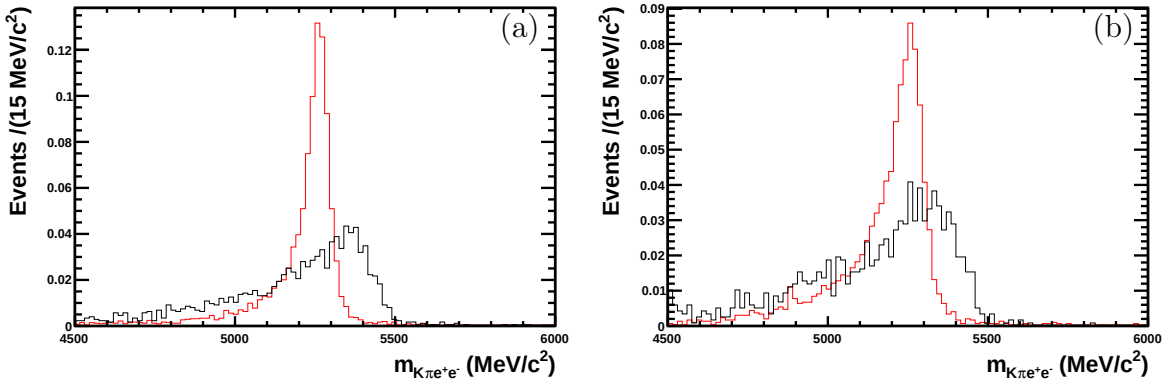

Figure 4.7: Normalised distributions of the reconstructed B mass from $B^0 \to K^{*0}\gamma$ (full red line) and $\Lambda_b^0 \to \Lambda^*\gamma$ (full black line) decays using *MC* 2012 samples for *DD* (a) and *LL* (b) configurations.

A sample of doubly misidentified events can be selected in the *MC* sample of $B^0 \to K^{*0}\gamma$ decay by a simple requirement on the true nature of the final state hadrons: the reconstructed kaon should have a true nature corresponding to a pion and vice versa. Using this sample, the relative contamination of doubly misidentified events with respect to signal is computed as the ratio of doubly misidentified and signal samples efficiencies (efficiencies are obtained using *PIDCalib* to take into account data-*MC* differences as explained in Sec. 3.3.6):

$$C_{MisID} = \frac{\epsilon_{MisID}}{\epsilon_{signal}} \tag{4.2}$$

This relative contamination is $\approx 3.25\%$. Considering the raw asymmetry A_{raw}, defined as:

$$A_{raw} = \frac{N_{\bar{B}^0} - N_{B^0}}{N_{\bar{B}^0} + N_{B^0}} \tag{4.3}$$

doubly misidentified events are identified as their opposite true CP state and have an impact on the measured A_{raw} as large as,

$$\Delta_{A_{raw}}^{(MisID)} = \frac{\pm 2 \times N_{MisID}}{N_{signal}} = \pm 2 \times C_{MisID} \tag{4.4}$$

which is $\approx 6.5\%$. This should be comparated to the expected statistical uncertainty on A_{RAW} which is $\frac{1}{\sqrt{N_{signal}}} \approx 2.7$ %, where the expected number of signal events N_{signal} is computed as in Sec. 4.1.1, using Eq. 4.1 and taking into account the selection efficiencies: $N_{signal} \approx 1400$. It is therefore necessary to further improve the PID selection in order to limit the impact of double misidentification on the raw asymmetry measurement.

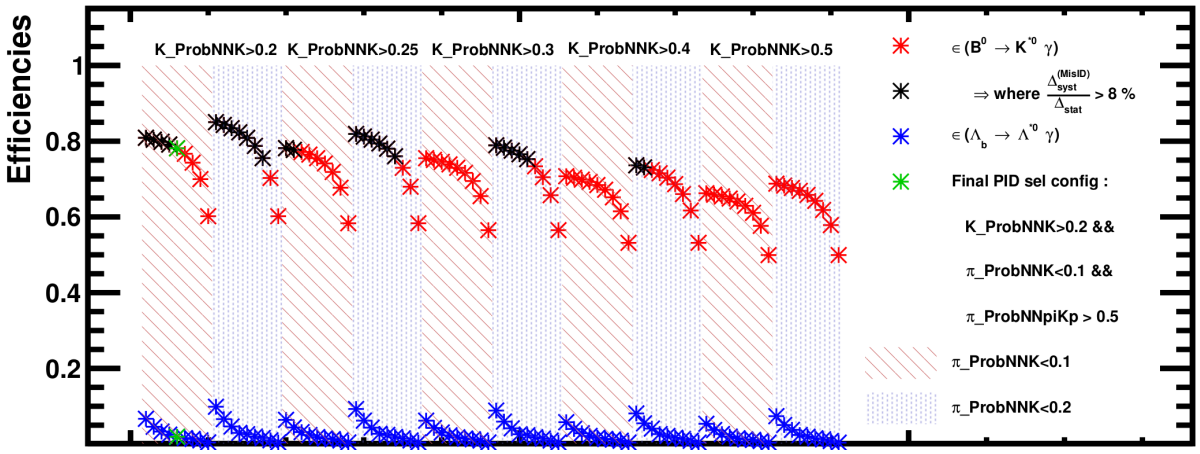

Figure 4.8: Efficiencies for $B^0 \to K^{*0}\gamma$ (red and black stars) and $\Lambda_b^0 \to \Lambda^*\gamma$ (blue stars) for all 3D-*PID* variable configuration. For each K_ProbNNK and π_ProbNNK cut combination, the nine stars on the plot represent the nine bins in π_ProbNNKpip from 0.1 to 0.9. The green star represents the choosen 3D-*PID* selection: ProbNNK(K) > 0.2, ProbNNK(π) < 0.1 and ProbNNpiKp(π) > 0.5.

Particle identification selection optimisation

Λ^* and doubly misidentified ($K\pi$) background contamination are reduced using a common *PID* selection strategy. Starting with the orthogonal cut on ProbNNK variable, which is requested to be > 0.2 for kaons and < 0.2 for pions, a cut on the ProbNN variables product ProbNNpi $\times(1-$ ProbNNK) $\times(1-$ ProbNNp) (called ProbNNpiKp) is applied on pions in order to remove Λ^* contamination. Background from double misidentification is reduced by tightening the cut on the ProbNNK variable.

A three dimensional optimisation is performed, by varying the three *PID* variables: ProNNK(K), ProNNK(π) and ProNNpiKp(π). Efficiencies are computed using *PIDCalib* for each combination as well as the expected uncertainties in the asymmetry measurement related to doubly misidentified events. The chosen cut value is a compromise between the efficiency, the double misidentification contamination and the Λ^* contamination. The combination which gives the best performance is ProbNNK(K) > 0.2, ProbNNK(π) < 0.1 and ProbNNpiKp(π) > 0.5. This 3D optimisation replaces the orthogonal cut on ProbNNK and is summarised in Fig. 4.8 and efficiencies of this selection are presented in Tab. 4.20.

Since the statistic of the $B_s^0 \to \phi\gamma$ decay is limited and the background is small, a loose selection on *PID* is applied. Both kaons from the ϕ decay are required to have a ProbNNK > 0.1. Efficiencies of this selection are given in Tab. 4.20.

Table 4.20: *PID* cut efficiencies computed using *PIDCalib*. Replaces the previous *PID* cuts values given in Tab.4.19.

Decay channel	year	$tt_{(e^+e^-)}$	ϵ_{PID}
$B^0 \to K^{*0}\gamma$	2011low	DD	0.765 ± 0.005
		LL	0.764 ± 0.005
	2011high	DD	0.805 ± 0.003
		LL	0.767 ± 0.005
	2012	DD	0.791 ± 0.003
		LL	0.766 ± 0.004
$B_s^0 \to \phi\gamma$	2011low	DD	0.948 ± 0.001
		LL	0.941 ± 0.001
	2011high	DD	0.952 ± 0.001
		LL	0.941 ± 0.001
	2012	DD	0.954 ± 0.001
		LL	0.945 ± 0.001

Table 4.21: Efficiencies of the ϕ veto cut: $m_{K^{*0}(\pi\to K)} > 1040\,\mathrm{MeV}/c^2$.

Decay channel	year	$tt_{(e^+e^-)}$	$\epsilon_{\phi\ Veto}$
$B^0 \to K^{*0}\gamma$	2011low	DD	0.997 ± 0.002
		LL	0.998 ± 0.001
	2011high	DD	0.998 ± 0.001
		LL	0.998 ± 0.001
	2012	DD	0.998 ± 0.001
		LL	0.999 ± 0.001

Specific veto on ϕ contamination to K^{*0}

The signal crossfeed contamination of $B_s^0 \to \phi\gamma$ to $B^0 \to K^{*0}\gamma$ where a kaon from ϕ decay is misidentified as a pion is a background which is peaking underneath the signal region. This background is partly removed by the *PID* selection, but to improve the rejection of these events, a cut is applied on the reconstructed mass of the K^{*0} where a kaon mass hypothesis is used instead of a pion mass. The distribution of this variable for $B^0 \to K^{*0}\gamma$ and $B_s^0 \to \phi\gamma$ reconstructed as $B^0 \to K^{*0}\gamma(e^+e^-)$ *MC* samples is shown in Fig. 4.9, and the cut is chosen to be $m_{K^{*0}(\pi\to K)} > 1040$ MeV/c^2. Applying this cut removes all the remaining $B_s^0 \to \phi\gamma$ events. Resulting efficiencies in the $B^0 \to K^{*0}\gamma$ signal sample are given in Tab. 4.21. This cut is only applied to the $B^0 \to K^{*0}\gamma$ sample. As said, the counterpart contamination of $B^0 \to K^{*0}\gamma$ to $B_s^0 \to \phi\gamma$ is negligible due to the tight ϕ mass window.

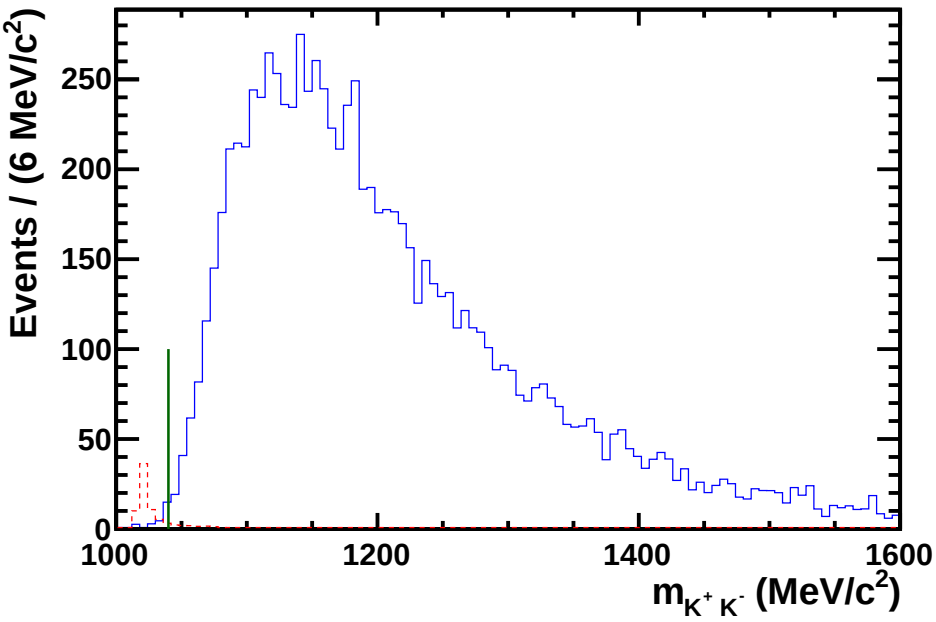

Figure 4.9: K^{*0} reconstructed invariant mass under the assumption that the reconstructed pion has a kaon mass in *MC* samples of $B^0 \to K^{*0}\gamma$ (full blue line) and $B_s^0 \to \phi\gamma$ reconstructed as $B^0 \to K^{*0}\gamma(e^+e^-)$ (dashed red line). The cut value is shown with the green line.

4.3.2 Contamination from V e^+e^- decays

B^0 or B_s^0 decaying into a vector meson and prompt e^+e^- produce non-negligible background to signal decays $B^0 \to K^{*0}\gamma(e^+e^-)$ and $B_s^0 \to \phi\gamma(e^+e^-)$ in LL configuration, i.e. when the photon has converted early in the detector. Final states are identical, and the topology of these events is similar to signal events. These backgrounds are only present in the LL sample.

Since these events are not misidentified and there is no missing particle in the final state, the resulting B meson mass peak is exactly at the same position as the signal. Furthermore, the resolution of the reconstructed B mass is expected to be similar to the signal one. Therefore, these decays should be carefully investigated since a veto cut to remove them is very difficult to apply. It was considered to cut on the origin vertex position of the dielectron (or the end vertex of the photon) along the detector axis (z-axis) which is expected to be close to the primary vertex in case of prompt e^+e^- and slightly shifted in case of a photon conversion. The distributions of this variable are too similar, as shown in Fig. 4.10, and since the contamination is small enough (see Sec. 4.4.3) no cut is applied.

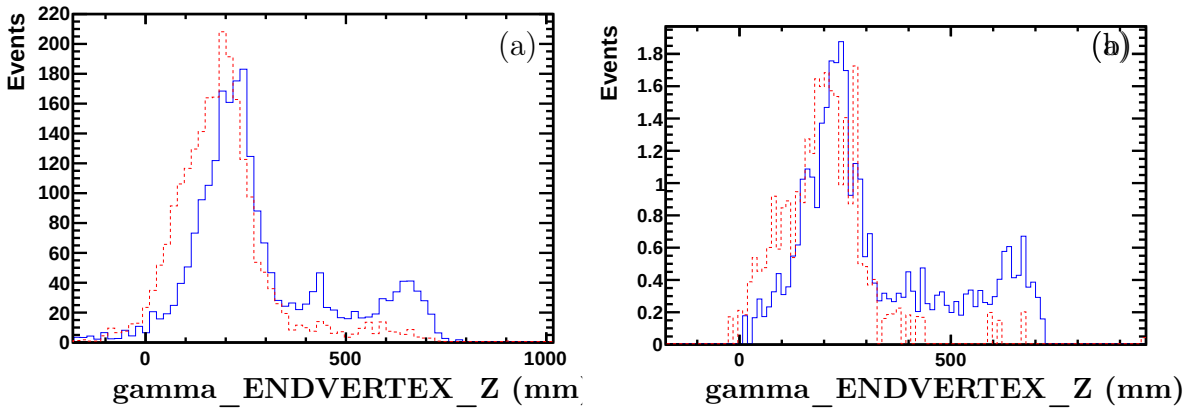

Figure 4.10: Position of the gamma end vertex along the z-axis (gamma_ENDVERTEX_Z) for $B^0 \to K^{*0}\gamma(e^+e^-)$ in LL configuration (full blue line) and $B^0 \to K^{*0}e^+e^-$ (dashed red line) 2012 MC samples (a) and for $B_s^0 \to \phi\gamma(e^+e^-)$ in LL configuration (full blue line) and $B_s^0 \to \phi e^+e^-$ (dashed red line) 2012 MC samples (b).

4.3.3 Contamination from partially reconstructed decays

Radiative decays

$B \to K\pi\pi\gamma$ decays such as $B^0 \to K_1(1270)^0\gamma$, $B^+ \to K_1(1270, 1400)^+\gamma$ or $B^+ \to \phi K^+\gamma$ are dangerous background decays and are merged into a common category called partially reconstructed background where the intermediate state is made of a K^{*0} or a ϕ plus an additional hadron. Missing this hadron leads to a final state with the same topology as the $B^0 \to K^{*0}\gamma$ and $B_s^0 \to \phi\gamma$ decays, but with a lower mass. Since these decays have branching ratios of the same order as the signal, they contribute to a non-negligible level to the selected events. Due to the non reconstructed hadron, these backgrounds populate the low part of the reconstructed B mass spectrum and, since some of the missing hadrons are soft pions or kaons (i.e. low energy particles), they feature a large tail which extends up to the signal region. To study these background contributions to the $B^0 \to K^{*0}\gamma$ sample, a MC sample is used, which is made of a combination of available simulated decays: $B^0 \to K_1(1270)^0\gamma$, $B^+ \to K_1(1270, 1400)^+\gamma$, $B^+ \to K_2{}^{*+}\gamma$, weighted according to their branching ratios (See Tab. 4.22) and efficiencies. The B mass distribution is shown in Fig.4.11.

In addition to these decays, the $B^0 \to K^{*0}\eta$ decay where the η decays into a pair of photons is considered independently as the reconstructed B mass shape is different in this case. Missing one of the photons gives the same final state as the signal decay $B^0 \to K^{*0}\gamma$. Since the shift of the reconstructed B mass is less important in this case than in previous ones, the resulting peak of this partially reconstructed decay is closer to the signal region than for $B \to K\pi\pi\gamma$ decays. Considering the low branching ratio of this decay (6×10^{-6}, to be compared to $\mathcal{B}(B^0 \to K^{*0}\gamma) \approx 2.88 \times 10^{-5}$), the resulting contamination is low but non-negligible. The B mass distribution of this decay reconstructed as a $B^0 \to K^{*0}\gamma$ is

Table 4.22: Branching fractions of the decays used to study the contribution of partially reconstructed background from radiative decays to the $B^0 \to K^{*0}\gamma$ sample.

Decay channel	branching fraction ($\times 10^{-6}$)
$B^0 \to K_1(1270)^0\gamma$	41 ± 4
$B^+ \to K_1(1270)^+\gamma$	36 ± 12
$B^+ \to K_1(1400)^+\gamma$	9.4 ± 0.6
$B^+ \to K_2{}^{*+}\gamma$	3.1 ± 0.9

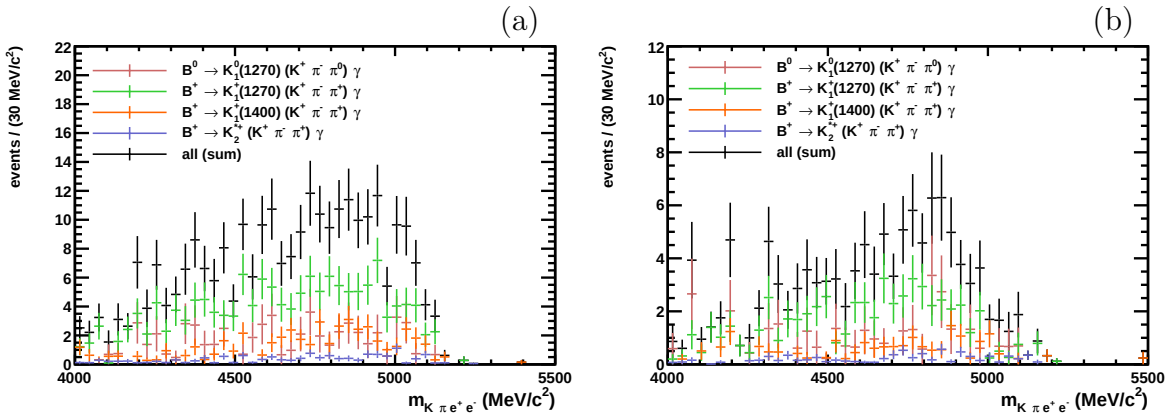

Figure 4.11: Distributions of the reconstructed B invariant mass in 2012 MC samples of partially reconstructed radiative decays for DD (a) and LL (b) configurations.

shown in Fig.4.12.

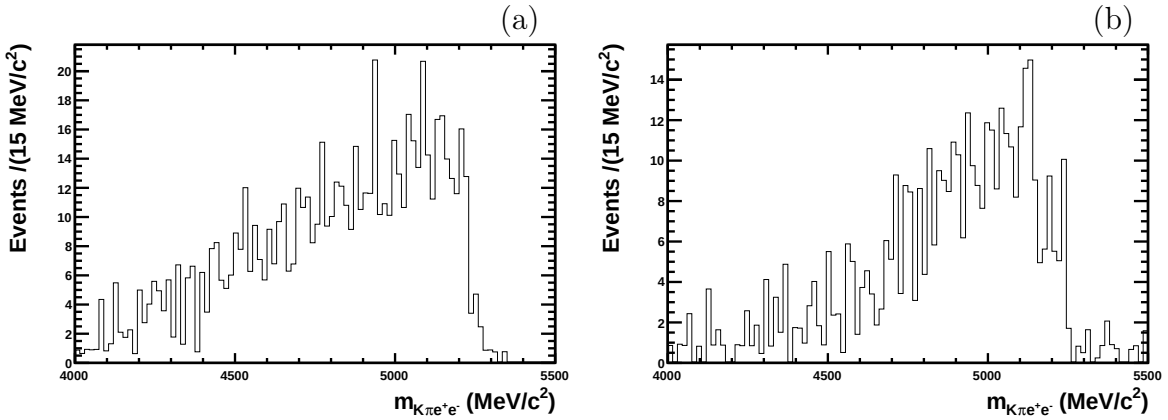

Figure 4.12: Distributions of the reconstructed B invariant mass in 2012 MC samples of $B^0 \to K^{*0}\eta$ decay for DD (a) and LL (b) configurations.

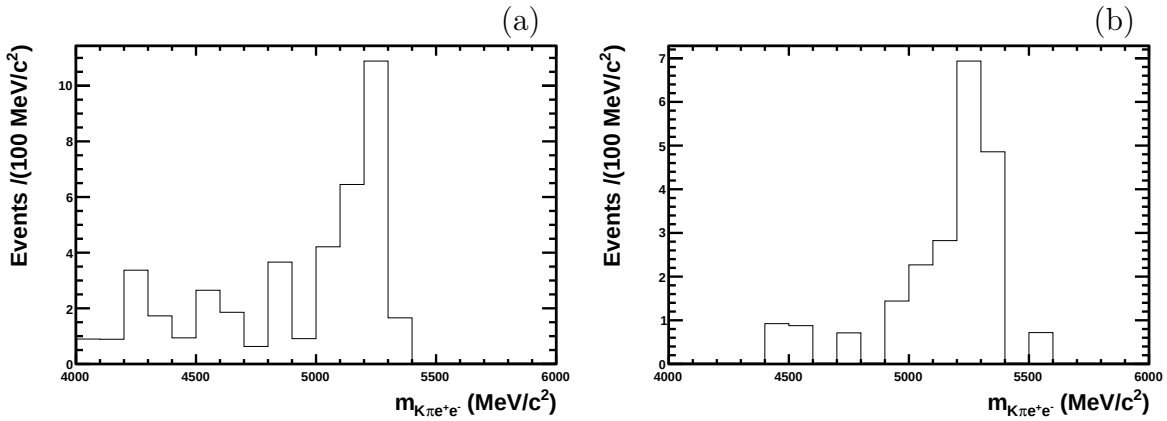

Figure 4.13: Distributions of the reconstructed B invariant mass in 2012 MC samples of $B^0 \to K\pi\pi^0$ decay for DD (a) and LL (b) configurations.

In the case of $B_s^0 \to \phi\gamma$ decay, the partialy reconstructed background mostly comes from the $B^+ \to \phi K^+\gamma$ decay. The expected number of events is too low to require a precise background model, partially reconstructed and combinatorial backgrounds are then included in a common model.

Decays with π^0

Similarly to radiative decays, background coming from partially reconstructed decays with π^0 corresponds to decays where the incomplete reconstructed final state has the same topology as the signal. These backgrounds are negligible for $B_s^0 \to \phi\gamma$ with respect to the statistical uncertainty.

$B^0 \to K\pi\pi^0$ where the π^0 decays into a photon pair is a background very similar to $B^0 \to K^{*0}\eta$. Missing a photon slightly shifts the reconstructed B mass peak at low mass, but this background is also peaking underneath the signal as the second photon from π^0 can be included as bremstrahlung to the conversion. The π^0 decay is dominated by di-photon channel $\mathcal{B}\,(\pi^0 \to \gamma\gamma) = 0.99$, and the Dalitz decay of the π^0 into a final state $\gamma\ e^+e^-$ is found to be negligible due to the low related branching ratio $\mathcal{B}\,(\pi^0 \to \gamma e^+e^-) = 0.01$. The distribution of the reconstructed B invariant mass for this background is shown in Fig. 4.13.

Partially reconstructed $B \to K^{*0}\pi^0 X$ decays contaminate the very low mass region. Since several decays contribute to this background, the overall branching ratio is huge with respect to the signal one, but this background is not expected to populate significantly the signal region. However, it is important to have a good modelisation of the shape of this background because it may impact the behaviour of the partially reconstructed background models when fitting data. Due to the lack of simulated event statistics, and since the conversion of the photon is not expected to have a large impact on the modeling

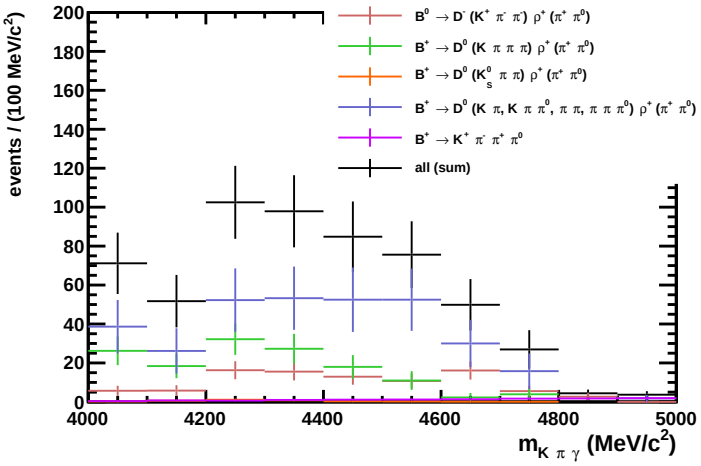

Figure 4.14: Distribution of the reconstructed B invariant mass in MC samples of low mass backgrounds to $B^0 \to K^{*0}\gamma$ from π^0, $B \to K^{*0}\pi^0 X$.

of these decays, a sample of these background decays reconstructed as $B^0 \to K^{*0}\gamma$ without conversion is used. The selection without the cuts related to photon conversion is applied and the shape of the reconstructed B invariant mass is derived from MC samples. The MC sample is a mixture of different decays such as: $B^+ \to D^0\rho^+$ (where D^0 decays into $K\pi$, $K\pi\pi^0$, $\pi\pi$, $\pi\pi\pi^0$, $K^0_S\pi\pi$, $K\pi\pi\pi$ and ρ^+ into $\pi\pi^0$), $B^0 \to D^-\rho^+$ ($D^- \to K^+\pi^-\pi^+$) or $B^+ \to K^+\pi^-\pi^+\pi^0$, weighted according to their branching ratios and efficiencies. The distribution of the reconstructed B invariant mass for this background is shown in Fig. 4.14.

4.3.4 Combinatorial background

The combinatorial background which comes from false vector meson is reduced by the mass windows cuts defined in Sec. 4.2.7 but some events still remain, and a dedicated selection is developed. A multivariate analysis is performed with the `TMVA` package [79] using only rectangular cuts on specific variables chosen for their discrimination power. The chosen cuts are those which maximise the significance defined as follow:

$$S = \frac{N_{Sig}}{\sqrt{N_{Sig} + N_{Bkg}}} \tag{4.5}$$

Different variables are used for DD and LL samples, since the combinatorial background is different between the two categories, as can be seen in Fig. 4.3: the dielectron mass distribution in the LL configuration shows at high mass a flat contribution (due to combinatorial background) which is not visible in the DD configuration. The same cut values are used for $B^0 \to K^{*0}\gamma$ and $B^0_s \to \phi\gamma$.

The transverse momentum of the $B^0_{(s)}$ is required to be greater than 3000 MeV/c in both DD and LL cases. In the DD case, the transverse momentum of the photon is required to be greater than 2100 MeV/c and the absolute value of the cosine of the helicity

Table 4.23: Combinatorial background veto cuts, for each dielectron track type.

DD	*LL*
$p_{\mathrm{T}}\ (B) > 3000$ MeV/c	$p_{\mathrm{T}}\ (B) > 3000$ MeV/c
$p_{\mathrm{T}}\ (\gamma) > 2100$ MeV/c	$acos(DIRA\ (B)) < 0.008\ rad$
$\lvert cos(\theta_H\ (V\ meson))\rvert < 0.89$	$min(log(\chi^2_{\mathrm{IP}}\ (e^{\pm}))) > 0.55$

angle of the Vertex meson (K^{*0} or ϕ), i.e. the angle between the momentum of any of the daughters of the vector meson and the momentum of the B candidate in the rest frame of the vector meson, shall be below 0.89. In the *LL* case, the arc-cosine of the DIRA of the $B^0_{(s)}$ meson shall be below 0.008 radian and the minimum of the logarithm of the χ^2 of the impact parameter with respect to the PV of the electron and the positron is requested to be greater than 0.55.

Variables and cut values are given in Tab. 4.23 and their distributions are shown in Fig. 4.15. Signal samples are made of $B^0 \to K^{*0}\gamma$ and $B^0_s \to \phi\gamma$ decay *MC* samples while background samples are made of the upper sideband ([5600,6800] MeV/c) of reconstructed B mass in data. In order to increase the statistic in the background samples, the K^{*0} and the ϕ mass windows defined in Sec 4.2.7 are released.

The cut values are chosen by maximising the significance (see Eq. 4.5) of the two signal decays simultaneously. The resulting values are given in Tab. 4.23 and the efficiency of the selection for each sample is given in Tab. 4.24. The distribution of the reconstructed B invariant mass for events which are removed by this cut are shown in Fig. 4.16 (for $B^0 \to K^{*0}\gamma$). It can be seen that the distribution of these events is compatible with an exponential shape when excluding the signal region.

4.4 Selection efficiencies, background contaminations

4.4.1 Selection summary

All the selection cuts are summarised in Tab. 4.25. Distributions of the reconstructed B invariant mass in data for $B^0 \to K^{*0}\gamma$ and $B^0_s \to \phi\gamma$ in *DD* and *LL* configurations after all selection cuts are shown in Fig. 4.17.

4.4.2 Selection efficiencies

Selection efficiencies are computed for each sample independently using $B^0 \to K^{*0}\gamma$ and $B^0_s \to \phi\gamma$ *MC* samples except for the *PID* selection (see Sec. 4.3.1) where efficiencies are obtained using the *PIDCalib* tool. Therefore, all efficiencies (except *PID*) are computed as:

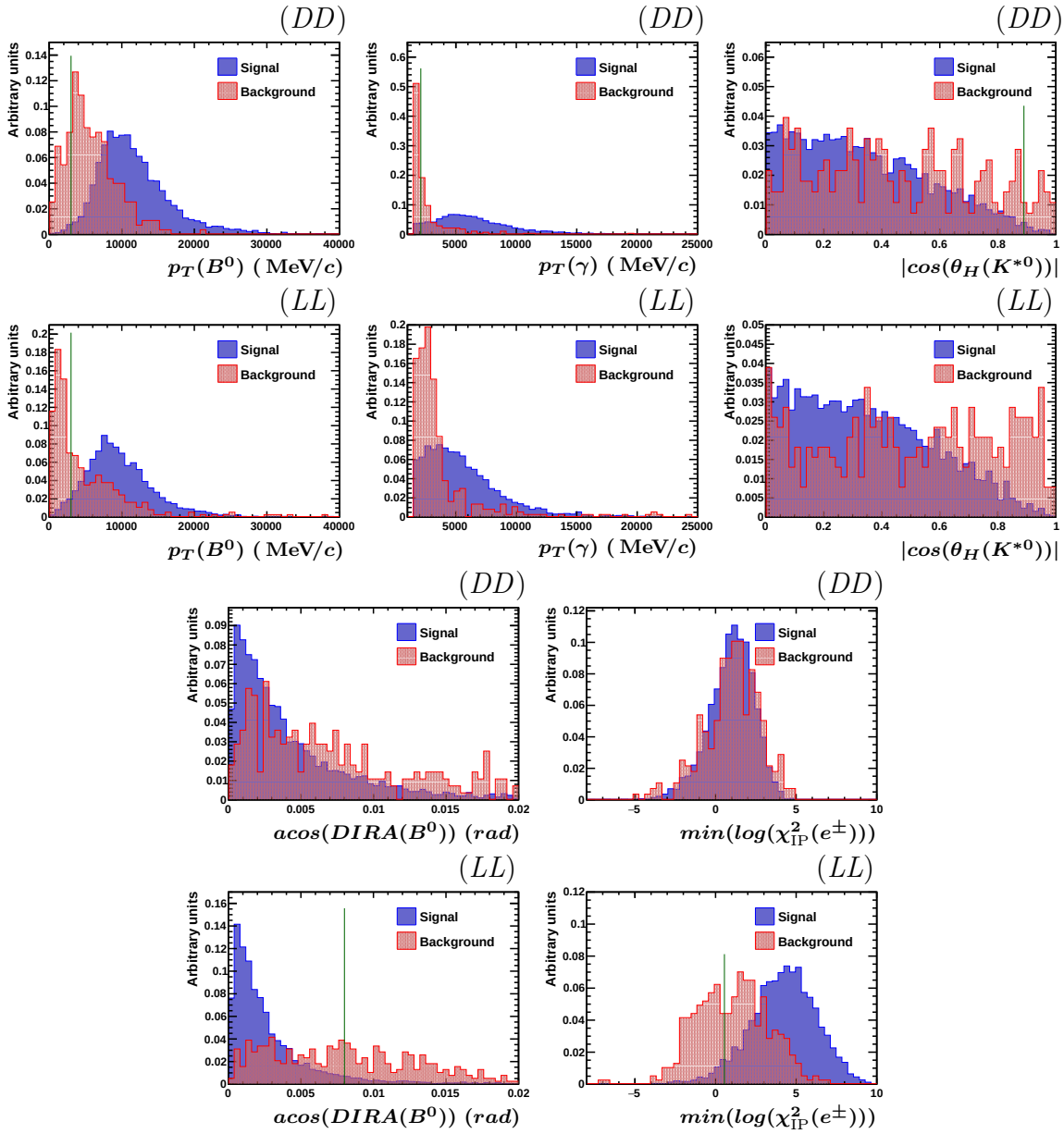

Figure 4.15: Distributions of the variables used to reject combinatorial background, the green line represents the value of the cut if any. Only $B^0 \to K^{*0}\gamma$ distributions are shown.

$$\epsilon = \frac{N_{after}}{N_{before}} \tag{4.6}$$

The associated statistical uncertainties are computed taking into account that the number of events having passed the selection is a subset of the number of events before applying cuts. Uncertainties Δ_ϵ are computed as:

Table 4.24: Efficiencies of the combinatorial background veto cuts.

Decay channel	year	$tt_{(e^+e^-)}$	$\epsilon_{comb\ Bkg\ Veto}$
$B^0 \to K^{*0}\gamma$	2011low	DD	0.932 ± 0.008
		LL	0.887 ± 0.008
	2011high	DD	0.960 ± 0.004
		LL	0.883 ± 0.008
	2012	DD	0.935 ± 0.004
		LL	0.863 ± 0.007
$B_s^0 \to \phi\gamma$	2011low	DD	0.918 ± 0.008
		LL	0.873 ± 0.008
	2011high	DD	0.945 ± 0.005
		LL	0.871 ± 0.008
	2012	DD	0.947 ± 0.004
		LL	0.883 ± 0.006

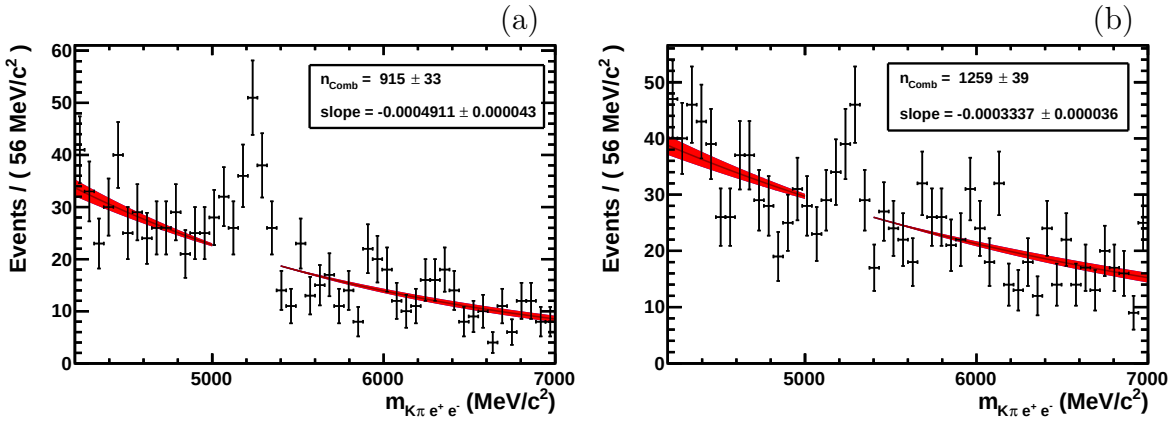

Figure 4.16: Distributions of the reconstructed B invariant mass for events which are removed by the combinatorial background veto selection for $B^0 \to K^{*0}\gamma$ data in DD (a) and LL configurations. An exponential shape is fitted to the distribution.

$$\Delta_\epsilon = \sqrt{N_{after} \times \frac{(N_{before} - N_{after})}{{N_{before}}^3}} \tag{4.7}$$

The total selection efficiency, including all selection cuts defined along this analysis, is given by the product of all intermediate efficiencies given in Tables 4.4, 4.6, 4.12, 4.13, 4.14, 4.15, 4.18, 4.20, 4.21, 4.24:

$$\epsilon^{total} = \prod_{selStep} \epsilon_{selStep} \tag{4.8}$$

Table 4.25: Summary of all selection cuts.

	$B^0 \to K^{*0}\gamma(e^+e^-)$ ($B_s^0 \to \phi\gamma(e^+e^-)$)	
	DD	*LL*
stripping	$m_{B^0_{(s)}} \in [4000, 7000]\,\mathrm{MeV}/c^2$	
	$\chi^2_{\mathrm{vtx}}/\mathrm{ndf}$ $(B^0_{(s)}) < 9$	
	$DIRA$ $(B^0_{(s)}) > 0.9998$	
	χ^2_{IP} $(B^0_{(s)}) < 9$	
	p_{T} $(K^{*0}(\phi)) > 1500\,\mathrm{MeV}/c$	
	$\Delta m_{K^{*0}(\phi)} < 150(15)\,\mathrm{MeV}/c^2$	
	$\chi^2_{\mathrm{vtx}}/\mathrm{ndf}$ $(K^{*0}(\phi)) < 9$	
	χ^2_{FD} $(K^{*0}(\phi)) > 81$	
	p_{T} $(\gamma \to e^+e^-) > 200\,\mathrm{MeV}/c$	
	$\chi^2_{\mathrm{vtx}}/\mathrm{ndf}$ $(\gamma \to e^+e^-) < 9$	
	$m_{e^+e^-} < 100\,\mathrm{MeV}/c^2$	
	$combDLL_e$ $(e^\pm) > -2.0$	
	p_{T} $(h^\pm) > 500\,\mathrm{MeV}/c$	
	p $(h^\pm) > 3000\,\mathrm{MeV}/c$	
	$min(\chi^2_{\mathrm{IP}})$ $(h^\pm) > 16$	
	χ^2_{track}/ndf $(h^\pm) < 3$	
	$P_{ghost-track}$ $(h^\pm) < 0.4$	
trigger (`L0`)	`Electron_TOS` or `Hadron_TOS` or `Global_TIS`	
trigger (`Hlt1`)	`TrackAllL0_TOS` or `TrackPhoton_TOS`	
trigger (`Hlt2`)	see Tab. 4.11	
p_{T} (γ)	p_{T} $(\gamma \to e^+e^-) > 1500\,\mathrm{MeV}/c$	
Converted γ selection	$m_{ee} - 0.04 \times z_{vtx}$ $(\gamma) < 20$	$m_{ee} - 0.083 \times z_{vtx}$ $(\gamma) < 17$
		$m_{ee} < 60\,\mathrm{MeV}/c^2$
	$combDLL_e$ $(e^\pm) > -1.0$	$combDLL_e$ $(e^\pm) > -1.0$
Mass windows	$\Delta m_{K^{*0}(\phi)} < 100(10)\,\mathrm{MeV}/c^2$	
	$m_{B^0_{(s)}} \in [4500, 6000]\,\mathrm{MeV}/c^2$	
PID binnig cuts	p $(h^\pm) \in [3, 300]\,\mathrm{GeV}/c$	
	η $(h^\pm) \in [1.5, 5.]$	
	$N_{tracks} < 500$	
PID cuts	`ProbNNK` $(K^+) > 0.2$ (`ProbNNK` $(K^+) > 0.1$)	
	`ProbNNK` $(\pi^-) < 0.1$ (`ProbNNK` $(K^-) > 0.1$)	
	`ProbNNpiKp` $(\pi^-) > 0.5$ (—)	
ϕ veto cut	$m_{K^{*0}(\pi \to K)} > 1040\,\mathrm{MeV}/c^2$ (—)	
Comb. bkg. veto cut	p_{T} $(B) > 3000$ MeV/c	p_{T} $(B) > 3000$ MeV/c
	p_{T} $(\gamma) > 2100$ MeV/c	$acos(Dira\ (B)) < 0.008$
	$\lvert cos(\theta_H\ (V\ meson))\rvert < 0.89$	$min(log(\chi^2_{\mathrm{IP}}\ (e^\pm))) > 0.55$

The total relative uncertainty is computed as the square root of the quadratic sum of relative error related to each efficiency, assuming the efficiencies are not correlated:

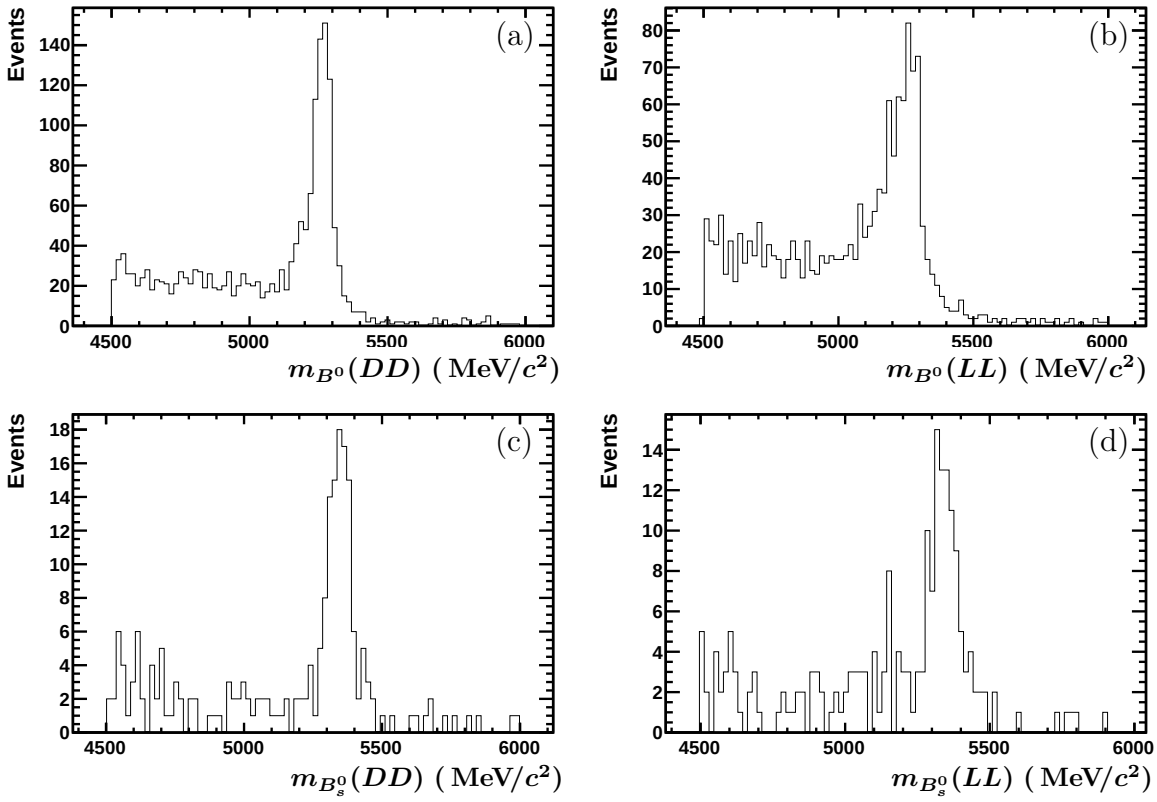

Figure 4.17: Distributions of the reconstructed B invariant mass in data after all selections are applied. Distributions are from $B^0 \to K^{*0}\gamma(e^+e^-)$, *DD* (a) and *LL* (b) and $B^0_s \to \phi\gamma(e^+e^-)$, *DD* (c) and *LL* (d) samples.

$$\Delta_\epsilon^{total} = \epsilon^{total} \times \sqrt{\sum_{selStep} (\frac{\Delta_{\epsilon selStep}}{\epsilon_{selStep}})^2} \tag{4.9}$$

Total efficiencies are presented in Tab. 4.26. The observed difference between $B^0 \to K^{*0}\gamma$ and $B^0_s \to \phi\gamma$ efficiencies is due to the difference in stripping efficiencies (see Sec. 4.2.1) while the lower efficiency observed for {*2011low*, *DD*} sample for each decay is due to the lower *Hlt2* trigger line efficiencies (see Sec. 4.2.4). Efficiencies are also lower in *2012* samples with respect to efficiencies in *2011* samples. This comes from the observed differences in the stripping and L0-trigger efficiencies between *2011* and *2012* where a 10 % effect is seen for both (See Tab. 4.6 and Tab. 4.9).

4.4.3 Background contamination

In order to estimate the contribution of all different background sources coming from physical decays for which a branching ratio has been measured or estimated, the shape of the reconstructed B invariant mass (after the full reconstruction and selection) is modeled

Table 4.26: Total efficiencies after all selection cuts, including detector acceptance, stripping and trigger.

Decay channel	year	$tt_{(e^+e^-)}$	ϵ_{total} ($\times 10^{-3}$)
$B^0 \to K^{*0}\gamma$	2011low	DD	0.077 ± 0.002
		LL	0.159 ± 0.004
	2011high	DD	0.152 ± 0.004
		LL	0.165 ± 0.004
	2012	DD	0.136 ± 0.002
		LL	0.142 ± 0.003
$B_s^0 \to \phi\gamma$	2011low	DD	0.103 ± 0.003
		LL	0.174 ± 0.004
	2011high	DD	0.171 ± 0.004
		LL	0.181 ± 0.004
	2012	DD	0.164 ± 0.003
		LL	0.166 ± 0.003

using *MC* samples, as it will be described in Sec. 5.1.1. To take these shapes into account in the fit on data and to minimise the number of degrees of freedom of the fit, the relative contamination $C_{H_b \to X}$ of each background decay is computed as follows:

$$C_{H_b \to X} = \frac{N^{sel}(H_b \to X)}{N^{sel}(signal)} = \frac{f_{trackType}(H_b \to X)}{f_{trackType}(signal)} \times \frac{\epsilon_{total}(H_b \to X)}{\epsilon_{total}(signal)} \times \frac{f_{H_b}}{f_{d(s)}} \times \frac{\mathcal{B}(H_b \to X)}{\mathcal{B}(signal)} \tag{4.10}$$

where *signal* corresponds to $B^0 \to K^{*0}\gamma$ or $B_s^0 \to \phi\gamma$. The fraction $f_{trackType}$ of events according to the dielectron track type configuration (*DD* or *LL*) is taken from *MC* after stripping but before the trigger requirement and is given in the Tab. 4.8. The total selection efficiency ϵ_{total} (including detector acceptance, stripping and trigger) is computed for the considered background decay and for the signal using *MC* samples and *PIDCalib* to get *PID* efficiencies. Values of quark fragmentation fractions f_X are taken from [74]. When available, branching fraction values, $\mathcal{B}()$, are taken from [7], except for $B^0 \to K^{*0}e^+e^-$ for which the value of the branching fraction has been measured by LHCb [80]. However, this value has been measured in the dielectron mass region from 30 to 1000 MeV/c^2 and should be extrapolated to the lower dielectron mass region from 0 to 30 MeV/c^2. To this purpose, a sample of simulated $B^0 \to K^{*0}e^+e^-$ events is produced without any selection on the dielectron mass to get the fraction of $B^0 \to K^{*0}e^+e^-$ event in the [30,1000] MeV/c^2 mass window as it is shown in Fig. 4.18. This number is used to extrapolate the measured value $\mathcal{B}(B^0 \to K^{*0}e^+e^-) = (3.07^{+0.86+0.16}_{-0.77-0.26} \pm 0.14) \times 10^{-7}$ to the low mass region $\mathcal{B}(B^0 \to K^{*0}e^+e^-)_{extrapol} = (1.38^{+0.37}_{-0.31}) \times 10^{-6}$.

The branching fraction of the $B_s^0 \to \phi e^+e^-$ decay has not been measured yet, but it is

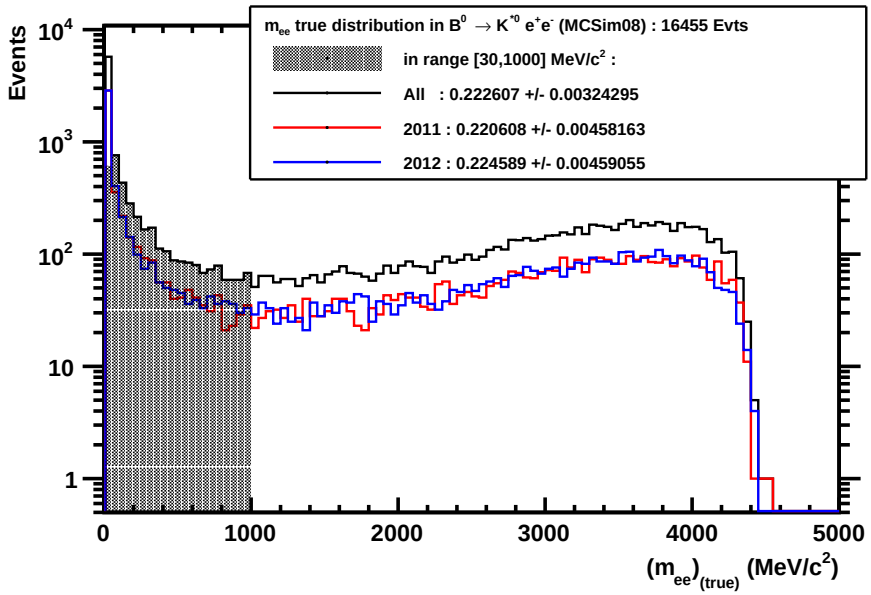

Figure 4.18: True dielectron mass from *MC* sample of $B^0 \to K^{*0}e^+e^-$ in the [0,5000] MeV/c^2 range. The values are the fraction of $B^0 \to K^{*0}e^+e^-$ events in the [30,1000] MeV/c^2 fraction in 2011 (red), 2012 (blue) and both years (black).

estimated from $B^0 \to K^{*0}e^+e^-$ branching fraction using the following relation:

$$\mathcal{B}(B_s^0 \to \phi e^+e^-) = \mathcal{B}(B^0 \to K^{*0}e^+e^-) \times \frac{\mathcal{B}(B_s^0 \to \phi\gamma)}{\mathcal{B}(B^0 \to K^{*0}\gamma)}, \tag{4.11}$$

The relative contamination by all significant background decays is given in Tab. 4.27. These numbers are used to build the background model used in the fit to the data described in the next chapter.

4.5 Conclusion

Selections defined in this chapter allow to significantly increase the signal purity, as it can be seen by comparing the distribution of the reconstructed B invariant mass before applying selection (see Fig. 4.1) and after applying the selection (see Fig. 4.17). In the last figure, a clear peak of signal is observed in each sample. The background sources have been identified, dedicated vetos have been developed. Higher purity means higher sensitivity to fit parameters related to signal such as the raw asymmetry in $B^0 \to K^{*0}\gamma$ defined as given in Eq. 4.3:

Table 4.27: Branching fractions and relative contamination of significant background for each dielectron track type configuration. The branching fractions include the intermediate decay (such as $K^{*0} \to K^+\pi^-$) branching fraction value. $\mathcal{B}$ ($\Lambda_b^0 \to \Lambda^*\gamma$) includes the $\frac{f_{\Lambda_b^0}}{f_d}$ value

Decay channel	branching fraction ($\times 10^{-6}$)	$B^0 \to K^{*0}\gamma(e^+e^-)$		$B_s^0 \to \phi\gamma(e^+e^-)$	
		DD (%)	LL (%)	DD (%)	LL (%)
$B^0 \to \rho^0\gamma$	0.86 ± 0.15	—	—	—	—
$\Lambda_b^0 \to \Lambda^*\gamma$	7.63 ± 5.80	0.81 ± 0.64	0.46 ± 0.42	3.47 ± 2.73	3.82 ± 3.02
$B^0 \to K^{*0}e^+e^-$	$0.92\ ^{+0.25}_{-0.21}$	—	$7.11\ ^{+1.96}_{-1.65}$	—	—
$B_s^0 \to \phi e^+e^-$	$0.58\ ^{+0.17}_{-0.15}$	—	—	—	$7.14\ ^{+2.25}_{-2.02}$
$B^0 \to K^{*0}\eta$	6.27 ± 0.40	3.91 ± 0.33	4.07 ± 0.36	—	—
$B^0 \to K\pi\pi^0$	37.4 ± 3.2	2.71 ± 0.52	2.62 ± 0.58	—	—

$$A_{raw} = \frac{N_{\bar{B}^0} - N_{B^0}}{N_{\bar{B}^0} + N_{B^0}}$$

and the ratio of yields defined as:

$$r_y = \frac{N(B^0 \to K^{*0}\gamma)}{N(B_s^0 \to \phi\gamma)} \tag{4.12}$$

Efficiencies of these selections have been computed for each sample (See Tab. 4.26). The global efficiency in $B^0 \to K^{*0}\gamma$ and $B_s^0 \to \phi\gamma$ can be computed using the fraction of events in each samples. These fractions come from the initial luminosity and dielectron track type fractions given in Tab. 4.1 and Tab. 4.8. Combining numbers from these tables, the two global efficiencies are:

$$\epsilon(B_s^0 \to \phi\gamma) = (0.164 \pm 0.003(stat)) \times 10^{-3} \tag{4.13}$$

$$\epsilon(B^0 \to K^{*0}\gamma) = (0.139 \pm 0.003(stat)) \times 10^{-3} \tag{4.14}$$

The ratio of the branching fractions of $B^0 \to K^{*0}\gamma$ and $B_s^0 \to \phi\gamma$ will be deduced from the efficiency ratio and the measured yield ratio:

$$r_{\mathcal{B}} = \frac{\mathcal{B}(B^0 \to K^{*0}\gamma)}{\mathcal{B}(B_s^0 \to \phi\gamma)} = r_y \times \frac{\mathcal{B}(\phi \to K^+K^-)}{\mathcal{B}(K^{*0} \to K^+\pi^-)} \times \frac{f_s}{f_d} \times \frac{\epsilon(B_s^0 \to \phi\gamma)}{\epsilon(B^0 \to K^{*0}\gamma)} \tag{4.15}$$

Chapter 5

Model, fits and measurements

This chapter describes the construction of a signal and background model of the reconstructed B invariant mass used to fit the data. Background and signal shapes are extracted from simulation. Then a fit to the data is performed to simultaneously extract the raw asymmetry in $B^0 \to K^{*0}\gamma$ decay and the ratio $B^0 \to K^{*0}\gamma$ and $B_s^0 \to \phi\gamma$ yields. The robustness of the fit is tested using toy generations and the validity of the simulation is checked by comparing it with a pure signal sample extracted from the data. Then, a complete study of all systematic sources is performed and relative uncertainties are computed. The ratio of yields and the raw asymmetry in $B^0 \to K^{*0}\gamma$ decay extracted from the fit are corrected to obtain the final measurement of the ratio of branching fractions and the direct CP asymmetry in $B^0 \to K^{*0}\gamma$ decay. A limit on the branching fraction of the $B_s^0 \to K^{*0}\gamma$ decay is also set using a statistical method described in the last part of this chapter.

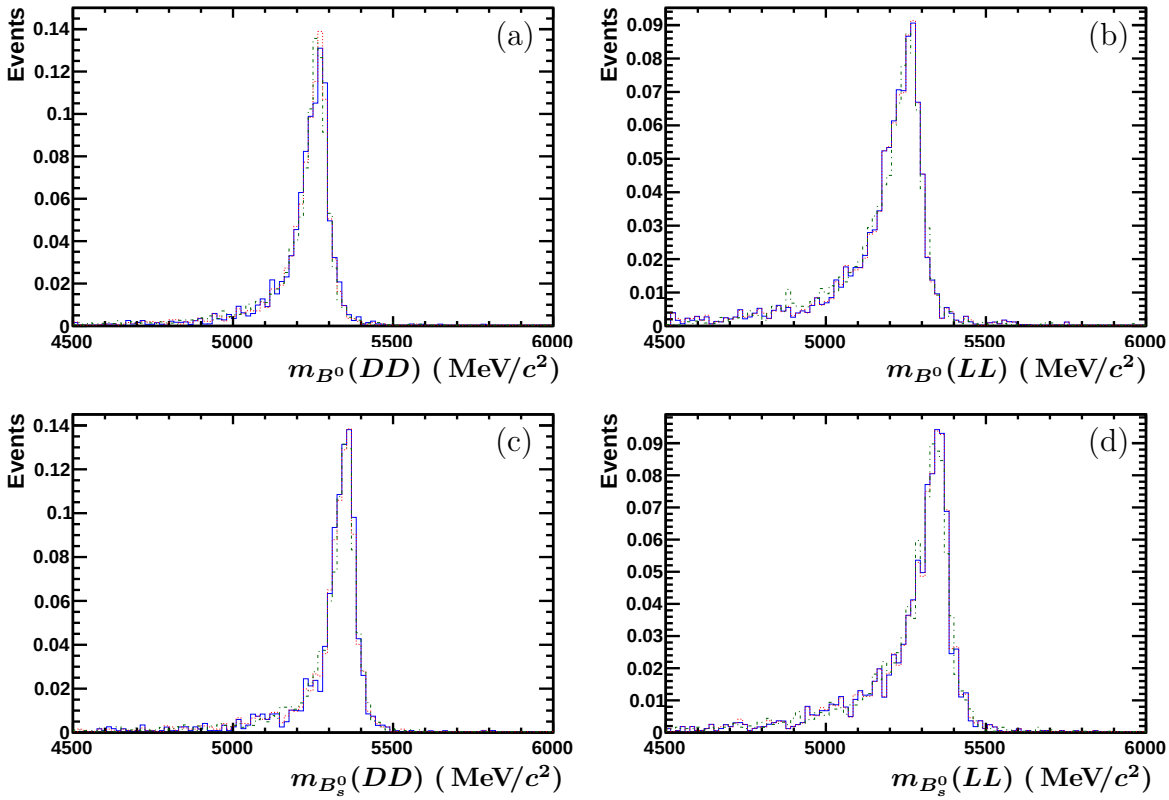

Figure 5.1: Reconstructed B invariant mass distributions in *MC 2011low* (full blue line), *2011high* (dotted red line) and *2012* (dashed-dotted green line) samples. The different distributions correspond respectively to $B^0 \to K^{*0}\gamma$ decay, *DD* (a) and *LL* (b) track configurations and $B^0_s \to \phi\gamma$ decay, *DD* (c) and *LL* (d) track configurations.

5.1 Modelisation and fitting procedure

5.1.1 Signal and background models

MC samples are used to get the shape of the reconstructed B invariant mass distribution for signal and background decays. Different functions are used depending on the decay type.

Signal modeling

A double tail Crystal Ball function [81] is used to model the signal shape:

$$f(M,\alpha_1,\alpha_2,n_1,n_2,\mu,\sigma) = \begin{cases} A_1 \times (B_1 - \frac{M-\mu}{\sigma})^{-n_1} & ,if\ \frac{M-\mu}{\sigma} \leq -\alpha_1 \\ e^{-\frac{(M-\mu)^2}{2\sigma^2}} & ,if\ -\alpha_1 < \frac{M-\mu}{\sigma} < \alpha_2 \\ A_2 \times (B_2 - \frac{M-\mu}{\sigma})^{-n_2} & ,if\ \alpha_2 \leq \frac{M-\mu}{\sigma} \end{cases} \quad (5.1)$$

With, for i = 1,2:

$$A_i = (\frac{n_i}{|M|})^{n_i} e^{-\frac{\alpha_i^2}{2}}$$
$$B_i = \frac{n_i}{|\alpha_i|} - |\alpha_i|$$

Since distributions are similar for $B^0 \to K^{*0}\gamma$ and $B_s^0 \to \phi\gamma$ *MC* samples, a simultaneous fit using common parameters is performed. Events are separated in the *DD* and *LL* categories since the B mass resolution is expected to be worse and the position of the mass peak is expected to be lower in the *LL* case, due to the higher probability to loose energy by multiple scattering and bremsstrahlung, than in the *DD* case. The differences between the *2011low*, *2011high* and *2012* samples are negligible, as shown in Fig. 5.1. Thus, year samples are merged, but histograms are re-weighted according to the expected fraction of events in each year category.

Four independent *MC* samples are used: $B^0 \to K^{*0}\gamma$ and $B_s^0 \to \phi\gamma$ both in *DD* and *LL* configurations. A simultaneous fit is performed, the resolution and parameters related to the tails of the double Crystal Ball (α_i, n_i) for each dielectron track type configuration are common to $B^0 \to K^{*0}\gamma$ and $B_s^0 \to \phi\gamma$ samples while the four amplitudes are independent. The peak position of the B^0 mass ($B^0 \to K^{*0}\gamma$) is left free for *DD* configuration ($\mu_{B^0}^{DD}$). The B_s^0 mass peak position is obtained by adding the measured mass difference $(m_{B_s^0} - m_{B^0}) = 87.33 \pm 0.23$ MeV/c^2 [7]. The position of the B mass peak in *LL* configuration is defined by an additionnal free parameter common to both decays: $\mu_B^{DD} - \mu_B^{LL}$. The result of the fit is shown in Fig. 5.2 while all parameters are given in Tab. 5.1.

The reconstructed B^0 mass value is shifted to low mass with respect to the nominal value [7]. The electrons from the conversion loose energy by emitting bremsstrahlung photons by interacting with the material of the detector. Some of these photons are not reconstructed as they may go out of the detector acceptance or their transverse momentum is below the ECAL threshold which is around 75 MeV/c. So these photons are lost and the reconstructed B mass is shifted. This effect also explains the mass peak difference between *DD* and *LL* events since in this last category the photon has converted early in the detector and thus, the produced dielectron have a higher probability to emit bremsstrahlung photons as they cross more material.

Background modeling

As for the signal, the background invariant mass distribution is extracted from *MC* samples, when available, by performing independent fits for each category. Since some backgrounds contribute dominantly in the B mass regions outside of the B invariant mass window defined in Sec. 4.2.7, this cut is removed to better describe the shape.

As described in Sec. 4.3, the $B^0 \to K^{*0}\gamma$ background is composed of several contributions: $\Lambda_b^0 \to \Lambda^*\gamma$, $B^0 \to K^{*0}e^+e^-$, partially reconstructed background from

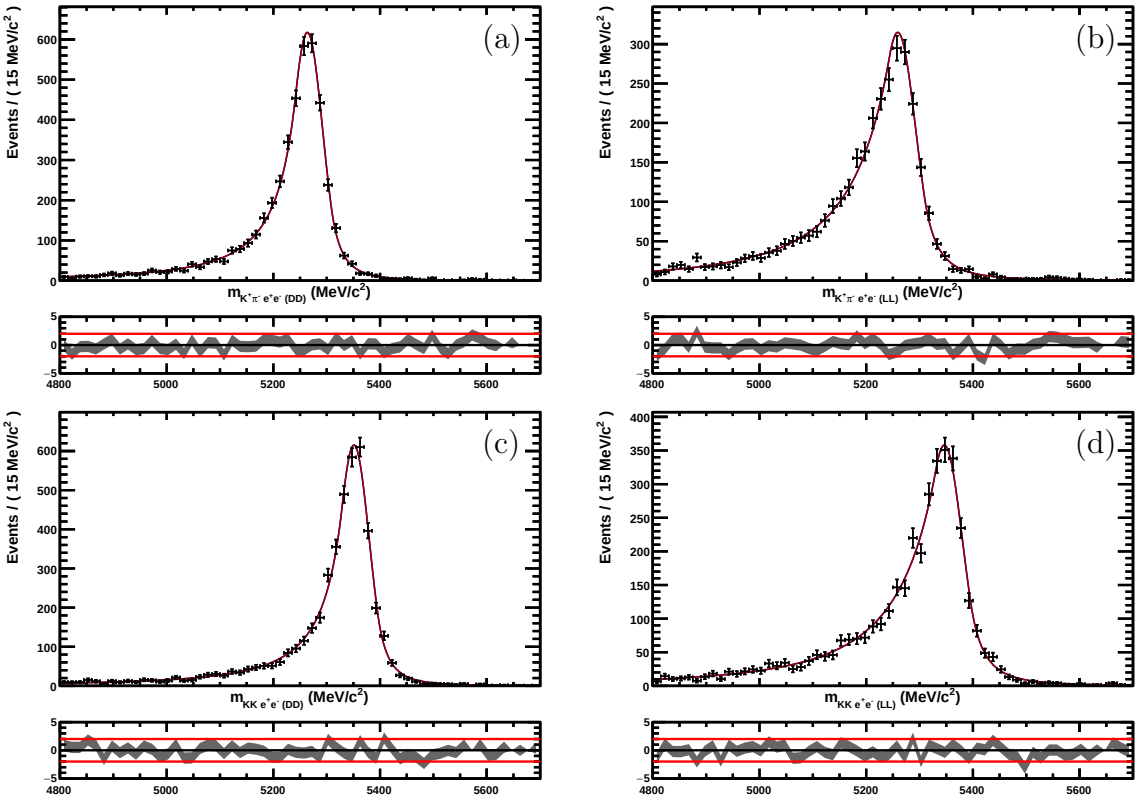

Figure 5.2: Fit on *MC* reconstructed B invariant mass distribution to extract the signal shape. Distributions are from $B^0 \to K^{*0}\gamma$, *DD* (a) and *LL* (b) and $B_s^0 \to \phi\gamma$, *DD* (c) and *LL* (d) *MC* samples.

radiative decays such as decays with $K\pi\pi\gamma$ in the final state or $B^0 \to K^{*0}\eta$, partially reconstructed background from π^0 ($K\pi\pi^0$ ($\to\gamma\gamma$)), low mass background $B \to K^{*0}\pi^0 X$ and combinatorial background.

The combinatorial background contribution to $B^0 \to K^{*0}\gamma$ is modeled by an exponential shape and extracted from the upper mass sideband ($m_B \in [5500, 6800]\,\mathrm{MeV}/c$). The result of the fit is shown in Fig. 5.3. Since there is not enough statistics available to use the same method for $B_s^0 \to \phi\gamma$, combinatorial background contribution to this decay is also modeled by an exponential shape whose slope is left free in the fit.

Table 5.1: Free parameters fitted to describe the reconstructed B invariant mass distribution in MC samples of $B^0 \to K^{*0}\gamma$ and $B_s^0 \to \phi\gamma$.

parameter	value
$\mu(B^0)^{DD}$	5263.72 ± 0.52 MeV/c^2
$(\mu^{DD} - \mu^{LL})$	4.7 ± 1.1 MeV/c^2
σ^{DD}	28.76 ± 0.56 MeV/c^2
σ^{LL}	33.96 ± 0.96 MeV/c^2
α_1^{DD}	0.763 ± 0.024
n_1^{DD}	2.039 ± 0.096
α_2^{DD}	-1.546 ± 0.057
n_2^{DD}	3.12 ± 0.31
α_1^{LL}	0.465 ± 0.023
n_1^{LL}	2.68 ± 0.24
α_2^{LL}	-1.447 ± 0.059
n_2^{LL}	2.79 ± 0.31

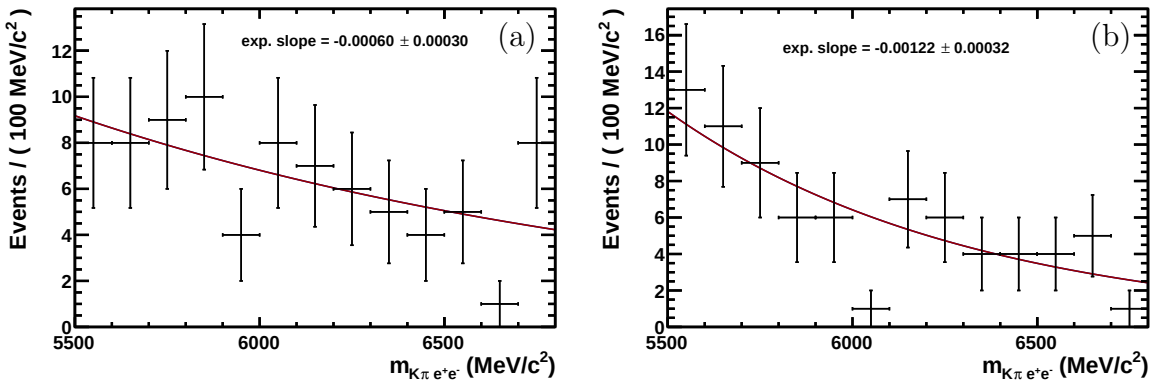

Figure 5.3: Result of the fit to the reconstructed B invariant mass distribution for the combinatorial background contribution to $B^0 \to K^{*0}\gamma$ for DD (a) and LL (b) configuration. An exponential function is used.

To model the contribution from low mass background $B \to K^{*0}\pi^0 X$, MC samples with calorimeter photons instead of converted photons are used in order to increase the statistics (see Sec. 4.3.3). However, the shape is expected to be dominated by the missing particles rather than by the photon conversion. This sample is composed of several contributing decays. Since the photon has not converted, it is not possible to infer the shape according to the dielectron track type. Therefore, the shape extracted from this low mass background sample is used for both track type configurations. A Crystal Ball function is used to model the shape of the reconstructed B^0 mass. The resulting

distribution, including all decays composing it, after the reconstruction and selection cuts except the photon conversion related cuts, and the result of the fit are shown in Fig. 5.4.

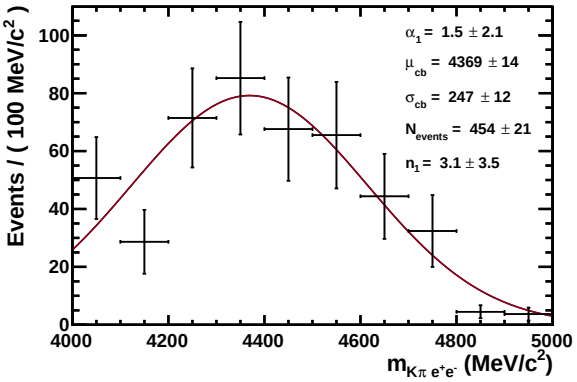

Figure 5.4: Results of the fit to the reconstructed B invariant mass distribution in MC samples of low mass backgrounds from π^0, $B \to K^{*0}\pi^0 X$ contributing to $B^0 \to K^{*0}\gamma$ decay, using a Crystal Ball function.

All other background shapes are extracted from a fit on MC samples. The $\Lambda_b^0 \to \Lambda^*\gamma$ shape is modeled using a Crystal Ball function and the result of the fit is shown in Fig. 5.5. Contributing only to the LL configuration, the $B^0 \to K^{*0}e^+e^-$ shape is modeled using a double tail Crystal Ball function and the result of the fit is shown in Fig. 5.6. The MC sample used to determine the shape of the partially reconstructed radiative decays with $K\pi\pi\gamma$ in the final state is made of a merged number of specific decays (see Sec. 4.3.3) while a specific sample of $B^0 \to K^{*0}\eta$ is used to model its shape. An ARGUS function convoluted with a gaussian function is used to model these two contributions, and the results of the fits are shown in Fig. 5.7. The $B^0 \to K\pi\pi^0$ decay contribution is modeled with a Crystal Ball function and the result of the fit is shown in Fig. 5.8.

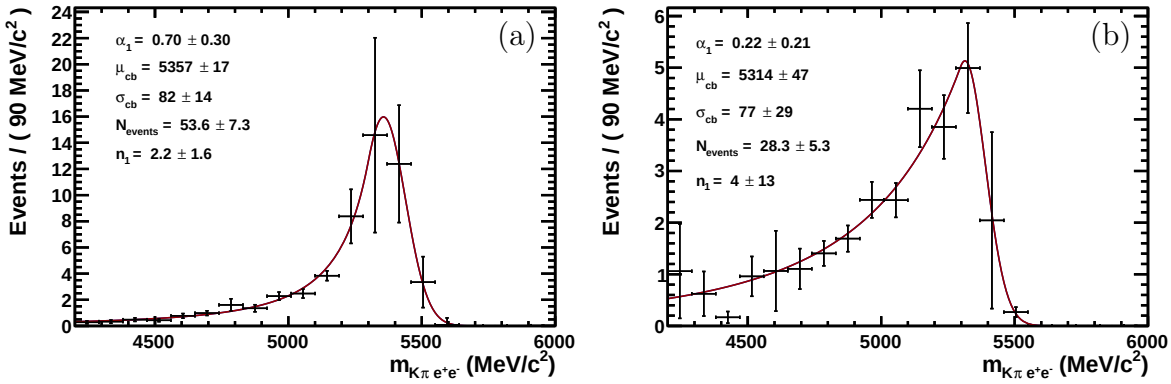

Figure 5.5: Results of the fit to the reconstructed B invariant mass distribution for the $\Lambda_b^0 \to \Lambda^* \gamma$ contribution as background to $B^0 \to K^{*0}\gamma$ for DD (a) and LL (b) configuration. A Crystal Ball function is used.

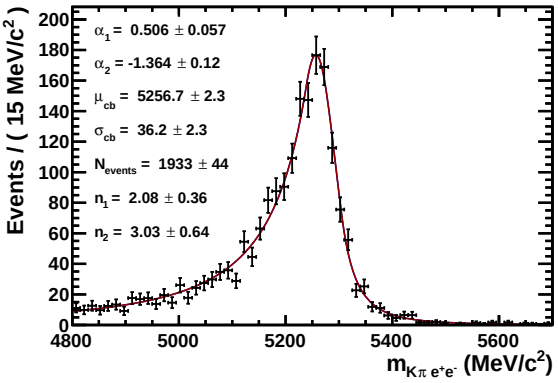

Figure 5.6: Results of the fit to the reconstructed B invariant mass distribution for the $B^0 \to K^{*0}e^+e^-$ contribution as background to $B^0 \to K^{*0}\gamma$ for LL configuration. A double Crystal Ball function is used.

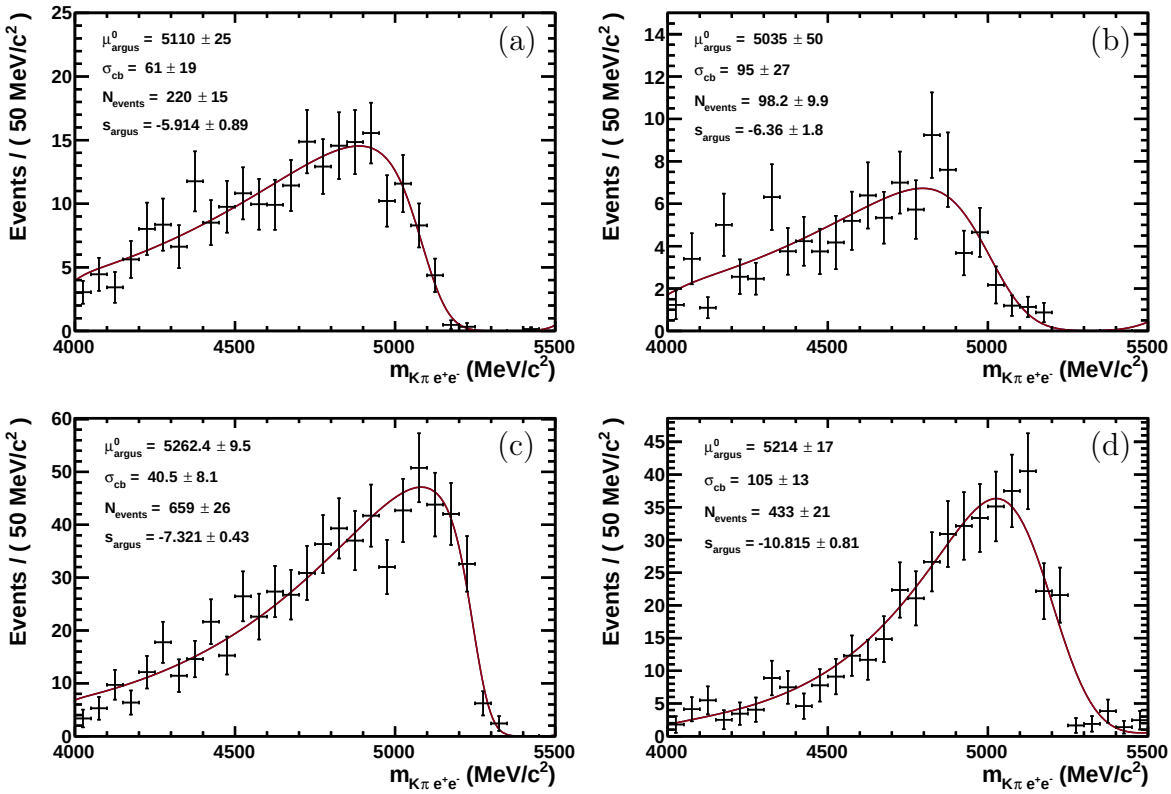

Figure 5.7: Results of the fit to the reconstructed B invariant mass distribution for the partialy reconstructed radiative decays (a,b) and $B^0 \to K^{*0}\eta$ (c,d) contribution as background to $B^0 \to K^{*0}\gamma$ for DD (a,c) and LL (b,d) configuration. An argus function convoluted with a gaussian function is used.

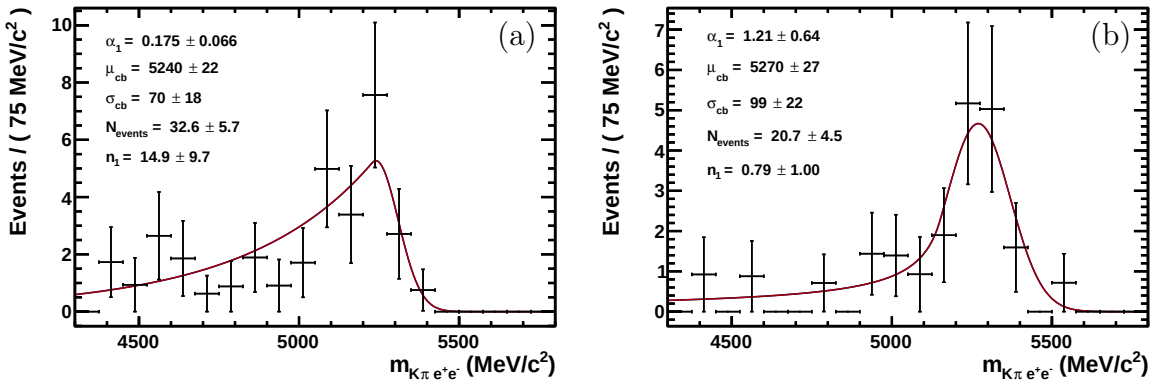

Figure 5.8: Results of the fit to the reconstructed B invariant mass distribution for the $B^0 \to K\pi\pi^0$ contribution as background to $B^0 \to K^{*0}\gamma$ for DD (a) and LL (b) configuration. A Crystal Ball function is used.

Due to the low statistics of $B^0_s \to \phi\gamma$ MC samples, a simple background model is

constructed. Only significant background decays such as $\Lambda_b^0 \to \Lambda^* \gamma$ and $B_s^0 \to \phi e^+ e^-$ are studied by using MC samples. $\Lambda_b^0 \to \Lambda^* \gamma$ shape is modeled using a Crystal Ball function and the result of the fit is shown in Fig. 5.9, while the shape of the $B_s^0 \to \phi e^+ e^-$ decay, contributing only for the LL track configuration, is modeled using a double tail Crystal Ball function and the result of the fit is shown in Fig. 5.10. An exponential shape whose parameters are free in the fit to the data is added to model all other sources of backgrounds.

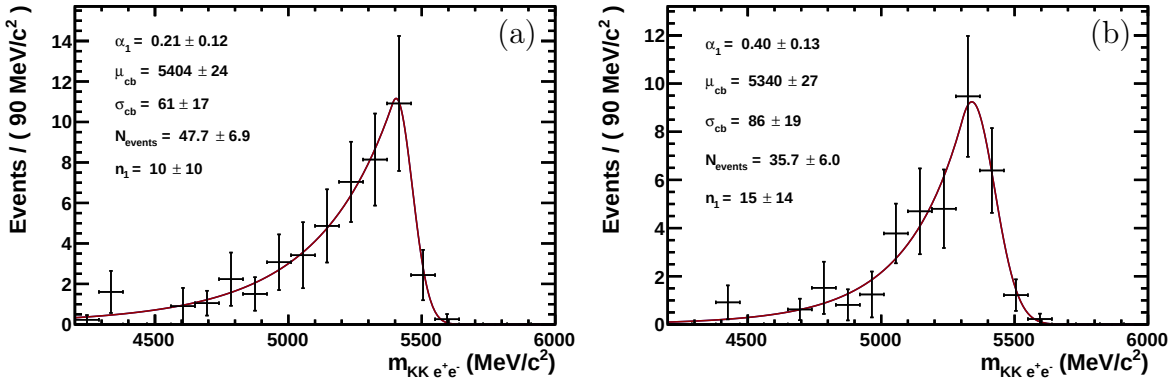

Figure 5.9: Results of the fit to the reconstructed B invariant mass distribution for the $\Lambda_b^0 \to \Lambda^* \gamma$ contribution as background to $B_s^0 \to \phi\gamma$ for DD (a) and LL (b) configurations. A Crystal Ball function is used.

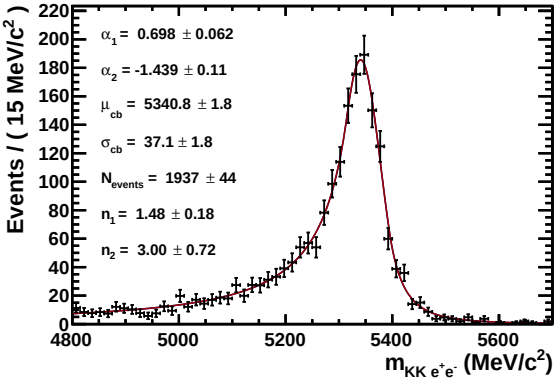

Figure 5.10: Results of the fit to the reconstructed B invariant mass distribution for the $B_s^0 \to \phi e^+ e^-$ contribution as background to $B_s^0 \to \phi\gamma$ for LL configurations. A double Crystal Ball function is used.

5.1.2 Fit to the data

Fit strategy

A simultaneous unbinned likelihood fit to the reconstructed B invariant mass observed in the data is performed to extract the raw asymmetry A_{RAW} (Eq. 4.3) in $B^0 \to K^{*0}\gamma$

decay and the ratio of yields r_y (Eq. 4.12). Events are separated according to the decay and the dielectron track type. In addition, $B^0 \to K^{*0}\gamma$ sub-samples are also separated according to the flavor of the B^0. It can be determined by looking at the charge of the K as a B^0 decays into a K^{*0} which decays into a $(K^+\pi^-)$ pair while a $\overline{B}^0$ decays into a $\overline{K}^{*0}$ which decays into a $(K^-\pi^+)$ pair.

The shapes defined in Sec. 5.1.1 for signal and background modeling are used for the fit. All parameters are fixed to the values previously determined in *MC* samples, except for the position of the mass peak in the sub-sample of $B^0 \to K^{*0}\gamma$ decay for the *DD* track configuration which is left free in the fit since the observed shift in reconstructed B mass due to energy loss with bremsstrahlung photons is not expected to be well reproduced in *MC*. For the same reason, the mass difference between *DD* and *LL* configuration ($\mu_{DD} - \mu_{LL}$, from the fit to signal *MC* samples) and between B^0 and B_s^0 ($\mu_{B_s^0} - \mu_{Bz}$, taken from the Ref. [7]) are let free in the fit with gaussian contrains on them corresponding to their relative uncertainties. Similarly, *MC* samples are expected to have optimistic B mass resolutions (i.e. lower than observed in data). It is corrected by two common ratios $\frac{\sigma_{(data)}}{\sigma_{(MC)}}$, one for each dielectron track type configuration, but common to all decay samples. These ratios are left free in the fit to data.

Background amplitudes are constrained in the fit from their expected relative contributions given in Tab. 4.27. They are all fixed in the fit except for the background from the partially reconstructed radiative decays with $K\pi\pi\gamma$ in the final state, where the relative contamination is left free. The amplitudes of combinatorial (for both signal decays) and low mass backgrounds from $B \to K^{*0}\pi^0 X$ decays are also left free in the fit. Finally, A_{RAW} and r_y are also free parameters of the fit.

Other free parameters are the total number of $B^0 \to K^{*0}\gamma$ signal events and the fraction of *DD* events in $B^0 \to K^{*0}\gamma$ selected events (considering this ratio is the same for B^0 and $\overline{B}^0$ decay) and $B_s^0 \to \phi\gamma$ events. The slope of exponential functions used to model the combinatorial background contribution to $B_s^0 \to \phi\gamma$ events is also free in the fit for each *DD* and *LL* samples. The A_{CP} in $B^0 \to K^{*0}\eta$ decay was measured to be (0.19 ± 0.05) [7]. Therefore, the amplitudes of the B^0 and $\overline{B}^0$ decay through this channel are corrected in the fit to take account of this effect. The A_{CP} in $B^0 \to K^{*0}e^+e^-$ was measured to be (-0.21 $\pm$ 0.19) [7] which is compatible with zero, then it is set to zero in the fit and it will be treated as a systematic uncertainties. All free parameters are listed in Tab. 5.2.

Fit results

The result of the simultaneous fit to the data (refered as the reference fit from now) is shown in Fig. 5.11. The raw asymmetry is measured to be $A_{RAW} = (2.9 \pm 2.5)\%$, while the ratio of yields is measured to be $r_y = 7.32 \pm 0.56$. The different contributions in the fit to the data are shown in Fig. 5.12. The fitted values of the free parameters are given in Tab. 5.2 while the number of signal events in each sample are given in Tab. 5.3.

The resolution of the reconstructed B^0 and B_s^0 masses, including the correction

Table 5.2: Free parameters in the simultaneous unbinned fit to the $B^0 \to K^{*0}\gamma$ and $B_s^0 \to \phi\gamma$ data and their fitted values

parameter	value
A_{RAW}	0.029 ± 0.025
r_y	7.32 ± 0.56
$\mathrm{N}(B^0 \to K^{*0}\gamma) = \mathrm{N}(B^0) + \mathrm{N}(\overline{B}^0)$	1795 ± 51
$N(B^0)_{DD}/N(B^0)$	0.566 ± 0.014
$N(B_s^0)_{DD}/N(B_s^0)$	0.484 ± 0.037
$\mu(B^0)_{DD}$	5266.7 ± 1.4 MeV/c^2
$(\sigma^{Data}/\sigma^{MC})_{DD}$	1.024 ± 0.052 MeV/c^2
$(\sigma^{Data}/\sigma^{MC})_{LL}$	1.144 ± 0.077 MeV/c^2
$(N(K\pi\pi\gamma)/N(B^0 \to K^{*0}\gamma))_{DD}$	0.324 ± 0.051
$(N(K\pi\pi\gamma)/N(B^0 \to K^{*0}\gamma))_{LL}$	0.228 ± 0.066
$N(B \to K^{*0}\pi^0 X)_{DD}^{(K^{*0}\gamma)}$	109 ± 23
$N(B \to K^{*0}\pi^0 X)_{LL}^{(K^{*0}\gamma)}$	86 ± 23
$N(B \to K^{*0}\pi^0 X)_{DD}^{(\overline{K}^{*0}\gamma)}$	108 ± 22
$N(B \to K^{*0}\pi^0 X)_{LL}^{(\overline{K}^{*0}\gamma)}$	78 ± 23
$N(comb)_{DD}^{(K^{*0}\gamma)}$	79 ± 18
$N(comb)_{LL}^{(K^{*0}\gamma)}$	99 ± 27
$N(comb)_{DD}^{(\overline{K}^{*0}\gamma)}$	81 ± 18
$N(comb)_{LL}^{(\overline{K}^{*0}\gamma)}$	134 ± 29
$N(comb)_{DD}^{(\phi\gamma)}$	89 ± 11
$N(comb)_{LL}^{(\phi\gamma)}$	76 ± 12
$c_{DD}^{comb\ (\phi\gamma)}$	-0.00162 ± 0.00032
$c_{LL}^{comb\ (\phi\gamma)}$	-0.00176 ± 0.00038

term $\sigma^{Data}/\sigma^{MC}$, is of the order of 30 MeV/c^2 and of 40 MeV/c^2 in the DD and LL configuration, respectively. These values can be compared to the resolution obtained in the analysis using calorimetric photons [29] shown in Fig. 3.22, which is about 90 MeV/c^2. Using converted photon improves the resolution by a factor 2 to 3. This improved resolution allows the study of the $B_s^0 \to K^{*0}\gamma$ decay but still no clear signal of this decay is observed in data.

The correlation between the free parameters of the reference fit are given in appendix A. Correlations of the order of 15 to 19 % are found between A_{RAW} and the amplitudes of the combinatorial background in the four $B^0 \to K^{*0}\gamma$ samples. A_{RAW} is also correlated with the $B \to K^{*0}\pi^0 X$ amplitudes in DD samples (12 and 6 %). The r_Y is found to be correlated with the number of B^0 (32%), as expected, and also with the amplitudes

Table 5.3: Number of signal events in the different samples obtained from the simultaneous unbinned fit to the $B^0 \to K^{*0}\gamma$ and $B_s^0 \to \phi\gamma$ data. These parameters are not free parameters of the fit but are computed from the 5 first parameters in the Tab. 5.2.

samples	N_{evt}
$N(B^0)_{DD}$	493 ± 22
$N(B^0)_{LL}$	378 ± 20
$N(\overline{B}^0)_{DD}$	522 ± 23
$N(\overline{B}^0)_{LL}$	401 ± 21
$N(B_s^0)_{DD}$	119 ± 12
$N(B_s^0)_{LL}$	127 ± 13

of the combinatorial background and the parameter of the slope of the exponential in the $B_s^0 \to \phi\gamma$ samples (from 10 to 26 %). The correlation of A_{RAW} and r_Y with the combinatorial background parameters is also expected as this background is the only contribution in the signal region which is not totally constrained. Furthermore, A_{RAW} and r_Y are not correlated (0.1%).

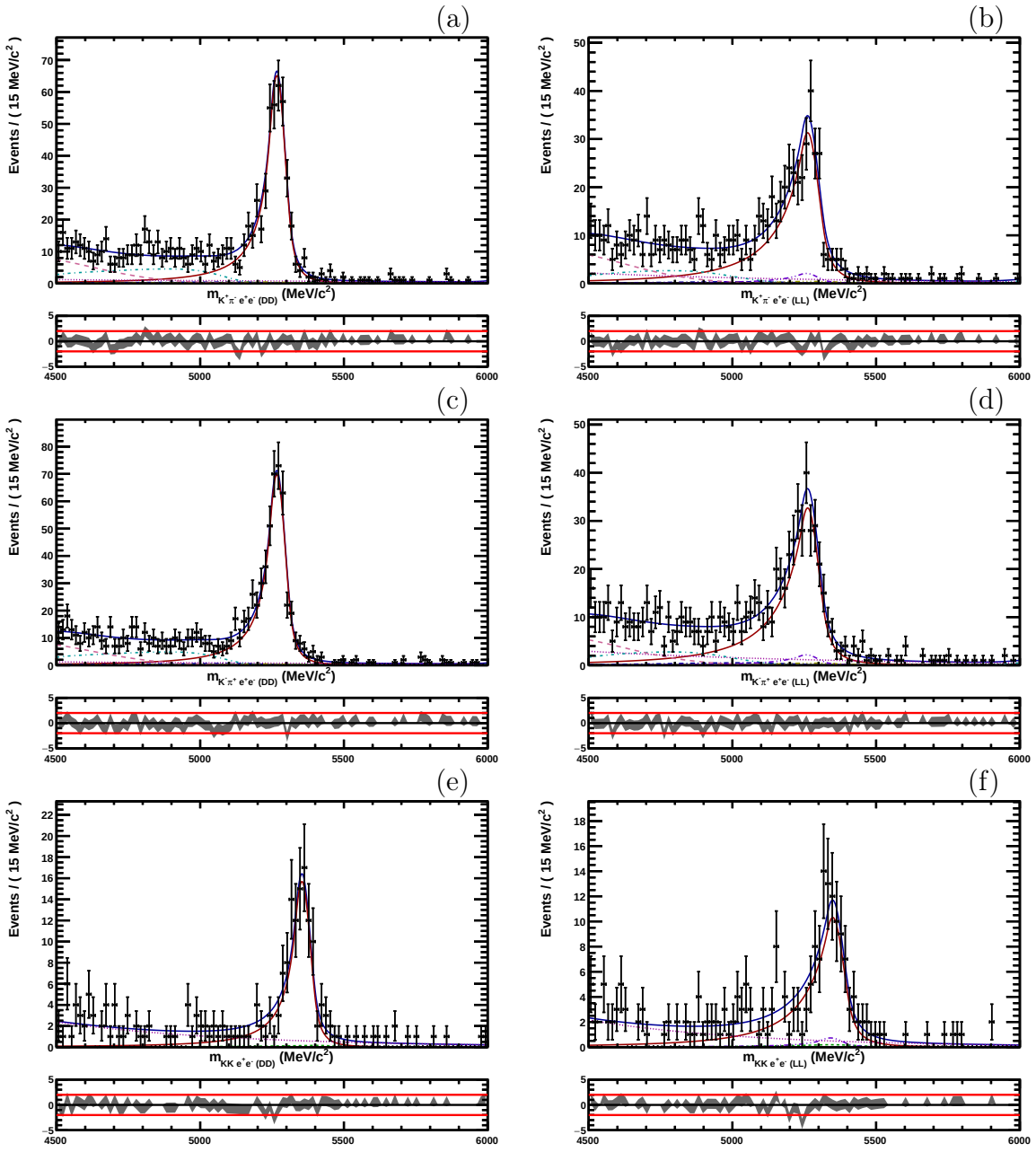

Figure 5.11: Simultaneous fit of the full dataset for $B^0 \to K^{*0}\gamma(e^+e^-)$ (a,b), $\overline{B}^0 \to \overline{K}^{*0}\gamma(e^+e^-)$ (c,d) and $B_s^0 \to \phi\gamma(e^+e^-)$ (e,f) decays. Plots on the left show distributions for the *DD* dielectron track type configuration while plots on the right show distributions for the *LL* configuration. Black points correspond to data, the full blue line is the fit result and signal is the full red line. Background contributions are combinatorial (dotted magenta), $\Lambda_b^0 \to \Lambda^*\gamma$ (dashed green), $B \to K^{*0}\pi\gamma$ (dashed dotted cyan), $B^0 \to K^{*0}\eta$ (long-dashed dotted blue), $B^0 \to K\pi\pi^0$ (dashed three-dotted yellow), $B^0 \to K^{*0}\pi^0 X$ (long-dashed pink) and $B \to Ve^+e^-$ only for the *LL* track type (long-dashed two-dotted violet). The quality of the fit is $\chi^2/ndof = 1.06$ which correspond to a probability p = 17 %.

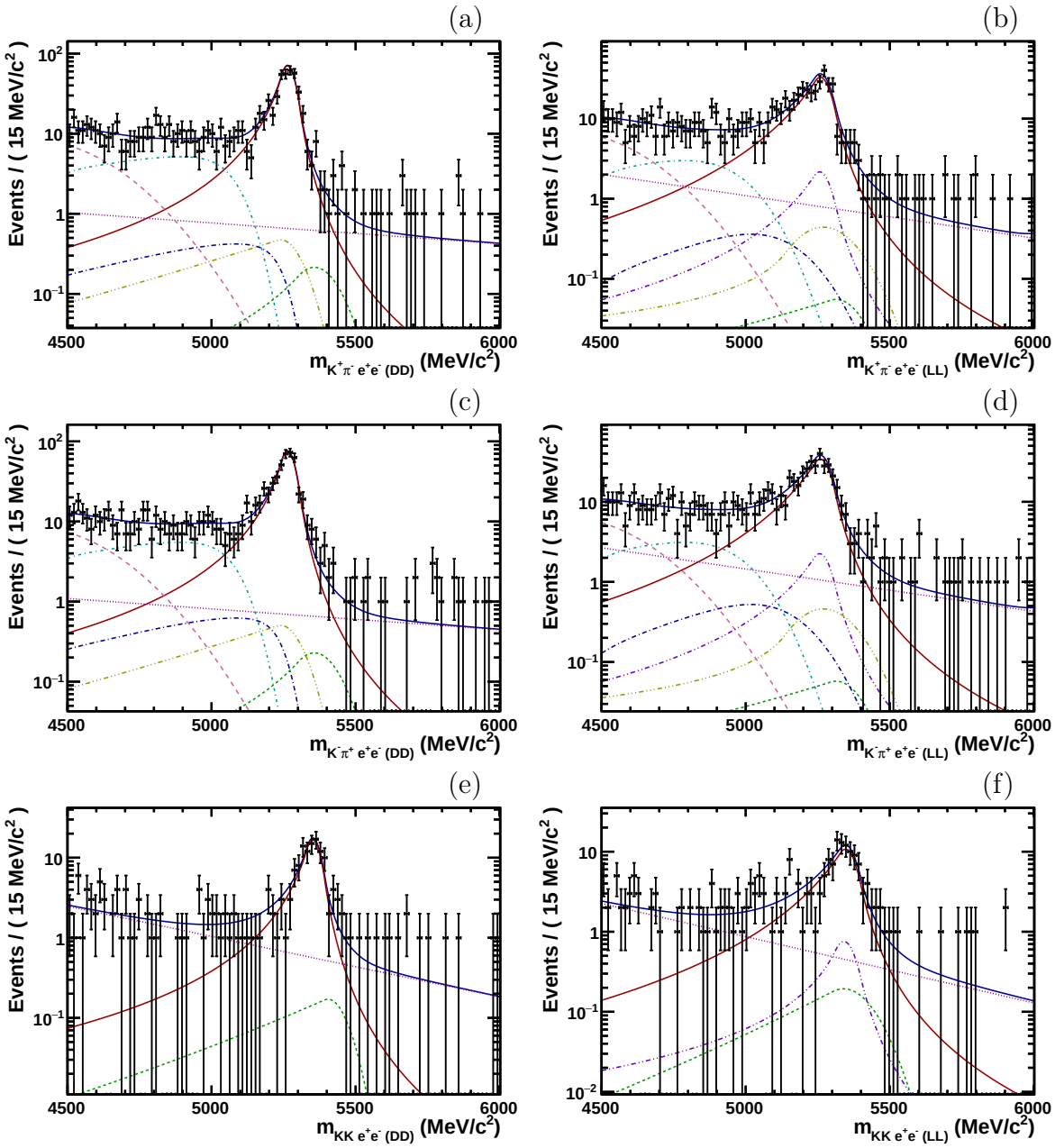

Figure 5.12: Same plots as in Fig. 5.11 in log scale. Black points correspond to data, the full blue line is the fit result and signal is the full red line. Background contributions are combinatorial (dotted magenta), $\Lambda_b^0 \to \Lambda^*\gamma$ (dashed green), $B \to K^{*0}\pi\gamma$ (dashed dotted cyan), $B^0 \to K^{*0}\eta$ (long-dashed dotted blue), $B^0 \to K\pi\pi^0$ (dashed three-dotted yellow), $B^0 \to K^{*0}\pi^0 X$ (long-dashed pink) and $B \to Ve^+e^-$ only for the LL track type (long-dashed two-dotted violet).

5.2 Validation of the fit

5.2.1 Data and simulation comparison

A statistical method, called the `sPLOT` method [82], is used to extract variable distribution for pure signal from the data sample populated by several sources of events (signal and backgrounds). This method is based on the result of a fit to the data of a reference variable (here the reconstructed B invarant mass) in which only the amplitude of each contribution is a free parameter. These amplitudes are independent. A weight, called *sWeight*, is extracted for each event from the result of the fit using the covariance matrix. These weights (which can take negative values) are used to obtain the distribution of variables which are not correlated to the reference one.

The fit to the data from which the *sWeights* are extracted is similar to the reference fit described in Sec. 5.1.2, but the $B^0 \to K^{*0}\gamma$ sample is not separated according to the flavor of the B^0 (only separated according to the dielectron track type). Furthermore, background contributions are merged into a single shape according to the result of the reference fit given in Sec. 5.1.2. The background and signal amplitudes are free and independent in the fit. All other parameters are fixed to the values found in simulation or from the reference fit. The results of this fit are shown in Fig. 5.13, the amplitudes of signal and background contributions for each sample are compatible with the results from the reference fit.

These variable distributions for pure signal are used to compare data and simulation distributions of some relevant variables used in the selection process. For these variables, the correlation with the reconstructed B invariant mass has been computed in simulated events and the maximum value observed is 18%, whereas most of the variables present a correlation below 10%. A Kolmogorov-Smirnov (KS) test of coherence between both distributions is performed. Distributions of $B^0 \to K^{*0}\gamma$ variables where differencies are observed between data en simulation in LL configuration are shown in Fig. 5.14, other distributions can be found in the appendix B. The low statistics in $B_s^0 \to \phi\gamma$ sample leads to higher probability values than in $B^0 \to K^{*0}\gamma$. This means that only very huge discrepencies between data and simulation can be observed. Therefore, $B^0 \to K^{*0}\gamma$ samples are used to infer data and simulation discrepancies.

A good agreement is observed for most of the variables, except for the track multiplicity, *nTracks*, and the z position of the vertex of the photon, *CombDLLe* for both e^+ and e^- as well as the *DIRA* of the B^0 and the minimum of the log of the χ^2_{IP} between e^+ and e^- for LL track type and the p_{T} of the pion for DD track type. These differences are expected for some of these variables as for the *CombDLLe* and *nTracks* for which it is known that the simulation does not well reproduce the data. In the case of *nTracks*, this should not have a huge impact on the measurements since the cut on this variable is far in the upper tail of the distribution. The impact on the measurements are treated as systematic uncertainties by varying the value of the cut (see Sec.5.3.5).

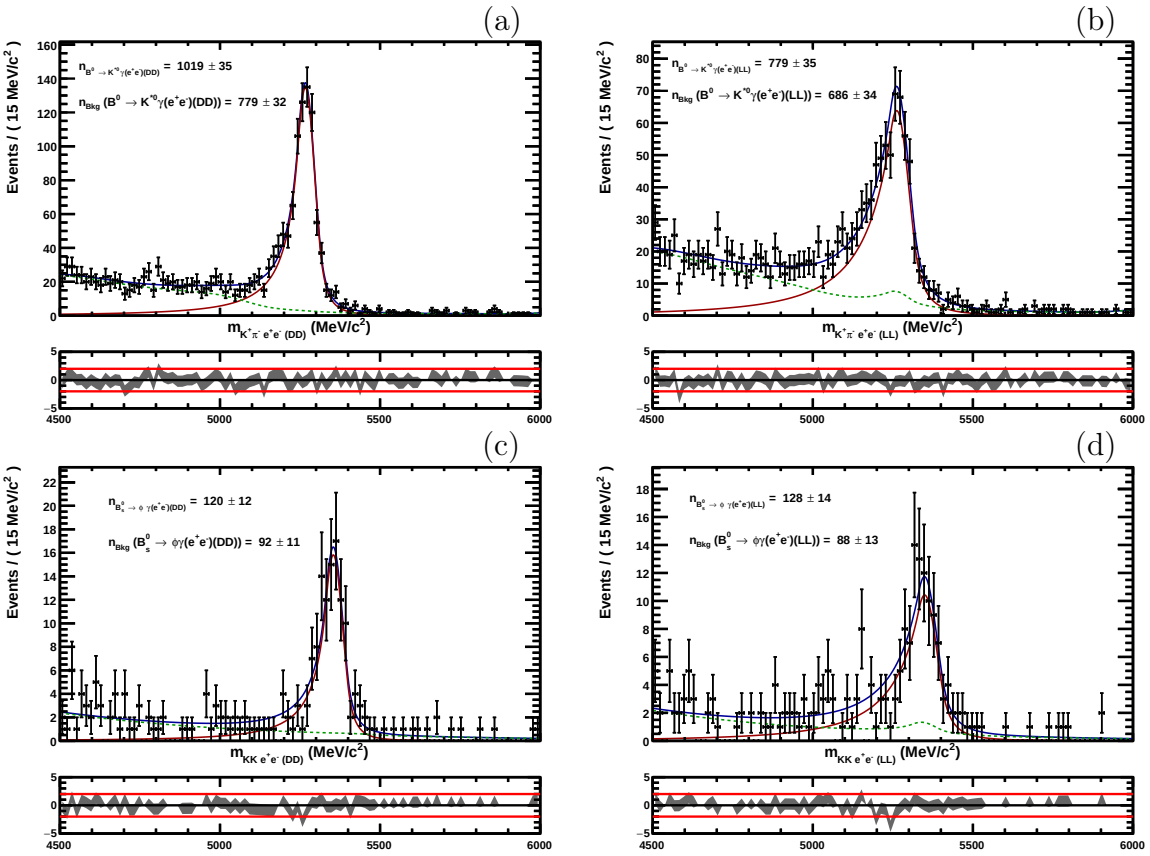

Figure 5.13: Simultaneous fit to the data from which *sWeights* are extracted using the `sPLOT` method to produce a pure sample of signal. Samples are: $B^0 \to K^{*0}\gamma$ in *DD* (a) and *LL* configurations (b) and $B^0_s \to \phi\gamma$ in *DD* (c) and *LL* configurations (d).

5.2.2 Fraction of events in each sample

As said in Sec. 5.1.1, the invariant mass shape of the signal is found to be independant upon the year category and is extracted from the samples corresponding to the three categories *2011low*, *2011high* and *2012*. These samples are merged with a weight corresponding to the expected fraction of events in each category. Using the pure sample of signal produced in Sec. 5.2.1 with the `sPLOT` method, the fraction of events in the three year samples is obtained and compared with the expected ones. The fraction of events in data, the expected one from simulation and the ratio between both are given in Tab. 5.4. Differences are observed up to four sigma pointing to a possible underestimation of the efficiencies for *2012* samples or an overestimation of the efficiencies for *2011* samples.

This effect might come from the stripping where a difference around 10% is observed between *2011* and *2012* efficiencies for both $B^0 \to K^{*0}\gamma$ and $B^0_s \to \phi\gamma$ decays (See Tab. 4.6) or from the L0 trigger level, in particular from the `L0Electron` line where a difference at the order of 10% is observed (see Tab. 4.9). These differences might be

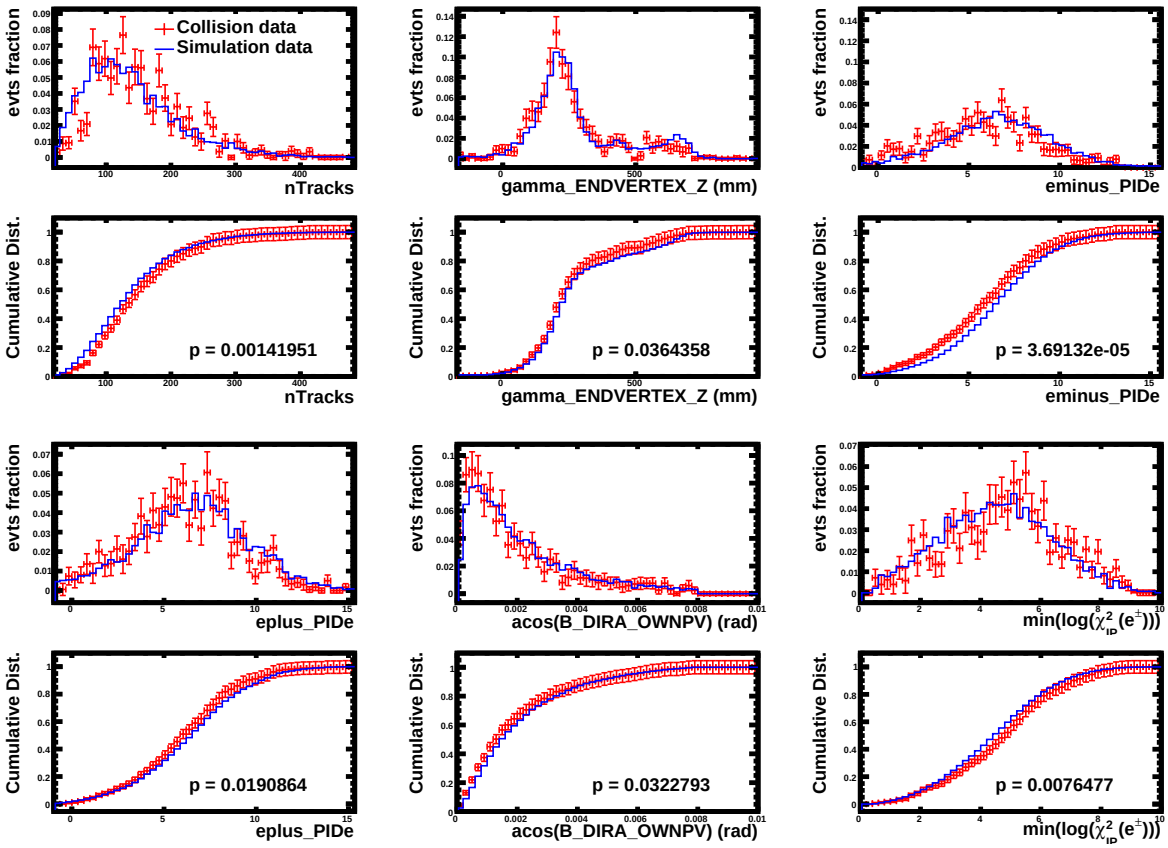

Figure 5.14: Normalized and cumulative distributions of variables where differences are observed between data and simulation, and used in the selection process for $B^0 \to K^{*0}\gamma$ decay in the LL track type configuration. Full blue lines corresponds to the simulation and red histograms to the weighted data. Kolmogorov-Smirnov test results are given.

due to the fact that different thresholds have been used and have not been propagated to simulation with enough accuracy. This effect is taken into account by setting a corresponding systematic uncertainty (see Sec. 5.3.1).

The fraction of events in DD and LL categories observed in the data is also compared with what is expected from simulation. The fraction of DD is a free parameter in the fit to the data for both $B^0 \to K^{*0}\gamma$ and $B_s^0 \to \phi\gamma$. The output values from the fit and from simulation are given in Tab. 5.5. The data and the simulation values are perfectly compatible for $B^0 \to K^{*0}\gamma$, a difference smaller than two sigma is observed for $B_s^0 \to \phi\gamma$. This difference could come from the background model which is more precisely defined for $B^0 \to K^{*0}\gamma$ than for $B_s^0 \to \phi\gamma$. A systematic uncertainty is also set to take into account this effect (See Sec. 5.3.1).

Table 5.4: Fractions ($f_{year}^{(data)}$) of events in *2011low*, *2011high* and *2012* data samples, expected fractions ($f_{year}^{(MC)}$) estimated in `MC` and their ratios ($f_{year}^{(data)}/f_{year}^{(MC)}$).

decay	$tt_{e^\pm}$	year	$f_{year}^{(data)}$	$f_{year}^{(MC)}$	$f_{year}^{(data)}/f_{year}^{(MC)}$
$B^0 \to K^{*0}\gamma$	*DD*	*2011low*	0.065 ± 0.006	0.070 ± 0.003	0.916 ± 0.090
		2011high	0.206 ± 0.010	0.258 ± 0.005	0.801 ± 0.040
		2012	0.729 ± 0.010	0.672 ± 0.005	1.085 ± 0.018
	LL	*2011low*	0.112 ± 0.008	0.131 ± 0.004	0.857 ± 0.069
		2011high	0.224 ± 0.011	0.251 ± 0.005	0.893 ± 0.047
		2012	0.664 ± 0.012	0.619 ± 0.006	1.073 ± 0.023
$B_s^0 \to \phi\gamma$	*DD*	*2011low*	0.066 ± 0.017	0.078 ± 0.003	0.843 ± 0.220
		2011high	0.184 ± 0.027	0.241 ± 0.005	0.764 ± 0.112
		2012	0.750 ± 0.030	0.681 ± 0.005	1.101 ± 0.044
	LL	*2011low*	0.069 ± 0.017	0.127 ± 0.004	0.547 ± 0.137
		2011high	0.241 ± 0.029	0.242 ± 0.005	0.993 ± 0.122
		2012	0.690 ± 0.031	0.631 ± 0.006	1.094 ± 0.051

Table 5.5: Fractions of events for the *DD* dielectron track-type category in data ($f_{DD}^{(data)}$) and expected fractions ($f_{DD}^{(MC)}$) from `MC`.

decay	$f_{DD}^{(data)}$	$f_{DD}^{(MC)}$
$B^0 \to K^{*0}\gamma$	0.566 ± 0.014	0.576 ± 0.004
$B_s^0 \to \phi\gamma$	0.484 ± 0.037	0.543 ± 0.004

5.2.3 Pseudo data samples generation

In order to validate the fitting procedure, pseudo B invariant mass distributions (toy samples) are produced using the result of the reference fit. Six samples, the same as defined for the reference fit, are generated from the global fitted function (See Sec. 5.1.2). The number of generated events in each sample is let free to vary following a Poissonian distribution. Each sample is then fitted using the same model as the reference fit and the pull distribution of raw asymmetry and yield ratio is computed as:

$$P_x = \frac{x_{fit} - x_{gen}}{\sigma_x} \tag{5.2}$$

where x_{fit} is the value of the parameters x extracted from the original fit, x_{gen} and σ_x are the value and the resolution of the parameter x extracted from the fit on the given generated sample. If the fit is well behaved, the distribution of P_x follows a Normal distribution.

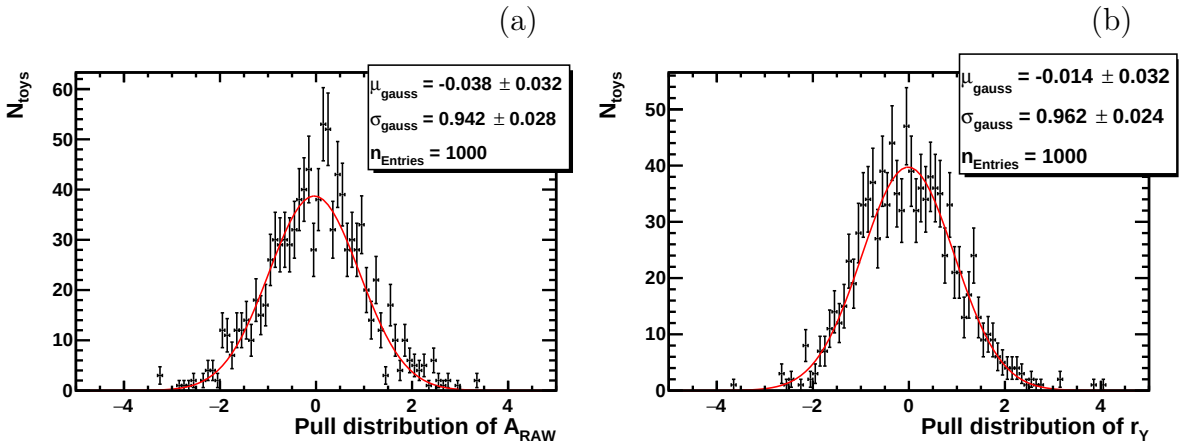

Figure 5.15: Pull distribution for the raw asymmetry (a) and the signal yield ratio (b). The red curve is the fit result.

The pull distribution of A_{RAW} and r_Y obtained by generating 1000 samples is given in Fig.5.15. The result of the fit to the pull distribution, using a Gaussian function, is also shown and their parameter values are given. No significant bias is observed in the A_{RAW} and r_Y distribution since the central value of the Gaussian is consistent with zero. The widths of both A_{RAW} and r_Y distributions are slightly lower than one, this indicates that measured statistical uncertainties are slightly over-estimated but, as bias are in conservative side, no correction is applied.

Furthermore, pull distributions of all the free parameters in the fit have been extracted from these toys. No bias is observed for any parameters and the widths of these pulls are all compatible with one within two standard deviations.

5.3 Systematic uncertainties

5.3.1 Fraction of events, data and simulation differences

Observed differences between the fraction of events in data and simulation sample corresponding to a given year and category described in Sec. 5.2.2 is taken into account by setting a systematical uncertainty on the efficiency ratio:

$$r_\epsilon = \frac{\epsilon(B_s^0 \to \phi\gamma)}{\epsilon(B^0 \to K^{*0}\gamma)} \tag{5.3}$$

To check the impact of these differences between the efficiencies, the stripping efficiency of *2012* sample is set at the same value than for *2011* sample. Then the new fractions of events are computed and given in Tab. 5.6. This artificial improvement of the *2012* stripping efficiency significantly reduces the difference between the fractions of events observed in data and expected from simulation studies.

Table 5.6: Fractions ($f_{year}^{(data)}$) of event in *2011low*, *2011high* and *2012* data samples, expected fractions ($f_{year}^{(MC)}$) estimated in `MC` and ratio ($f_{year}^{(data)}/f_{year}^{(MC)}$) after having changed the stripping efficiency to *2012* values.

decay	$tt_{e^\pm}$	year	$f_{year}^{(data)}$	$f_{year}^{(MC)}$	$f_{year}^{(data)}/f_{year}^{(MC)}$
$B^0 \to K^{*0}\gamma$	*DD*	*2011low*	0.065 ± 0.006	0.066 ± 0.003	0.977 ± 0.096
		2011high	0.206 ± 0.010	0.241 ± 0.005	0.854 ± 0.043
		2012	0.729 ± 0.010	0.692 ± 0.005	1.053 ± 0.017
	LL	*2011low*	0.112 ± 0.008	0.123 ± 0.004	0.910 ± 0.073
		2011high	0.224 ± 0.011	0.236 ± 0.005	0.948 ± 0.051
		2012	0.664 ± 0.012	0.641 ± 0.006	1.036 ± 0.021
$B_s^0 \to \phi\gamma$	*DD*	*2011low*	0.066 ± 0.017	0.074 ± 0.003	0.890 ± 0.232
		2011high	0.184 ± 0.027	0.228 ± 0.004	0.807 ± 0.118
		2012	0.750 ± 0.030	0.698 ± 0.005	1.075 ± 0.043
	LL	*2011low*	0.069 ± 0.017	0.121 ± 0.004	0.576 ± 0.145
		2011high	0.241 ± 0.029	0.231 ± 0.005	1.044 ± 0.128
		2012	0.690 ± 0.031	0.649 ± 0.005	1.063 ± 0.049

Since the signal shapes observed in each sample of a given year and category are similar, the observed differences between data and simulation are not expected to impact the reference fit. However, the impact on efficiencies shall be estimated. The efficiencies are the same for both $K^{*0}\gamma$ and $\overline{K}^{*0}\gamma$, so the CP asymmetry in $B^0 \to K^{*0}\gamma$ is not expected to be impacted. The ratio of the total $B^0 \to K^{*0}\gamma$ and $B_s^0 \to \phi\gamma$ efficiencies is used to compute the final ratio of branching fractions.

The reference efficiency ratio is found to be:

$$r_\epsilon = 1.176 \pm 0.033. \tag{5.4}$$

If the *2012* stripping efficiency is increased by 10 %, this ratio is found to be:

$$r_\epsilon^{'} = 1.165 \pm 0.033. \tag{5.5}$$

A variation of the 2012 efficiencies of the order of 10% for both $B^0 \to K^{*0}\gamma$ and $B_s^0 \to \phi\gamma$ samples leads to a variation of the efficiency ratio at the level of 0.94%. Considering the other 10% difference between *2011* and *2012* L0 trigger efficiencies, the impact on the ratio of final efficiencies is not expected to be larger than 2%. Therefore, a systematic uncertainty of 2 % is added to the efficiency ratio and translated into a systematic uncertainty on the ratio of branching fractions (See Eq. 4.15): $\frac{\Delta r_\mathcal{B}}{r_\mathcal{B}} = 0.020$.

To take into account the observed difference between the fraction of *DD* $B_s^0 \to \phi\gamma$ events in data and *MC*, a new fit to the data is performed to check the impact of this effect by fixing the fraction of *DD* events in the data to the value given by simulation (see

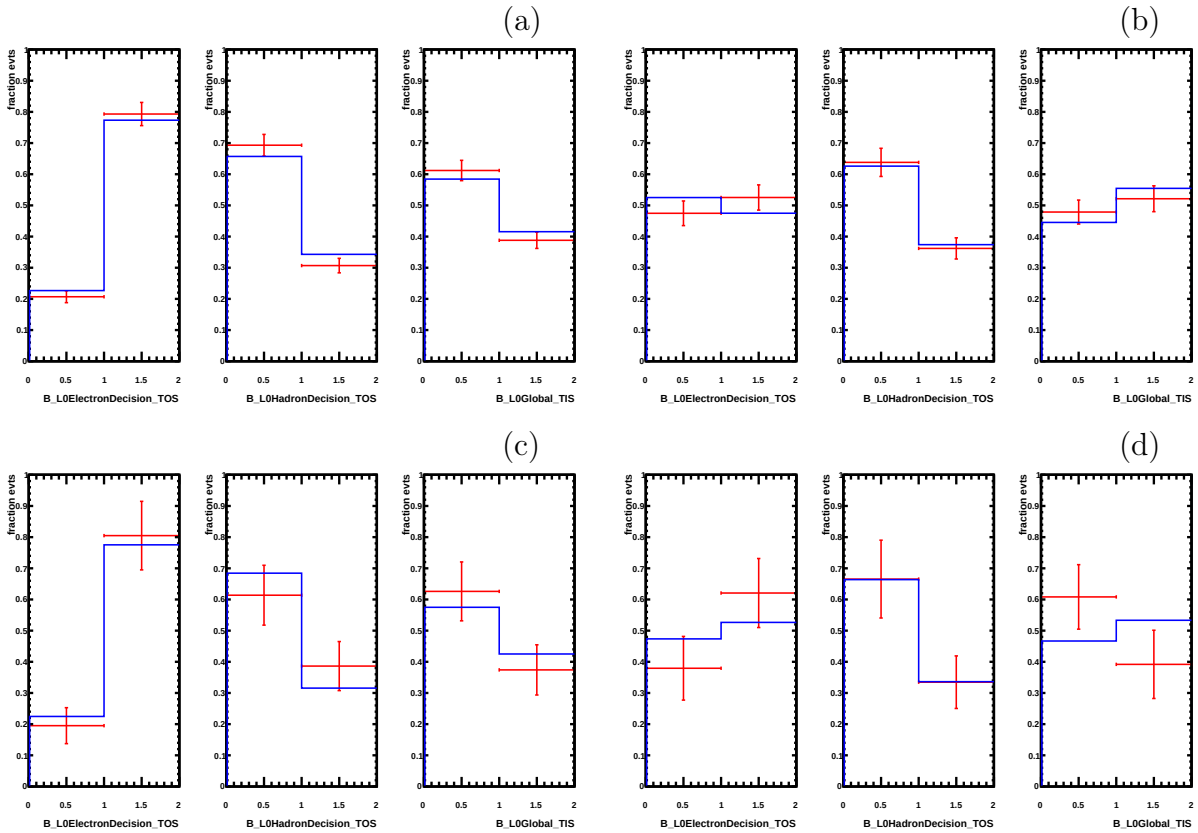

Figure 5.16: L0-trigger line distributions for *2012*, bin 0 corresponds to the fraction of events which have not triggered the line and bin 1 corresponds to the fraction of events which have triggered the line. Blue histograms correspond to simulation and red crosses correspond to sWeighted data. Distributions for $B^0 \to K^{*0}\gamma(e^+e^-)$ samples in *DD* (a) and *LL* (b) configuration and for $B_s^0 \to \phi\gamma(e^+e^-)$ samples in *DD* (c) and *LL* (d) configuration are shown.

Tab. 4.8). The raw asymmetry in $B^0 \to K^{*0}\gamma$ is not modified while the value of the yield ratio is now: $r_Y^{'} = 7.35 \pm 0.57$ to be compared with the reference value: $r_Y = 7.32 \pm 0.56$. Therefore a systematic uncertainty is added to r_Y: $\Delta r_Y = \pm\ 0.03$, which is propagated to a systematic uncertainty to the ratio of branching fractions: $\frac{\Delta r_{\mathcal{B}}}{r_{\mathcal{B}}} = 0.004$.

5.3.2 L0-Trigger

Using the pure signal sample obtained from the `sPLOT` method (see Sec. 5.2.1), the fraction of events selected by each L0 trigger line (e.g. `L0ElectronDecision_TOS`, `L0HadronDecision_TOS` or `L0Global_TIS`) is obtained for each track type and year sample. They are compared to simulation in Fig. 5.16 for *2012*. Results for *2011* can be found in appendix C.

Small differences between data and simulation are observed. Then, events are separated

Table 5.7: Ratios of fractions of events in sWeighted data and simulation samples, for each L0-trigger category. The *2011low* samples for $B_s^0 \to \phi\gamma$ are not set in this table since there is not enough statistics.

Decay channel	year	$tt_{(e^+e^-)}$	$f_{(data)}/f_{(MC)}$		
			ElectronTOS	*HadronTOS*	*GlobalTIS*
$B^0 \to K^{*0}\gamma$	2011low	DD	0.826 ± 0.086	1.667 ± 0.369	1.206 ± 0.451
		LL	1.009 ± 0.086	0.889 ± 0.208	1.080 ± 0.223
	2011high	DD	0.989 ± 0.029	0.860 ± 0.208	1.415 ± 0.360
		LL	0.875 ± 0.063	1.243 ± 0.185	1.173 ± 0.177
	2012	DD	1.026 ± 0.022	0.873 ± 0.104	0.958 ± 0.118
		LL	1.106 ± 0.054	0.810 ± 0.080	0.983 ± 0.079
	merged	DD	1.000 ± 0.017	0.947 ± 0.092	1.068 ± 0.113
		LL	1.008 ± 0.036	0.918 ± 0.071	1.056 ± 0.070
$B_s^0 \to \phi\gamma$	2011high	DD	1.056 ± 0.075	0.547 ± 0.401	1.052 ± 0.717
		LL	1.052 ± 0.132	0.490 ± 0.264	1.287 ± 0.361
	2012	DD	1.038 ± 0.057	1.243 ± 0.351	0.525 ± 0.225
		LL	1.179 ± 0.108	0.956 ± 0.225	0.684 ± 0.165
	merged	DD	1.055 ± 0.045	0.926 ± 0.248	0.660 ± 0.225
		LL	1.205 ± 0.076	0.709 ± 0.160	0.761 ± 0.143

into three exclusive samples, according to which L0-trigger line has been triggered:

- *ElectronTOS*: Contains events which have triggered the `L0ElectronDecision_TOS` line.
- *HadronTOS*: Contains events which have not triggered the `L0ElectronDecision_TOS` line, but have triggered the `L0HadronDecision_TOS` line.
- *GlobalTIS*: Contains events which have not triggered any of the two previous lines, but have triggered the `L0Global_TIS` line.

The ratios of fractions of events in sWeighted data and simulation are computed for each sample, results are given in Tab. 5.7 and shown in Fig. 5.17. The incoherent values for $B_s^0 \to \phi\gamma(e^+e^-)$, *2011low* samples are explained by the low statistics in these samples (less than 10 events) and the fact that sWeights can take negative values. From these results, it can be observed that some ratios are not compatible with one, in particular for *2011* samples, but discrepancies are reduced once different year samples are merged.

Since distributions of the reconstructed B invariant mass in simulation samples are different for these three trigger categories, as it is shown in Fig. 5.18, the observed difference

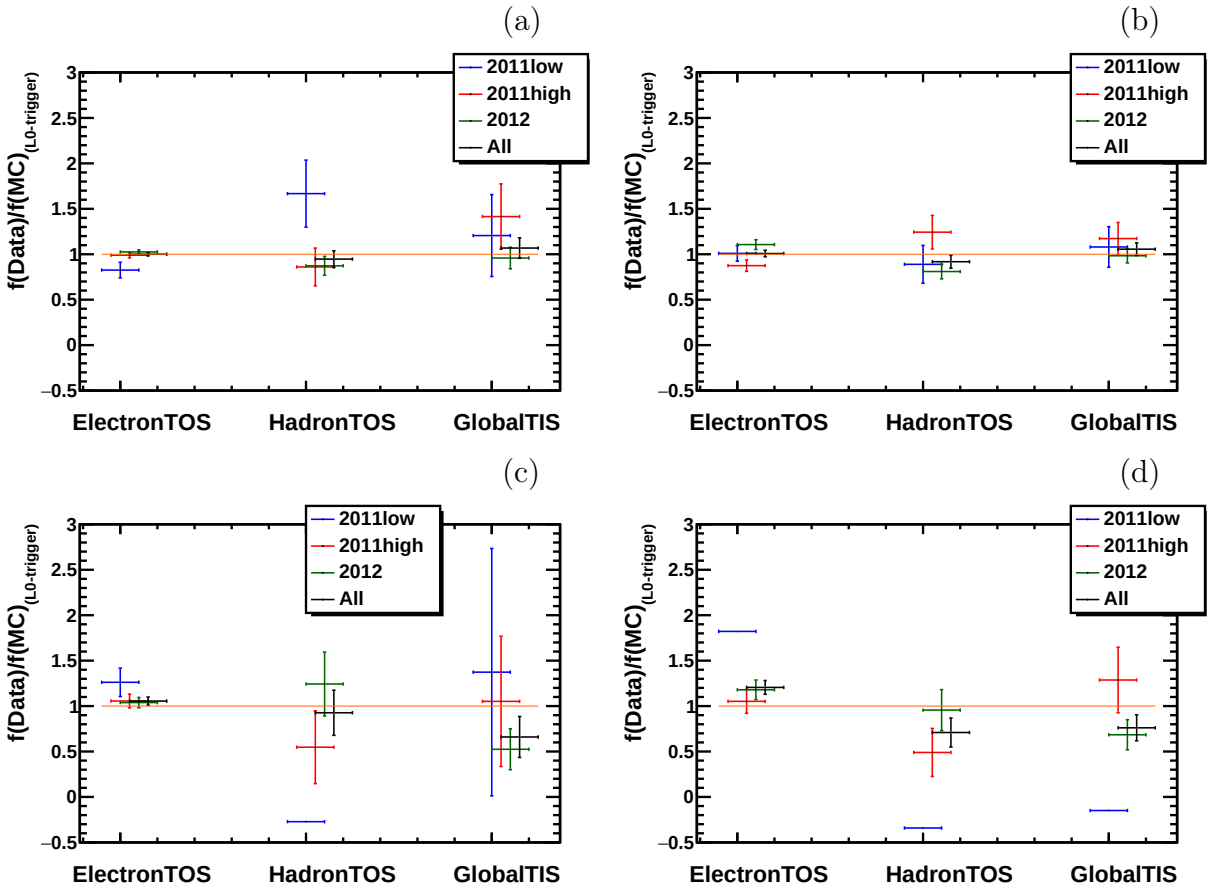

Figure 5.17: Ratios of fractions of events in sWeighted data and simulation samples for each L0-trigger category for $B^0 \to K^{*0}\gamma(e^+e^-)$ samples in DD (a) and LL (b) configurations and for $B_s^0 \to \phi\gamma(e^+e^-)$ samples in DD (c) and LL (d) configurations.

in the distributions between data and simulation could have a non negligible impact. In order to check this impact a data driven approach is performed using $B^0 \to J/\Psi K^{*0}$ and $B_s^0 \to J/\Psi\phi$ decays where the J/Ψ decays into a dielectron pair. This only allows to study the impact on the LL category and the effect is assumed to be similar in DD category as the trigger is not based on the track information but on the calorimeter one.

$B^0 \to J/\Psi K^{*0}$ and $B_s^0 \to J/\Psi\phi$ samples are reconstructed and selected as it is done for $B^0 \to K^{*0}\gamma$ and $B_s^0 \to \phi\gamma$, except the J/ψ for which the stripping selections are: $m_{ee} \in [2200, 4200]$ MeV/c^2, $\chi^2_{\text{vtx}} < 16$ and the electron and positron should have $p_{\text{T}} > 300$ MeV/c, $\chi^2_{track}/ndf < 5$ and $combDLL_e > -2.0$. All cuts given in Tab. 4.5, corresponding to the stripping of $B^0 \to K^{*0}\gamma(e^+e^-)$ and $B_s^0 \to \phi\gamma(e^+e^-)$ decays, are applied on the two J/ψ samples, except the dielectron mass requirement. Then, the shape of the signal contribution is modeled using simulation samples and a simultaneous fit, with a simple background model is performed on data. The `sPLOT` method is

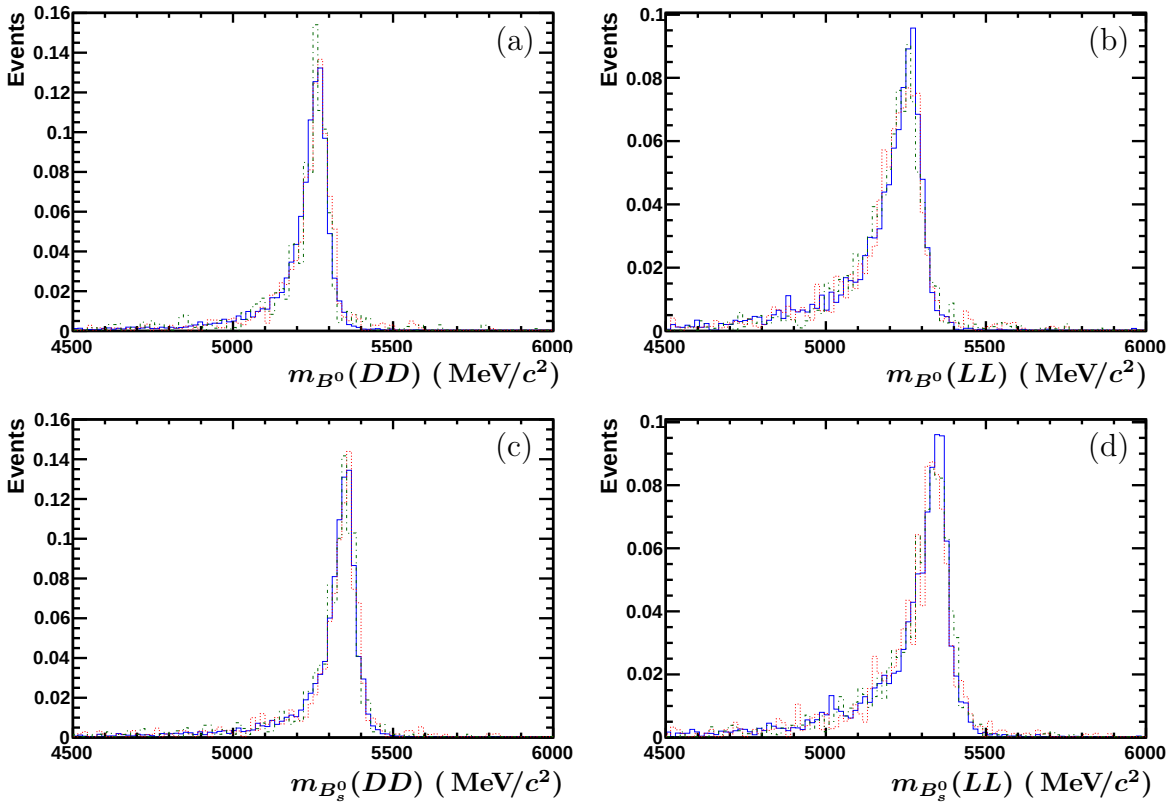

Figure 5.18: Reconstructed B invariant mass distribution sin simulation samples for $B^0 \to K^{*0}\gamma(e^+e^-)$ decay in DD (a) and LL (b) configurations and for $B^0_s \to \phi\gamma(e^+e^-)$ decay in DD (c) and LL (d) configurations. The blue full line corresponds to *ElectronTOS* events, the dotted red line corresponds to *HadronTOS* events and the dashed-dotted green line corresponds to *GlobalTIS* events.

used to extract pure signal samples from the fit and to compare L0-trigger line distributions with simulation. The obtained ratios are given in Tab. 5.8 and shown in Fig. 5.19.

These ratios, after normalisation in order to conserve the total number of events, are applied as weights to $B^0 \to K^{*0}\gamma$ and $B^0_s \to \phi\gamma$ events in simulation. Then, the new signal shape is extracted from simulation performing a simultaneous fit, as described in Sec. 5.1.1. The parameters obtained for LL events are compatible with initial values. Using this new signal shape into the fit to data leads to the same measured values of A_{RAW} and r_Y while the quality of the fit is the same. Thus, the different shape obtained with different distributions of events in the L0-trigger has a negligible impact on the measurements.

The impact on the efficiencies is also studied. Simulation samples are separated according to the three L0-trigger categories previously defined and used to compute the selection efficiency (after trigger and stripping) in each L0-trigger sample. Then, L0-trigger samples are merged by applying the same weights as defined before, and the

Table 5.8: Ratios of fractions of events in sWeighted data and simulation samples of $B^0 \to J/\Psi K^{*0}$ and $B_s^0 \to J/\Psi\phi$ decays, for each L0-trigger category. Only LL configuration samples are available.

Decay channel	year	$f_{(data)}/f_{(MC)}$		
		ElectronTOS	*HadronTOS*	*GlobalTIS*
$B^0 \to J/\Psi K^{*0}$	2011low	1.051 ± 0.022	0.482 ± 0.105	1.001 ± 0.104
	2011high	1.047 ± 0.022	0.489 ± 0.107	1.012 ± 0.105
	2012	0.987 ± 0.019	0.961 ± 0.091	1.059 ± 0.057
	merged	1.006 ± 0.015	0.832 ± 0.072	1.052 ± 0.050
$B_s^0 \to J/\Psi\phi$	2011low	0.895 ± 0.025	1.423 ± 0.265	1.506 ± 0.153
	2011high	0.893 ± 0.025	1.447 ± 0.269	1.521 ± 0.154
	2012	0.954 ± 0.022	0.955 ± 0.145	1.153 ± 0.069
	merged	0.935 ± 0.016	1.097 ± 0.125	1.221 ± 0.060

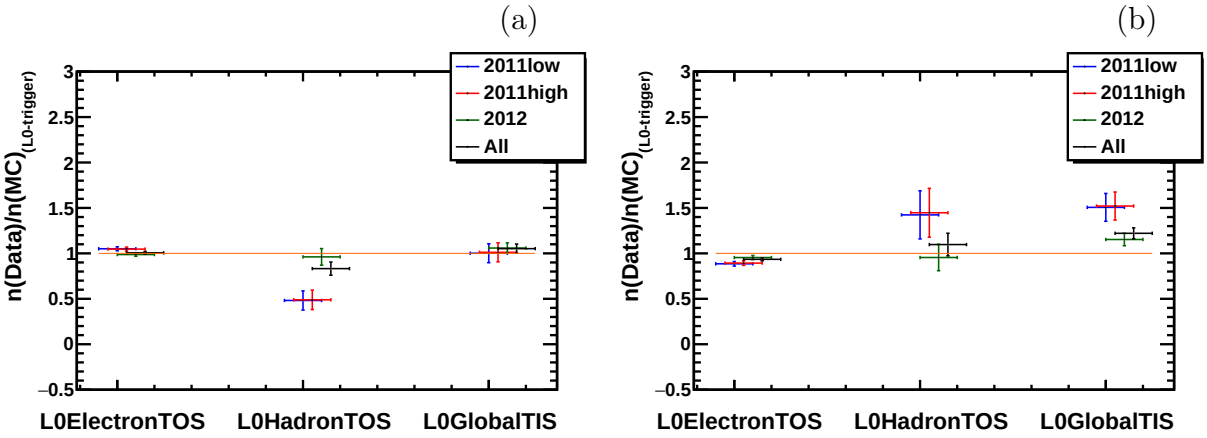

Figure 5.19: Ratios of fractions of events in sWeighted data and simulation samples for each L0-trigger category in LL configuration for $B^0 \to J/\Psi K^{*0}$ (a) and $B_s^0 \to J/\Psi\phi$ (b) samples.

total efficiency is computed. This efficiency is compared to the default one and shown in Fig. 5.20. It can be observed that in LL samples, applied weights change the values by less than one sigma. The maximum deviation is found to be 1.8 % in $B^0 \to K^{*0}\gamma(e^+e^-)$ *2011low* sample. This value is set as a systematical uncertainty on the efficiencies (the statistical uncertainty is 1.4 %).

The efficiency ratio is used to compute the ratio of branching fractions (see Eq. 4.15). Therefore, the systematic uncertainty on individual efficiency can be propagated to the efficiency ratio as:

$$\frac{\Delta r_\epsilon}{r_\epsilon} = \sqrt{2}\frac{\Delta\epsilon}{\epsilon} = 0.025 \tag{5.6}$$

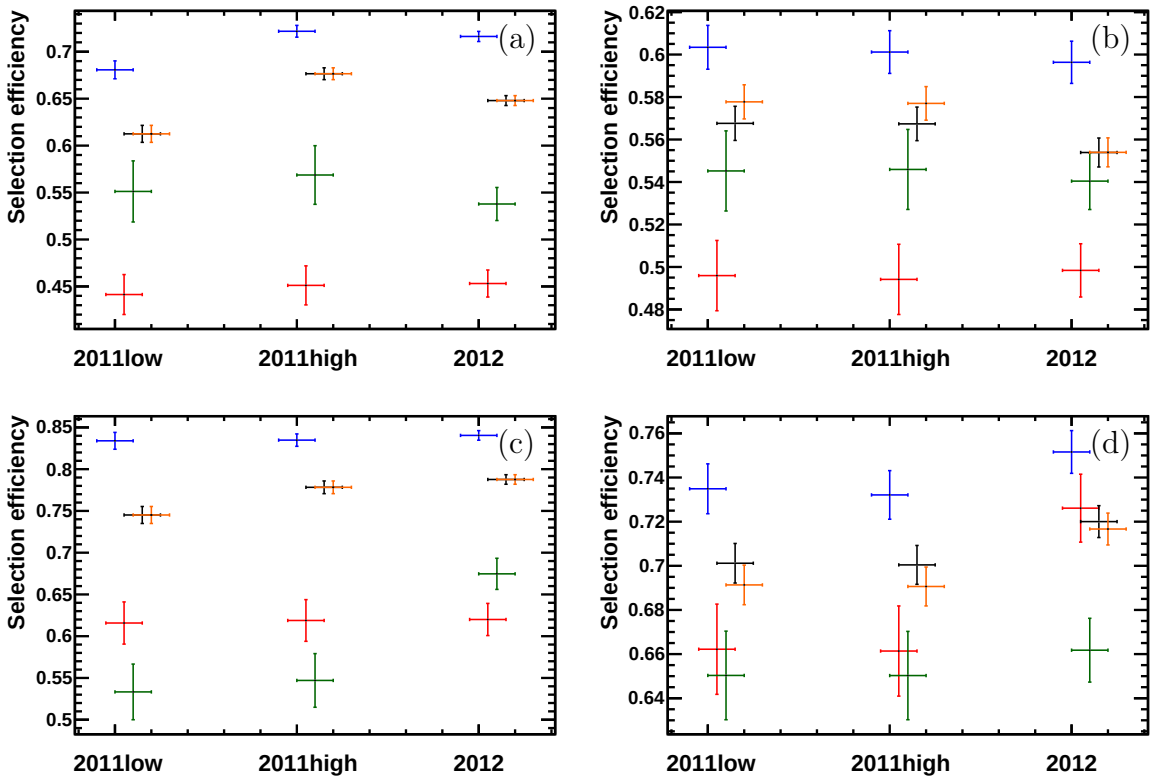

Figure 5.20: Selection efficiencies, computed from simulation samples of $B^0 \to K^{*0}\gamma(e^+e^-)$ decay in *DD* (a) and *LL* (b) configuration and $B_s^0 \to \phi\gamma(e^+e^-)$ decay in *DD* (c) and *LL* (d) configuration. Efficiencies corresponds to *ElectronTOS* (blue), *HadronTOS* (red) and *GlobalTIS* (green) samples, merged samples without reweighting (black) and merged samples with reweighting (orange).

where the $\sqrt{2}$ term comes from the fact that this uncertainty affects both efficiencies of r_ϵ. This uncertainty is propagated to the ratio of branching fractions: $\frac{\Delta r_\mathcal{B}}{r_\mathcal{B}} = 0.025$.

5.3.3 Fit parameters

The systematic uncertainties induced by the signal and background modelling (see Sec. 5.1.1 and Sec. 5.1.1), including the relative contamination of backgrounds described in Sec. 4.4.3, is studied by varying the corresponding parameters within their known uncertainties. Parameters are separated into four categories which are investigated independently: parameters related to the *signal shape* ($(\mu_{LL} - \mu_{DD})$, $\sigma_{DD(LL)}$, tail parameters: see Tab. 5.1), parameters related to *peaking background shapes* ($\Lambda_b^0 \to \Lambda^*\gamma$, $B \to K\pi\pi^0$, prompt e^+e^- decays: see Figs. 5.5 5.8 5.6 5.9 5.10), parameters related to *low mass background shapes* ($B \to K\pi\pi\gamma$, $B \to K^{*0}\pi^0 X$: see Figs. 5.3 5.4 5.7) including the CP asymmetry of the $B^0 \to K^{*0}\eta$ decay ($A_{CP}(B^0 \to K^{*0}\eta) = 0.19 \pm 0.05$ [7]) and parameters related to *relative contaminations* (see Sec. 4.4.3).

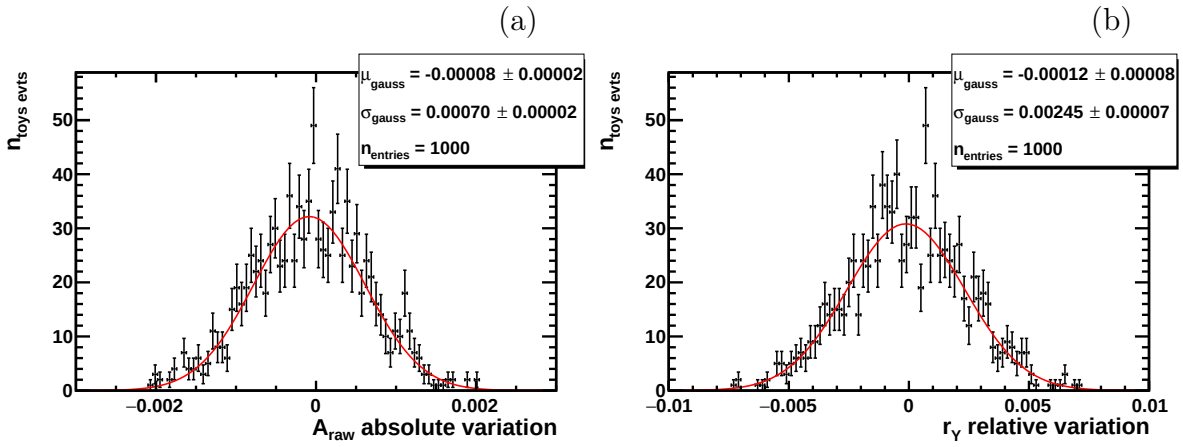

Figure 5.21: Absolute variation of A_{RAW} (a) and relative variation of r_Y (b) when varying the fixed parameters of the signal model.

The fit is repeated 1000 times for each category. For each fit, a new set of parameters is randomly generated using a gaussian generator where the mean of the generator is the default value of the parameter and the width is the known uncertainty on the parameter. The gaussian resolution for the parameters related to the $B \to K^{*0}\pi^0 X$ decays is fixed to three standard deviations to take into account the fact that calorimetric photons are used in the simulation samples instead of converted ones (see Sec. 4.3.3).

The result of the fit is stored and the absolute variation of the raw asymmetry and the relative variation of the yield ratio is computed. The distribution of these two variables for the *signal shape* parameter category is shown in Fig. 5.21 whereas the distributions for the others parameter categories can be found in appendix D. These distributions, as well as those corresponding to the three others parameter categories, are compatible with a gaussian distribution. The values of the mean and the width of these distributions are given in Tab. 5.9.

The mean of the gaussian is taken as a correction to the measured value (A_{RAW}, r_Y) while the width of the gaussian is taken as a systematic uncertainty. The total correction is computed as the sum of the four corrections for the parameter categories and the total systematic uncertainty is computed as the quadratic sum of the uncertainties for the four parameter categories. The result is given in Tab. 5.9. A small correction to the raw asymmetry at $\Delta(A_{RAW})$ = -0.001 is found, and a systematic uncertainty of ± 0.003 is applied. The value of the yield ratio should be corrected by $\Delta(r_Y)$ = +0.02 with a systematic uncertainty of ± 0.13.

the largest effect on both the raw asymmetry and the yield ratio comes from the *low mass background shape* parameter category.

The CP asymmetry in $B^0 \to K^{*0}e^+e^-$ decay is measured to be: -0.21 ± 0.19 [7]. Since

Table 5.9: Mean μ and width σ of the gaussian distributions obtained from the absolute and the relative variation of A_{RAW} and r_Y when varying fixed parameters. Corrections that have to be applied to A_{RAW} and r_Y are also shown.

	ΔA_{RAW}		$\Delta r_Y/r_Y$	
	μ_{gauss} ($\times 10^{-2}$)	σ_{gauss} ($\times 10^{-2}$)	μ_{gauss} ($\times 10^{-2}$)	σ_{gauss} ($\times 10^{-2}$)
Signal shape	-0.008 ± 0.002	0.070 ± 0.002	-0.012 ± 0.008	0.243 ± 0.007
Peaking Bkg shape	0.005 ± 0.001	0.015 ± 0.001	0.055 ± 0.016	0.461 ± 0.012
Low mass Bkg shape	-0.084 ± 0.012	0.323 ± 0.009	0.274 ± 0.030	0.897 ± 0.025
Relative cont.	0.009 ± 0.001	0.033 ± 0.001	0.264 ± 0.057	1.500 ± 0.047
	Correction and systematic uncert.			
	$\Delta(A_{RAW})$		$\Delta r_Y/r_Y$	
	-0.001 ± 0.003		+0.006 ± 0.018	

this value is compatible with zero, it is set to zero in the fit to the data. To estimate the impact on the measured raw asymmetry and yield ratio, a new fit is performed, including this CP asymmetry value in the fit. As expected, the value of r_Y is not modified while a non negligible variation of $\Delta A_{RAW} = +0.006$ is observed. This value is set as a systematical uncertainty.

5.3.4 Double misidentified $B^0 \to K^{*0}\gamma$ events

Another source of uncertainties which have already been mentioned in Sec. 4.3.1 is due to the estimation of double misidentified $B^0 \to K^{*0}\gamma$ background contamination, where the $K\pi$ pair in the final state is reconstructed as a πK. This background does not affect the measurement of the ratio of branching fractions, but has an important impact on the raw asymmetry measurement. Even with the PID selection designed to reduce this background and defined in Sec. 4.3.1, a fraction of double misidentified events still remains. Its relative contamination is estimated with simulation samples, reweighted using `PIDCalib`. The relative contamination to the signal is about 0.2%. Using Eq. 4.4, a systematic uncertainty of ± 0.004 is estimated and applied to the raw asymmetry measurement.

5.3.5 Data and simulation differences

As shown in Sec 5.2.1, some variables are not well described by simulation. In order to investigate the impact of these differences between collision and simulation data, the cuts applied to these variables are set to a lower and a higher (when possible) value. The initial and modified values are given in Tab. 5.10.

Efficiencies, expected fractions of events for each data acquisition time and relative contaminations from specific backgrounds are computed again. Then, the new signal shape is extracted from a fit to the simulation and used in the fit to the data. New raw

Table 5.10: Values of the cuts used to investigate the impact of the differences observed between data and *MC* for some variables. Resulting variation of the raw asymmetry and of the ratio of branching fractions are also given. The most important variations between the up and low variable cut's modification are indicated in bold.

variable	initial cut value DD	initial cut value LL	new cut value DD	new cut value LL	$\frac{\Delta(r_{\mathcal{B}})}{r_{\mathcal{B}}}$ (%)	$\Delta(A_{RAW})$ (%)
nTracks	< 500		< 450		**-0.03**	**-0.044**
$p_{\mathrm{T}}(h^-)$ (MeV/c)	> 500		> 550		**-0.65**	**0.311**
Conv. photon 2D-cut	< 20	< 17	< 10		-0.94	-0.085
			< 30	< 24	**1.21**	**0.178**
$CombDLL_e$	> -1.0		> -2.0		**1.75**	**-0.268**
			> 0.0		-0.56	-0.126
acos(B_DIRA) (rad)	—	< 0.008	—	< 0.007	0.01	0.131
			—	< 0.009	**0.26**	**0.148**
$\min(\log(e^{\pm}))$	—	> 0.55	—	> 0.05	-0.99	**-0.234**
			—	> 1.05	**-1.88**	0.114
Systematic uncertainties (%)					2.93	0.528

asymmetry and yield ratio are stored as well as the efficiency ratio (see Eq. 5.3), which is used to compute the ratio of branching fractions (see Eq. 4.15). For each cut value, the relative variation of the raw asymmetry and of the ratio of branching fractions are computed:

$$\Delta(A_{RAW}) = A_{RAW}^{(init)} - A_{RAW}^{(new)} \tag{5.7}$$

$$\Delta(r_{\mathcal{B}}) = \frac{r_Y^{(init)} r_\epsilon^{(init)} - r_Y^{(new)} r_\epsilon^{(new)}}{r_Y^{(init)} r_\epsilon^{(init)}} \tag{5.8}$$

The different cut values used to perform this study as well as the resulting raw asymmetry and the ratio of branching fractions variations are given in Tab 5.10. The resulting systematic uncertainties are computed as the quadratic sum of the largest variation for each variable. A relative uncertainty of $\pm$ 2.93 % is found for the ratio of branching fractions while an absolute uncertainty of $\pm$ 0.005 is found for the raw asymmetry.

5.3.6 Magnet polarity asymmetry

An instrumental bias which should be investigated is the possible asymmetry induced by the magnetic field that spreads out the opposite charge particles in different regions of the detector. Any non-uniformity of the detector performance introduces an effect on

Table 5.11: Raw asymmetry in $B^0 \to K^{*0}\gamma$ as a function of the magnet polarity. Fraction of luminosity for both polarities is also given.

	MagUp	MagDown	Average
A_{RAW}	0.031 ± 0.037	0.027 ± 0.034	0.029 ± 0.025
$f_{\mathcal{L}}$	0.469	0.531	1.

the asymmetry measurement. The polarity of the magnet is regularly flipped during the data taking in order to reduce this bias. The reference fit is repeated separately for each magnet polarity. Due to the low available statistics, in particular in the $B_s^0 \to \phi\gamma$ samples, and to reduce the number of degrees of freedom, the correction factors $(\sigma^{Data}/\sigma^{MC})_{DD(LL)}$ are fixed in these fits to the values given in Tab 5.2. The raw asymmetry measured for both magnet polarities as well as the corresponding fraction of integrated luminosity are given in Tab 5.11.

Both values are compatible within statistical errors and the luminosity-weighted average is compatible with the raw asymmetry measured on the full data sample (see Eq. 5.9 below). No evidence of an asymmetry is observed, but a systematic uncertainty is set to the raw asymmetry corresponding to the difference between asymmetries measured for both magnet polarities and asymmetry extracted from the reference fit to the data: $\Delta A_{RAW} = \pm 0.002$.

5.3.7 Systematic uncertainties summary

The systematic uncertainties and corrections to apply to the raw asymmetry and the ratio of branching fractions are summarised in Tab. 5.12. All uncertainties coming from the yield ratio r_Y have been translated to uncertainties on the ratio of branching fractions.

The measured raw asymmetry, including the systematic uncertainties, is:

$$A_{RAW} = 0.028 \pm 0.025(stat) \pm 0.009(syst) \tag{5.9}$$

5.4 Results

5.4.1 Measurement of the ratio of branching fractions

The ratio of branching fractions $r_{\mathcal{B}}$ is computed using Eq. 4.15. The value of the ratio of yields: $r_Y = \frac{Y_{B^0\to K^{*0}\gamma}}{Y_{B_s^0\to\phi\gamma}}$ is obtained as an output from the reference fit:

$$r_Y = 7.32 \pm 0.56(stat) \tag{5.10}$$

Table 5.12: Summary of the systematical uncertainties and correction to the raw asymmetry and the ratio of branching fractions.

source	$\Delta(A_{RAW})$		$\frac{\Delta(r_{\mathcal{B}})}{r_{\mathcal{B}}}$	
	correction	uncertainty	correction	uncertainty
year Fractions				$\pm$ 0.020
$f_{DD}(B_s^0)$				$\pm$ 0.004
L0 trigger				$\pm$ 0.025
fit parameters	-0.001	$\pm$ 0.003	+0.006	$\pm$ 0.018
$A_{CP}(B^0 \to K^{*0}e^+e^-)$		$\pm$ 0.006		
double Mis-ID		$\pm$ 0.004		
Data/MC difference		$\pm$ 0.005		$\pm$ 0.029
magnet polarity		$\pm$ 0.002		
total	-0.001	$\pm$ 0.009	+0.006	$\pm$ 0.047

The ratio of the branching fractions of the vector meson decays: $\frac{\mathcal{B}(\phi \to K^\pm K^\mp)}{\mathcal{B}(K^{*0} \to K^\pm \pi^\mp)}$ is computed using the branching fractions values from [7]:

$$\mathcal{B}(K^{*0} \to K^\pm \pi^\mp) = \frac{2}{3} \times \mathcal{B}(K^{*0} \to (K\pi)^0) = (66.503 \pm 0.014) \times 10^{-2} \tag{5.11}$$

$$\mathcal{B}(\phi \to K^\pm K^\mp) = (48.9 \pm 0.5) \times 10^{-2} \tag{5.12}$$

leading to:

$$\frac{\mathcal{B}(\phi \to K^\pm K^\mp)}{\mathcal{B}(K^{*0} \to K^\pm \pi^\mp)} = 0.735 \pm 0.008 \tag{5.13}$$

The ratio of the hadronisation fractions $\frac{f_s}{f_d}$ is taken from the combined LHCb measurement [83]:

$$\frac{f_s}{f_d} = 0.256 \pm 0.020 \tag{5.14}$$

Global efficiencies used in the ratio $r_\epsilon = \frac{\epsilon(B_s^0 \to \phi\gamma)}{\epsilon(B^0 \to K^{*0}\gamma)}$ have been computed in Sec. 4.5 and results are given in Eqs. 4.13 and 4.14:

$$\epsilon(B_s^0 \to \phi\gamma) = (0.164 \pm 0.003(stat)) \times 10^{-3}$$

$$\epsilon(B^0 \to K^{*0}\gamma) = (0.139 \pm 0.003(stat)) \times 10^{-3}$$

The efficiency ratio r_ϵ is hence:

$$r_\epsilon = \frac{\epsilon(B_s^0 \to \phi\gamma)}{\epsilon(B^0 \to K^{*0}\gamma)} = 1.176 \pm 0.033(stat) \tag{5.15}$$

Combining all these contributions as well as the correction and the systematical uncertainties given in Tab. 5.12, the measured ratio of branching fractions is:

$$r_\mathcal{B} = \frac{\mathcal{B}(B^0 \to K^{*0}\gamma)}{\mathcal{B}(B_s^0 \to \phi\gamma)} = 1.63 \pm 0.13(stat) \pm 0.08(syst) \pm 0.13(f_s/f_d) \tag{5.16}$$

where the statistical uncertainty contains the statistical uncertainty on the yield ratio r_Y given in Eq. 5.10 and the uncertainty on the efficiency ratio r_ϵ given in Eq. 5.15. The systematic uncertainty is made of the systematic uncertainty of the ratio of branching fractions of the vector mesons given in Eq. 5.13 and all the systematic uncertainties related to the ratio of branching fraction $r_\mathcal{B}$ given in Tab. 5.12. The uncertainty coming from the ratio of the hadronisation fractions f_s/f_d is separated from the other as it is a common source of uncertainty for all analyses performing this measurement. Therefore, it should not be included when comparing this result with similar analyses.

5.4.2 Measurement of the *CP* asymmetry of $B^0 \to K^{*0}\gamma$

Detection and production asymmetries

In order to obtain the value of the CP asymmetry in the $B^0 \to K^{*0}\gamma$ decay, the raw asymmetry extracted from the fit has to be corrected for asymmetries induced by the detector geometry, event reconstruction and final state particle strong interaction with the material of the detector. The CP asymmetry can be derived from the raw asymmetry using the following formula:

$$\mathcal{A}_{CP}(B^0 \to K^{*0}\gamma) = A_{RAW}(B^0 \to K^{*0}\gamma) - A_D(K\pi) - \kappa A_P(B^0), \tag{5.17}$$

where $A_D(K\pi)$ is the detection asymmetry, while $A_P(B^0)$ is the production asymmetry. κ is a correction term which represents the dilution factor due to neutral B meson oscillations.

The detection asymmetry is induced by the different quark content of the final state hadron inducing a different interaction rate with the detector material, depending upon the charge. It can be expressed in terms of two distinct contributions [84]:

$$A_D(K\pi) = A_I(K\pi) + \alpha(K\pi)A_R(K\pi), \tag{5.18}$$

where $A_I(K\pi)$ is an asymmetry due to the different strong interaction cross-sections with the detector material of the final state particles ($K^+\pi^-$ or $K^-\pi^+$) while $A_R(K\pi)$ represents the possible reconstruction and detection asymmeties. The factor $\alpha(K\pi)$ takes into account the yield asymmetry in data sets with opposite polarities. Following the LHCb prescription, the overall detection asymmetry has been estimated using a sample of charmless two-body decay of B_s^0 mesons [84]:

$$A_D(K\pi) = -0.010 \pm 0.002, \tag{5.19}$$

where the uncertainty is due to the limited statistics of the data sample.

The second correction that has to be applied to the raw asymmetry is the production asymmetry $A_P(B^0)$ of the B^0 meson. B^0 and $\overline{B}^0$ are not produced with the same rate in proton-proton collisions. The B^0 production asymmetry can be expressed in terms of the different production rates:

$$A_P(B^0) = \frac{R(\overline{B}^0) - R(B^0)}{R(\overline{B}^0) + R(B^0)} \tag{5.20}$$

The values of $A_P(B^0)$ for both 2011 and 2012 samples have been measured using a sample of $B^0 \to J/\psi\, K^{*0}$ decays [85] and found to be:

$$A_P(B^0)(\sqrt(s) = 7\,\text{TeV}) = (0.20 \pm 0.88(stat) \pm 0.11(syst))\% \tag{5.21}$$

$$A_P(B^0)(\sqrt(s) = 8\,\text{TeV}) = (-1.49 \pm 0.55(stat) \pm 0.12(syst))\% \tag{5.22}$$

Using the fraction of integrated luminosity for 2011 and 2012 given in Tab.4.1, the luminosity-weighted average value of the production asymmetry of the B^0 meson is found to be:

$$A_P(B^0) = -0.009 \pm 0.007 \tag{5.23}$$

The dilution factor κ is a correction induced by the neutral B meson oscillation which dilutes the impact of the production asymmetry of the B^0 meson. κ is defined as [84]:

$$\kappa = \frac{\int cos(\Delta_{m_d} t) e^{-\Gamma_d t} \epsilon(t) dt}{\int cosh(\frac{\Delta_{\Gamma_d} t}{2}) e^{-\Gamma_d t} \epsilon(t) dt}, \tag{5.24}$$

where $\epsilon(t)$ is the proper time acceptance function of the selected signal. Γ_t is the B^0 decay width while Δ_{Γ_d} and Δ_{m_d} are, respectively, the decay width and the mass difference between the light and heavy B^0 mass eigenstates. The values of Γ_t and Δ_{Γ_d} are taken from [86] while the value used for Δ_{m_d} is taken from [7].

In order to derive the proper time acceptance function $\epsilon(t)$ from the data, the distribution of the B^0 lifetimes in the pure signal sample derived using the `sPLOT` method (See Sec. 5.2.1) is fitted using the following function:

$$f(t) = n_{B^0} \times e^{-\Gamma_d t} \otimes G(0, \sigma) \times \frac{(at)^c}{1. + (at)^c}, \tag{5.25}$$

where n_{B^0} is a normalisation factor and $G(0, \mu)$ is a Gaussian function centered at 0 and with a resolution, σ, which correspond to the proper-time resolution. This parameter

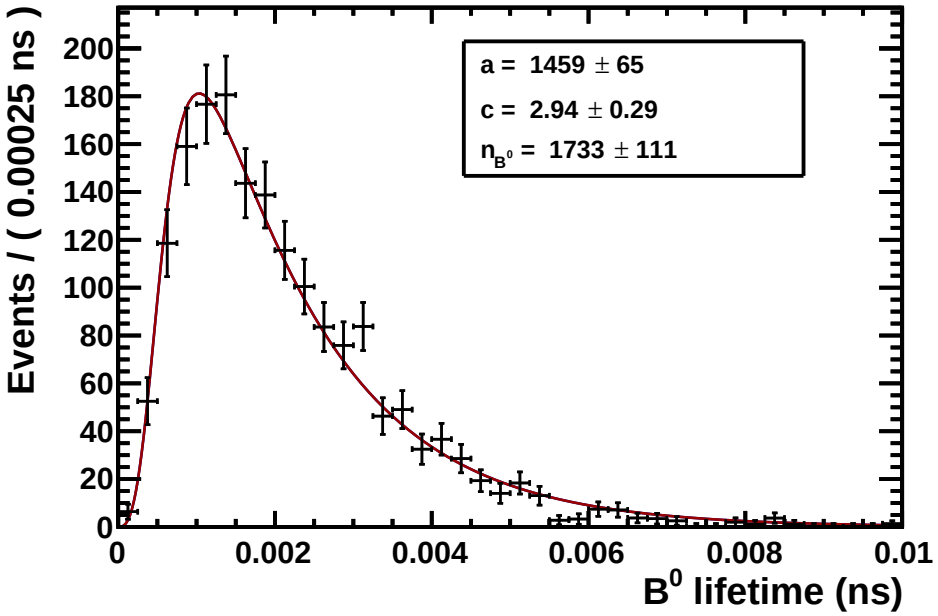

Figure 5.22: Fit of the proper-time acceptance function of signal events.

is let free in the fit and initialised with the expected proper-time resolution: 40 fs. a and c are free parameters governing the proper time acceptance of the selection. The result of the fit is shown in Fig. 5.22.

Using the proper time acceptance function $\epsilon(t)$ extracted from the fit and Eq.5.24, the value of the dilution factor is found to be: $\kappa = 0.374 \pm 0.028$.

Result

Starting from the raw asymmetry value given in Eq. 5.9 and applying all the corrections, summarised in Tab. 5.13, the direct CP asymmetry in the $B^0 \to K^{*0}\gamma$ decay is measured to be:

$$\mathcal{A}_{CP}(B^0 \to K^{*0}\gamma) = 0.041 \pm 0.025(stat) \pm 0.012(syst) \tag{5.26}$$

5.5 Limit on the branching fraction of the $B_s^0 \to K^{*0}\gamma$ decay

5.5.1 The CL_S method

Since no clear signal of $B_s^0 \to K^{*0}\gamma$ decay is observed in data, an upper limit on the branching fraction of this decay is extracted using a statistical method, the CL_s method [87] [88]. Now the signal is the $B_s^0 \to K^{*0}\gamma$ decay, which is modeled using

Table 5.13: Corrections to the raw asymmetry measured in the $B^0 \to K^{*0}\gamma$ decay and corresponding corrections and systematic uncertainties.

Asymmetry		correction	uncertainty
Detection	$-A_D(K\pi)$	$+0.010$	$\pm$ 0.002
B^0 production	$-\kappa A_P(B^0)$	$+0.003$	$\pm$ 0.003
Total		$+0.013$	$\pm$ 0.004

the same shape as used for $B^0 \to K^{*0}\gamma$ decay with a shift in mass from m_{B^0} to $m_{B_s^0}$ ($m_{B_s^0} - m_{B^0} = 87.33 \pm 0.23\,\text{MeV}$ [7]). The background shape is the same as for $B^0 \to K^{*0}\gamma$ including this one as a background. It is necessary to define two hypotheses, the background only hypothesis, which is the reference (or null) hypothesis, referred to as H_0, and the signal plus background hypothesis, referred to as $H_{\mathcal{B}}$ where a signal contribution corresponding to the $B_s^0 \to K^{*0}\gamma$ branching fraction value $\mathcal{B}_H$ being tested is added.

A statistic test $q_{\mathcal{B}}$ is used to test the hypothesis H_0 against the hypothesis $H_{\mathcal{B}}$. The definition of $q_{\mathcal{B}}$ is described in the Ref. [89], it is the ratio of likelihoods given the $\mathcal{B}_H$ hypothesis value and the best fit value:

$$q_{\mathcal{B}} = \begin{cases} -2\ ln\ \frac{\mathcal{L}(data|\mathcal{B}_H, \hat{\theta}_{\mathcal{B}_H})}{\mathcal{L}(data|0, \hat{\theta}_0)} & \hat{\mathcal{B}} < 0 \\ -2\ ln\ \frac{\mathcal{L}(data|\mathcal{B}_H, \hat{\theta}_{\mathcal{B}_H})}{\mathcal{L}(data|\hat{\mathcal{B}}, \hat{\theta}_{\hat{\mathcal{B}}})} & 0 \leq \hat{\mathcal{B}} \leq \mathcal{B}_H \\ 0 & \hat{\mathcal{B}} > \mathcal{B}_H \end{cases} \tag{5.27}$$

where, $\hat{\mathcal{B}}$ is the best fit branching fraction and $\hat{\theta}_{\mathcal{B}}$, $\hat{\theta}_{\hat{\mathcal{B}}}$ and $\hat{\theta}_0$ represent the nuisance parameters at their best fit values given the hypothesis branching fraction value $\mathcal{B}_H$ or the best fit value $\hat{\mathcal{B}}$ or the case where $\mathcal{B}_H = 0$. The best fit from which is extracted the $\hat{\mathcal{B}}$ value corresponds to a fit where the value of $\mathcal{B}$ is left free to float. The nuisance parameters considered here are the values used to transform the ratio of yields defined as $\frac{N(B_s^0 \to K^{*0}\gamma)}{N(B^0 \to K^{*0}\gamma)}$ to the branching fraction of the $B_s^0 \to K^{*0}\gamma$ decay and all the parameters which are expected to have a non negligible impact to $\mathcal{B}$ ($B_s^0 \to K^{*0}\gamma$) as the parameters which described the shape of the signal and the main peaking backgrounds ($B^0 \to K^{*0}e^+e^-$, $\Lambda_b^0 \to \Lambda^*\gamma$). These parameters are added in the fit with Gaussian constraints, the mean of the Gaussian corresponding to the value of the parameter and the width corresponding to the associated uncertainty. Therefore, uncertainties associated to these parameters are included in the output likelihood value of the fit.

Since the goal is to extract an upper limit, a constraint is set on the statistic test by requiring $q_{\mathcal{B}} = 0$ when $\hat{\mathcal{B}}$ is greater than $\mathcal{B}_H$, as explained in [89]. Moreover, as a branching fraction is a positive (or null) value, the best fit branching fraction value $\hat{\mathcal{B}}$ is replaced by setting $\mathcal{B} = 0$ if it is found that $\hat{\mathcal{B}} < 0$. Then, a fit is performed with the hypothesis of a null branching fraction and the result of the fit is used to compute the $q_{\mathcal{B}}$ value.

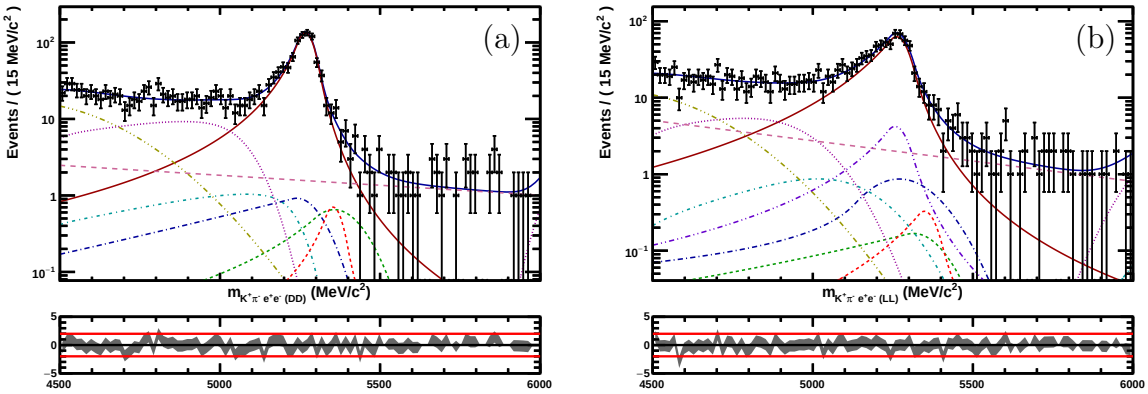

Figure 5.23: Result of the fit to the data with the $B_s^0 \to K^{*0}\gamma$ branching fraction left free. The distribution (a) corresponds to the DD sample whereas the distribution (b) corresponds to the LL sample. Black points correspond to data, the full blue line is the fit result. Background contributions are $B^0 \to K^{*0}\gamma$ decay (full red line), combinatorial (dotted magenta), $\Lambda_b^0 \to \Lambda^*\gamma$ (dashed green), $B \to K^{*0}\pi\gamma$ (dashed dotted cyan), $B^0 \to K^{*0}\eta$ (long-dashed dotted blue), $B^0 \to K\pi\pi^0$ (dashed three-dotted yellow), $B^0 \to K^{*0}\pi^0 X$ (long-dashed pink) and $B \to Ve^+e^-$ only for the LL track type (long-dashed two-dotted violet).The $B_s^0 \to K^{*0}\gamma$ contribution is the red dotted line and the fitted value is: $\mathcal{B}(B_s^0 \to K^{*0}\gamma) = (0.9 \pm 2.4) \times 10^{-6}$.

To extract the upper limit value on the $B_s^0 \to K^{*0}\gamma$ branching fraction, the CL_s method is used. This method is fully described in Refs. [87] and [88], while a practical example can be found in the chapter 6 of Ref. [90]. The CL_s method consists in computing two probabilities based on the distribution of the statistic test results of two hypotheses:

$$CL_b = \int_{q_{\mathcal{B}}^{obs}}^{\infty} f(q_{\mathcal{B}}|\mathcal{B}=0)dq_{\mathcal{B}}$$
$$CL_{s+b} = \int_{q_{\mathcal{B}}^{obs}}^{\infty} f(q_{\mathcal{B}}|\mathcal{B}=\mathcal{B}_H)dq_{\mathcal{B}} \quad (5.28)$$

where, $f(q_{\mathcal{B}}|\mathcal{B})$ is the distribution of the statistic test for the hypothesis with value $\mathcal{B}$ and $q_{\mathcal{B}}^{obs}$ is the observed value of the statistic test in data. The result of the fit to the data with the free $B_s^0 \to K^{*0}\gamma$ branching fraction is shown in Fig. 5.23. The fitted value is: $\mathcal{B}(B_s^0 \to K^{*0}\gamma) = (0.9 \pm 2.4) \times 10^{-6}$. These p-values are referred to as: CL_b for the one corresponding to the background hypothesis H_0 and CL_{s+b} for the one corresponding to the signal plus background hypothesis $H_{\mathcal{B}}$. Therefore, it is possible to build a third p-value: $CL_s = \frac{CL_{s+b}}{CL_b}$, where $(1 - CL_s)$ corresponds to the exclusion power of the limit $\mathcal{B}(B_s^0 \to K^{*0}\gamma) < \mathcal{B}_H$.

The common method used to produce the distribution of the statistic test results for the two hypotheses is to generate pseudo-data under each hypothesis. Therefore,

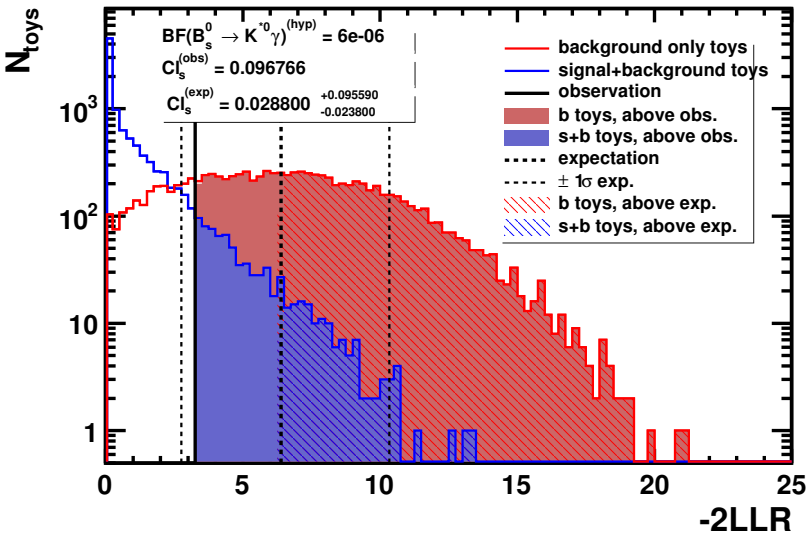

Figure 5.24: The statistic test distribution for an hypothetic $B_s^0 \to K^{*0}\gamma$ branching fraction of 6×10^{-6}.

background only pseudo-data are generated from the fit to the observed reconstructed B invariant mass distribution in the $K^{*0}\gamma$ sample. The B^0 and $\overline{B}^0$ samples are merged into a common sample. Two samples are used, corresponding to DD and LL $K^{*0}\gamma$ data. Some parameters, which are left free in the reference fit (see Tab. 5.2), are now fixed to the values resultinthe from the reference fit, in order to reduce the number of degrees of freedom: the sigma ratios used to correct the resolution values coming from simulation in both DD and LL samples as well as the ratios between the number of combinatorial events and the number of low mass background events in both DD and LL samples. A parameter corresponding to the branching fraction of the $B_s^0 \to K^{*0}\gamma$ decay is added and the nuisance parameters are included with Gaussian constraints. Then, the result of this fit to the data is used to generate pseudo-data samples. The number of generated events is left free to vary following a Poissonian distribution in order to avoid any bias introduced by a fixed number of events in the generated samples as explained in Ref. [91].

As an illustration of the CL_s method, the distribution of the statistic test for background and signal plus background models and the corresponding p-values are displayed in Fig. 5.24. The hypothesis branching fraction value is set to 6×10^{-5}. The observed $q_{\mathcal{B}}$ value is also shown as the full black line. The obtained CL_s value is about 0.10, which means that branching fractions values above 6×10^{-6} are excluded at the 90 % confidence level.

In addition to the observed limit, the expected limit can be computed by replacing the $q_{\mathcal{B}}^{obs}$ value by the median value of the background hypothesis $q_{\mathcal{B}}$ distribution.

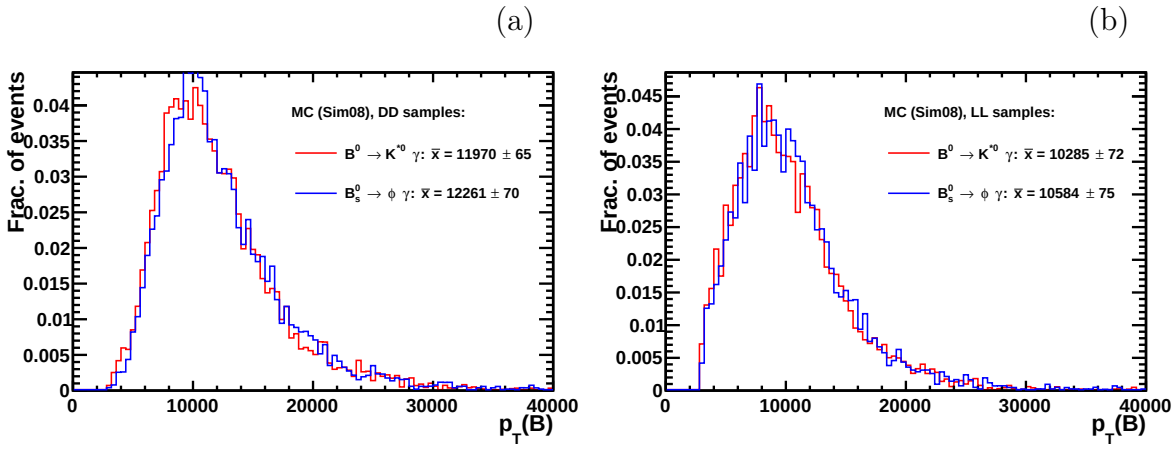

Figure 5.25: Transverse momentum distribution of the B-mesons for the *DD* (a) and *LL* (b) samples.

5.5.2 Result

The nuisance parameters are the ratio of hadronisation factors $\frac{f_s}{f_d}$, the ratio of efficiencies $\frac{\epsilon(B_s^0 \to K^{*0}\gamma)}{\epsilon(B^0 \to K^{*0}\gamma)}$, the branching fraction of the $B^0 \to K^{*0}\gamma$ decay, the parameters of the shape of the signal and the parameters of the shape and the amplitude of the main peaking backgrounds: $B^0 \to K^{*0}e^+e^-$, $\Lambda_b^0 \to \Lambda^*\gamma$. The branching fraction of the $B^0 \to K^{*0}\gamma$ decay and the associated uncertainty are taken from Ref. [7]:

$$\mathcal{B}(B^0 \to K^{*0}\gamma) = (4.33 \pm 0.15) \times 10^{-5} \tag{5.29}$$

The value of the hadronisation fraction is the one given in Eq. 5.14. The ratio of $B_s^0 \to K^{*0}\gamma$ and $B^0 \to K^{*0}\gamma$ efficiencies is set to one as efficiencies of both decay are expected to be close to each other. The only difference may come from the difference in mass of B^0 and B_s^0 which can impact the kinematic variables of the photon and the K^{*0}. As the reconstruction efficiency of the photon varies much more than the one of the K^{*0}, the largest impact is expected to come from the photon efficiency. The efficiency of the reconstruction and selection of the converted photons varies linearly with the transverse momentum of the photon, as shown in Ref. [37]. Therefore, *MC* samples of $B^0 \to K^{*0}\gamma$ and $B_s^0 \to \phi\gamma$ are used to compare the transverse momentum distribution of the B mesons. These distributions are displayed in Fig. 5.25. A difference of about 2.5 % is observed between the mean of the transverse momentum of the B^0 and the B_s^0. In the relevant p_{T} range, this difference corresponds to a variation of about 2.5% in efficiency for both *DD* and *LL* categories. Therefore, an uncertainty of ±2.5% is set on the ratio of efficiencies to reconstruct the $B_s^0 \to K^{*0}\gamma$ and the $B^0 \to K^{*0}\gamma$ decays.

Five different branching fraction hypotheses have been tested with this method. This allows the construction of the curves (observation and expectation) shown in Fig. 5.26. The upper limits at 90% and 95% of confidence level can be extracted from these curves

for both observation and expectation cases. The observed upper limit is:

$$\begin{aligned} \mathcal{B}(B_s^0 \to K^{*0}\gamma) &< 6.0 \times 10^{-6} \; at \; 90\% \; CL \\ \mathcal{B}(B_s^0 \to K^{*0}\gamma) &< 7.3 \times 10^{-6} \; at \; 95\% \; CL \end{aligned} \tag{5.30}$$

while, the expected SM value is:

$$\mathcal{B}_{th}(B_s^0 \to K^{*0}\gamma) \cong \mathcal{B}(B^0 \to K^{*0}\gamma) \times \left|\frac{V_{td}}{V_{ts}}\right|^2 = (2.0 \pm 0.7) \times 10^{-6}, \tag{5.31}$$

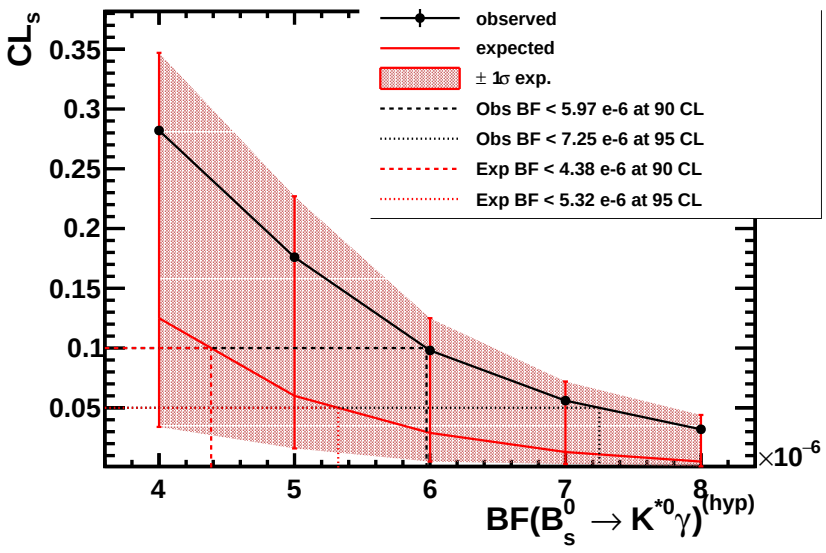

Figure 5.26: The CL_s result for the different $\mathcal{B}(B_s^0 \to K^{*0}\gamma)$ hypotheses tested. The upper limits set on this branching fraction at 90 % and 95 % of confidence level are also given.

Chapter 6

Conclusion and outlook

The work presented in this thesis is one of the first analyses on radiative decays of B mesons using converted photons. The results of this analysis are competitive with measurements performed with calorimetric photons despite the lower statistic. The use of converted photons improves the B mass resolution by a factor 2 to 3. Converted photon reconstruction uses information from both tracking and calorimeter systems and takes advantage of the good resolution of the trackers, $\Delta p/p \approx 0.6$ %, with respect to the energy resolution of the calorimeters, $\sigma_E/E \approx 9\%/\sqrt{E} \oplus 0.8\%$ for the ECAL.

The analysis presented in this thesis has focused on $B^0 \to K^{*0}\gamma$ and $B_s^0 \to \phi\gamma$ decays. The CP asymmetry in the $B^0 \to K^{*0}\gamma$ decay, $\mathcal{A}_{CP}(B^0 \to K^{*0}\gamma)$, and the ratio of the $B^0 \to K^{*0}\gamma$ and $B_s^0 \to \phi\gamma$ branching fractions, $\frac{\mathcal{B}(B^0 \to K^{*0}\gamma)}{\mathcal{B}(B_s^0 \to \phi\gamma)}$, have been measured. The measured value of $\mathcal{A}_{CP}(B^0 \to K^{*0}\gamma)$ is:

$$\boxed{\mathcal{A}_{CP}(B^0 \to K^{*0}\gamma)^{(exp.)} = 0.041 \pm 0.025(stat) \pm 0.012(syst)} \tag{6.1}$$

This value can be compared to the world average measurement including LHCb and Belle results:

$$\mathcal{A}_{CP}(B^0 \to K^{*0}\gamma)^{(ave.)} = -0.002 \pm 0.015 \tag{6.2}$$

and with the prediction [34]:

$$\mathcal{A}_{CP}(B^0 \to K^{*0}\gamma)^{(th.)} = -(6.1 \pm 4.6) \times 10^{-3}. \tag{6.3}$$

Including both experimental and theoretical uncertainties, the CP asymmetry in the $B^0 \to K^{*0}\gamma$ decay is found to be compatible within 2 standard deviations (σ) with the theoretical prediction. This measurement is also compatible within 1.5 σ with the current world average.

The ratio of branching fractions measured in this analysis is:

$$\boxed{\left(\frac{\mathcal{B}(B^0\to K^{*0}\gamma)}{\mathcal{B}(B_s^0\to\phi\gamma)}\right)^{(exp.)} = 1.63\pm0.13(stat)\pm0.08(syst)\pm0.13(f_s/f_d)} \tag{6.4}$$

This value is compatible within 2.5 σ with the best current measurement provided by LHCb [29]:

$$\left(\frac{\mathcal{B}(B^0\to K^{*0}\gamma)}{\mathcal{B}(B_s^0\to\phi\gamma)}\right)^{(prev.LHCb)} = 1.23\pm0.06(stat)\pm0.04(syst)\pm0.10(f_s/f_d) \tag{6.5}$$

where the uncertainties related to f_s/f_d are fully correlated between the two measurements. The ratio of branching fractions measured in this analysis is also compatible within 2.5 σ with the theoretical prediction [26]:

$$\left(\frac{\mathcal{B}(B^0\to K^{*0}\gamma)}{\mathcal{B}(B_s^0\to\phi\gamma)}\right)^{(th.)} = 1.0\pm0.2 \tag{6.6}$$

In addition, and using the better reconstructed B^0 mass resolution, a limit is set on the branching fraction of the unseen $B_s^0\to K^{*0}\gamma$ decay. This is not possible for analyses using calorimetric photons as the B mass resolution ($\sim 90\,\mathrm{MeV}/c^2$) is too large to separate the $B_s^0\to K^{*0}\gamma$ signal from the $B^0\to K^{*0}\gamma$ decay. Using the CL_s method, the observed limit is:

$$\boxed{\begin{array}{l}\mathcal{B}(B_s^0\to K^{*0}\gamma) < 6.0\times10^{-6}\ at\ 90\%\ CL\\ \\ \mathcal{B}(B_s^0\to K^{*0}\gamma) < 7.3\times10^{-6}\ at\ 95\%\ CL\end{array}} \tag{6.7}$$

while the expected value is: $\mathcal{B}(B_s^0\to K^{*0}\gamma) = 2.0\times10^{-6}$ (see Sec. 2.2.3).

The next step of this analysis is to use the data recorded by LHCb at $\sqrt{s} = 13$ TeV. Since the LHC restart in 2015, LHCb has an integrated luminosity of about 2 fb^{-1}. Thanks to the higher energy, the $b\bar{b}$ production rate is higher than for the previous runs at $\sqrt{s} = 7$ TeV and $\sqrt{s} = 8$ TeV. LHCb has measured the $b\bar{b}$ production cross-section in the acceptance of the detector at $\sqrt{s} = 13$ TeV [92]:

$$\sigma(pp\to b\bar{b}X)(13\,\mathrm{TeV}) \approx 165\,\mu\mathrm{b} \tag{6.8}$$

This value is more than twice higher than what was measured at $\sqrt{s} = 7$ TeV [53]:

$$\sigma(pp\to b\bar{b}X)(7\,\mathrm{TeV}) = (75.3\pm5.4\pm13.0)\,\mu\mathrm{b} \tag{6.9}$$

Therefore, the 2 fb^{-1} of data collected since 2015 correspond to approximately 2500 $B^0\to K^{*0}\gamma$ events and 350 $B_s^0\to\phi\gamma$ events with converted photons (assuming the

reconstruction and selection efficiencies are the same that what is estimated in this analysis). Including these data will reduce the statistic uncertainty by a factor 1.5. Moreover, more statistics shall allow to perform the first observation of the $B_s^0 \to K^{*0}\gamma$ decay and the measurement of its branching ratio.

With more statistic, it is possible to reduce the systematic uncertainties. Due to the low available statistic, the background model is very simple in the $B_s^0 \to \phi\gamma$ case and can be improved. This will be possible in the near future, using events recorded by LHCb since the end of *2015*. A more precise $B_s^0 \to \phi\gamma$ background description should lead to a better measurement of the ratio of branching fractions.

Moreover, it is necessary to produce more simulated events of specific background decays in order to improve the background model and to reduce the related systematical uncertainties. In particular, decays contributing to the low mass backgrouds in the $B^0 \to K^{*0}\gamma$ case, $B \to K^{*0}\pi^0 X$, with enough events to perform the reconstruction of the converted photon or the $B^+ \to \phi K^+\gamma$ decay for the $B_s^0 \to \phi\gamma$ case.

The observed differences between *2011* and *2012* stripping and L0-trigger selection efficiencies have been considered as systematic uncertainties and are not fully understood. Simulated samples of $B^0 \to K^{*0}\gamma$ and $B_s^0 \to \phi\gamma$ events before the stripping is applied can be used to understand the difference in the stripping efficiencies. The energy threshold value of the L0-trigger lines used in simulation has been briefly investigated and seems to be different than what is found in data. More precise study of this effect can also be performed to reduce the associated systematic uncertainties.

Some sources of uncertainties are very difficult to reduce, as the systematical uncertainties from the double misidentified events in $B^0 \to K^{*0}\gamma$, or are dependent on other analyses, as the measurement of the CP asymmetry in the $B^0 \to K^{*0}e^+e^-$ decay which is the most important source of uncertainty on the raw asymmetry in the $B^0 \to K^{*0}\gamma$ decay. Using the LHCb data to perform a more precise measurement of this observable should reduce the systematical uncertainties on the CP asymmetry in the $B^0 \to K^{*0}\gamma$ decay. Whatever, improvements of the results of this analysis are possible in the near future, in particular using the data collected by LHCb since the restart of the LHC.

In this thesis, the use of the converted photon in the radiative decays $B^0 \to K^{*0}\gamma$, $B_s^0 \to \phi\gamma$ and $B_s^0 \to K^{*0}\gamma$ study has been investigated and found to provide good results. This method can therefore be applied on all other radiative decays analysis as a complement to the analyses using calorimetric photons. As events with converted photons have not been considered in previous analyses, using them can increase the available statistic and therefore, improve the measurements of the different observables accessible with radiative decays.

Bibliography

[1] T. Nakano and K. Nishijima, *Charge Independence for V-particles*, Progress of Theoretical Physics **10** (1953) 581.

[2] M. Gell-Mann, *The interpretation of the new particles as displaced charge multiplets*, Il Nuovo Cimento (1955-1965) **4** (1956), no. 2 848.

[3] P. W. Higgs, *Spontaneous Symmetry Breakdown without Massless Bosons*, Phys. Rev. **145** (1966) 1156.

[4] J. Schwinger, *The theory of quantized fields. i*, Phys. Rev. **82** (1951) 914.

[5] G. Luders, *On the Equivalence of Invariance under Time Reversal and under Particle-Antiparticle Conjugation for Relativistic Field Theories*, Kong. Dan. Vid. Sel. Mat. Fys. Med. **28N5** (1954) 1.

[6] W. Pauli and L. F. Curtiss, *Niels Bohr and the Development of Physics*, Am. J. Phys. **24** (1956) 292.

[7] Particle Data Group, K. A. Olive *et al.*, *Review of particle physics*, Chin. Phys. **C38** (2014) 090001, and 2015 update.

[8] T. D. Lee and C. N. Yang, *Question of parity conservation in weak interactions*, Physical Review (U. S.) Superseded in part by Phys. Rev. A, Phys. Rev. B: Solid State, Phys. Rev. C, and Phys. Rev. D **Vol: 104** (1956) .

[9] C. S. Wu *et al.*, *Experimental Test of Parity Conservation in Beta Decay*, Phys. Rev. **105** (1957) 1413.

[10] M. Goldhaber, L. Grodzins, and A. W. Sunyar, *Helicity of neutrinos*, Physical Review (U. S.) Superseded in part by Phys. Rev. A, Phys. Rev. B: Solid State, Phys. Rev. C, and Phys. Rev. D **Vol: 109** (1958) .

[11] J. H. Christenson, J. W. Cronin, V. L. Fitch, and R. Turlay, *Evidence for the 2pi decay of the ksub2sup0 meson*, Phys. Rev. Letters **Vol: 13** (1964) .

[12] N. Cabibbo, *Unitary symmetry and leptonic decays*, Phys. Rev. Lett. **10** (1963) 531.

[13] M. Kobayashi and T. Maskawa, *CP Violation in the Renormalizable Theory of Weak Interaction*, Prog. Theor. Phys. **49** (1973) 652.

[14] J. J. Aubert *et al.*, *Experimental observation of a heavy particle j*, Phys. Rev. Lett. **33** (1974) 1404.

[15] M. L. Perl *et al.*, *Evidence for anomalous lepton production in $e^+ - e^-$ annihilation*, Phys. Rev. Lett. **35** (1975) 1489.

[16] S. W. Herb *et al.*, *Observation of a dimuon resonance at 9.5 gev in 400-gev proton-nucleus collisions*, Phys. Rev. Lett. **39** (1977) 252.

[17] CDF, F. Abe *et al.*, *Observation of top quark production in $\bar{p}p$ collisions*, Phys. Rev. Lett. **74** (1995) 2626, arXiv:hep-ex/9503002.

[18] D0, S. Abachi *et al.*, *Search for high mass top quark production in $p\bar{p}$ collisions at $\sqrt{s} = 1.8$ TeV*, Phys. Rev. Lett. **74** (1995) 2422, arXiv:hep-ex/9411001.

[19] CKMfitter Group, J. Charles *et al.*Eur. Phys. J. **C41** (2005) arXiv:hep-ph/0406184.

[20] T. De, *Particle Physics, A Primer*, Levant Books, Kolkata, India, 2011.

[21] LHCb, R. Aaij *et al.*, *Angular analysis of the $B^0 \to K^{*0}e^+e^-$ decay in the low-q^2 region*, JHEP **04** (2015) 064, arXiv:1501.03038.

[22] LHCb, R. Aaij *et al.*, *Angular analysis of the $B^0 \to K^{*0}\mu^+\mu^-$ decay using 3 fb^{-1} of integrated luminosity*, JHEP **02** (2016) 104, arXiv:1512.04442.

[23] LHCb, CMS, V. Khachatryan *et al.*, *Observation of the rare $B_s^0 \to \mu^+\mu^-$ decay from the combined analysis of CMS and LHCb data*, Nature **522** (2015) 68, arXiv:1411.4413.

[24] A. J. Buras, R. Fleischer, J. Girrbach, and R. Knegjens, *Probing New Physics with the $B_s^0 \to \mu^+\mu^-$ Time-Dependent Rate*, JHEP **07** (2013) 77, arXiv:1303.3820.

[25] S. Descotes-Genon, D. Ghosh, J. Matias, and M. Ramon, *Exploring New Physics in the C7-C7' plane*, JHEP **06** (2011) 099, arXiv:1104.3342.

[26] A. Ali, B. D. Pecjak, and C. Greub, *$B \to V\gamma$ Decays at NNLO in SCET*, Eur. Phys. J. **C55** (2008) 577, arXiv:0709.4422.

[27] CLEO collaboration, R. Ammar *et al.*, *Evidence for penguin-diagram decays: First observation of $B \to K^*(892)\gamma$*, Phys. Rev. Lett. **71** (1993) 674.

[28] Belle, J. Wicht *et al.*, *Observation of $B_s^0 \to \phi\gamma$ and Search for $B_s^0 \to \gamma\gamma$ Decays at Belle*, Phys. Rev. Lett. **100** (2008) 121801, arXiv:0712.2659.

[29] LHCb, R. Aaij *et al.*, *Measurement of the ratio of branching fractions $\mathcal{B}(B^0 \to K^{*0}\gamma)/BR(B_s^0 \to \phi\gamma)$ and the direct CP asymmetry in $B^0 \to K^{*0}\gamma$*, Nucl. Phys. **B867** (2013) 1, arXiv:1209.0313.

[30] CLEO, T. E. Coan *et al.*, *Study of exclusive radiative B meson decays*, Phys. Rev. Lett. **84** (2000) 5283, arXiv:hep-ex/9912057.

[31] Belle, M. Nakao *et al.*, *Measurement of the $B \to K^*$ gamma branching fractions and asymmetries*, Phys. Rev. **D69** (2004) 112001, arXiv:hep-ex/0402042.

[32] Belle, D. Dutta *et al.*, *Search for $B_s^0 \to \gamma\gamma$ and a measurement of the branching fraction for $B_s^0 \to \phi\gamma$*, Phys. Rev. **D91** (2015), no. 1 011101, arXiv:1411.7771.

[33] BaBar, B. Aubert *et al.*, *Measurement of Branching Fractions and CP and Isospin Asymmetries in $B \to K^*(892)$gamma Decays*, Phys. Rev. Lett. **103** (2009) 211802, arXiv:0906.2177.

[34] Y. Y. Keum, M. Matsumori, and A. I. Sanda, *CP asymmetry, branching ratios and isospin breaking effects of $B \to K^*$ gamma with perturbative QCD approach*, Phys. Rev. **D72** (2005) 014013, arXiv:hep-ph/0406055.

[35] LHCb, R. Aaij *et al.*, *Measurement of the $\chi_b(3P)$ mass and of the relative rate of $\chi_{b1}(1P)$ and $\chi_{b2}(1P)$ production*, JHEP **10** (2014) 88, arXiv:1409.1408.

[36] M. Kenzie and P. Owen, *Search for the decay $B_s^0 \to J/\psi\gamma$*, .

[37] E. Tournefier, *Converted photons: selection, efficiency and angular distribution studies*, LHCb-INT-2015-040.

[38] LHCb, R. Aaij *et al.*, *Observation of Photon Polarization in the $b \to s\gamma$ Transition*, Phys. Rev. Lett. **112** (2014), no. 16 161801, arXiv:1402.6852.

[39] LHCb, R. Aaij *et al.*, *First experimental study of photon polarization in radiative B_s^0 decays*, arXiv:1609.02032.

[40] Y. Grossman and D. Pirjol, *Extracting and using photon polarization information in radiative B decays*, JHEP **06** (2000) 029, arXiv:hep-ph/0005069.

[41] F. Bishara and D. J. Robinson, *Probing the photon polarization in $B \to K^*\gamma$ with conversion*, JHEP **09** (2015) 013, arXiv:1505.00376.

[42] M. Borsato, M.-H. Schune, and N. Arnaud, *Study of the $B^0 \to K^{*0}e^+e^-$ decay with the LHCb detector and development of a novel concept of PID detector: the Focusing DIRC*, PhD thesis, Paris U., IV, 2015, Presented 08 Sep 2015.

[43] A. Paul and D. M. Straub, *Constraints on new physics from radiative B decays*, arXiv:1608.02556.

[44] L. Evans and P. Bryant, *LHC Machine*, Journal of Instrumentation **3** (2008), no. 08 S08001.

[45] ATLAS, G. Aad *et al.*, *The ATLAS Experiment at the CERN Large Hadron Collider*, Journal of Instrumentation **3** (2008), no. 08 S08003.

[46] CMS, S. Chatrchyan *et al.*, *The CMS experiment at the CERN LHC*, Journal of Instrumentation **3** (2008), no. 08 S08004.

[47] LHCb, A. Augusto-Alves-Jr *et al.*, *The LHCb Detector at the LHC*, Journal of Instrumentation **3** (2008), no. 08 S08005.

[48] ALICE, K. Aamodt *et al.*, *The ALICE experiment at the CERN LHC*, Journal of Instrumentation **3** (2008), no. 08 S08002.

[49] ATLAS, G. Aad *et al.*, *Observation of a new particle in the search for the Standard Model Higgs boson with the ATLAS detector at the LHC*, Phys. Lett. **B716** (2012) 1, arXiv:1207.7214.

[50] CMS, S. Chatrchyan *et al.*, *Observation of a new boson at a mass of 125 GeV with the CMS experiment at the LHC*, Phys. Lett. **B716** (2012) 30, arXiv:1207.7235.

[51] LHCb, B. Adeva *et al.*, *Roadmap for selected key measurements of LHCb*, arXiv:0912.4179.

[52] E. Maurice, O. Leroy, and R. Le Gac, *Mesure de la violation de CP dans les désintégrations $B_s^0 \to J/\psi\phi$, auprès du détecteur LHCb*, PhD thesis, Aix-Marseille U., Jun, 2012, Presented 18 Jul 2012.

[53] LHCb, R. Aaij *et al.*, *Measurement of $\sigma(pp \to b\bar{b}X)$ at $\sqrt{s} = 7$ TeV in the forward region*, Phys. Lett. **B694** (2010) 209, arXiv:1009.2731.

[54] LHCb, R. Aaij *et al.*, *Measurement of the CKM angle γ from a combination of $B^\pm \to Dh^\pm$ analyses*, Phys. Lett. **B726** (2013) 151, arXiv:1305.2050.

[55] LHCb, R. Aaij *et al.*, *Measurement of the CP-violating phase ϕ_s in $\overline{B}_s^0 \to J/\psi\pi^+\pi^-$ decays*, Phys. Lett. **B736** (2014) 186, arXiv:1405.4140.

[56] LHCb, R. Aaij *et al.*, *Precision measurement of CP violation in $B_s^0 \to J/\psi K^+K^-$ decays*, Phys. Rev. Lett. **114** (2015), no. 4 041801, arXiv:1411.3104.

[57] LHCb, R. Aaij *et al.*, *Observation of $D^0 - \overline{D}^0$ oscillations*, Phys. Rev. Lett. **110** (2013), no. 10 101802, arXiv:1211.1230.

[58] LHCb, R. Aaij *et al.*, *First Evidence for the Decay $B_s^0 \to \mu^+\mu^-$*, Phys. Rev. Lett. **110** (2013), no. 2 021801, arXiv:1211.2674.

[59] LHCb, R. Aaij *et al.*, *Measurement of the $B^0_s \to \mu^+\mu^-$ branching fraction and search for $B^0 \to \mu^+\mu^-$ decays at the LHCb experiment*, Phys. Rev. Lett. **111** (2013) 101805, arXiv:1307.5024.

[60] R. Aaij *et al.*, *Performance of the LHCb Vertex Locator*, JINST **9** (2014) 09007, arXiv:1405.7808.

[61] LHCb Collaboration, P. R. Barbosa-Marinho *et al.*, *LHCb VELO (VErtex LOcator): Technical Design Report*, Technical Design Report LHCb, CERN, Geneva, 2001.

[62] LHCb Collaboration, P. R. Barbosa-Marinho *et al.*, *LHCb inner tracker: Technical Design Report*, Technical Design Report LHCb, CERN, Geneva, 2002. revised version number 1 submitted on 2002-11-13 14:14:34.

[63] LHCb Collaboration, P. R. Barbosa-Marinho *et al.*, *LHCb outer tracker: Technical Design Report*, Technical Design Report LHCb, CERN, Geneva, 2001.

[64] J. Prisciandaro, F. Blanc, and T. Nakada, *Improved magnetic field map with 2011 measurements for the LHCb dipole magnet*, Tech. Rep. LHCb-INT-2012-012. CERN-LHCb-INT-2012-012, CERN, Geneva, Mar, 2012.

[65] LHCb RICH Group, M. Adinolfi *et al.*, *Performance of the LHCb RICH detector at the LHC*, Eur. Phys. J. **C73** (2013) 2431, arXiv:1211.6759.

[66] S. Monteil, *Mesures de précision électrofaibles*, accreditation to supervise research, Université Blaise Pascal - Clermont-Ferrand II, Dec., 2009, HDR 280.

[67] LHCb Collaboration, S. Amato *et al.*, *LHCb calorimeters: Technical Design Report*, Technical Design Report LHCb, CERN, Geneva, 2000.

[68] LHCb, P. Perret, *First Years of Running for the LHCb Calorimeter System*, PoS **TIPP2014** (2014) 030, arXiv:1407.4289.

[69] LHCb, R. Aaij *et al.*, *Measurement of the ratio of branching fractions $BR(B_0 \to K^{\star 0}\gamma)/BR(B_{s0} \to \phi\gamma)$ and the direct CP asymmetry in $B_0 \to K^{\star 0}\gamma$*, Nucl. Phys. **B867** (2013) 1, arXiv:1209.0313.

[70] LHCb, R. Aaij *et al.*, *Measurement of the CP-violating phase ϕ_s in the decay $B^0_s \to J/\psi\phi$*, Phys. Rev. Lett. **108** (2012) 101803, arXiv:1112.3183.

[71] V. V. Gligorov, C. Thomas, and M. Williams, *The HLT inclusive B triggers*, Tech. Rep. LHCb-PUB-2011-016. CERN-LHCb-PUB-2011-016. LHCb-INT-2011-030, CERN, Geneva, Sep, 2011. LHCb-INT-2011-030.

[72] LHCb collaboration, R. Aaij *et al.*, *LHCb Detector Performance*, Int. J. Mod. Phys. A **30** (2014) 1530022. 82 p.

[73] C. Burr *et al.*, *Prompt charm production in pp collisions at* $\sqrt{s} = 13\,\text{TeV}$ *in 2015 data*, .

[74] Y. K. Hsiao, P. Y. Lin, L. W. Luo, and C. Q. Geng, *Fragmentation fractions of two-body b-baryon decays*, Phys. Lett. **B751** (2015) 127, arXiv:1510.01808.

[75] T. Sjöstrand *et al.*, *An Introduction to PYTHIA 8.2*, Comput. Phys. Commun. **191** (2015) 159, arXiv:1410.3012.

[76] L. Collaboration, *Ibackgroundcategory class reference*, http://lhcb-release-area.web.cern.ch/.

[77] M. Williams *et al.*, *The HLT2 Topological Lines*, Tech. Rep. LHCb-PUB-2011-002. CERN-LHCb-PUB-2011-002, CERN, Geneva, Jan, 2011.

[78] A. Puig, *The HLT2 Radiative Topological Lines*, Tech. Rep. LHCb-PUB-2012-002. CERN-LHCb-PUB-2012-002, CERN, Geneva, Feb, 2012.

[79] A. Hocker *et al.*, *TMVA - Toolkit for Multivariate Data Analysis*, PoS **ACAT** (2007) 040, arXiv:physics/0703039.

[80] LHCb, R. Aaij *et al.*, *Measurement of the* $B^0 \to K^{*0}e^+e^-$ *branching fraction at low dilepton mass*, JHEP **05** (2013) 159, arXiv:1304.3035.

[81] T. Skwarnicki, *A study of the radiative CASCADE transitions between the Upsilon-Prime and Upsilon resonances*, PhD thesis, Cracow, INP, 1986.

[82] M. Pivk and F. R. Le Diberder, *SPlot: A Statistical tool to unfold data distributions*, Nucl. Instrum. Meth. **A555** (2005) 356, arXiv:physics/0402083.

[83] LHCb, R. Aaij *et al.*, *Measurement of the fragmentation fraction ratio* f_s/f_d *and its dependence on B meson kinematics*, JHEP **04** (2013) 001, arXiv:1301.5286.

[84] LHCb, R. Aaij *et al.*, *First evidence of direct CP violation in charmless two-body decays of* B_s^0 *mesons*, Phys. Rev. Lett. **108** (2012) 201601, arXiv:1202.6251.

[85] A. Carbone, F. Ferrari, S. Perazzini, and V. Vagnoni, *Measurement of* B^0, B_s^0, B^+ *and* Λ_b^0 *production asymmetries in 7 TeV and 8 TeV pp collisions* , .

[86] LHCb, R. Aaij *et al.*, *Measurements of the* B^+, B^0, B_s^0 *meson and* Λ_b^0 *baryon lifetimes*, JHEP **04** (2014) 114, arXiv:1402.2554.

[87] T. Junk, *Confidence level computation for combining searches with small statistics*, Nucl. Instrum. Meth. **A434** (1999) 435, arXiv:hep-ex/9902006.

[88] A. L. Read, *Presentation of search results: the cl s technique*, Journal of Physics G: Nuclear and Particle Physics **28** (2002), no. 10 2693.

[89] G. Cowan, K. Cranmer, E. Gross, and O. Vitells, *Asymptotic formulae for likelihood-based tests of new physics*, Eur. Phys. J. **C71** (2011) 1554, arXiv:1007.1727, [Erratum: Eur. Phys. J.C73,2501(2013)].

[90] M. Kenzie and P. Dauncey, *Properties of the Higgs-like state around 125 GeV in its decay into two photons at the CMS experiment*, PhD thesis, Imperial Coll., London, Apr, 2014, Presented 09 05 2014.

[91] T. M. Karbach and M. Schlupp, *Constraints on Yield Parameters in Extended Maximum Likelihood Fits*, arXiv:1210.7141.

[92] M. Artuso, *b-hadron production at lhcb*, in *International Conference On High Energy Physics, Chicago*, 2016.

Appendix A

Correlation tables from reference fit

Table A.1: Correlation coefficients (%) of free parameters of the reference fit. First part.

fit parameters	A_{RAW}	r_Y	$N(B^0 \to K^{*0}\gamma)$	$N(B^0)_{DD}/N(B^0)$	$N(B^0_s)_{DD}/N(B^0_s)$	$\mu(B^0)_{DD}$ (MeV/c^2)	$\mu_{DD} - \mu_{LL}$ (MeV/c^2)	$\mu_{B^0} - \mu_{B^0_s}$ (MeV/c^2)
A_{RAW}	100							
r_y	0.1	100						
$N(B^0 \to K^{*0}\gamma)$	1.5	31.5	100					
$N(B^0)_{DD}/N(B^0)$	-0.3	-1.4	-12.7	100				
$N(B^0_s)_{DD}/N(B^0_s)$	0.1	2.6	-2.7	5	100			
$\mu(B^0)_{DD}$ (MeV/c^2)	-1.9	-1.1	-14.9	1.6	0.6	100		
$\mu_{DD} - \mu_{LL}$ (MeV/c^2)	0.1	0	-3.6	6.1	1.9	-14.4	100	
$\mu_{B^0} - \mu_{B^0_s}$ (MeV/c^2)	-0	-0	0	-0	0.1	-1.5	-0.1	100
$(\sigma^{Data}/\sigma^{MC})_{DD}$	4.2	0.4	21.3	11.9	5.6	-35.9	4.6	-0.2
$(\sigma^{Data}/\sigma^{MC})_{LL}$	1.6	-1.3	32	-32.4	-12.3	-20.4	-12.8	-0
$(N(K\pi\pi\gamma)/N(B^0 \to K^{*0}\gamma))_{DD}$	-4	-9.1	-35.2	-26.7	-2.6	23	-3	-0
$(N(K\pi\pi\gamma)/N(B^0 \to K^{*0}\gamma))_{LL}$	-3.2	-6.2	-31.9	24.4	1.5	20.3	5.5	-0
$N(B \to K^{*0}\pi^0 X)^{(K^{*0}\gamma)}_{DD}$	12.2	2.1	15.1	9.8	2.5	-18	2.3	-0
$N(B \to K^{*0}\pi^0 X)^{(K^{*0}\gamma)}_{LL}$	2.5	3.1	22	-12	-0.4	-17.4	-2	-0
$N(B \to K^{*0}\pi^0 X)^{(\bar{K}^{*0}\gamma)}_{DD}$	-6.3	2.1	13.9	9.3	2.2	-16.3	2.1	-0
$N(B \to K^{*0}\pi^0 X)^{(\bar{K}^{*0}\gamma)}_{LL}$	2.8	3.3	21.7	-14.2	-1	-15.1	-2.5	-0
$N(comb)^{(K^{*0}\gamma)}_{DD}$	15.3	-3.2	-12	-9.9	-1.1	3.5	-0.4	0.1
$N(comb)^{(K^{*0}\gamma)}_{LL}$	18.9	-4.7	-23.1	25.2	3.5	4.3	2.4	0
$N(comb)^{(\bar{K}^{*0}\gamma)}_{DD}$	-14.8	-3.4	-12.5	-10	-1	3.5	-0.4	0.1
$N(comb)^{(\bar{K}^{*0}\gamma)}_{LL}$	-18.1	-4.9	-23.6	27.1	4	3.2	2.7	0
$N(comb)^{(\phi\gamma)}_{DD}$	-0.5	16.6	-2.3	-1.3	-18.8	3.2	-0.4	-0.1
$N(comb)^{(\phi\gamma)}_{LL}$	-0.3	25.9	-7	7	28.9	4.4	2.8	0
$c^{comb(\phi\gamma)}_{DD}$	-0.2	9.9	-1.2	-0.8	-11.1	0.5	-0	-0.2
$c^{comb(\phi\gamma)}_{LL}$	-0.1	14.7	-3.1	3.3	16.2	0.8	0.4	-0.2

Table A.2: Correlation coefficients (%) of free parameters of the reference fit. Second part.

fit parameters	$(\sigma^{Data}/\sigma^{MC})_{DD}$	$(\sigma^{Data}/\sigma^{MC})_{LL}$	$(N(K\pi\pi\gamma)/N(B^0\to K^{*0}\gamma))_{DD}$	$(N(K\pi\pi\gamma)/N(B^0\to K^{*0}\gamma))_{LL}$	$N(B\to K^{*0}\pi^0X)^{(K^{*0}\gamma)}_{DD}$	$N(B\to K^{*0}\pi^0X)^{(K^{*0}\gamma)}_{LL}$	$N(B\to K^{*0}\pi^0X)^{(\bar{K}^{*0}\gamma)}_{DD}$	$N(B\to K^{*0}\pi^0X)^{(\bar{K}^{*0}\gamma)}_{LL}$
$(\sigma^{Data}/\sigma^{MC})_{DD}$	100							
$(\sigma^{Data}/\sigma^{MC})_{LL}$	9.6	100						
$(N(K\pi\pi\gamma)/N(B^0\to K^{*0}\gamma))_{DD}$	-49.7	-5.8	100					
$(N(K\pi\pi\gamma)/N(B^0\to K^{*0}\gamma))_{LL}$	-31.8	-28.5	16.4	100				
$N(B\to K^{*0}\pi^0X)^{(K^{*0}\gamma)}_{DD}$	45.4	4.8	-61.9	-14.8	100			
$N(B\to K^{*0}\pi^0X)^{(K^{*0}\gamma)}_{LL}$	35.5	21.9	-18	-59.2	16.3	100		
$N(B\to K^{*0}\pi^0X)^{(\bar{K}^{*0}\gamma)}_{DD}$	40.4	4.1	-60.8	-12.9	40.3	14.3	100	
$N(B\to K^{*0}\pi^0X)^{(\bar{K}^{*0}\gamma)}_{LL}$	28.5	23.1	-14.5	-57.7	13.2	36.5	11.5	100
$N(comb)^{(K^{*0}\gamma)}_{DD}$	-17.8	-1	-2.6	5.1	-22.6	-6	0	-4.7
$N(comb)^{(K^{*0}\gamma)}_{LL}$	-3.2	-28.5	1.4	-11.9	0.4	-34.7	-2.9	3.7
$N(comb)^{(\bar{K}^{*0}\gamma)}_{DD}$	-17.2	-1.3	-0.6	5.5	-2.1	-6.1	-22.2	-5
$N(comb)^{(\bar{K}^{*0}\gamma)}_{LL}$	0.6	-30.4	0.2	-11.3	-1.6	4.4	1.6	-37
$N(comb)^{(\phi\gamma)}_{DD}$	-10.9	-0.9	5.4	3.4	-4.9	-3.8	-4.4	-3.1
$N(comb)^{(\phi\gamma)}_{LL}$	-2.1	-21.6	1.3	6.2	-1	-4.8	-0.9	-5
$c^{comb(\phi\gamma)}_{DD}$	-6	-0.3	2.9	1.7	-2.7	-2	-2.4	-1.6
$c^{comb(\phi\gamma)}_{LL}$	-0.5	-9.9	0.3	2.6	-0.3	-2	-0.2	-2.2

Table A.3: Correlation coefficients (%) of free parameters of the reference fit. Third part.

fit parameters	$N(comb)^{(K^{*0}\gamma)}_{DD}$	$N(comb)^{(K^{*0}\gamma)}_{LL}$	$N(comb)^{(\overline{K}^{*0}\gamma)}_{DD}$	$N(comb)^{(\overline{K}^{*0}\gamma)}_{LL}$	$N(comb)^{(\phi\gamma)}_{DD}$	$N(comb)^{(\phi\gamma)}_{LL}$	$c^{comb\ (\phi\gamma)}_{DD}$	$c^{comb\ (\phi\gamma)}_{LL}$
$N(comb)^{(K^{*0}\gamma)}_{DD}$	100							
$N(comb)^{(K^{*0}\gamma)}_{LL}$	3.5	100						
$N(comb)^{(\overline{K}^{*0}\gamma)}_{DD}$	6	-2.2	100					
$N(comb)^{(\overline{K}^{*0}\gamma)}_{LL}$	-3.1	19	2.3	100				
$N(comb)^{(\phi\gamma)}_{DD}$	2	0.3	1.9	-0.1	100			
$N(comb)^{(\phi\gamma)}_{LL}$	0.2	6.2	0.3	6.6	0.2	100		
$c^{comb(\phi\gamma)}_{DD}$	1.1	0.1	1.1	-0.1	17.8	0.1	100	
$c^{comb(\phi\gamma)}_{LL}$	0.1	2.9	0.1	3.1	0	27.3	0	100

Appendix B

Selection variable comparison

- $B^0 \to K^{*0}\gamma$ decay in the *DD* track type configuration: Figs. B.1 B.2 B.3.

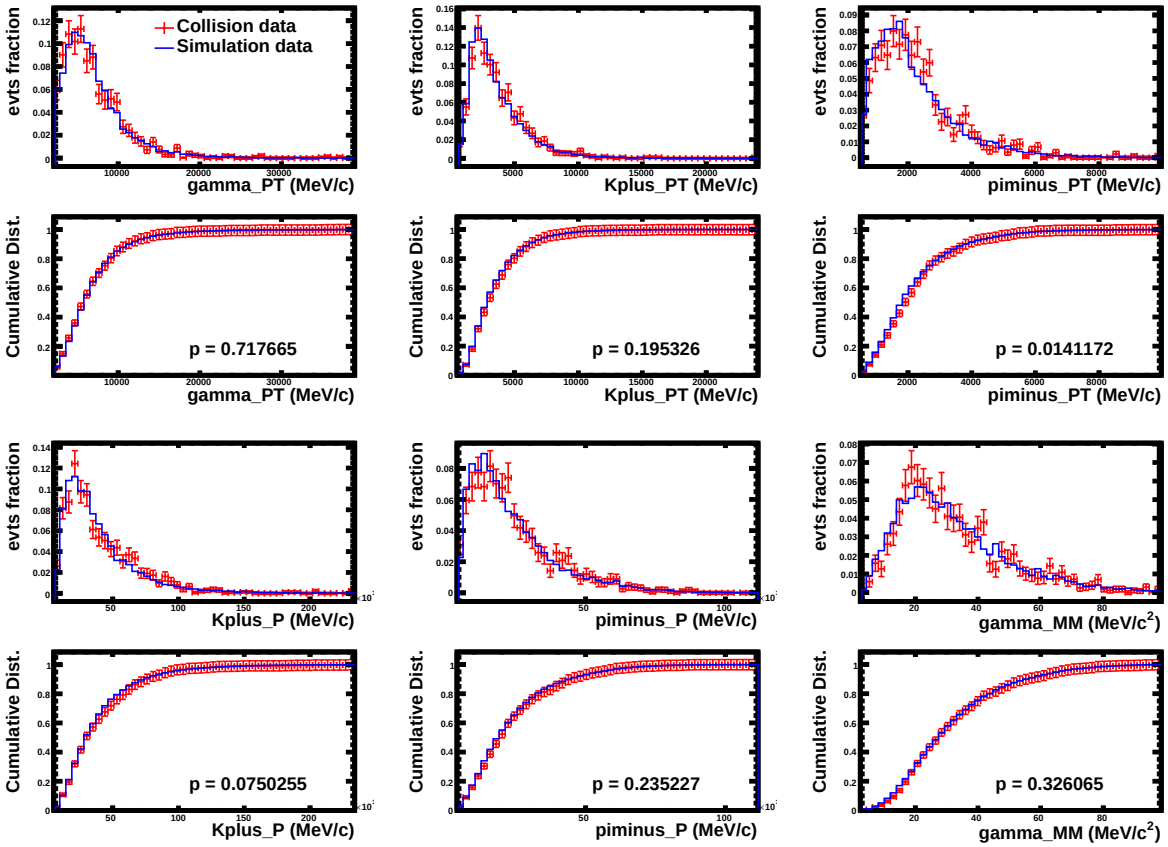

Figure B.1: Normalized and cumulative distributions of variables (1) used in the selection process for $B^0 \to K^{*0}\gamma$ in the *DD* track type configuration simulation sample (full blue line) and weighted data (red histogram). Kolmogorov-Smirnov test result are given.

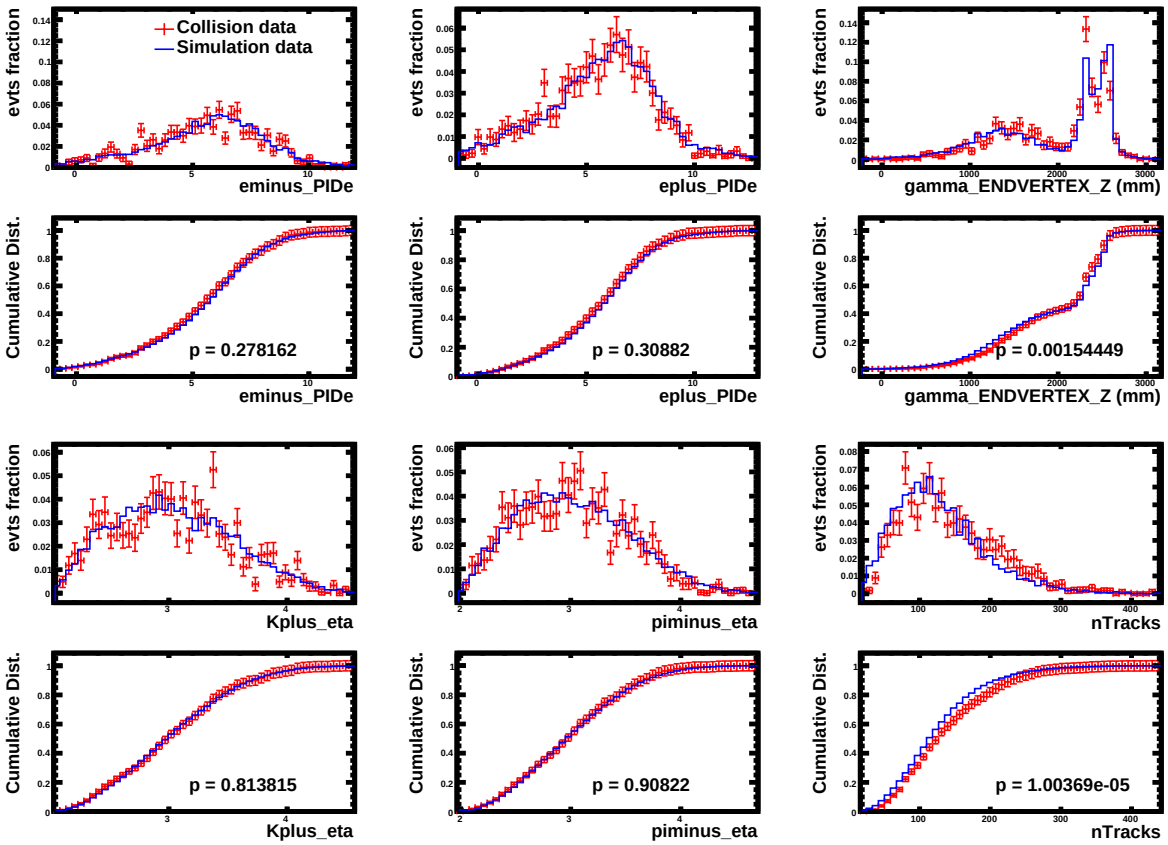

Figure B.2: Normalized and cumulative distributions of variables (2) used in the selection process for $B^0 \to K^{*0}\gamma$ in the *DD* track type configuration simulation sample (full blue line) and weighted data (red histogram). Kolmogorov-Smirnov test result are given.

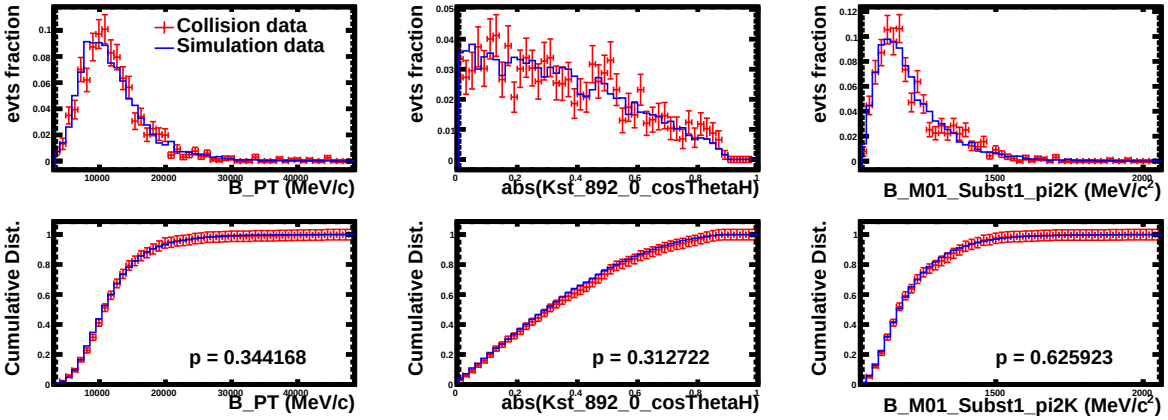

Figure B.3: Normalized and cumulative distributions of variables (3) used in the selection process for $B^0 \to K^{*0}\gamma$ in the *DD* track type configuration simulation sample (full blue line) and weighted data (red histogram). Kolmogorov-Smirnov test result are given.

- $B^0 \to K^{*0}\gamma$ decay in the LL track type configuration: Figs. B.4 B.5 B.6.

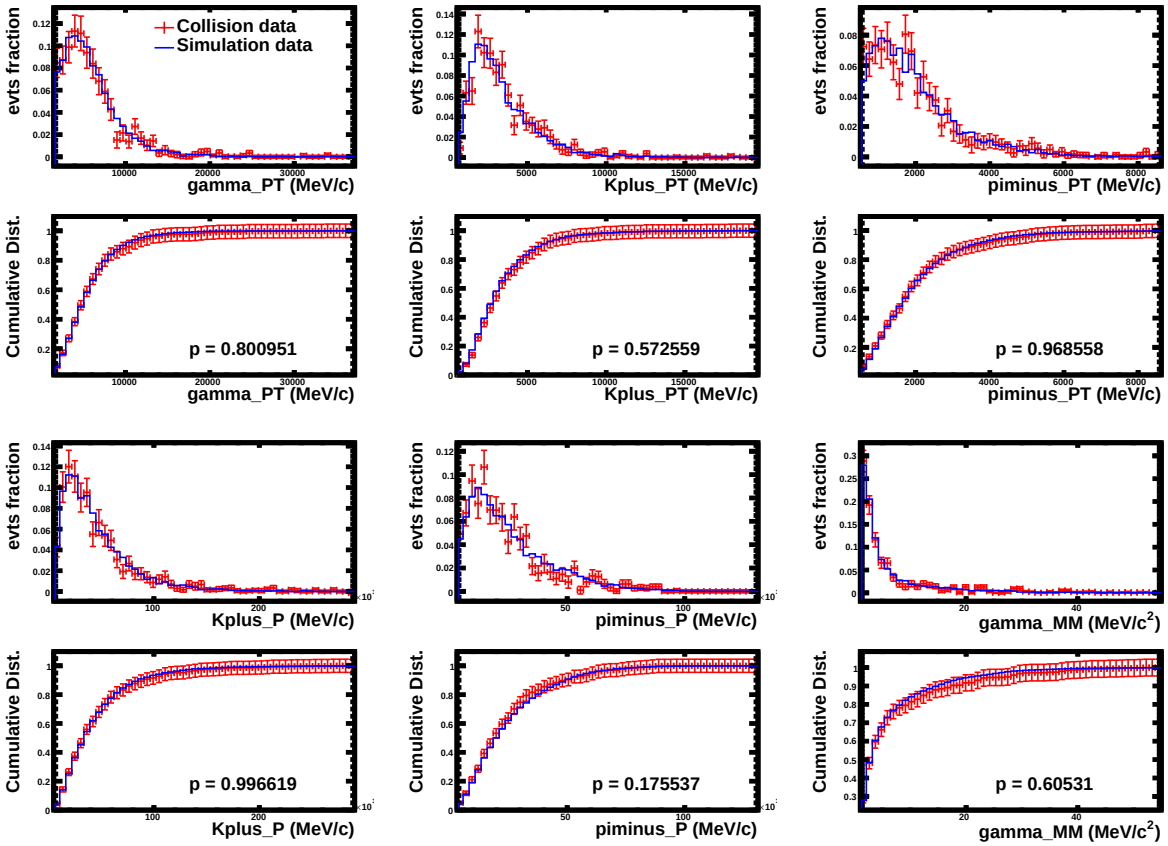

Figure B.4: Normalized and cumulative distributions of variables (1) used in the selection process for $B^0 \to K^{*0}\gamma$ in the LL track type configuration simulation sample (full blue line) and weighted data (red histogram). Kolmogorov-Smirnov test result are given.

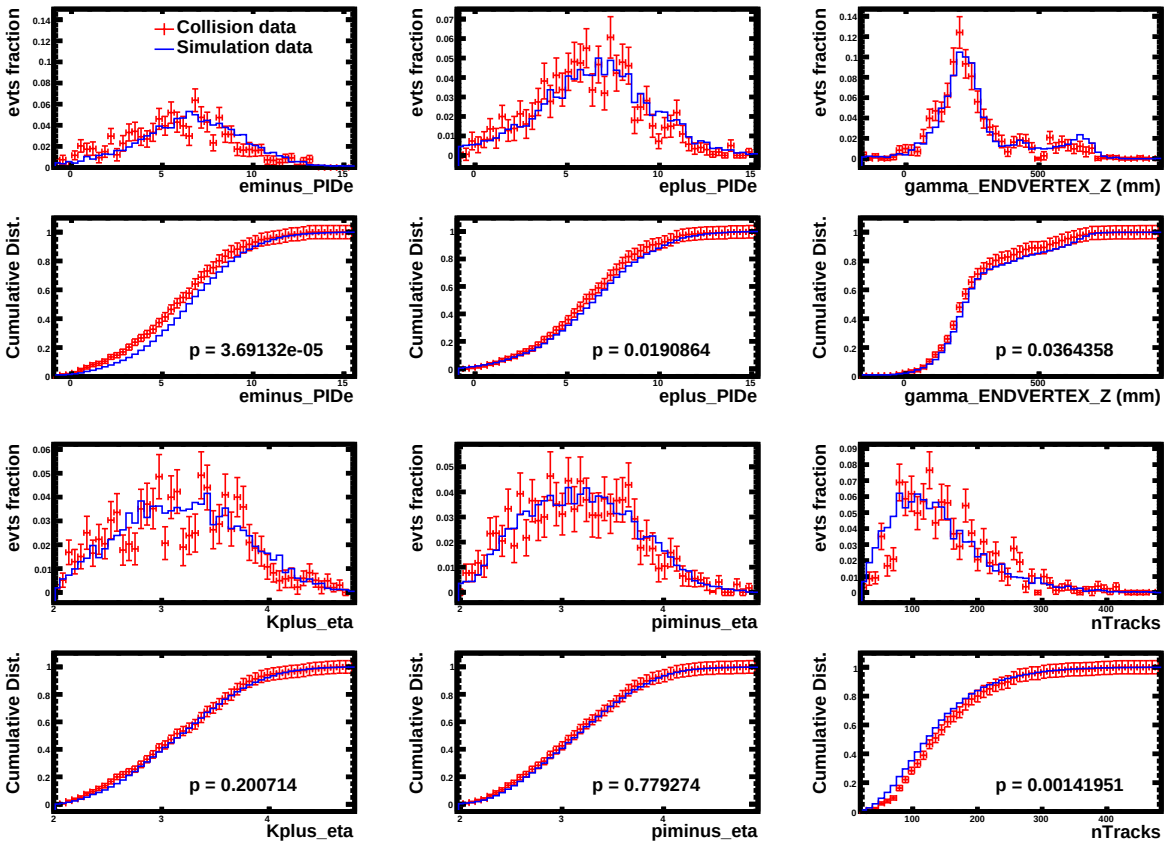

Figure B.5: Normalized and cumulative distributions of variables (2) used in the selection process for $B^0 \to K^{*0}\gamma$ in the LL track type configuration simulation sample (full blue line) and weighted data (red histogram). Kolmogorov-Smirnov test result are given.

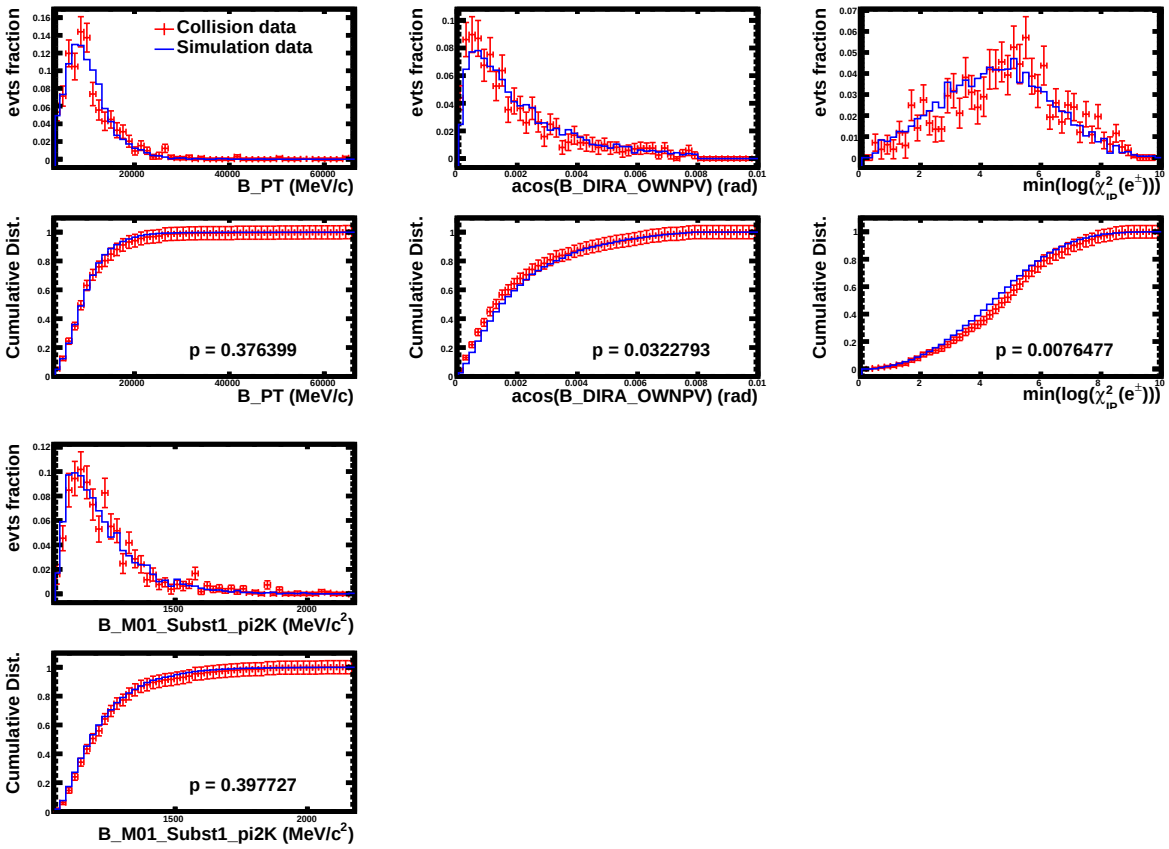

Figure B.6: Normalized and cumulative distributions of variables (3) used in the selection process for $B^0 \to K^{*0}\gamma$ in the LL track type configuration simulation sample (full blue line) and weighted data (red histogram). Kolmogorov-Smirnov test result are given.

- $B_s^0 \to \phi\gamma$ decay in the DD track type configuration: Figs. B.7 B.8 B.9.

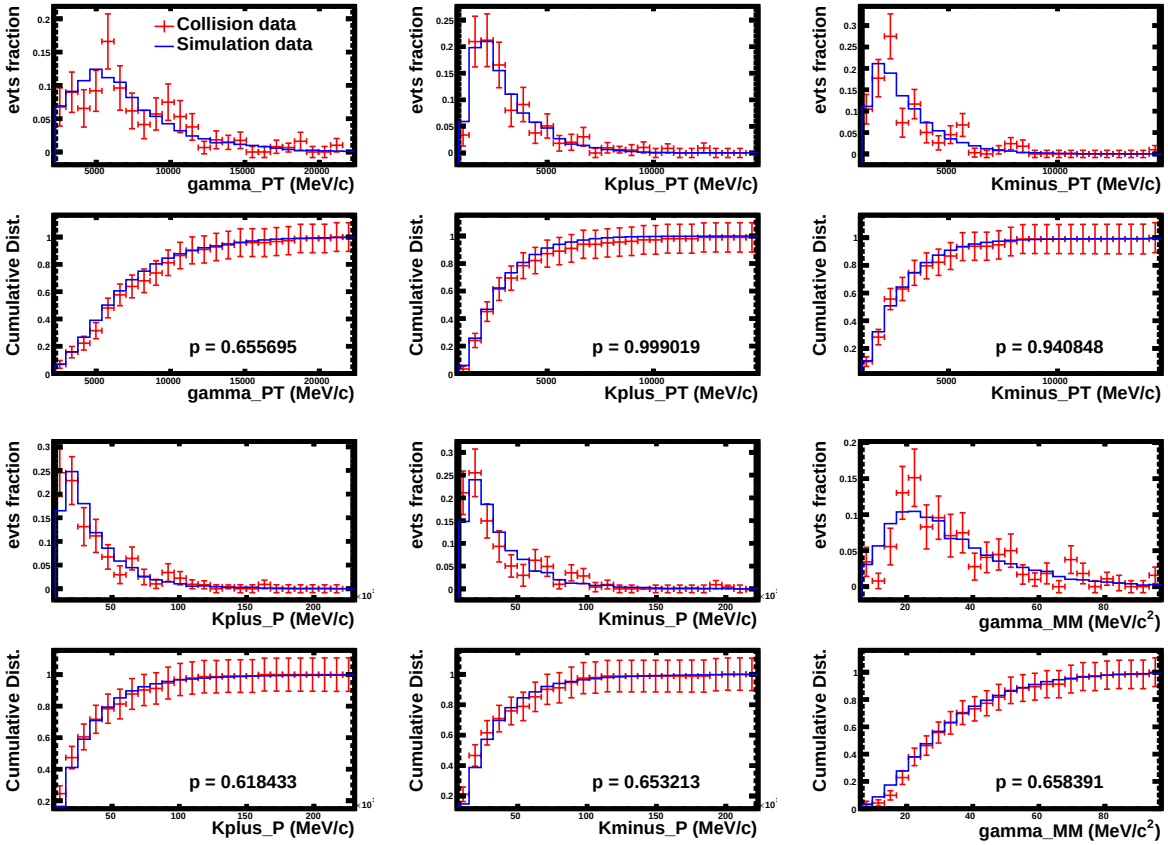

Figure B.7: Normalized and cumulative distributions of variables (1) used in the selection process for $B_s^0 \to \phi\gamma$ in the DD track type configuration simulation sample (full blue line) and weighted data (red histogram). Kolmogorov-Smirnov test result are given.

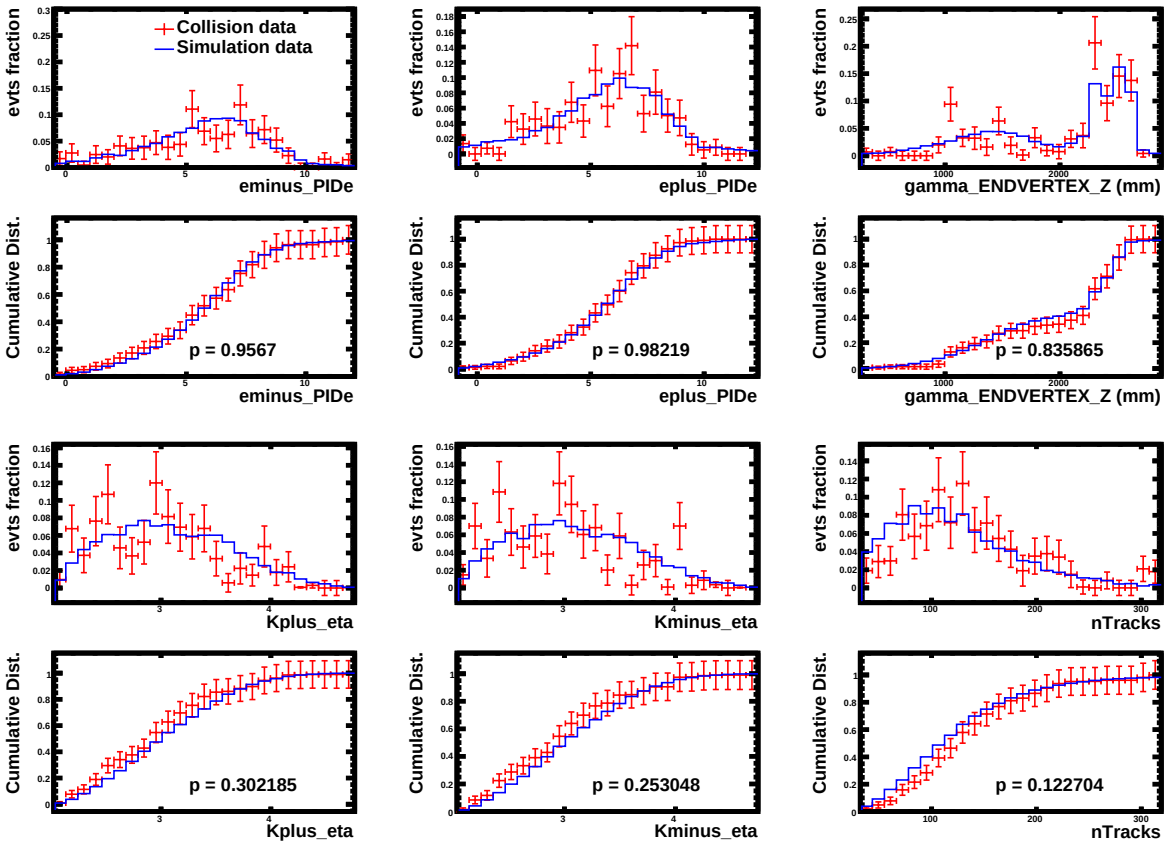

Figure B.8: Normalized and cumulative distributions of variables (2) used in the selection process for $B_s^0 \to \phi\gamma$ in the *DD* track type configuration simulation sample (full blue line) and weighted data (red histogram). Kolmogorov-Smirnov test result are given.

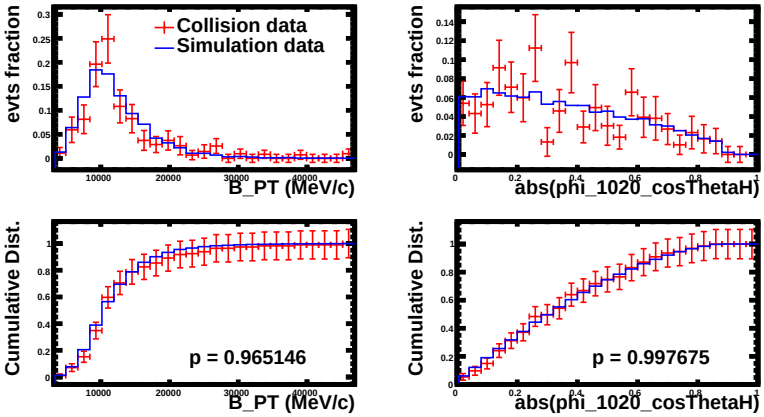

Figure B.9: Normalized and cumulative distributions of variables (3) used in the selection process for $B_s^0 \to \phi\gamma$ in the *DD* track type configuration simulation sample (full blue line) and weighted data (red histogram). Kolmogorov-Smirnov test result are given.

- $B_s^0 \to \phi\gamma$ decay in the LL track type configuration: Figs. B.10 B.11 B.12.

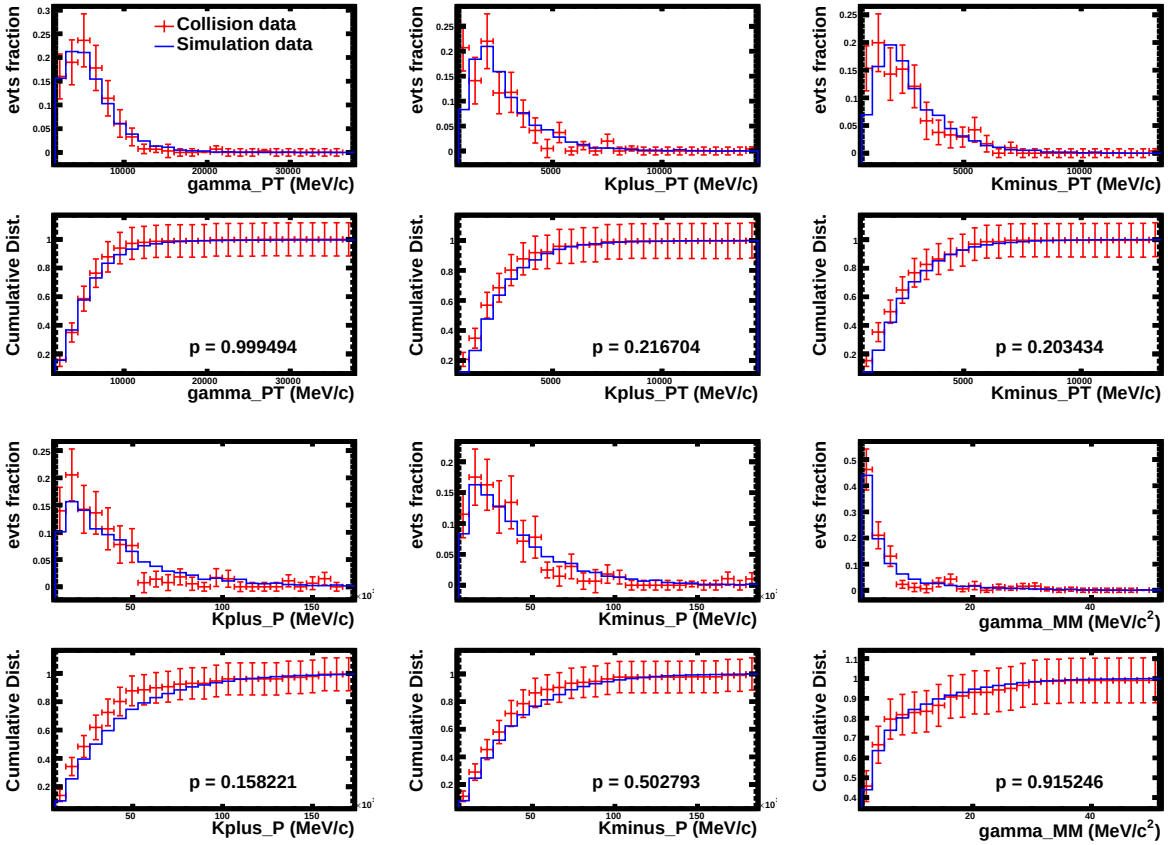

Figure B.10: Normalized and cumulative distributions of variables (1) used in the selection process for $B_s^0 \to \phi\gamma$ in the LL track type configuration simulation sample (full blue line) and weighted data (red histogram). Kolmogorov-Smirnov test result are given.

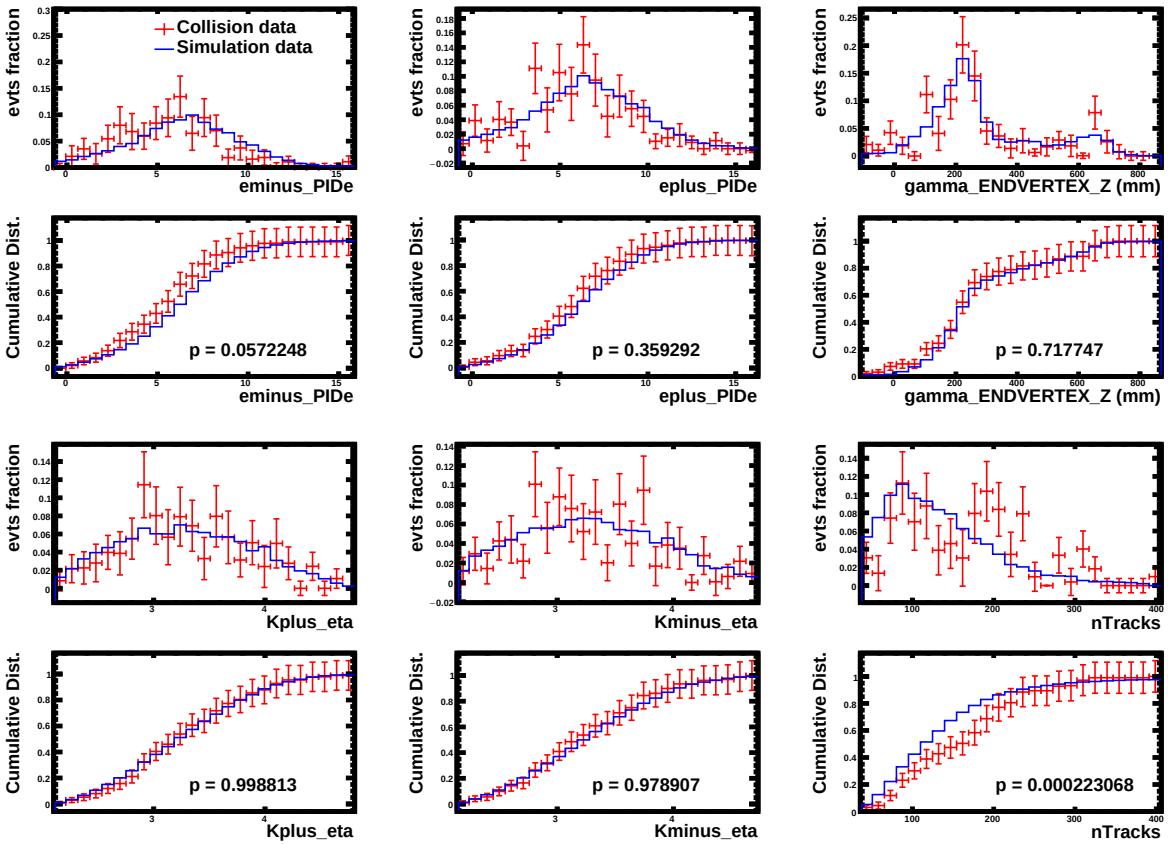

Figure B.11: Normalized and cumulative distributions of variables (2) used in the selection process for $B_s^0 \to \phi\gamma$ in the LL track type configuration simulation sample (full blue line) and weighted data (red histogram). Kolmogorov-Smirnov test result are given.

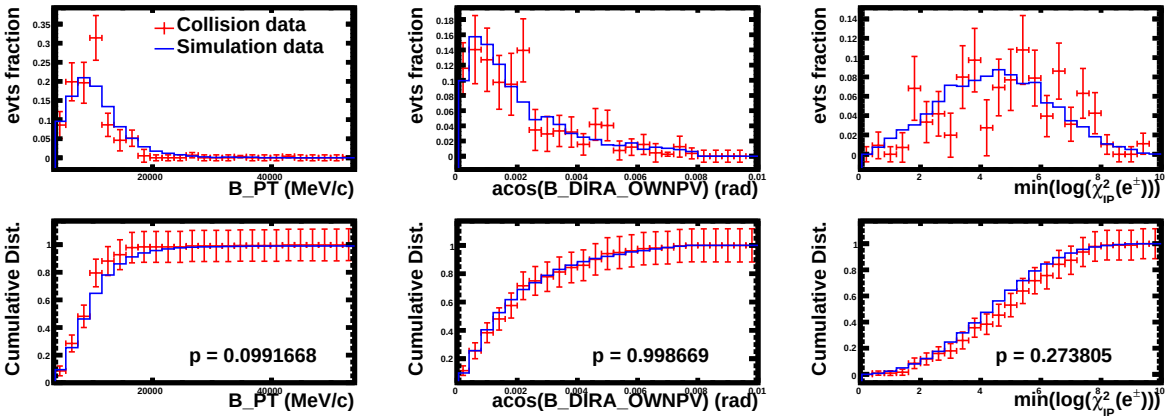

Figure B.12: Normalized and cumulative distributions of variables (3) used in the selection process for $B_s^0 \to \phi\gamma$ in the LL track type configuration simulation sample (full blue line) and weighted data (red histogram). Kolmogorov-Smirnov test result are given.

Appendix C

L0-trigger distribution comparison

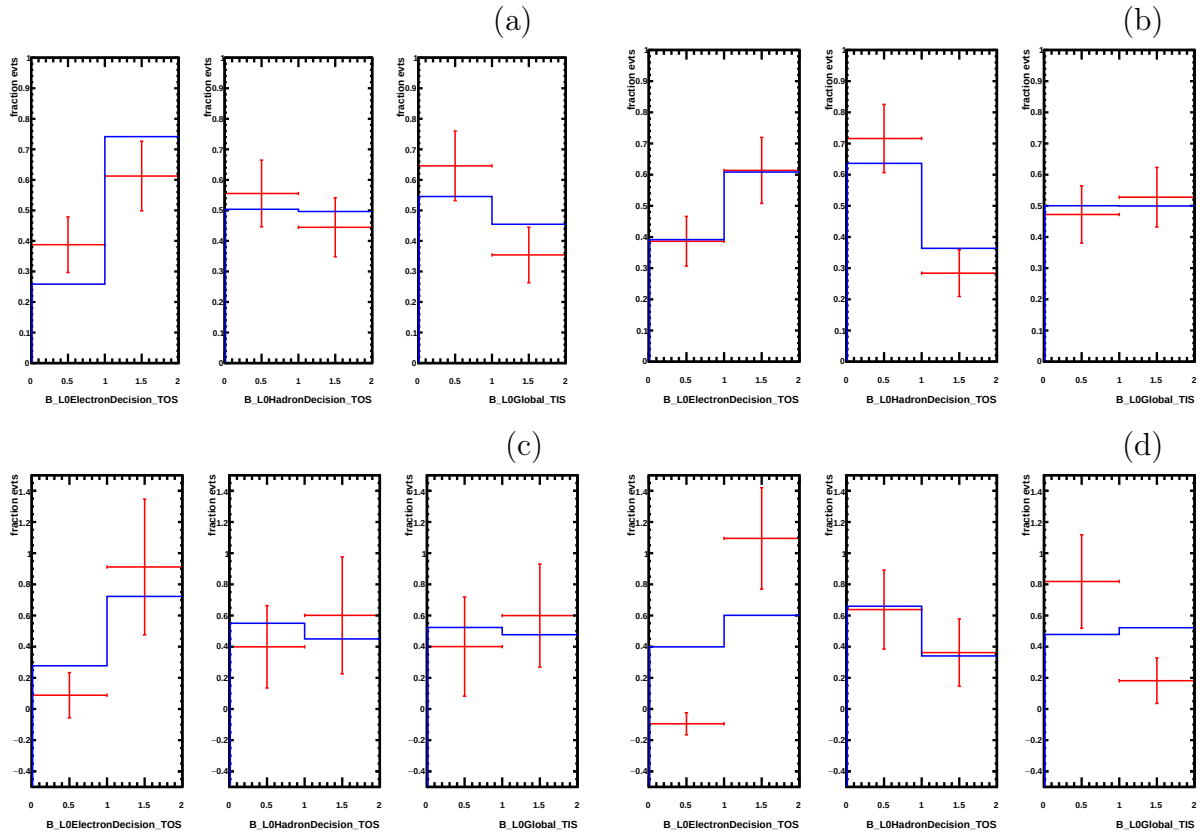

Figure C.1: L0-trigger line distribution for *2011low* samples, where bin 1 correspond to events which have triggered the line. Blue histogram correspond to simulation and red cross correspond to sWeighted data. Distributions for $B^0 \to K^{*0}\gamma(e^+e^-)$ samples in DD (a) and LL (b) configuration and for $B_s^0 \to \phi\gamma(e^+e^-)$ samples in DD (c) and LL (d) configuration are shown.

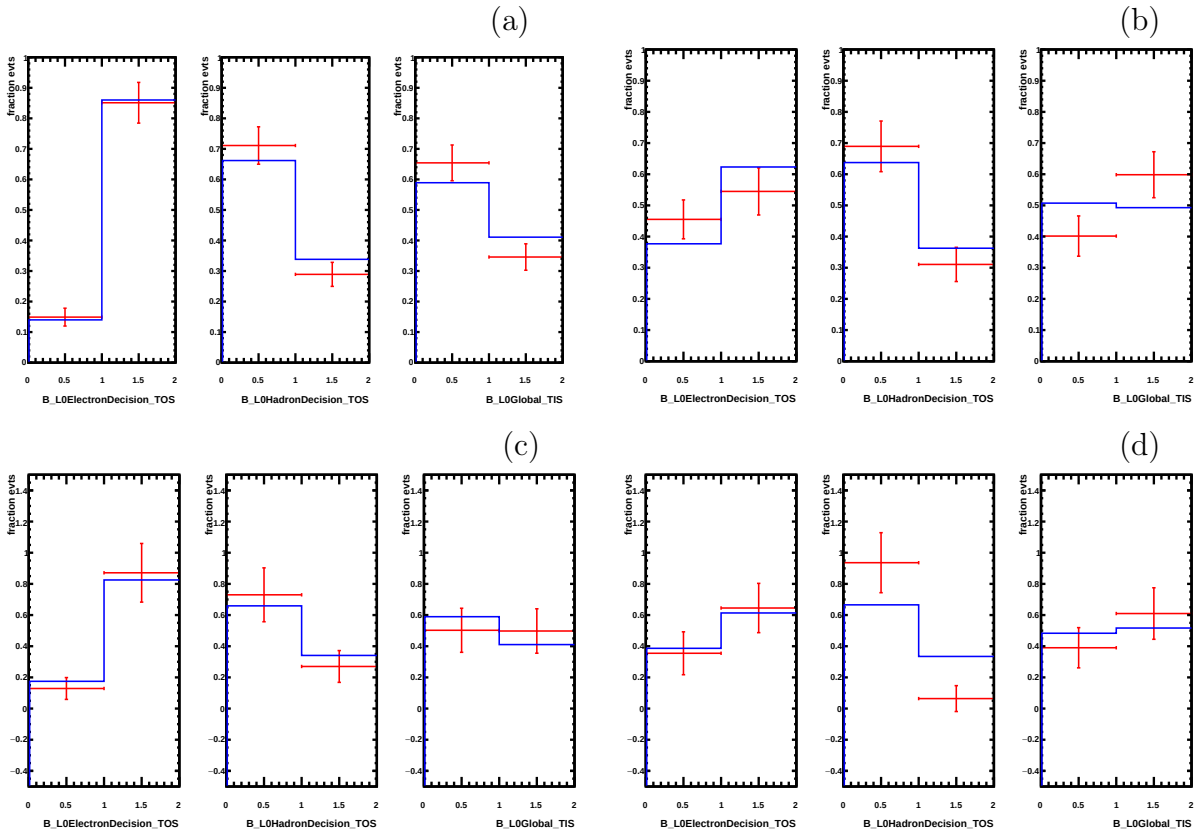

Figure C.2: L0-trigger line distribution for *2011high* samples, where bin 1 correspond to events which have triggered the line. Blue histogram correspond to simulation and red cross correspond to sWeighted data. Distributions for $B^0 \to K^{*0}\gamma(e^+e^-)$ samples in DD (a) and LL (b) configuration and for $B_s^0 \to \phi\gamma(e^+e^-)$ samples in DD (c) and LL (d) configuration are shown.

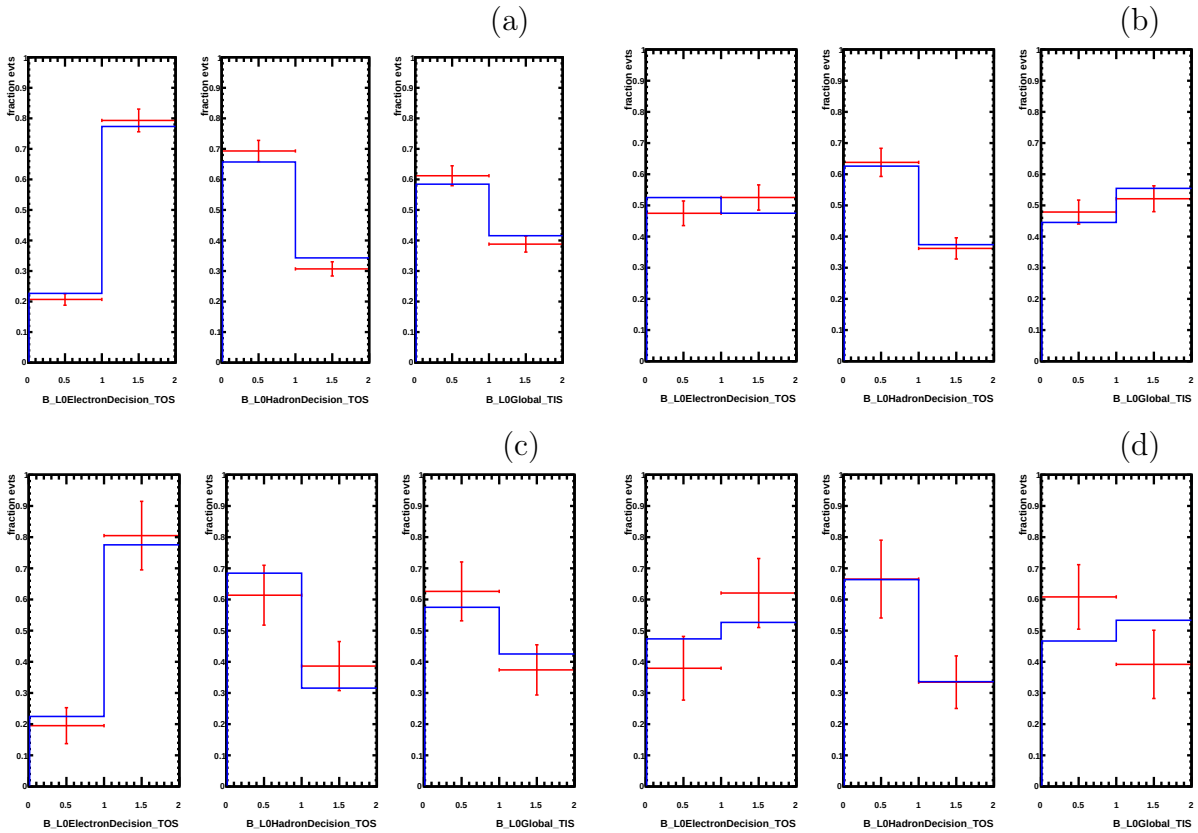

Figure C.3: L0-trigger line distribution for *2012* samples, where bin 1 correspond to events which have triggered the line. Blue histogram correspond to simulation and red cross correspond to sWeighted data. Distributions for $B^0 \to K^{*0}\gamma(e^+e^-)$ samples in *DD* (a) and *LL* (b) configuration and for $B_s^0 \to \phi\gamma(e^+e^-)$ samples in *DD* (c) and *LL* (d) configuration are shown.

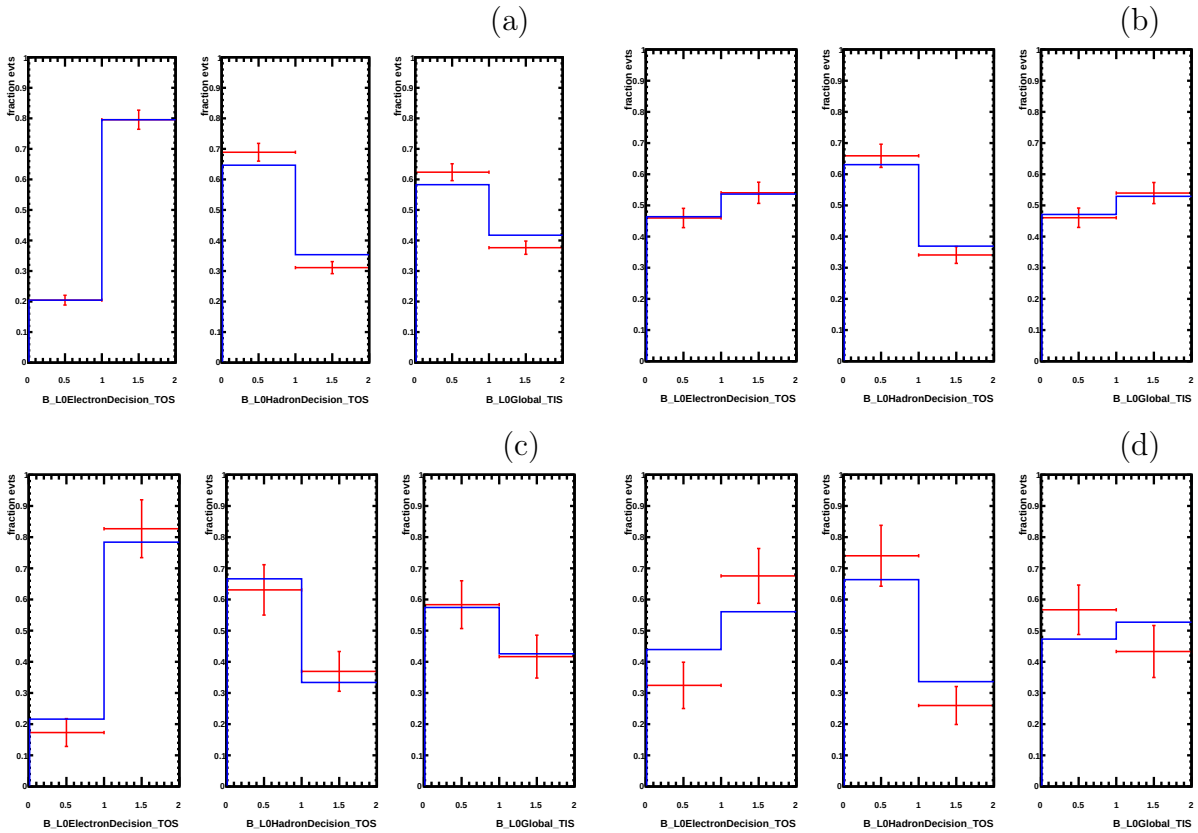

Figure C.4: L0-trigger line distribution for merged samples, where bin 1 correspond to events which have triggered the line. Blue histogram correspond to simulation and red cross correspond to sWeighted data. Distributions for $B^0 \to K^{*0}\gamma(e^+e^-)$ samples in DD (a) and LL (b) configuration and for $B_s^0 \to \phi\gamma(e^+e^-)$ samples in DD (c) and LL (d) configuration are shown.

Appendix D

Systematics from fixed parameters

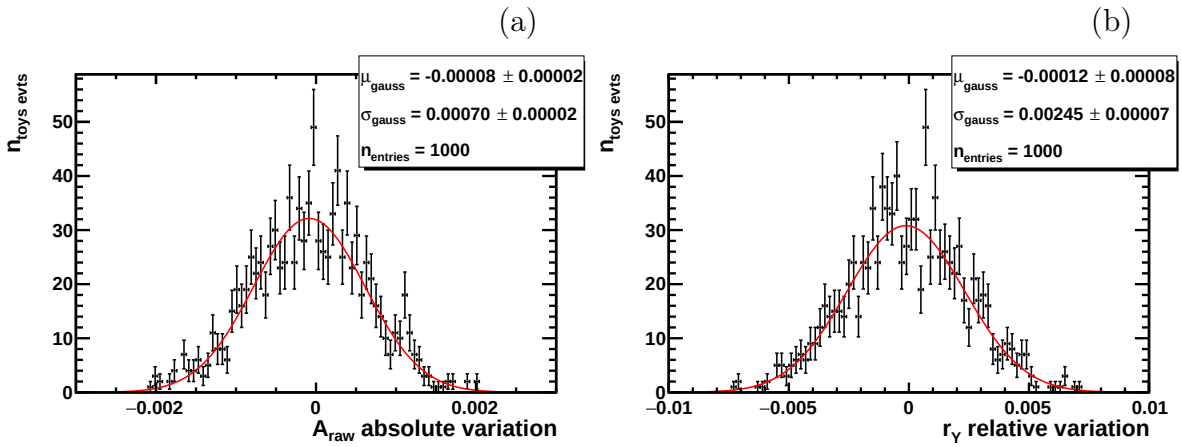

Figure D.1: Absolute variation of A_{RAW} (a) and relative variation of r_Y (b) when varying the fixed parameters of the signal model.

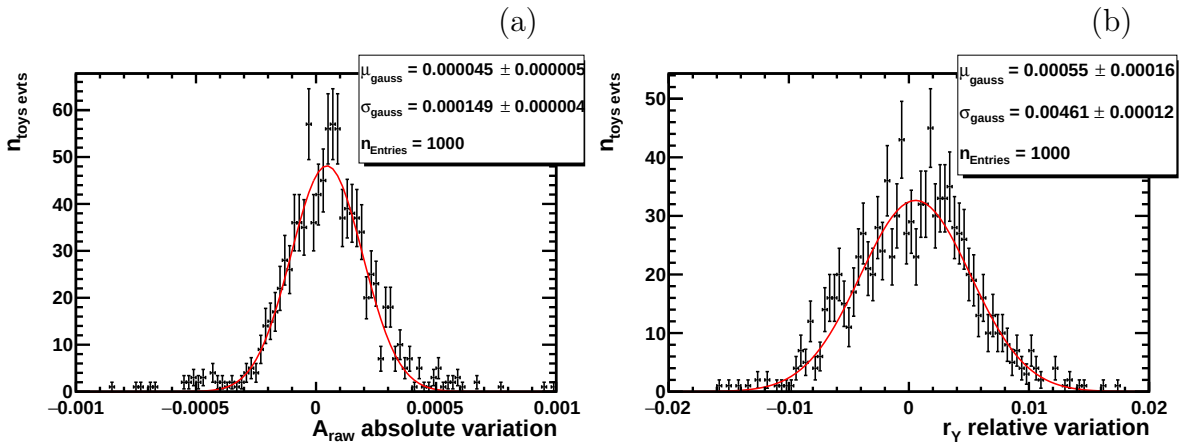

Figure D.2: Absolute variation of A_{RAW} (a) and relative variation of r_Y (b) when varying the fixed parameters of the peaking backgrounds model.

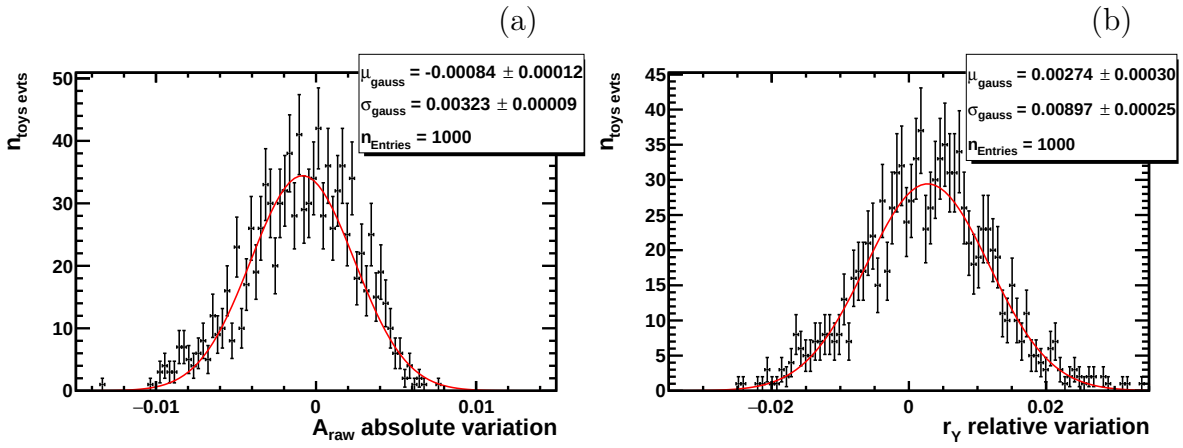

Figure D.3: Absolute variation of A_{RAW} (a) and relative variation of r_Y (b) when varying the fixed parameters of the low mass backgrounds model.

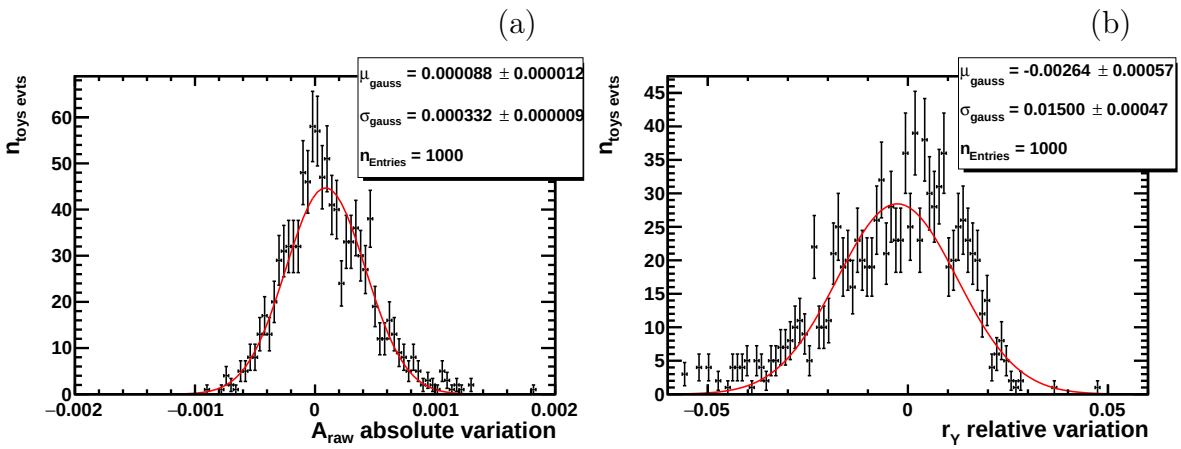

Figure D.4: Absolute variation of A_{RAW} (a) and relative variation of r_Y (b) when varying the fixed parameters of the background relative contaminations.